



**HAL**  
open science

# Precursor chemistry of novel metal triazenides: Solution and vapor phase elaborations of Fe and Al<sub>13</sub>Fe<sub>4</sub> nanomaterials

Khaled Soussi

► **To cite this version:**

Khaled Soussi. Precursor chemistry of novel metal triazenides: Solution and vapor phase elaborations of Fe and Al<sub>13</sub>Fe<sub>4</sub> nanomaterials. Catalysis. Université de Lyon, 2017. English. NNT: 2017LYSE1006 . tel-01513076

**HAL Id: tel-01513076**

**<https://theses.hal.science/tel-01513076>**

Submitted on 24 Apr 2017

**HAL** is a multi-disciplinary open access archive for the deposit and dissemination of scientific research documents, whether they are published or not. The documents may come from teaching and research institutions in France or abroad, or from public or private research centers.

L'archive ouverte pluridisciplinaire **HAL**, est destinée au dépôt et à la diffusion de documents scientifiques de niveau recherche, publiés ou non, émanant des établissements d'enseignement et de recherche français ou étrangers, des laboratoires publics ou privés.



N° d'ordre NNT : 2017LYSE1006

## THÈSE DE DOCTORAT DE L'UNIVERSITÉ DE LYON

opérée au sein de  
l'Université Claude Bernard Lyon 1

École Doctorale ED206  
Chimie, Procédés, Environnement

Spécialité de doctorat : Chimie  
Discipline : Chimie

Soutenue publiquement le 27/01/2017, par :  
**Khaled Soussi**

---

### Precursor chemistry of novel metal triazenides : Solution and vapor phase elaborations of *Fe* and *Al<sub>13</sub>Fe<sub>4</sub>* nanomaterials

---

Devant le jury composé de :

Mme. Catherine Santini, Directeur de Recherche, CPE Lyon	Présidente
M. Franck Denat, Professeur, Université de Bourgogne	Rapporteur
Mme. Elisabeth Blanquet, Directrice de Recherche, INP Grenoble	Rapporteur
M. Constantin Vahlas, Directeur de Recherche, CIRIMAT Toulouse	Examineur
M. Christophe Darcel, Professeur, Université de Rennes1	Examineur
Mme. Amandine Cabiac, Ingénieur de recherche, IFP Energies nouvelles	Examinatrice
M. Stéphane Daniele, Professeur, Université de Lyon1	Directeur de thèse
M. Shashank Mishra, Maître de conférences- HDR, Université de Lyon1	Co-directeur de thèse
M. Franck Morfin, Ingénieur de recherche, IRCELYON/CNRS	Invité



## Abstract

Polyethylene production from the polymerization of ethylene is an industrial process of great importance. Ethylene stream for the polymerization of polyethylene is produced by the steam cracking of a wide range of hydrocarbon feedstocks and usually contains acetylene impurities (1%) which poisons the polymerization catalyst. The ethylene stream has to be purified by the selective semi-hydrogenation of acetylene which requires a catalyst with high selectivity to hydrogenate acetylene to ethylene. The intermetallic compound  $Al_{13}Fe_4$  was introduced in 2012 by Armbuster *et al.* as an active and selective catalyst for the semi-hydrogenation of acetylene for polyethylene production [1]. It has a crystal structure with high average inter-atomic distances Fe-Fe and a low coordination number of iron atoms, which falls under the concept of "site isolation principle". This compound is also attractive because of its low cost (without any noble metals compared to Pd/ $Al_2O_3$  industrial catalysts) and low toxicity. However, it has been produced in the form of unsupported powder by the Czochralski method [2] which limits its use in catalytic engineering. In this context, supporting the catalyst presents many advantages as the ease of separation of the heterogeneous catalyst from the reaction mixture. In contrast to homogeneous catalysts- in which separation is often costly and difficult, separating the supported heterogeneous catalyst can be achieved by a variety of methods such as filtration for example. Another advantage of supported catalysts is the higher surface area of the catalyst. Since catalysis is a surface reaction, consequently, maximizing the surface area of a catalyst by distributing it over the support will enhance/optimize the catalytic activity.

Chemical synthetic routes such as Metal Organic Chemical Vapor Deposition (MOCVD) and Metal Organic Deposition (MOD) referred as "Chimie douce" process are reputed to be a flexible and economically competitive methods to prepare nanoparticles or thin films. Our work is thus aimed at developing  $Al_{13}Fe_4$  as supported films or nanoparticles by MOCVD and/or MOD.

The first step to meet our objective is the development of compatible molecular precursors of metallic aluminum and iron followed by MOCVD or MOD of those precursors

to form the intermetallic compound in the good stoichiometry.

Among the numerous aluminum MOCVD precursors used in the literature, dimethyl ethylaminealane (DMEAA,  $[AlH_3(NMe_2Et)]$ ) is used due to its properties such as high vapor pressure and low deposition temperatures. Moreover, the absence of aluminum-oxygen and aluminum-carbon bonds leads to the production of carbon and oxygen free films.

However, iron molecular precursors for the MOCVD of pure iron films are scarce and less developed. Apart from iron pentacarbonyl that produces pure iron films, amidinates and guanidinates are used as iron precursors. However, oxygen and carbides impurities are present in high percentages. Thus the main objective of this Ph-D work is to design and synthesize novel and original iron molecular complexes that serve as precursors for the low temperature MOCVD of iron films.

The first chapter of this thesis presents the state of the art of precursors used for the MOCVD of aluminium and iron containing thin films. The second chapter of the manuscript presents the synthesis and characterization of iron and aluminium triazenide complexes. The third chapter discusses in details the preparation of films and nanomaterials of aluminium and iron. The fourth chapter presents the preparation and catalytic tests of  $Al_{13}Fe_4$  films and nanoparticles. The triazenide chemistry was extended to other transition metals. The synthesis and characterization of titanium, niobium and tantalum triazenide compounds will be discussed in chapter 5.

In this Ph-D work, nanoparticles of the intermetallic complex were prepared via solution reduction of novel Fe triazenide precursors and Al metal. Supported films were also prepared via sequential MOCVD deposition by using DMEAA and iron pentacarbonyl as molecular precursors. Its catalytic properties have been explored and showed that it is very little active in the hydrogenation reaction of acetylene. It showed very little activity of less than 1% with high selectivity before deactivating rapidly. Regeneration under hydrogen or oxygen was not very successful and only some activity restored. The catalytic tests have been further extended to  $Al_{13}Fe_4$  powder prepared by solution reduction as well as to  $Al_{13}Fe_4$  powder bought commercially and found that  $Al_{13}Fe_4$  was non active catalytically in all forms (in our conditions of reactions).

**Key-words:**  $Al_{13}Fe_4$ ; nanoparticles; metal organic chemical vapor deposition (MOCVD); Metal Organic Deposition (MOD); triazenides; precursors.

## Résumé

La production de polyéthylène par la polymérisation de l'éthylène est un procédé industriel de grande importance. L'éthylène, issue de la pétrochimie contient des impuretés d'acétylène (1%), ce qui empoisonne le catalyseur de polymérisation, et donc le besoin d'un catalyseur qui soit sélectif pour hydrogéner l'acétylène en éthylène.

Le composé intermétallique  $Al_{13}Fe_4$  a été développé par Armbuster *et al.* en 2012 comme un catalyseur actif et sélectif pour la semi-hydrogénation de l'acétylène pour la production de polyéthylène [1]. Il présente une structure cristalline avec des distances inter-atomiques Fe-Fe élevées et un faible nombre de coordination des atomes de fer, qui tombe sous le concept de "site isolation principle". Ce composé est également intéressant en raison de son faible coût (sans métaux nobles par rapport à Pd /  $Al_2O_3$  catalyseurs industriels) et une faible toxicité. Cependant, il a été produit sous la forme de poudre non supportée par la méthode Czochralski [2] ce qui limite son utilisation dans le domaine du génie catalytique. Dans ce contexte, supporter le catalyseur présente de nombreux avantages comme la facilité de séparation du catalyseur hétérogène à partir du mélange réactionnel obtenu par une variété de procédés telle que la filtration par exemple. Un autre avantage des catalyseurs supportés est la plus grande surface exposée du catalyseur ou dispersion. Etant donné que la catalyse est une réaction de surface, maximiser la surface d'un catalyseur, en le dispersant sur le support améliorera / optimisera l'activité catalytique.

Les procédés de "chimie douce" dénommés Metal Organic Chemical Vapor Deposition (MOCVD) et Metal Organic Deposition (MOD) sont réputés pour être efficaces et économiquement compétitifs pour déposer des nanoparticules ou des films minces, à partir de précurseurs moléculaires appropriés. Notre travail vise donc à développer  $Al_{13}Fe_4$  sous forme de films ou de nanoparticules supportées par MOCVD.

La première étape pour atteindre cet objectif est le développement des précurseurs moléculaires d'aluminium métallique et de fer, dans des conditions compatibles suivies par co-dépôt ou le dépôt séquentiel des deux précurseurs de fer et d'aluminium pour former le composé intermétallique dans la bonne stoechiométrie.

Parmi les nombreux précurseurs d'aluminium MOCVD, le diméthyl ethylaminealane (DMEAA,  $[AlH_3(NMe_2Et)]$ ) est utilisé en raison de sa pression de vapeur importante et des températures de dépôt faibles. En outre, l'absence de liaisons aluminium-oxygène et aluminium-carbone conduit à la production de films sans impuretés carbone et oxygène.

Cependant, des précurseurs moléculaires de fer pour le dépôt pour MOCVD de films de fer purs sont rares et moins développés. En dehors du pentacarbonyle de fer qui produit des films de fer pur, amidinates et guanidinates sont utilisés comme précurseurs de fer. Cependant, l'oxygène et des carbures sont présents dans des pourcentages élevés. Ainsi, l'objectif principal de ce travail de thèse est de concevoir et de synthétiser de nouveaux complexes moléculaires de fer qui servent de précurseurs pour la MOCVD.

Le premier chapitre de cette thèse présente l'état de l'art des précurseurs utilisés pour la MOCVD d'aluminium et de fer et l'obtention des films minces. Le deuxième chapitre présente la synthèse et la caractérisation de composés de fer et aluminium à base de triazinure pour la préparation de nanomatériaux de fer et aluminium. Le troisième chapitre traite de la MOCVD de films d'aluminium à partir de DMEAA ainsi que la synthèse de nanomatériaux de fer par la MOD à partir de triazinures de fer. La préparation et les tests catalytiques de  $Al_{13}Fe_4$  seront discutés dans le chapitre 4. Le chapitre 5 présente la synthèse et la caractérisation de triazinures de titane, de niobium et de tantale triazenide.

Dans ce travail, des nanoparticules de composé intermétallique  $Al_{13}Fe_4$  sont préparées par réduction en solution et des films par dépôt séquentiel MOCVD en utilisant DMEAA et le pentacarbonyle de fer en tant que précurseurs moléculaires. Les propriétés catalytiques ont été étudiées et ont montré d'une activité très peu active dans la réaction d'hydrogénation de l'acétylène: moins de 1 % avant de se désactiver rapidement. La régénération sous hydrogène ou sous oxygène n'a qu'une faible restauration de l'activité. Les tests catalytiques ont été encore étendus à  $Al_{13}Fe_4$  poudre préparée par réduction en solution ainsi que  $Al_{13}Fe_4$  en poudre commerciale et ont constaté que  $Al_{13}Fe_4$  était non catalytiquement actif sous toutes ses formes (dans nos conditions de réaction).

**Mots-clé :**  $Al_{13}Fe_4$ ; nanoparticules; CVD; triazinures; metal organic chemical vapor deposition (MOCVD); Metal Organic Deposition (MOD); précurseurs.

# Acknowledgements

First and the foremost, I would like to express my sincere gratitude to my advisors Prof. Stéphane DANIELE and Dr. Shashank MISHRA for their support and trust. They are most responsible for helping me complete this thesis as well as the challenging research that lies behind it. Their wide knowledge and their logical way of thinking have been of great value for me. They were always there to meet and talk about my ideas throughout the weekly discussions and meetings. Without their encouragement, constant guidance, all their tolerance and patience, I could not have finished this thesis. They have spent very much precious time to discuss my work and to help me analyse the existed problems and so on during the last three years. I would like to extend my gratitude for Dr. Constantin VAHLAS, Dr. Thomas DUGUET, Daniel SADOWSKI, Dr. Yiannis AVIZIOTIS and to all my my colleagues at CIRIMAT Toulouse for all their help and support during various visits to Toulouse for CVD experiments.

I would also like to thank Mr. Thibault CORNIER for giving me and to every one in IRCELYON technical helps. Without him, many experiments would have never been made. I am thankfull to my dear colleagues at IRCELYON for kindly, professional sharing the experience on their study and work. I take this opportunity to thank the jury members for spending their precious time to read and review this thesis, for taking a long trip to attend this defence, and for giving me valuable comments. I am grateful for the financial support of IFPEN and Labex iMUST.

I am very grateful to all our colleagues who collaborated with us and helped us enrich our work. I would like to thank Dr. Jean-Marc MILLET, Dr. Erwann JEANNEAU, Dr. Franck MORFIN, Dr. Jean-Luc ROUSSET, Dr. Jean-Bernard TOMMASINO, Mr. Lhoussain KHROUZ and Mr. Bishoy MORCOS.

In addition, I would like to extend my special gratitude to my family: my mother, father and sisters and my family in law. Their unconditional support has always helped me to bounce back whenever I felt low. And to my wife, I can't thank you enough. You have believed in me and kept my spirit high. You taught me how to be optimistic and supported me unconditionally. I love you.

Finally, I would like to take this opportunity to thank my dear friends for their kindness and help all these years.

# Contents

<b>Abstract</b>	<b>i</b>
<b>Résumé</b>	<b>iii</b>
<b>Acknowledgements</b>	<b>v</b>
<b>Acronyms</b>	<b>xxii</b>
<b>1 Introduction</b>	<b>1</b>
1.1 Acetylene semi-hydrogenation: From Pd based catalysts to cheaper un-supported $Al_{13}Fe_4$ intermetallics . . . . .	2
1.1.1 $Al_{13}Fe_4$ Intermetallic Catalyst . . . . .	4
1.1.2 Supported $Al_{13}Fe_4$ by MOCVD . . . . .	6
1.2 Principles and requirements of precursors for MOCVD process . . . . .	7
1.2.1 MOCVD principles . . . . .	7
1.2.2 MOCVD precursor requirements . . . . .	8
1.3 MOCVD Precursors for metallic aluminium and iron . . . . .	8
1.3.1 Aluminium MOCVD precursors . . . . .	8
1.3.2 Iron MOCVD precursors . . . . .	10
1.4 Thesis objectives . . . . .	17
<b>2 Iron and Aluminium triazenide complexes</b>	<b>19</b>
2.1 Introduction . . . . .	20
2.2 Iron(II) precursors with Fe-P bond . . . . .	20
2.2.1 Results and Discussion . . . . .	20
2.3 Iron(II) precursors with Fe-N bond . . . . .	23
2.3.1 Results and Discussion . . . . .	24
2.3.2 Mössbauer spectroscopy . . . . .	33
2.3.3 Electron Paramagnetic Resonance EPR . . . . .	37

2.3.4	Electrochemistry . . . . .	41
2.3.5	Thermal properties . . . . .	45
2.4	Aluminium triazenide complexes . . . . .	47
2.4.1	Starting from $Al_2(CH_3)_6$ . . . . .	48
2.4.2	Starting from $AlH_3(NMe_2Et)$ . . . . .	53
2.4.3	Thermal behavior of aluminium triazenide compounds . . . . .	57
2.5	Conclusion . . . . .	59
<b>3</b>	<b>Aluminium and Iron nanomaterials</b> . . . . .	<b>61</b>
3.1	Introduction . . . . .	61
3.2	Results and Discussion . . . . .	62
3.2.1	Al CVD from DMEAA . . . . .	63
3.2.2	Iron CVD from iron triazenide complexes . . . . .	69
3.2.3	Iron nanomaterials from iron triazenides: solid state MOD . . . . .	72
3.3	Conclusion . . . . .	78
<b>4</b>	<b>Preparation and catalytic tests of <math>Al_{13}Fe_4</math></b> . . . . .	<b>81</b>
4.1	Introduction . . . . .	81
4.2	Results and Discussion . . . . .	82
4.2.1	$Al_{13}Fe_4$ films via MOCVD . . . . .	82
4.2.2	$Al_{13}Fe_4$ nanoparticles via MOD . . . . .	85
4.3	Catalytic activity of $Al_{13}Fe_4$ nanoparticles and thin films for the semi hydrogenation of acetylene . . . . .	88
4.4	Conclusion . . . . .	90
<b>5</b>	<b>Titanium, niobium and tantalum triazenide complexes</b> . . . . .	<b>93</b>
5.1	Introduction . . . . .	94
5.2	Results and Discussion . . . . .	97
5.2.1	Synthesis and characterization of titanium, niobium and tantalum triazenide compounds . . . . .	97
5.2.2	Thermal behaviours of of titanium, niobium and tantalum triazenides . . . . .	101
5.2.3	X-ray crystal structure . . . . .	103
5.2.4	Titanium nanomaterials: MOD in solution . . . . .	104
5.2.5	Deposition of of NbN films using Niobium triazenide complex . . . . .	105
5.3	Conclusion . . . . .	108
<b>6</b>	<b>General Conclusions and Perspectives</b> . . . . .	<b>109</b>

---

<b>7</b>	<b>General Experimental Part</b>	<b>113</b>
7.1	Characterization methods . . . . .	114
7.2	Synthesis of the compounds . . . . .	118
	<b>Bibliography</b>	<b>137</b>
	<b>List of publications</b>	<b>145</b>



# List of Tables

2.1	Selected bond lengths of complexes <b>1</b> and <b>3</b> . . . . .	31
2.2	Selected bond angles of complexes <b>1</b> and <b>3</b> . . . . .	31
2.3	Selected bond lengths of complexes <b>4</b> and <b>5</b> . . . . .	31
2.4	Selected bond angles of complexes <b>4</b> and <b>5</b> . . . . .	32
2.5	Selected bond lengths of complexes <b>6</b> and <b>7</b> . . . . .	32
2.6	Selected bond angles of complexes <b>6</b> and <b>7</b> . . . . .	32
3.1	Experimental conditions of the deposition experiments of 1hr till 8 <sup>th</sup> run and 2 hrs for the 9 <sup>th</sup> run. . . . .	64
3.2	Characterization data of aluminium films deposited. . . . .	68
3.3	Experimental conditions for the CVD experiments of ( <b>4</b> ). . . . .	71
3.4	% atomic concentration and position in eV of species present after the decomposition of ( <b>1</b> ) on silica. . . . .	75
3.5	Species present, isomer shifts, quadrupole splitting and relative intensities of iron (0) nanoparticles prepared in solution decomposition of $[Fe(N_3^tBuEt)_2(TMEDA)]$ ( <b>4</b> ). . . . .	77
4.1	% atomic concentration of species present on the least oxidized part A and in the most oxidized one B in the sample of $Al_{13}Fe_4$ nanoparticles. . . . .	88
5.1	TGA data of the the compounds <b>14-18</b> . . . . .	103
5.2	Selected bond lengths and angles of $[Ti(N_3^tBu_2)_2(NMe_2)_2]$ ( <b>16</b> ). . . . .	104
7.1	Crystallographic and refinement data for complexes <b>1, 3, 4, 5, 6, 7</b> and <b>16</b> . . . . .	118



# List of Figures

1.1	Hydrogenation of acetylene; Path A: through a bi-sigma bonded intermediate. Path B: through a pi-bonded intermediate [3]. . . . .	3
1.2	Aluminium-iron phase diagram [8]. . . . .	5
1.3	Unit cell of $Al_{13}Fe_4$ illustrating the site isolation of Fe atoms; colour scheme: green (Al), blue (Fe) [1]. . . . .	5
1.4	Schematic representation of MOCVD mechanism [11]. . . . .	7
1.5	Commonly used precursors for the deposition of thin Al films: a) <i>Triiso</i> -butyl aluminum (TIBA), b) dimethyl aluminum hydride (DMAH) and c) dimethylethylamine alane (DMEAA). . . . .	9
1.6	$H_2Fe[P(CH_3)_3]_4$ used for the MOCVD of iron films. . . . .	11
1.7	Complexes used as suitable precursors for the MOCVD of iron films. . . . .	13
1.8	a) Amidinate and; b) guanidinate ligand. . . . .	14
1.9	Coordination modes of amidinates and guanidinates. . . . .	14
1.10	Some amidinate and guanidinate complexes as CVD precursors. . . . .	15
1.11	Different bonding modes for triazenide ligand; a: monodentate, b: chelating, c: bridging. . . . .	16
1.12	Near parallel projection of the 2 N-donor atom orbitals in triazenide ligand increasing its tendency to act as a bridging ligand. . . . .	17
2.1	a) $[H_2Fe(PMe_3)_4]$ purified by sublimation. b) $[H_2Fe(PMe_3)_4]$ decomposes readily. . . . .	21
2.2	Perspective view of $[FeH_2(BH_3)(dmpe)_2]$ with thermal ellipsoids at 50% level. H-atoms are omitted for clarity. . . . .	22
2.3	TGA of $[FeH_2(BH_3)(dmpe)_2]$ . . . . .	22
2.4	FT-IR spectra for <b>L1-L4</b> . . . . .	25
2.5	TGA curves of triazene ligands <b>L1-L4</b> . . . . .	25
2.6	FT-IR spectra for complexes <b>1-3</b> . . . . .	26
2.7	FT-IR spectra for complexes <b>4-7</b> . . . . .	27

2.8	Perspective view of <b>1</b> and <b>3</b> with thermal ellipsoids at 50% level. H-atoms are omitted for clarity. . . . .	29
2.9	Perspective view of <b>4-7</b> with thermal ellipsoids at 50% level. H-atoms are omitted for clarity. . . . .	30
2.10	Mössbauer spectra of $[Fe(N_3^tBu_2Et)_2(TMEDA)]$ ( <b>4</b> ). . . . .	33
2.11	Variable temperature Mössbauer spectra of $[Fe_2(N_3^tBuEt)_4]$ ( <b>1</b> ) at 4.2K (a), 77K (b), 150K (c) and 298K (d) while being heated gradually. . . . .	35
2.12	Variable temperature Mössbauer spectra of $[Fe_2(N_3^tBuEt)_4]$ ( <b>1</b> ) at 250K (a), 200K (b) and 77 K (c) while being cooled gradually. . . . .	36
2.13	EPR experimental spectrum of $[Fe_2(N_3^tBuEt)_4]$ ( <b>1</b> ); blue: solid, red: in THF solution, green: in hexane solution, at 112K, standard cavity, a) low fields, and b) high fields. . . . .	37
2.14	EPR experimental spectrum of $[Fe_2(N_3^tBuEt)_4]$ ( <b>1</b> ) solid, perpendicular mode: a) Iepr at low fields, and b) Iepr at high fields c) $\chi''$ Vs T d) $1/\chi''$ Vs T. . . . .	38
2.15	EPR experimental spectrum of $[Fe_2(N_3^tBuEt)_4]$ ( <b>1</b> ) solid, perpendicular mode: a) $\chi''$ Vs T, and b) $1/\chi''$ Vs T. . . . .	38
2.16	EPR experimental spectrum of $[Fe_2(N_3^tBuEt)_4]$ ( <b>1</b> ) solid in parallel mode: a) Iepr at low fields, and b) Iepr at high fields. . . . .	40
2.17	EPR experimental spectrum of $[Fe_2(N_3^tBuEt)_4]$ ( <b>1</b> ) solid in parallel mode: a) $\chi''$ Vs T, and b) $1/\chi''$ Vs T. . . . .	40
2.18	$[Fe_2(N_3^tBuEt)_4]$ ( <b>1</b> ) solid , a) blue: experimental @20K in parallel mode, green: simulated b) blue: experimental @112K with standard cavity, green: simulated. . . . .	41
2.19	EPR experimental spectrum of $[Fe(N_3^tBuEt)_2(TMEDA)]$ ( <b>4</b> ) in solid state. . . . .	41
2.20	Voltammogram of $[Fe_2(N_3^tBuEt)_4]$ ( <b>1</b> ), $[Fe_2(N_3^tBu^iPr)_4]$ ( <b>2</b> ) and $[Fe_2(N_3^tBu^nBu)_4]$ ( <b>3</b> ). . . . .	42
2.21	Cyclic voltammogram of $[Fe(N_3^tBuEt)_2(TMEDA)]$ ( <b>4</b> ), $[Fe(N_3^tBu^iPr)_2(TMEDA)]$ ( <b>5</b> ) and $[Fe(N_3^tBu^nBu)_2(TMEDA)]$ ( <b>6</b> ). . . . .	44
2.22	Cyclic voltammogram of $[Fe_2(N_3^tBuEt)_4]$ ( <b>1</b> ) in anhydrous $CH_2Cl_2$ , 0.1 M ( $^nBu_4N$ )PF <sub>6</sub> , 100 mV. . . . .	44
2.23	TGA curves of $[Fe_2(N_3^tBuEt)_4]$ ( <b>1</b> ), $[Fe_2(N_3^tBu^iPr)_4]$ ( <b>2</b> ) and $[Fe_2(N_3^tBu^nBu)_4]$ ( <b>3</b> ). . . . .	45
2.24	TGA curves of $[Fe(N_3^tBuEt)_2(TMEDA)]$ ( <b>4</b> ), $[Fe(N_3^tBu^iPr)_2(TMEDA)]$ ( <b>5</b> ), $[Fe(N_3^tBu^nBu)_2(TMEDA)]$ ( <b>6</b> ) and $[Fe(N_3^tBu_2)_2(TMEDA)]$ ( <b>7</b> ). . . . .	47
2.25	<sup>1</sup> H NMR spectrum of $[Al(N_3^tBuEt)_2(CH_3)]_m$ ( <b>8</b> ). . . . .	49
2.26	<sup>27</sup> Al spectrum of $[Al(N_3^tBuEt)_2(CH_3)]_m$ ( <b>8</b> ). . . . .	49

2.27	$^1H$ NMR spectrum of $[Al(N_3^tBuEt)_3(py)_3]_m$ ( <b>11</b> ).	50
2.28	$^{27}Al$ NMR spectrum of $[Al(N_3^tBuEt)_3(py)_3]_m$ ( <b>11</b> ).	51
2.29	$^1H$ NMR spectrum of $[Al(N_3^tBu^iPr)_3]_m$ ( <b>9</b> ).	52
2.30	$^{27}Al$ NMR spectrum of $[Al(N_3^tBu^iPr)_3]_m$ ( <b>9</b> ).	52
2.31	$^1H$ NMR spectrum of $[Al(N_3^tBu^nBu)_3]_m$ ( <b>10</b> ).	53
2.32	$^{27}Al$ NMR spectrum of $[Al(N_3^tBu^nBu)_3]_m$ ( <b>10</b> ).	53
2.33	$^1H$ NMR spectrum of $[Al(N_3^tBuEt)_3]_m$ ( <b>12</b> ).	54
2.34	$^{27}Al$ NMR spectrum of $[Al(N_3^tBuEt)_3]_m$ ( <b>12</b> ).	55
2.35	$^1H$ NMR spectrum of $[Al(N_3^tBu_2)_3]_m$ ( <b>13</b> ).	55
2.36	$^{27}Al$ NMR spectrum of $[Al(N_3^tBu_2)_3]_m$ ( <b>13</b> ).	56
2.37	Proposed equilibrium of aluminium triazenide complexes in solution.	56
2.38	TGA curves of $[Al(N_3^tBuEt)_2(CH_3)]_m$ ( <b>8</b> ) $[Al(N_3^tBuEt)_3(py)_3]_m$ ( <b>11</b> ) and $[Al(N_3^tBuEt)_3]_m$ ( <b>12</b> ).	57
2.39	TGA curves of $[Al(N_3^tBu^iPr)_3]_m$ ( <b>9</b> ), $[Al(N_3^tBu^nBu)_3]_m$ ( <b>10</b> ), $[Al(N_3^tBuEt)_3]_m$ ( <b>12</b> ), and $[Al(N_3^tBu_2)_3]_m$ ( <b>13</b> ).	58
3.1	MOCVD reactor setup.	63
3.2	SEM images of the films deposited at 140°C: a) and b) surface of the film at the center, c) cross section of the film in the center, d) cross section of the film on the right edge.	65
3.3	SEM images of the films deposited at 215°C: a) and b) surface of the film at the center, c) cross section of the film in the center, d) cross section of the film on the right edge.	65
3.4	SEM images of the films deposited at 260°C: a) and b) surface of the film at the center, c) cross section of the film in the center, d) cross section of the film on the right edge.	66
3.5	EDS analysis of films deposited: a) 140°C; b) at 200°C.	66
3.6	Arrhenius plot of Al MOCVD from DMEAA.	68
3.7	Setup of thermolysis of $[Fe_2(N_3^tBuEt)_4]$ ( <b>1</b> ) and $[Fe(N_3^tBuEt)_2(TMEDA)]$ ( <b>4</b> ).	72
3.8	Powder x-ray diffraction pattern for $[Fe_2(N_3^tBuEt)_4]$ ( <b>1</b> ) under hydrogen treatment at 200°C and 500°C.	73
3.9	Fe 2p XPS spectra of the decomposed complexes $[Fe_2(N_3^tBuEt)_4]$ ( <b>1</b> ) and $[Fe(N_3^tBuEt)_2(TMEDA)]$ ( <b>4</b> ) on silica.	74
3.10	Fitting of Fe 2p XPS spectra of the decomposed complex $[Fe_2(N_3^tBuEt)_4]$ ( <b>1</b> ) on silica.	74
3.11	<i>In situ</i> Fe 2p XPS spectra of the decomposed complex $[Fe_2(N_3^tBuEt)_4]$ ( <b>1</b> ) at 200°C and 500°C.	75

3.12 Mossbauer spectrum of iron (0) nanoparticles prepared in solution decomposition of $[Fe(N_3^tBuEt)_2(TMEDA)]$ ( <b>4</b> ). . . . .	76
3.13 TEM images of iron (0) nanoparticles prepared in solution decomposition of $[Fe(N_3^tBuEt)_2(TMEDA)]$ ( <b>4</b> ). . . . .	77
3.14 EDX analysis on iron nanoparticles prepared from solution reduction in toluene. . . . .	78
4.1 XRD pattern of $Al_{13}Fe_4$ film (top) with the calculated pattern (bottom). . . . .	83
4.2 XPS spectra of films prepared from sequential deposition. . . . .	84
4.3 FIB-SEM images of $Al_{13}Fe_4$ films. Top: surface and bottom: cross section. . . . .	84
4.4 Quantitative EDX spectra of $Al_{13}Fe_4$ films. . . . .	85
4.5 XRD pattern of $Al_{13}Fe_4$ powder. . . . .	86
4.6 HR-TEM images of $Al_{13}Fe_4$ nanoparticles. . . . .	87
4.7 Selectivity and conversion of acetylene semi-hydrogenation with 25 mg film sample without pretreatment. . . . .	89
4.8 Ethane, ethene and c4 product distribution after hydrogenation of acetylene by $Al_{13}Fe_4$ film without pretreatment. . . . .	89
5.1 Titanium CVD precursors reported in the literature for the deposition of TiN films. . . . .	95
5.2 Niobium CVD precursors reported in the literature for the deposition of NbN films. . . . .	96
5.3 Tantalum CVD precursors described in the literature for the deposition of TaN films. . . . .	97
5.4 $^1H$ NMR spectrum of $[Ti(N_3^tBuEt)_2(NMe_2)_2]$ ( <b>14</b> ). . . . .	98
5.5 $^1H$ NMR spectrum of $[Ti(N_3^tBu^iPr)_2(NMe_2)_2]$ ( <b>15</b> ). . . . .	99
5.6 $^1H$ NMR spectrum of $[Ti(N_3^tBu_2)_2(NMe_2)_2]$ ( <b>16</b> ). . . . .	99
5.7 $^1H$ NMR spectrum of $[Nb(N_3^tBuEt)(NMe_2)_4]$ ( <b>17</b> ). . . . .	100
5.8 $^1H$ NMR spectrum of $[Ta(N_3^tBuEt)(NMe_2)_4]$ ( <b>18</b> ). . . . .	100
5.9 TGA curves of titanium complexes. . . . .	102
5.10 TGA analysis of heteroleptic Nb and Ta triazenides. . . . .	102
5.11 Single crystal XRD structure of $[Ti(N_3^tBu_2)_2(NMe_2)_2]$ ( <b>16</b> ). Ellipsoids are drawn at 50% probability and hydrogen atoms are omitted for clarity. . . . .	103
5.12 Powder XRD pattern for the nanoparticles obtained from solution reduction of $[Ti(N_3^tBuEt)_2(NMe_2)_2]$ ( <b>14</b> ) and calcined at 600°C under air. . . . .	104
5.13 Schematic representation of the reactor used for the deposition experiments. . . . .	105

---

5.14	EDX spectra of NbN films obtained by thermal ALD. . . . .	107
5.15	EDX spectra of NbN films obtained by plasma assisted ALD. . . . .	108
7.1	Vacuum-Schlenk system with Schlenk glassware to work under inert atmosphere. . . . .	114
7.2	TEM shuttle sample holder. . . . .	115
7.3	XPS shuttle sample holder. . . . .	117
7.4	X-ray sample holder equipped with a kapton film. . . . .	117
7.5	$^1\text{H}$ NMR spectrum of <b>(L1)</b> . . . . .	121
7.6	Mass spectrum of <b>(L1)</b> . . . . .	122
7.7	$^1\text{H}$ NMR spectrum of <b>(L2)</b> . . . . .	123
7.8	Mass spectrum of <b>(L2)</b> . . . . .	123
7.9	$^1\text{H}$ NMR spectrum of <b>(L3)</b> . . . . .	124
7.10	Mass spectrum of <b>(L3)</b> . . . . .	125
7.11	$^1\text{H}$ NMR spectrum of <b>(L4)</b> . . . . .	126
7.12	Mass spectrum of <b>(L4)</b> . . . . .	126



# List of Schemes

2.1	Synthetic route for iron hydride complexes with Fe-P bond. . . . .	21
2.2	Synthesis of new triazene ligands <b>L1-L4</b> . . . . .	24





## Acronyms

<b>CVD</b>	Chemical Vapor Deposition
<b>MOCVD</b>	Metal Organic Chemical Vapor Deposition
<b>ALD</b>	Atomic Layer deposition
<b>DMEAA</b>	Dimethylethylamine alane
<b>TIBA</b>	Tri <i>iso</i> -butyl aluminium
<b>DMAH</b>	Dimethyl aluminium hydride
<b>TMEDA</b>	Tetramethylene ethylene diamine
<b>DMPE</b>	Dimethylphosphino ethane
<b><math>Fe(CO)_5</math></b>	Iron pentacarbonyl
<b>Et</b>	Ethyl
<b><i>iPr</i></b>	Isopropyl
<b><i>tBu</i></b>	Tertbutyl
<b>DLI</b>	Direct liquid injection
<b>eV</b>	Electron volt
<b><i>nBu</i></b>	n-Butyl
<b>BE</b>	Binding energy
<b>rt</b>	Room temperature
<b>NPs</b>	Nanoparticles
<b>py</b>	Pyridine
<b>sccm</b>	Standard cubic centimeters per minute
<b>cp</b>	cyclopentadiene
<b>sccm</b>	Standard cubic centimeters per minute
<b>XPS</b>	X-ray photoelectron spectroscopy
<b>XRD</b>	X-ray diffraction
<b>TGA</b>	Thermogravimetric analysis
<b>EPR</b>	Electron paramagnetic resonance
<b>EDX</b>	Energy-dispersive X-ray spectroscopy
<b>NMR</b>	Nuclear magnetic resonance
<b>FT-IR</b>	Fourier transform infrared spectroscopy
<b>SEM</b>	Scanning electron microscopy
<b>TEM</b>	Transmission electron microscopy

# 1

## Introduction

### Contents

---

<b>1.1 Acetylene semi-hydrogenation: From Pd based catalysts to cheaper unsupported <math>Al_{13}Fe_4</math> intermetallics</b> . . . . .	<b>2</b>
1.1.1 $Al_{13}Fe_4$ Intermetallic Catalyst . . . . .	4
1.1.2 Supported $Al_{13}Fe_4$ by MOCVD . . . . .	6
<b>1.2 Principles and requirements of precursors for MOCVD process</b> . . . . .	<b>7</b>
1.2.1 MOCVD principles . . . . .	7
1.2.2 MOCVD precursor requirements . . . . .	8
<b>1.3 MOCVD Precursors for metallic aluminium and iron</b> . . . . .	<b>8</b>
1.3.1 Aluminium MOCVD precursors . . . . .	8
1.3.2 Iron MOCVD precursors . . . . .	10
<b>1.4 Thesis objectives</b> . . . . .	<b>17</b>

---

## 1.1 Acetylene semi-hydrogenation: From Pd based catalysts to cheaper unsupported $Al_{13}Fe_4$ intermetallics

Selective hydrogenation of acetylene to ethylene is a crucial industrial process to remove trace amounts of acetylene impurities from the ethylene feed for the polyethylene production. The presence of acetylene in the ethylene feed for the polyethylene production poisons the polymerization catalyst by getting adsorbed on the surface of the catalyst and thus blocking the active sites for ethylene [3]. Therefore the acetylene content in the ethylene feed has to be eliminated or reduced to minimum ppm amount. The semi-hydrogenation of acetylene in the presence of ethylene for the polyethylene production requires a highly active and selective catalyst in order to prevent the hydrogenation of ethylene all the way up to ethane [4] and to prevent the dimerization and oligomerization of ethylene into 1,3 butadiene which can be further hydrogenated into numerous C4 hydrocarbon compounds [5], that in turn will be deposited and, therefore, poisoning the catalyst. The industrial catalysts for the semi-hydrogenation of acetylene consist typically of Pd-supported on metal oxides like alumina. Palladium is highly active in the hydrogenation reactions of alkynes and dienes into the corresponding alkenes. The reasons for the high activity of Pd is its ability to dissociate and adsorb hydrogen gas and to chemisorb the unsaturated bonds. Although palladium is a highly active catalyst, it shows only limited selectivity with enhanced formation of ethane, C4 and higher hydrocarbons [3]. Another problem is the deactivation of Pd catalyst by carbonaceous deposits. The limited selectivity of Pd catalysts can be explained by the presence of neighbouring active atoms on the catalyst surface which leads to a bi-sigma bonded intermediate on two adjacent Pd atoms which is responsible for the formation of ethane [4] (Path A1, Figure 1.1). The bi-sigma bonded ethylene is stable at high temperatures and can be hydrogenated to ethane or further decomposed into carbonaceous deposits. However, by increasing the active Pd-Pd distances and reducing the Pd-Pd coordination numbers by alloying or introducing a catalytically inactive metal or a spacer, one can achieve site isolated active atoms. This geometric effect modifies the adsorption and desorption properties of the catalyst and leads to the formation of weakly pi bonded intermediate (Path B1, Figure 1.1) which will be selectively hydrogenated into ethylene. However, this can be tricky because in order to have a complete site isolation, the concentration of Pd atoms has to be decreased considerably. This will lead to a higher selectivity but also to a low activity due to the very little concentration of the catalytically active atom.

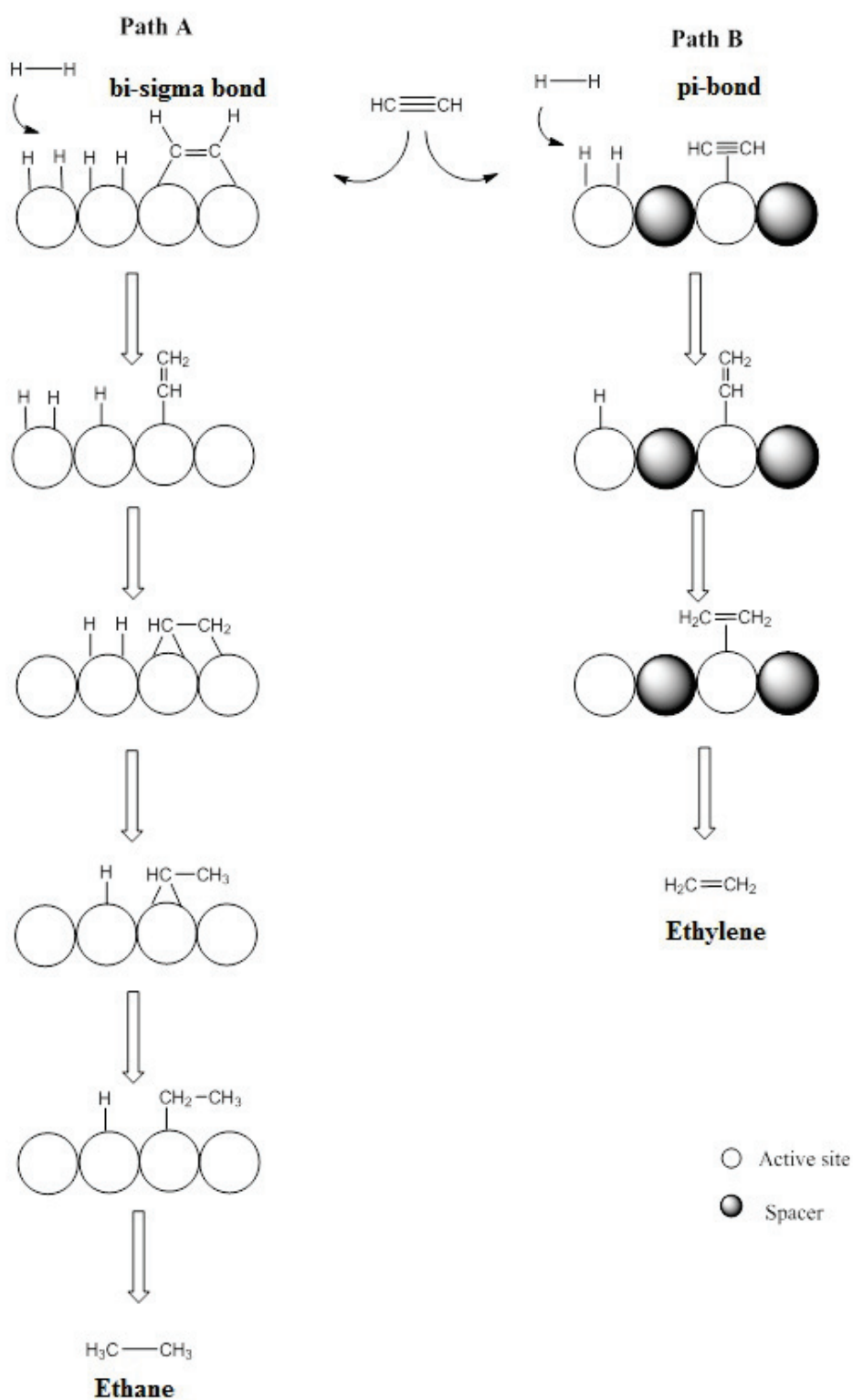


Figure 1.1 – Hydrogenation of acetylene; Path A: through a bi-sigma bonded intermediate. Path B: through a pi-bonded intermediate [3].

Replacing Pd based industrial catalysts with non-precious metals is attracting tremendous interest. The earth-abundant transition metal iron is desirable in this context because of its low cost and low toxicity. However, iron itself is not a good catalyst and hydrogenation of alkenes and alkynes in the presence of Fe catalysts requires high temperatures (200°C) and high pressure of  $H_2$  gas (250-300 atm) with only limited selectivity due to the harsh reaction conditions.

Activity and selectivity of Fe catalysts can be enhanced by the active site isolation by introducing aluminium which is catalytically inactive in hydrogenation of unsaturated bonds. The incorporation of aluminium as a spacer atom will enhance selectivity of the hydrogenation catalyst. However, alloying iron is not a suitable technique to have an active catalyst due to the highly diluted ratio of iron in the alloy and the consequent decrease in activity as mentioned above. Instead, active site isolated iron can be achieved in the form of intermetallic compounds. This would lead to a high concentration of the Fe atoms with complete site isolation resulting in higher activity and selectivity.

### 1.1.1 $Al_{13}Fe_4$ Intermetallic Catalyst

Intermetallic compounds consist of two or more metals in a particular stoichiometric composition showing a well ordered crystal structure. The bonding in the intermetallic compounds is partly ionic and partly covalent which results in high stability and less phase segregation compared to alloys. Intermetallics are ideal to obtain active site isolated Fe atoms because of their well-defined structure and alternate arrangement of the different metals.

The Al-Fe binary system was investigated extensively since the 1920s [6,7]. Figure 1.2 shows the Al-Fe phase diagram as reported by Massalski *et al.* [8]. The aluminium rich  $Al_{13}Fe_4$  intermetallic complex was selected as a site isolated Fe catalyst due to the increased or high average inter-atomic Fe-Fe distances and reduced coordination number [9].

Figure 1.3 shows a unit cell of  $Al_{13}Fe_4$  in which the Fe atoms are either coordinated by aluminium or arranged in Fe-Al-Fe groups located in the cavities of the three-dimensional Al framework, resulting in a complete encapsulation of the potentially active transition-metal sites by a pentagon of Al atoms, thus, following the site-isolation concept [1].

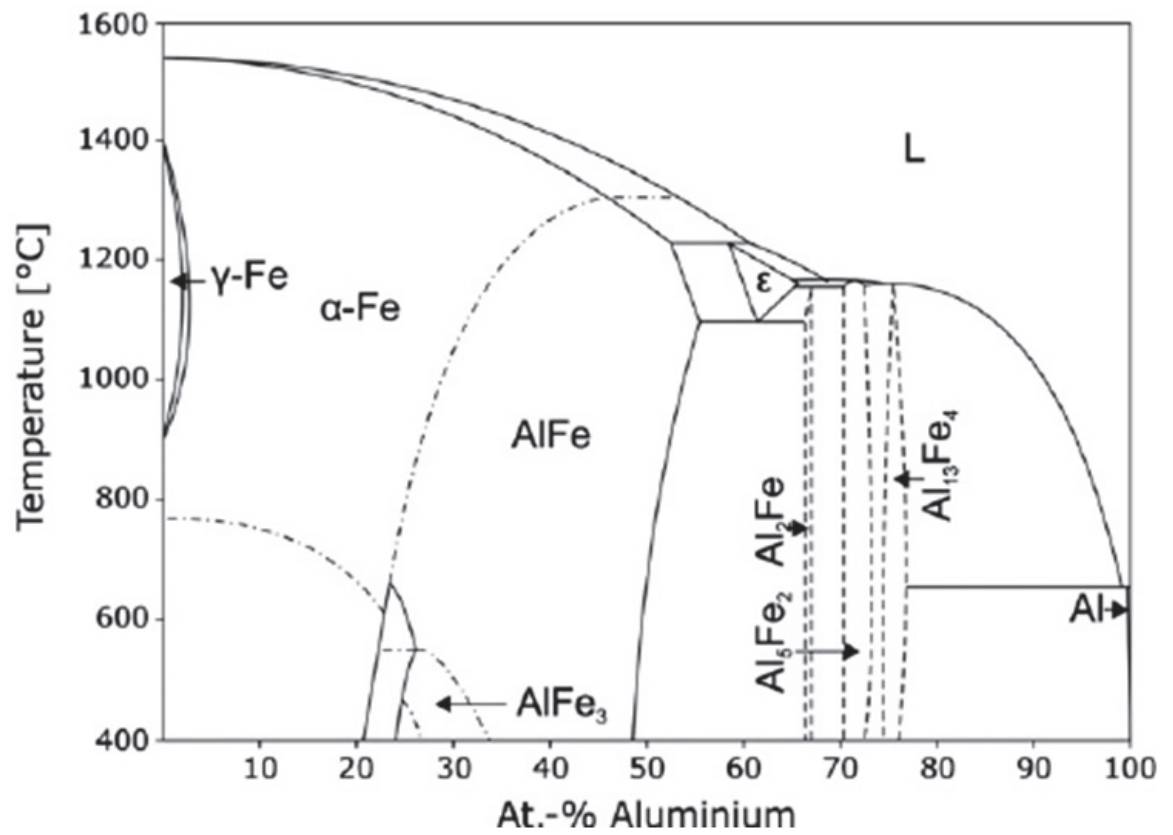


Figure 1.2 – Aluminium-iron phase diagram [8].

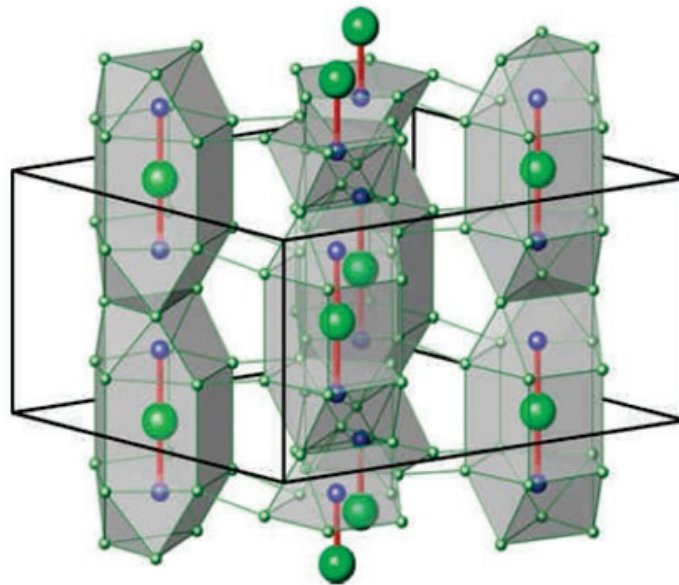


Figure 1.3 – Unit cell of  $\text{Al}_{13}\text{Fe}_4$  illustrating the site isolation of Fe atoms; colour scheme: green (Al), blue (Fe) [1].

The lattice parameters of crystalline  $Al_{13}Fe_4$  are: space group  $C2/m$ ;  $a = 15.492(2)$  Å,  $b = 8.078(2)$  Å,  $c = 12.471(1)$  Å,  $\beta = 107.69(1)^\circ$ ; RF = 0.053, RF(w) = 0.044 for 1127 reflections and 137 refined parameters. The coordination numbers of iron atoms are 9, 10 and 11 for iron whereas aluminium atoms have 10, 12, 13 and 14 coordination numbers. The shortest interatomic distances are 2.902 Å for Fe–Fe, 2.374 Å for Fe–Al, and 2.533 Å for Al–Al. *In situ* PXRD studies during thermal treatment under reducing or oxidizing atmospheres show high thermal stability for this intermetallic up to 450°C [1]. In addition, it does not dissolve hydrogen under strong reducing atmospheres and it also shows remarkable activity and selectivity for the hydrogenation of butadiene under mild reaction conditions [10].

### 1.1.2 Supported $Al_{13}Fe_4$ by MOCVD

Whereas  $Al_{13}Fe_4$  has achieved promising catalytic performances as the material itself and without any support (grounded powder), optimization of the catalytic activity may be achieved by supporting the material in the form of nanoparticles and/or films. Supporting a catalyst leads to easier separation of the heterogeneous catalyst from the reaction mixture. Another advantage of supported catalysts is increased surface area. To develop supported nanoparticles and or films of  $Al_{13}Fe_4$ , we choose a technique that ensures control of the thickness and size and high throughput.

Amongst chemical synthetic approaches, Metal Organic Chemical Vapor Deposition (MOCVD) process is a flexible and economically competitive method because it combines high deposition rates and mild deposition conditions from appropriate molecular precursors. Like MOCVD, Atomic Layer Deposition (ALD) film growth method is well-suited for nanoscale film growth, since it affords conformal coverage and film thickness control, due to its self-limiting growth mechanism. For these reasons, MOCVD has been selected to prepare supported  $Al_{13}Fe_4$  films and nanoparticles. However all these processes require appropriate molecular precursors having high volatility and thermal stability to allow their transport in the gas phase as well as a high (thermal or chemical) reactivity with the substrate. Gathering all these physico-chemical properties within the same derivative requires a precise molecular engineering in terms of 3D-structure (steric hindrance) and strength of the intra-molecular (Chemical bonds) and inter-molecular interactions (Hydrogen and Van der Waals bonds).

## 1.2 Principles and requirements of precursors for MOCVD process

### 1.2.1 MOCVD principles

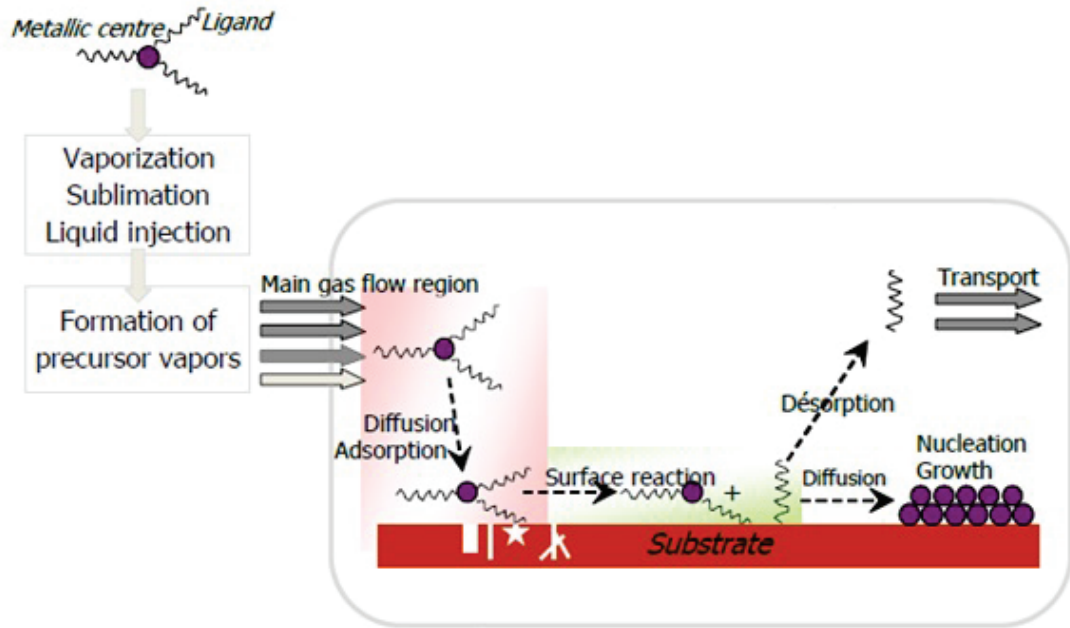


Figure 1.4 – Schematic representation of MOCVD mechanism [11].

MOCVD is a gas-phase deposition technique to produce single or polycrystalline films and nanoparticles on a substrate surface [11]. In a typical MOCVD process, the precursor is transported in the vapour phase by a flow of inert or reactive gas and introduced into the reaction chamber. Once in the gaseous phase, the precursor has different possibilities of the reaction:

1. Gaseous phase reaction/decomposition of the precursor.
2. Diffusion and adsorption on the substrate surface.

The adsorbed precursor will undergo a chemical reaction near or on the hot substrate surface and the reaction by-products are removed from the reactor by the continuous flow of the gas as shown in Figure 1.4. Chemical reactions involved in a CVD deposition include thermal decomposition, oxidation, reduction, hydrolysis, carburization, nitridation, etc. The gas flow rate, substrate temperature, reactor pressure and precursor concentration will determine the growth rate and properties of the grown film.

### 1.2.2 MOCVD precursor requirements

Ideally, MOCVD or ALD molecular precursors need to be volatile (liquids are preferable) and thermally stable with good shelf life which should be decomposed cleanly at low deposition temperatures, and compatible with other precursors in the system. Co-depositing several metals requires considering the different chemistry of the metals. This is the case for our system containing aluminum and iron. Aluminium and iron are electropositive and oxophilic metals which necessitate the exclusion of electronegative elements such as oxygen and halides from the precursors. These metals also have high affinity to carbon which makes it necessary to exclude precursors with direct metal-carbon bond. Finally, the Fe and Al precursors must have a decomposition behaviour in a same and common temperature window. The requirements for metallic Fe and Al MOCVD precursors are summarized as follows:

1. These precursors should be thermally stable and volatile with preferably a vapor pressure higher than 1 Torr at room temperature [12]. Precursors with monomeric structure must be favoured while aromatic groups should be avoided to eliminate the pi-stacking intermolecular interaction.
2. They should have relatively low decomposition temperature with a relatively large temperature window between evaporation and decomposition. These precursors should be devoid of electronegative elements and direct metal-carbon bond and should be decomposed cleanly into non-toxic by-products.

The first step to meet our objective is the development of unary deposition of aluminum and iron films, separately, under compatible conditions. Once the deposition conditions of each metal has been explored and understood, co-deposition or sequential deposition of compatible iron and aluminum precursors will be conducted.

## 1.3 MOCVD Precursors for metallic aluminium and iron

### 1.3.1 Aluminium MOCVD precursors

Aluminium MOCVD is an important technique to produce thin Al films with good control of the thickness at relatively high deposition rates. *Triiso*-butyl aluminum (TIBA), dimethyl aluminum hydride (DMAH) [13] and the dimethylethylamine alane (DMEAA) are among the most commonly used precursors for the deposition of Al films. The structures of these precursors are shown in Figure 1.5.

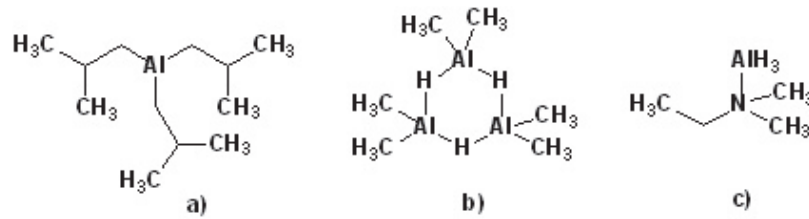
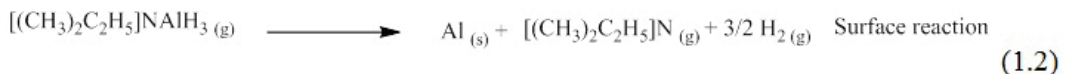
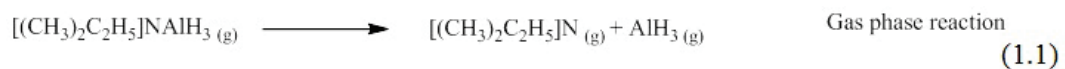


Figure 1.5 – Commonly used precursors for the deposition of thin Al films: a) Triisobutyl aluminum (TIBA), b) dimethyl aluminum hydride (DMAH) and c) dimethylethylamine alane (DMEAA).

TIBA has been used for the deposition of Al microelectronics. However, the films obtained had rough morphology [14]. It is a poorly reactive compound due to the shielding effect of its branched ligands. It is in the form of a colorless liquid, pyrophoric, explosive on contact with water and is toxic. It has a low saturated vapor pressure of 0.1 Torr at room temperature. DMAH has been used for the deposition of high purity Al films with a very low carbon contamination  $< 0.05\%$  over the temperature range of 250–340°C [15]. It has a convenient vapor pressure for CVD applications (2 Torr at 20 °C). However, it is a pyrophoric material and thus hazardous to transport and use. Furthermore, DMAH is present in trimeric form in liquid state. This renders it extremely viscous and thus hard to introduce into the CVD reactor. In order to overcome the technical problems of using DMAH, the related adduct  $Me_2AlH.(NMe_3)$  is used for the CVD of Al films, the presence of the donor ligand  $NMe_3$  renders the adduct non pyrophoric and reduces the intramolecular interactions and thus making it less viscous. It retains its high vapor pressure (5 Torr at 0°C). However, it freezes close to room temperature (17–25°C) making it necessary to heat conventional CVD bubblers. It has been shown that replacement of  $NMe_3$  by  $NMe_2Et$  leads to a significant lowering of the melting point of the  $AlH_3(NR_3)$  adducts, without causing any appreciable loss in precursor vapor pressure [16]. DMEAA was, therefore, investigated and used to produce pure aluminum films at relatively low deposition temperatures. The mechanism of DMEAA decomposition is well established [17] as presented in the equations below:



DMEAA has numerous interesting properties; it is a liquid precursor with a relatively high vapor pressure at room temperature (1.5 Torr) and a long shelf life. Furthermore, there is no direct aluminum-carbon or aluminum-oxygen bond which may lead to films with no C nor O contamination, thus providing an attractive precursor for co-deposition with oxophilic and carbophilic elements such as iron.

### 1.3.2 Iron MOCVD precursors

Electropositive elements such as iron [ $E_{(Fe^{2+}/Fe)}^{\circ} = -0.447$  V/ENH] are hard to reduce and form stable bonds with nitrogen, oxygen and carbon. As a result, very few iron (0) molecular compounds have been used as precursors for the MOCVD of high purity Fe films.

#### Carbon-based iron complexes

Iron pentacarbonyl  $Fe(CO)_5$  was largely used as precursor for the MOCVD of metallic iron films because it is reasonably air stable at ambient temperatures and has sufficient volatility and can be transported in the vapor phase at relatively low temperatures [18–21]. Since iron center in this compound is in the zero-valent state and the CO ligand is by itself a stable gas, MOCVD even in the absence of reducing environments can, in principle produce high-quality metallic films.  $FeCp_2$  [22, 23], and  $Fe_2Cp_2(CO)_4$  [24], where iron is in the +2 and +1 oxidation state, respectively, have been also used as iron precursors to produce iron films. When  $FeCp_2$  was used without any reactive gas, pulverulent graphitic carbon, untextured iron, and some cementite  $Fe_3C$  were produced. When  $H_2O$  was used as an additive, the film composition varied. When  $H_2O/FeCp_2$  ratios were lower than 10, it yielded films with no carbon contamination, but containing cementite above 773 K.  $H_2O/FeCp_2$  ratios higher than approximately 14.5 yielded ferrous oxide, FeO. Iron thin films obtained from  $Fe_2Cp_2(CO)_4$  containing only 1.89 and 0.9 % of carbon and oxygen contamination, respectively. However, these carbonbased iron complexes do not meet our criteria due to the presence of a direct iron-carbon bond and/or the presence of oxygen in the CO ligand which might lead to carbon contamination or the oxidation of aluminium during the preparation of the  $Al_{13}Fe_4$  intermetallic compound.

#### Hydride-based iron complexes

The MOCVD growth of pure  $\alpha$  Fe films has been reported using the iron dihydride tetrakis(trimethylphosphinoethane) complex  $H_2Fe[P(CH_3)_3]_4$  (Figure 1.6) with an *in situ* source of hydrogen to assist the reduction of the iron from +2 to zero oxidation

state. The deposition was carried at temperatures between 230°C and 280°C, but very limited information was provided on the deposition process itself [25].

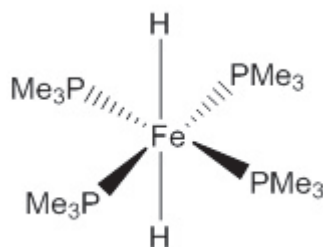


Figure 1.6 –  $H_2Fe[P(CH_3)_3]_4$  used for the MOCVD of iron films.

### Nitrogen-based iron complexes

Nitrogen containing ligands are interesting in the design of precursors suitable for MOCVD because of the high reactivity of the metal-nitrogen bond and the low M-N bond strength compared to M-O or M-Cl which allows the deposition at moderately low temperatures. The absence of metal-oxygen and metal-carbon bonds is also beneficial for obtaining pure metallic films.

### O, N ligand

Winter *et al.* [26] reported the growth of Fe metal using the  $\alpha$ -imino alkoxide precursor  $[Fe(^tBuNCCMe^tBuO)_2]$  (Figure 1.7, a) using  $N_2$  as carrier and purge gas and  $BH_3(NHMe_2)$  as the reducing agent at a deposition temperature of 180°C and a reactor pressure of 8-12 mbar. A very low growth rate of 0.074 Å/cycle was observed. Only ALD film growth was successful on Ru (5 nm)/ $SiO_2$  (100 nm)/Si substrates, and only after application of a nucleation process that entailed 50 cycles comprising 20 s pulses of the metal precursor, 1 s pulses of  $BH_3(NHMe_2)$ , and purge times of 5 and 10 s after the metal precursor and  $BH_3(NHMe_2)$  pulses, respectively. Winter group has also reported the synthesis, structure, and properties of Cu, Ni, Co, Fe, Mn and Cr complexes containing the carbohydrazide ligands [27]  $[R_2NCC(R)O]^-$  (Figure 1.7, b). The Cu, Ni, Co, and Cr complexes are monomeric and square planar, with bidentate N,O-coordination of the carbohydrazide ligands, whereas the Fe and Mn complexes are dimeric with 5-coordinate metal centers. The Fe complex is non volatile due to its dimeric structure. The five membered ring formed upon chelating coordination of the ligand to the metal ions is not enough bulky to block dimerization of the larger metal ions such as iron and may not protect the metal centers from intermolecular decomposition pathways. Providing additional steric hindrance of the metal centers but using a six-membered chelating rings (such as hydrazonate

ligands [ $RNNCR^1CR^2O$ ]<sup>-</sup>) leads to volatile, and thermally stable transition metal complexes. A series of Ni, Co, Fe, Mn and Cr (II) complexes were synthesized and displayed monomeric, distorted tetrahedral structures [28]. By changing the R group (Me, *i*Pr, *t*Bu, H), three different Fe (II) complexes have been synthesized (Figure 1.7, c-e). The complexes have high volatilities and sublime between 105°C and 120°C and solid state decomposition temperatures range from 241°C and 307°C. Solid state reaction treatment of [ $Co(^tBuNNCHC^tBuO)_2$ ] in tetrahydrofuran with 5 equivalents of hydrazine,  $BH_3(L)$  (L =  $NHMe_2$ ,  $SMe_2$ , THF), pinacol borane, and  $LiAlH_4$  both at room temperature and by refluxing led to rapid formation of cobalt metal which suggests that complexes containing hydrazonate ligands are promising precursors for the growth of the respective metals in gas phase processes.

### N, N ligand

Winter and his co-workers [29] investigated series of Cr(II), Mn(II), Fe(II), Co(II) and Ni(II) complexes containing 1,5-triazapentadienyl ligand (Figure 1.7, f). These complexes are monomeric and crystallize in a tetrahedral geometry. Complex with R = *t*Bu sublimates between 155°C and 175°C at 0.05 Torr and has decomposition temperatures that range from 280°C to 310°C, whereas complex with R =  $NMe_2$  sublimates at 105°C at 0.05 Torr but decomposes between 181°C and 225 °C. The thermal decomposition of Ni(II) complex resulted in the rapid reduction of the complex into metallic Ni. This shows that this family of precursors exhibit excellent properties as MOCVD and ALD precursors. The same group showed that the iron diazabutadiene complex [ $Fe(^tBuNCCN^tBu)_2$ ] is useful as ALD and MOCVD precursors [30]. In this work, a series of Cr, Mn, Fe, Co, Ni complexes containing 1,4-di-*tert*-butyl-1,3-diazadiene radical anion ligand ( $^tBu_2DAD$ ) were studied (Figure 1.7, g). These monomeric complexes crystallize in tetrahedral structure, and sublime between 85°C and 115°C at 0.05 Torr. Solid state decomposition temperatures range from 230°C to 325°C. These complexes decompose thermally to metal foils. The thermolysis of the iron complex leads to the formation of zero-valent Fe(110) and Fe(200). The reduction is proposed to occur via electron transfer from the radical anion  $^tBu_2DAD$  ligands to the metal centers. These new complexes thus represent a new class of potential film growth precursors, and may be useful in MOCVD and ALD processes. Finally, Cloud *et al.* [31] described the MOCVD of Fe using the bis[di(*tert*-Butyl)amido]Fe(II) [ $Fe(N^tBu_2)_2$ ] (Figure 1.7 h) at temperature less than 300°C to obtain  $Fe_4N$  iron nitride films with negligible carbon impurities.

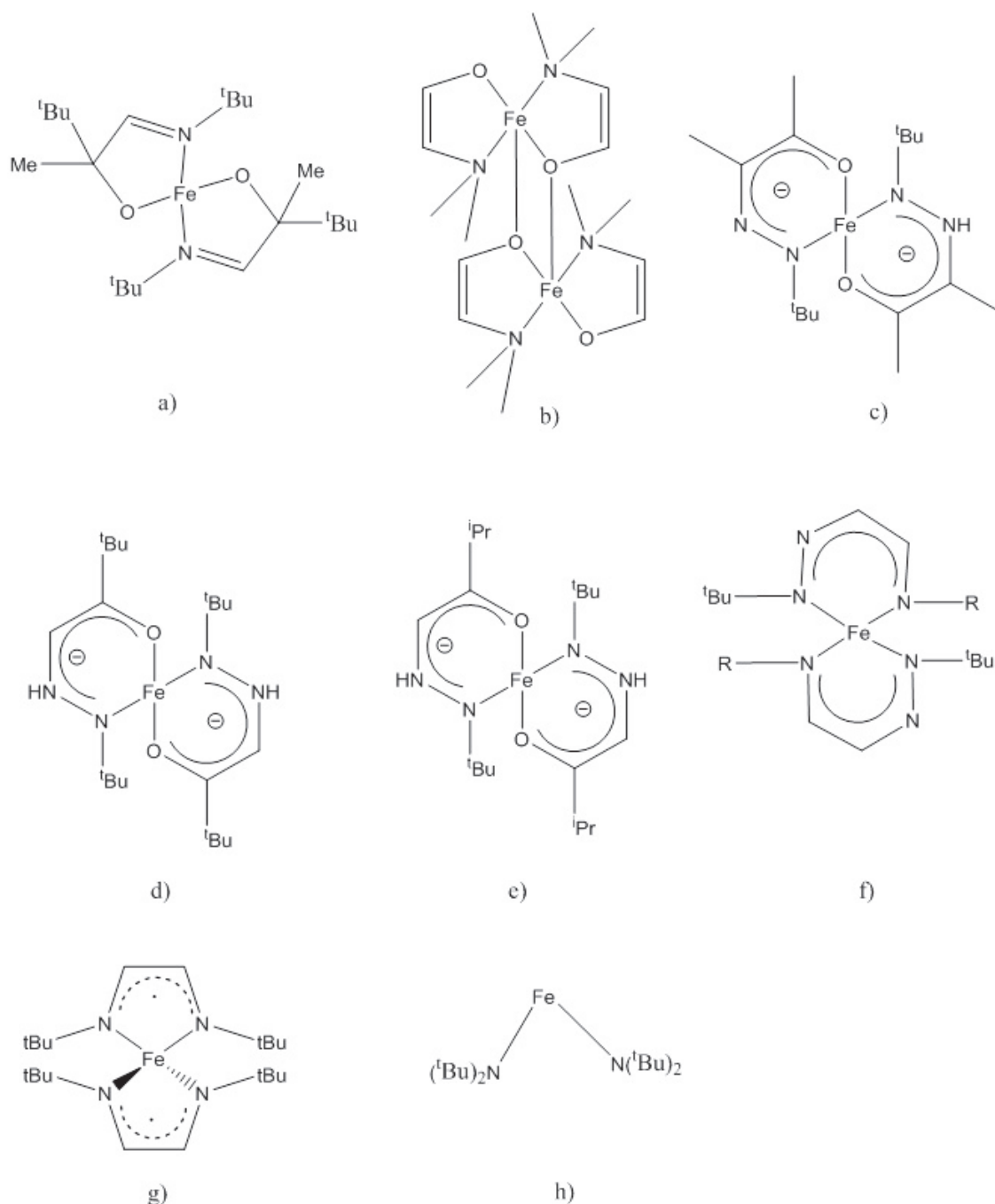


Figure 1.7 – Complexes used as suitable precursors for the MOCVD of iron films.

However, the main studied precursors are the three-membered ring analogues of the general formula  $[RC(NR')_2]^-$  and  $[R_2NC(NR')_2]^-$  and called amidinates and guanidinates, respectively. Both are interesting due to the commercial availability of a wide range of synthetic precursors. Of significant importance is the simplicity of preparation of amidinate complexes. Moreover, amidinate ligand is known to enhance the thermodynamic stability of a corresponding complex; thus, many cationic

intermediates, which are unstable for related metallocene analogues, were isolated for amidinate derivatives. As illustrated in Figure 1.8, all three substituents on the N-C-N backbone can be varied in order to modify the steric, electronic and volatility requirements. Guanidinate ligands differ only in that they contain a tertiary amino group at the central carbon atom of the NCN unit.

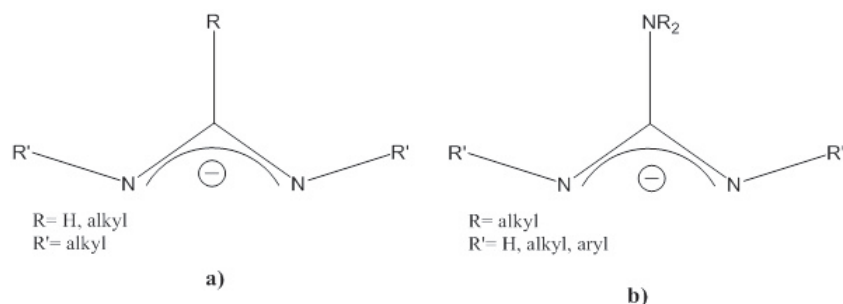


Figure 1.8 – a) Amidinate and; b) guanidinate ligand.

The beginning of their coordination chemistry dates back to the year 1970, when Lappert *et al.* [32] reported the first transition metal guanidinate complexes. Like the amidinates, these anions make attractive ligands because of the similar steric and electronic tunability through systematic variations of the substituents at the carbon and nitrogen atoms. Coordination modes of amidinates and guanidinates are summarized in Figure 1.9. Mono- or bidentate (chelating and bridging) modes can be achieved. By far, the most common coordination mode is chelating mode A and to lesser extent mode C [33].

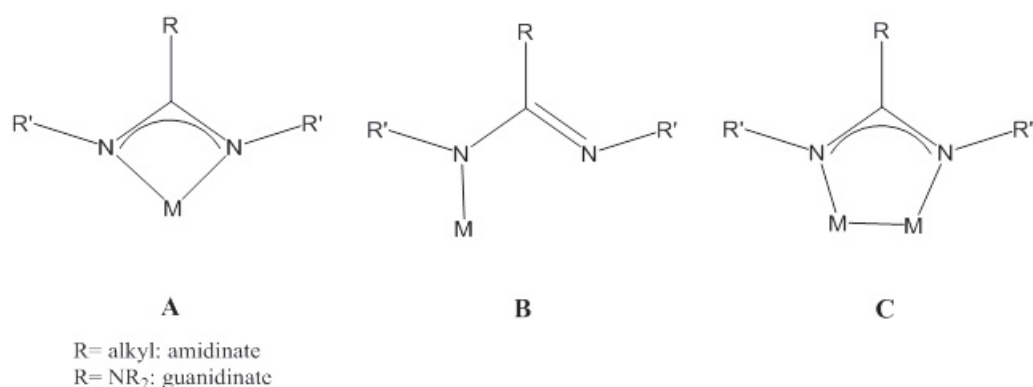


Figure 1.9 – Coordination modes of amidinates and guanidinates.

There have been several examples of amidinates and guanidinates in MOCVD and ALD. This work started with copper compounds used by Gordon [34], who deposited copper metal by ALD from  $[\text{Cu}\{(N^s\text{Bu})_2\text{CMe}\}]_2$  (Figure 1.10 a) with a high growth rate of copper at temperatures above 200°C (2Å/cycle on silica and

silicon nitride). Gordon *et al.* [35] have also studied MOCVD of Rhenium metal by using  $[Ru(N^tBu)_2CMe(CO)]_2$  (Figure 1.10 b). In the case of iron, Vahlas *et al.* [36] described the MOCVD of Fe using two commercial Fe amidinate precursors  $[Fe(BuNCMeNBu)_2]$  (Figure 1.10 c) and  $[Fe_2(PrNCMeNPr)_4]$  (Figure 1.10 d). However, Fe films obtained were contaminated by carbides and nitrides. The percentage of carbon contamination ranged from 12% to 33% with the identified species  $Fe_3C$  and  $Fe_4C$ . The percentage of nitrogen contamination ranged from 7% to 9% with the identified species  $Fe_3N$  and  $Fe_4N$ . The growth of Fe metal films was reported [37], using the amidinate precursor  $[Fe(tBuNCMeN^tBu)_2]$  (Figure 1.10 e) and  $H_2$  at a deposition temperature of 250°C but supplementary data supporting the deposition were not reported. The literature dealing with molecular precursors of iron(0) is quite scarce and underlines the difficulty of iron centers to be reduced and the carbon and nitrogen contamination in the final materials. Hence the design of new iron precursor for iron (0) should take these difficulties into account.

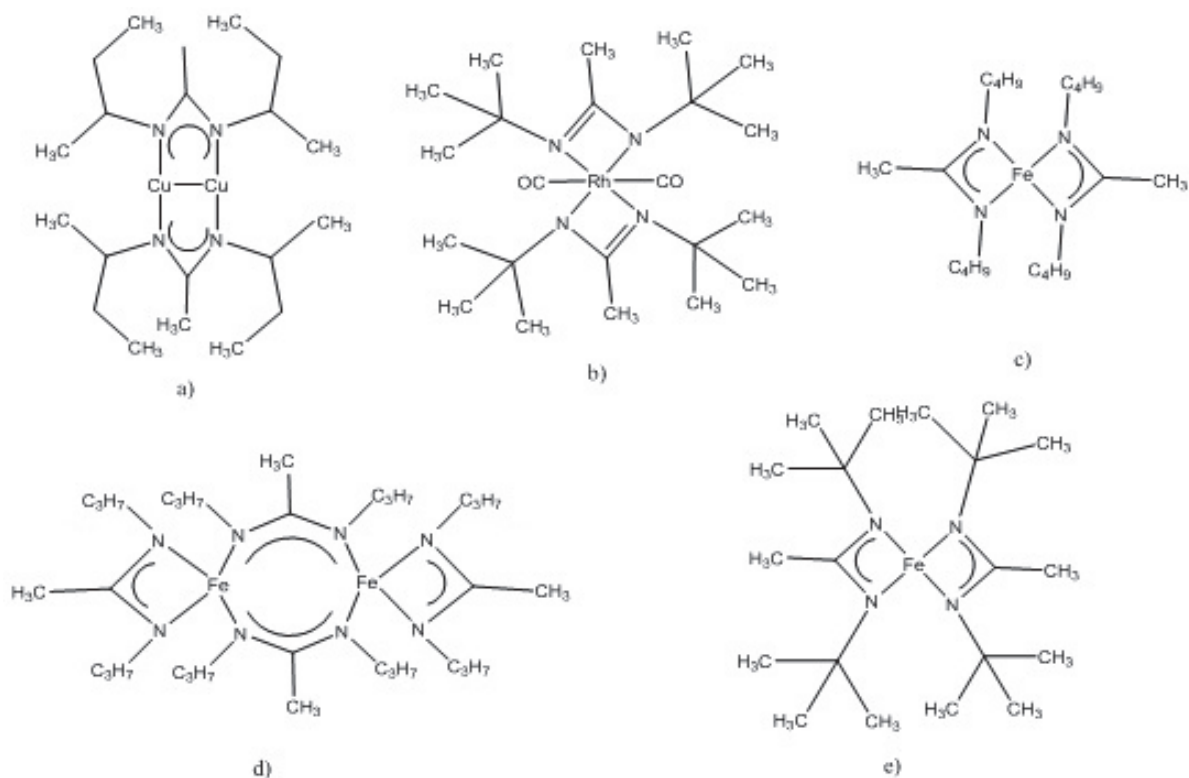


Figure 1.10 – Some amidinate and guanidinate complexes as CVD precursors.

Triazenes or diazoamines is a family of organic compounds containing an unsaturated chain of three nitrogen atoms. Triazene chemistry was initially developed by Griess [38] in the middle of the 19th century. Dimroth [39] described their synthesis

in 1906. Since then, they have been studied for their anticancer potential [40,41], used as protecting groups in natural product synthesis [42], incorporated into polymer synthesis [43], and used to form novel heterocycles [44]. Metal compounds containing the triazenide anion have been known since the development of the parent triazenes. Coordination complexes of the triazenide anions have been developed by Dwyer in 1941 and later by Hoskins *et al.* [45] who published crystal structures of the first chelating and bridging triazenides, thus showing the polymeric nature of the triazenide ligands. Pfeiffer *et al.* [46] prepared organometallic triazenide complexes of transition metals of Fe, Co, Ni, Mo, W and Pd with composition  $[(\mu^5 - C_5H_5)(L)_nRN_3R]M$  with  $L = CO, NO, PPh_3$ . Structural and electronic properties can be tuned by modifying the terminal alkyl groups and bulky or unsymmetrical constituents should provide more volatility to the complexes. Different types of bonding modes of this ligand have been proposed and established by X-Ray methods (Figure 1.11).

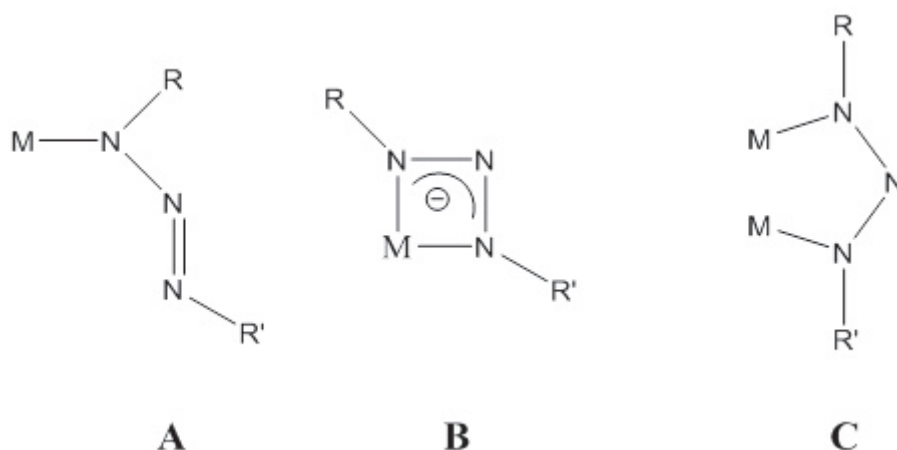


Figure 1.11 – Different bonding modes for triazenide ligand; a: monodentate, b: chelating, c: bridging.

As the MOCVD using amidinate precursors  $[Fe_2(PrNCMePrN)_4]$  and  $[Fe(BuNCMeBuN)_2]$  leads to carbon and nitrogen contaminated films [36], their replacement by triazenide ligand is proposed in this work as a promising approach based on the following arguments:

1. Compared to amidinates, the incorporation of the electronegative central N atom reduces the electron donor ability of the triazenide ligands. This makes triazenides weaker electron donors. This increases the electropositive character on the iron center after coordination, which makes its reduction easier.
2. The absence of carbon in the coordination sphere of iron metal could possibly lead to films with no carbon contamination.

3. Like amidinates and guanidates, triazenide ligands are also attractive for precursor designing because of the similar steric and electronic tunability through systematic variations of the substituents at the nitrogen atoms.
4. Triazenide ligands have the tendency to act as a bridging ligand due to the near parallel projection of the bonding orbitals of two terminal N atoms (Figure 1.12) leading to the formation of oligomeric complexes. This would make the triazenide complexes less stable due to low entropic effect and we would benefit of less stability from chelating entropic effect.

Although this field is known since the middle of the 19th century, triazenide complexes have never been used as molecular precursors. The main motivation of this thesis was to the study of the potential use of original metal triazenide complexes as molecular precursors for the large scale synthesis of the intermetallic catalyst  $Al_{13}Fe_4$  as supported film and/ or nanoparticles by metal organic chemical vapor deposition (MOCVD) or metal organic deposition (MOD) methods.

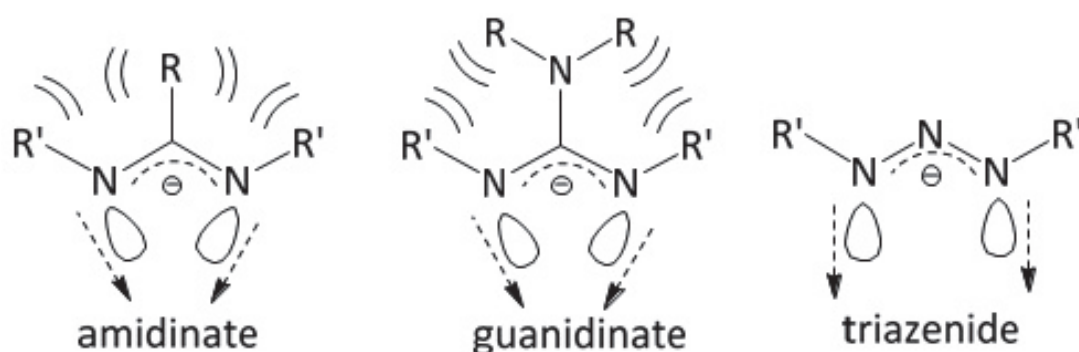


Figure 1.12 – Near parallel projection of the 2 N-donor atom orbitals in triazenide ligand increasing its tendency to act as a bridging ligand.

## 1.4 Thesis objectives

As mentioned earlier, the main thesis motivation was to elaborate supported  $Al_{13}Fe_4$  intermetallic nanocrystals/thin films on suitable supports ( $SiO_2$ ,  $Al_2O_3$  or silicon wafers) using metal organic chemical vapour deposition (MOCVD) and employing novel metal-organic complexes with triazenide ligand and to test these supported  $Al_{13}Fe_4$  intermetallic catalyst for semi hydrogenation reactions. Another objective was to extend triazenide chemistry to other transition metals (Ti, Nb, Ta) and see whether these nitrogen- rich complexes could be used as precursors to get metal nitride or

nitrogen doped metal oxide materials. In order to achieve these goals, following objectives were set at the beginning of this doctoral work:

1. To synthesize novel Fe(II) molecular complexes having high electrophilicity (redox standard potential) with nitrogen containing weakly donor triazenide ligands.
2. To investigate the volatility, thermal and electrochemical properties of these novel complexes to assess their potential as MOCVD precursors.
3. To realize MOCVD of pure Al films and pure Fe films and to optimize the deposition conditions of the co-deposition of Al and Fe to obtain  $Al_{13}Fe_4$  intermetallic NPs and thin films.
4. To investigate the catalytic properties of  $Al_{13}Fe_4$  intermetallic compound in the selective semi hydrogenation of acetylene.
5. To extend triazenide chemistry to other transition metals such as Ti, Nb and Ta to explore their suitability as precursors for metal nitride or N- doped metal oxide nanomaterials.

# 2

## Iron and Aluminium triazenide complexes

### Contents

---

<b>2.1</b>	<b>Introduction</b>	<b>20</b>
<b>2.2</b>	<b>Iron(II) precursors with Fe-P bond</b>	<b>20</b>
2.2.1	Results and Discussion	20
<b>2.3</b>	<b>Iron(II) precursors with Fe-N bond</b>	<b>23</b>
2.3.1	Results and Discussion	24
2.3.2	Mössbauer spectroscopy	33
2.3.3	Electron Paramagnetic Resonance EPR	37
2.3.4	Electrochemistry	41
2.3.5	Thermal properties	45
<b>2.4</b>	<b>Aluminium triazenide complexes</b>	<b>47</b>
2.4.1	Starting from $Al_2(CH_3)_6$	48
2.4.2	Starting from $AlH_3(NMe_2Et)$	53

2.4.3 Thermal behavior of aluminium triazenide compounds	57
2.5 Conclusion . . . . .	59

---

## 2.1 Introduction

Molecular precursors of iron for the preparation of high purity iron nanoparticles and thin films are scarce because of its electropositivity and tendency to form stable bonds with nitrogen, oxygen and carbon. While the organometallic compounds such as  $Fe(CO)_5$  [18],  $FeCp_2$  [22] and  $Fe_2Cp_2(CO)_4$  [24] have many advantages (reasonably air stable, sufficiently volatile, iron in zero/low valent state, volatile byproducts during decomposition. . .) to be used as CVD precursors even in the absence of reducing environment, they do contain iron-carbon bond and/or oxygen in the ligand, which might lead to carbon contamination or metal oxidation.

Nitrogen and phosphorus containing ligands are interesting in the design of precursors because of the high reactivity of the metal-nitrogen bond and the low M-N bond strength compared to M-O. The absence of metal-oxygen and metal-carbon bonds is expected to provide pure metallic films.

## 2.2 Iron(II) precursors with Fe-P bond

$[H_2Fe(PMe_3)_4]$  has been used for the MOCVD of pure Fe films [25]. This complex that has an *in situ* hydrogen source yielded pure  $\alpha$  Fe films in a temperature window of 230–280°C. Despite of the fact that only limited informations were available, we decided to investigate this complex as a precursor for MOCVD of pure iron films mainly because it matched our conditions of no direct iron-carbon or iron-oxygen bonds and the fact that its MOCVD characteristics were compatible with commercial aluminium precursor DMEAA to get  $Al_{13}Fe_4$  nanomaterials.

### 2.2.1 Results and Discussion

Tetrakis(trimethylphosphino) dihydride Fe(II) complex  $[H_2Fe(PMe_3)_4]$  was synthesized according to the published procedure [47] and crystallized by sublimation as bright yellow crystals (Figure 2.1). However, this complex was found to be kinetically unstable which decomposed readily even when stored in a closed Schlenck under argon at 0°C (Figure 2.1).

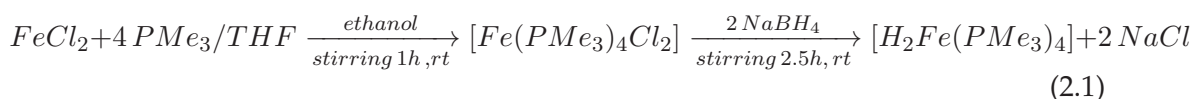
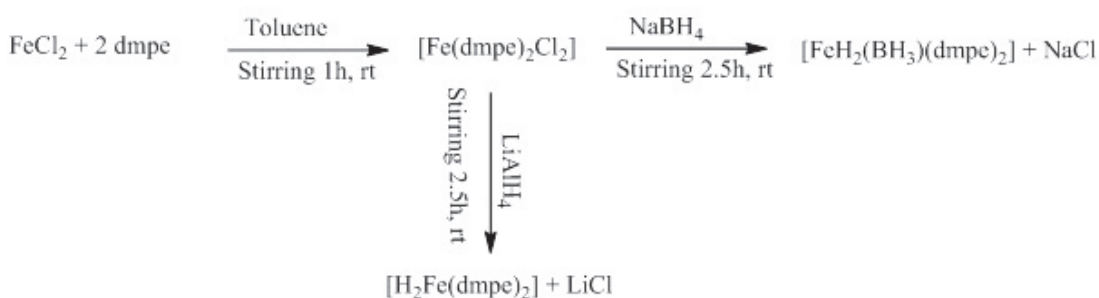


Figure 2.1 – a)  $[H_2Fe(PMe_3)_4]$  purified by sublimation. b)  $[H_2Fe(PMe_3)_4]$  decomposes readily.



Scheme 2.1 – Synthetic route for iron hydride complexes with Fe-P bond.

To overcome its high reactivity towards oxygen and humidity, we replaced the  $PMe_3$  ligand with a bidentate one, dimethylphosphino ethane ( $dmpe$ ). However, the reaction with two equivalents of this ligand gave two different products depending on the hydride source used (Scheme 2.1). While  $LiAlH_4$  gave the desired dihydride complex  $[H_2Fe(dmpe)_2]$ , albeit in a very low yield (8%), the use of  $NaBH_4$  as the hydride source, afforded  $[FeH_2(BH_3)(dmpe)_2]$  in 65% yield. Its single crystal X-ray structure showed the presence of one terminal hydride and a hydrogen-bridged  $BH_4$  group in trans apart from two chelating  $dmpe$  present in almost same plane (Figure 2.2). This structure has previously been reported [48].

Thermogravimetric analysis of this compound (Figure 2.3) showed a single step weight loss between 175 - 295°C which is compatible with the decomposition window of  $DMEAA$ . However, the organic residues upon reaching 450°C were 48% confirming that this complex is not volatile enough for CVD applications. The kinetic

instability of  $[H_2Fe(PMe_3)_4]$  along with a very low yield of  $[H_2Fe(dmpe)_2]$  and the low volatility of  $[FeH_2(BH_3)(dmpe)_2]$  suggested that these iron hydride complexes containing Fe-P bond are not useful for the MOCVD applications.

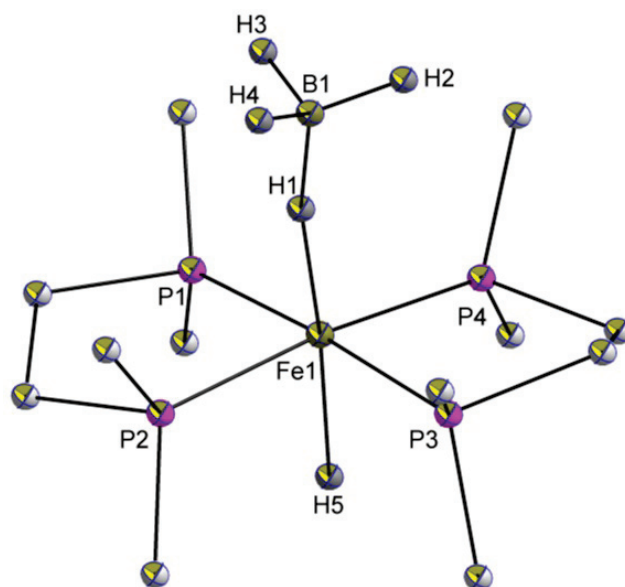


Figure 2.2 – Perspective view of  $[FeH_2(BH_3)(dmpe)_2]$  with thermal ellipsoids at 50% level. H-atoms are omitted for clarity.

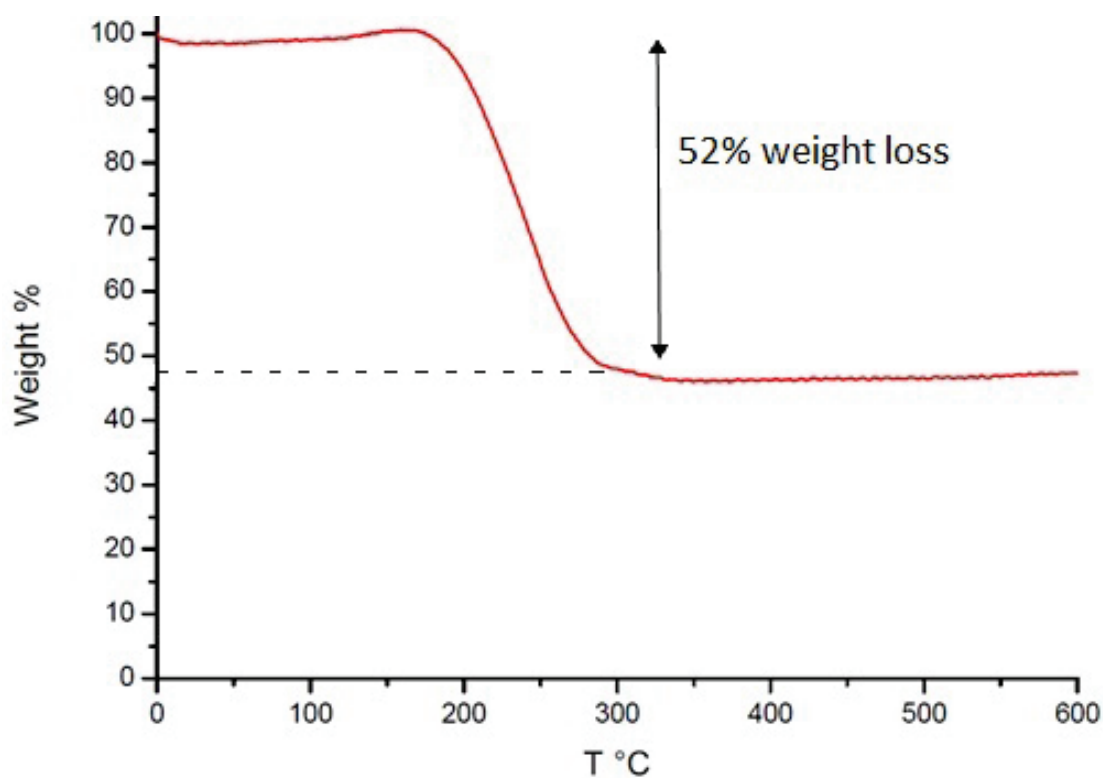


Figure 2.3 – TGA of  $[FeH_2(BH_3)(dmpe)_2]$ .

## 2.3 Iron(II) precursors with Fe-N bond

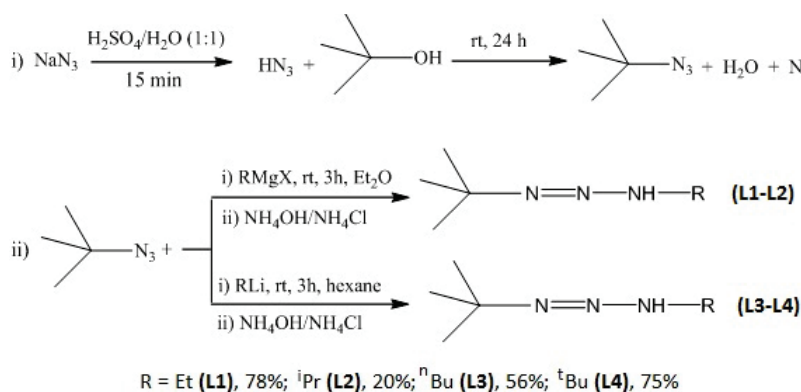
Nitrogen containing ligands are interesting in the design of precursors because of the high reactivity of the metal-nitrogen bond and the low M-N bond strength compared to M-O. Few precursors with nitrogen containing ligands such as  $[Fe\{N(SiMe_3)_2\}_2]$  [49] and  $[Fe(^tBuNCCN^tBu)_2]$  [30] have been shown to produce Fe(0) NPs by thermolysis using reducing reagents, but have not been evaluated for ALD and MOCVD. Among metal complexes with M-N bond, metal amidinates and guanidinate are valuable MOCVD and ALD precursors in materials science because of i) their relatively low molecular weight, high volatility and high thermal stability, ii) simple synthetic routes to sterically bulky variants and iii) high and properly self-limiting reactivity with  $H_2$  (for ALD) [33, 50]. Moreover, their steric and electronic properties can easily be modified through variation of the substituents. One potential disadvantage of these ligands is that they might yield films with carbon/nitrogen impurity. For example, the iron films obtained using amidinate precursors  $[Fe(BuNCMeNR)_2]$  ( $R = ^iPr, ^tBu$ ) were found to be contaminated by carbides and nitrides, the percentage of carbon and nitrogen contamination varying in the range 12-33% and 7-9%, respectively [36]. The closely related triazenes or diazoamines is also a small-bite angle N-containing ligand obtained by replacing the central carbon atom of the amidinate and guanidinate ligands with a nitrogen atom. Similar to amidinate and guanidinate ligands, the structural and electronic properties of a triazenide ligand can also be tuned by modifying the terminal alkyl groups. Triazenide ligands with bulky or unsymmetrical constituents are expected to provide more volatility to the complexes.

However, triazenide complexes have been never used as precursors in material sciences. We introduce here, for the first time, the triazene ligands in the precursor chemistry for their ability to afford oxygen-free molecular complexes having good volatility and low electron density at metal center. In this chapter, we report synthesis and complete characterization of new asymmetric triazene ligands,  $HN_3^tBuR$  ( $R = Et, ^iPr, ^nBu, ^tBu$ ), featuring different alkyl substituents at 1, 3-N centers and their use to develop novel homo- and heteroleptic Fe(II) triazenides with the goal of utilizing them as precursors for the large-scale synthesis of the intermetallic  $Al_{13}Fe_4$  catalyst as supported films and/or nanoparticles by Chemical Vapor Deposition (CVD) or Metal Organic Deposition (MOD) methods.

### 2.3.1 Results and Discussion

#### Synthesis and characterization of new triazene ligands

The triazene ligands  $HN_3^tBuEt$  (**L1**),  $HN_3^tBu^iPr$  (**L2**),  $HN_3^tBu^nBu$  (**L3**) were prepared as colorless liquids by treating freshly prepared *tert*-butylazide with either the corresponding Grignard reagent in diethyl ether or an alkyllithium in hexane (Figure 2.2). The asymmetric substitution at 1, 3-N centers in **L1-L3** was aimed to increase the volatility of the metal complexes. For the same reason, the use of aromatic groups was also avoided which could otherwise decrease the volatility due to possible intermolecular  $\pi$ -stacking. For the sake of comparison of the properties, a symmetrically substituted triazene ligand  $HN_3^tBu_2$  (**L4**), was also prepared.



Scheme 2.2 – Synthesis of new triazene ligands **L1-L4**.

The infrared spectra of **L1-L4** (Figure 2.4) show the presence of the broad peaks between 3233 and 3283  $cm^{-1}$  characteristic of NH groups with strong peaks in the range of 1456 and 1520  $cm^{-1}$  corresponding to the stretching frequency of N=N bond. The peaks in the region 2800 to 3000  $cm^{-1}$  correspond to C-H stretching frequencies.

Thermogravimetric analyses (TGA) were performed on ligands to understand their volatilities and thermal stabilities. All ligands have similar TGA traces with single-step weight losses occurring between 50°C and 160°C (Figure 2.5). Except for  $HN_3^tBu^iPr$  (**L2**) which showed 7% residue left at 400°C, the residual mass for all other ligands was less than 4%. This shows that triazene ligands are volatile enough at low temperatures and that all ligands display clean decomposition. These TGA curves show that volatility of ligands follows the order:  $HN_3^tBu^iPr$  (**L2**) >  $HN_3^tBuEt$  (**L1**) >  $HN_3^tBu_2$  (**L4**) >  $HN_3^tBu^nBu$  (**L3**).

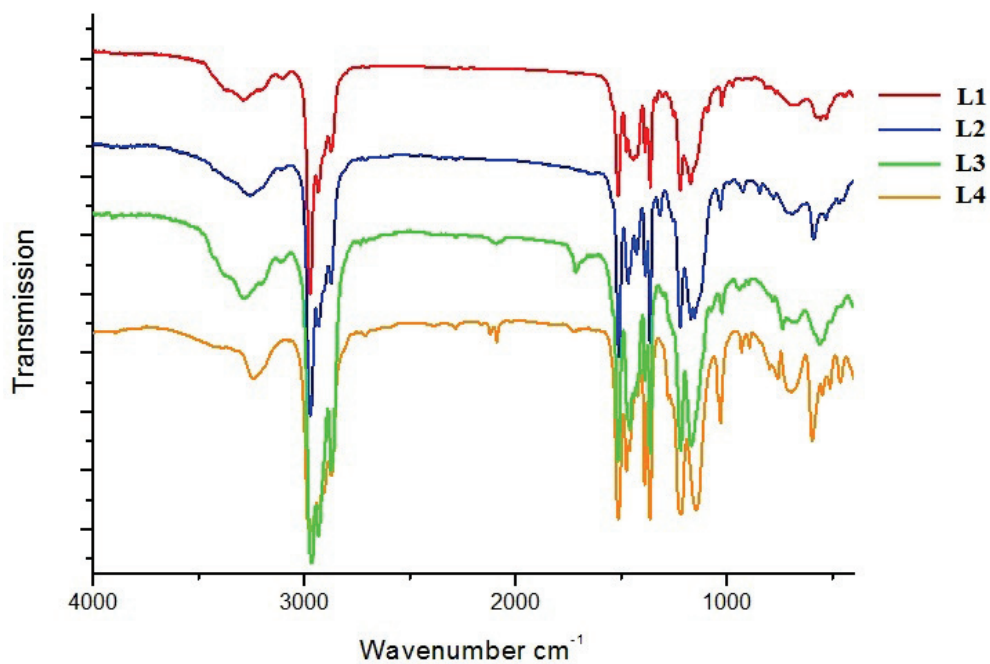


Figure 2.4 – FT-IR spectra for L1-L4.

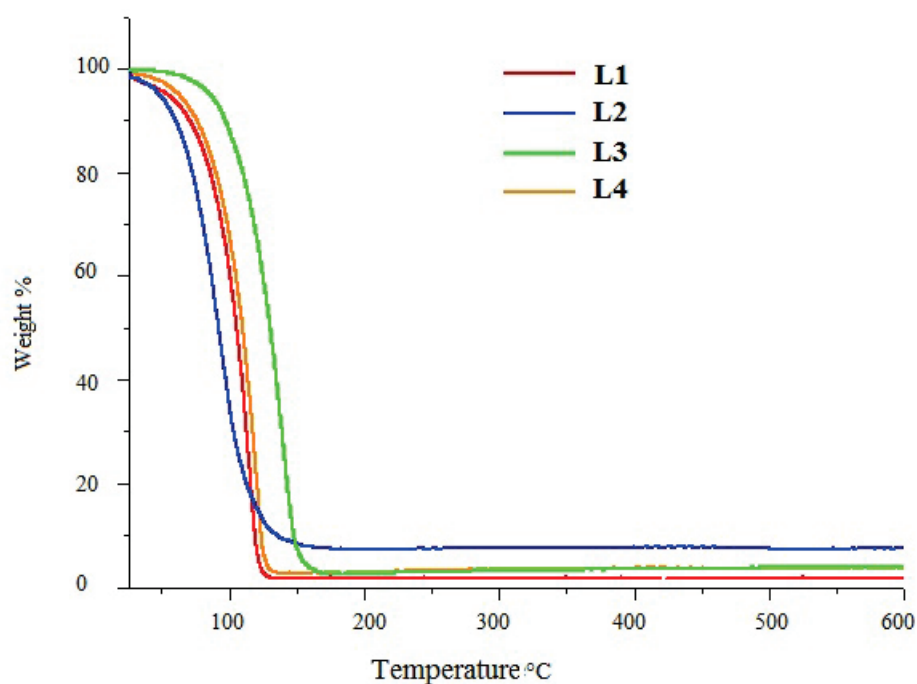


Figure 2.5 – TGA curves of triazene ligands L1-L4.

### Synthesis and characterization of new Fe(II) triazenides

The reaction of iron bis(trimethylsilyl)amide,  $[Fe\{N(SiMe_3)_2\}_2]$  with two equivalents of newly synthesized asymmetric triazene ligands in hexane afforded homoleptic

complexes **(1-3)** as brown-orange crystalline solid after crystallization at  $-20^{\circ}\text{C}$ . Complexes **(1-3)** show good solubility in common organic solvents but are highly susceptible towards oxidation (*vide infra*, discussion on Mössbauer and EPR spectroscopy). To improve their stability and thermal characteristics, we then carried out above reactions in the presence of an ancillary ligand, tetramethylethylenediamine (TMEDA), which afforded diamine-stabilized monomeric complexes as brown-orange solids, which could be crystallized from hexane at  $-20^{\circ}\text{C}$ .

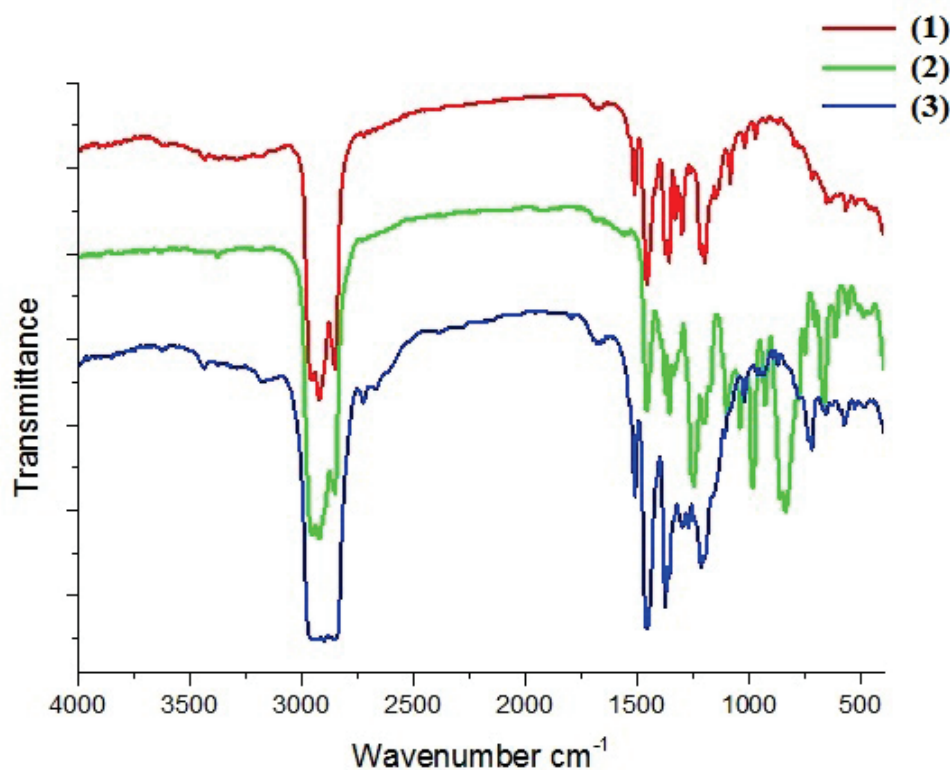
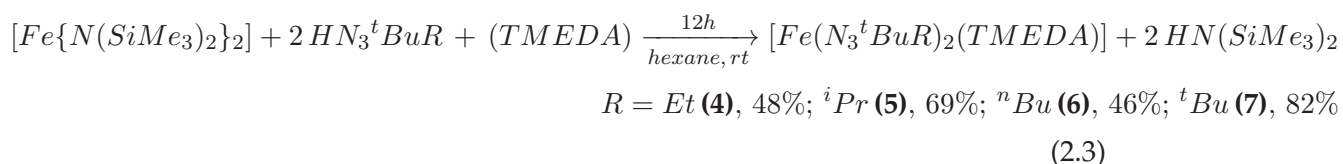
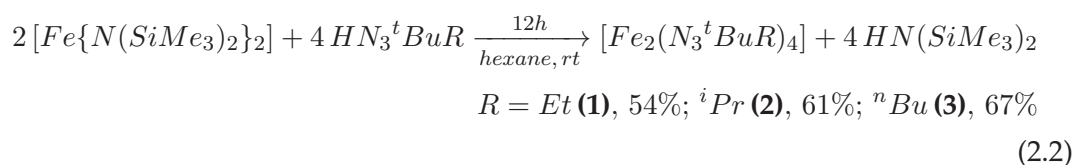


Figure 2.6 – FT-IR spectra for complexes **1-3**.

The infrared spectra in Nujol of complexes **1-7** (Figure 2.6 and Figure 2.7) show the

absence of the broad peaks at about  $3200\text{ cm}^{-1}$  due to the coordination of the ligand to the iron center and the loss of hydrogen atom. The stretching frequencies of N=N bonds is unaltered and remains at the same frequencies as those in the free ligands. It is worth mentioning that the C-H stretching frequencies at about  $2800\text{ to }3000\text{ cm}^{-1}$  correspond to that of nujol oil.

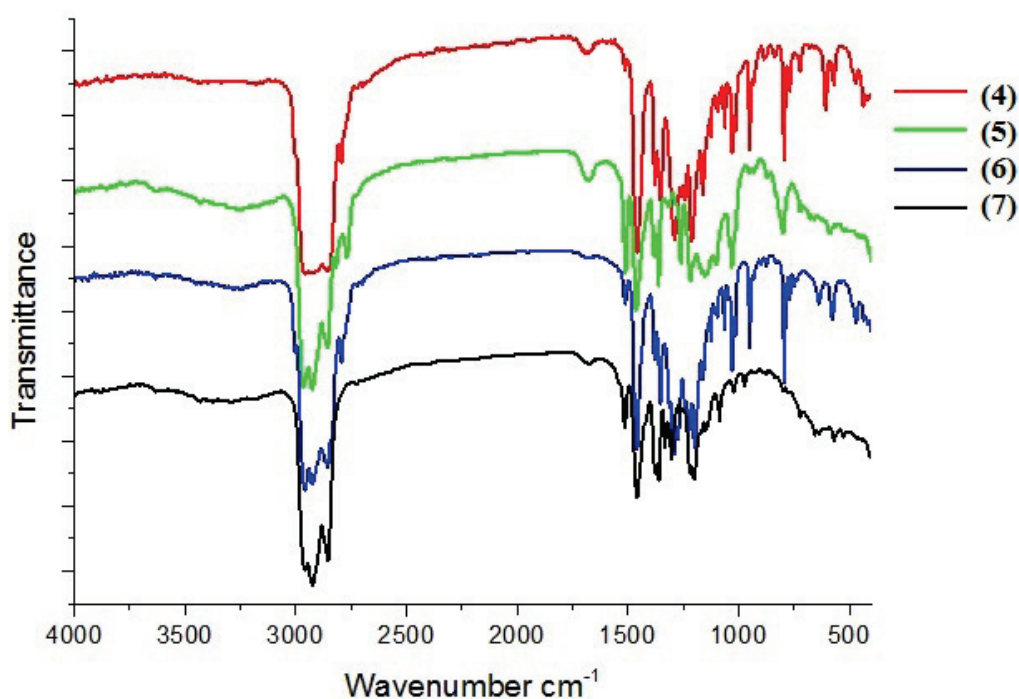


Figure 2.7 – FT-IR spectra for complexes 4-7.

### X-ray crystal structures

The homoleptic complexes  $[Fe_2(N_3^tBuEt)_4]$  (**1**) and  $[Fe_2(N_3^tBu^nBu)_4]$  (**3**), which crystallize in orthorhombic space group  $Pccn$  and monoclinic space group  $C2/c$ , respectively, are isostructural and adopt a paddlewheel dimeric structure where two iron(II) centers are bridged by four triazenide ligands bonded in an  $\mu\text{-}n^1, n^1$ -fashion (Figure 2.8). Two *trans* bridges are not exactly in the same plane and there is a considerable torsion angle of  $15.4\text{--}17.3^\circ$ , most probably due to the small bite angle of the ligand. The most remarkable feature of this dimeric structure is an exceedingly short iron-iron distance ( $2.167\text{ \AA}$ ), which is comparable to the shortest Fe(I)-Fe(I) distances  $2.1516(5)\text{ \AA}$  and  $2.1270(7)\text{ \AA}$  known for the closely related guanidinate complexes  $[Fe_2\{\mu\text{-}(^tBu)_2C=N\}C(NDipp)_2\}_2]$  [51] and  $[Fe_2\{\mu\text{-}(cis\text{-}2,6\text{-}Me_2NC_5H_8)C(NDipp)_2\}_2]$  (dipp = 2,6-diiso-propylphenyl) [52], respectively, but is significantly shorter than  $2.979(1)\text{ \AA}$  in  $[Fe(^iPrNCMeN^iPr)_2]_2$  [53] and  $2.8399(6)\text{ \AA}$

in the guanidinate complex  $[FeBr\{\mu - CyN)_2C(HNCy)\}]_2$  [54]. The iron-nitrogen distances found in the range 1.929(7) Å-2.004(7) Å, are slightly shorter as compared to iron- nitrogen distances 2.033(2)-2.134(2) Å in the dimeric iron (II) guanidinate complex  $[Fe\{\mu - (CyN)_2C(HNCy)\}(CyN)_2C(HNCy)\}]_2$  [55]. Because of the short Fe-Fe distance, the geometry around iron centre is distorted square pyramidal as indicated by the N-Fe-N angles which are spread in the range 88.12-90.83°. Selected bond lengths and angles are summarised in Tables 2.1 and 2.2.

Suitable single crystals of the TMEDA-stabilized complexes 4-7 were grown from their hexane solution at -20 °C. Single-crystal X-ray diffraction results confirmed that all of the complexes are monomeric, a favorable characteristic for optimum volatility, as shown in the Figure 2.9. Selected bond lengths and selected bond angles are summarized in Tables 2.3, 2.5, 2.4 and 2.6. In all complexes, the triazenide ligands are coordinated to the Fe(II) center in a chelating bidentate manner with a small bite angle of 57.2-61.5°. A chelating TMEDA ligand with a relatively large bite angle (78.2-79.5°) then completes a distorted octahedral geometry around the Fe(II) center.

The presence of ancillary TMEDA ligand not only completes the most common coordination number (i.e. six) of the iron center and makes it monomer but also, compared to the homoleptic complexes 1-3, enables the target compounds more stable towards oxidation and to have much improved thermal features (*vide infra*). The triazenide bite angle < N-Fe-N in the symmetrical triazenide complex 7 are identical (57.2°). However, the asymmetry of the triazenide ligands in 4-6 leads to an inequality of two bite angle < N-Fe-N (e.g., 59.9° and 61.5° in 6). This modest variation in the above bite angle can be explained by the bulkiness of the different alkyl substituents. The average Fe-N bond lengths of triazenide ligand (av. Fe-N(triazenide) = 2.17 Å) are shorter than those involving TMEDA ligand (av. Fe-N (TMEDA) = 2.31 Å) but are slightly longer than those involving the amidinate ligands in the monomeric iron (II) complex  $[Fe(PhC(NAr)_2)(CH_2SiMe_3)(py)]$  [55], (2.0864(18)-2.1226(18) Å) and of the monomeric iron (II) complex  $[Fe\{PhC(NAr)_2\}_2]$  [56] (2.0532-2.0662 Å). The longer Fe-N involving the triazenides compared to those involving amidinates reflects the weaker electron donor ability of triazenide ligands as compared to those of amidinate and guanidinate ligands.

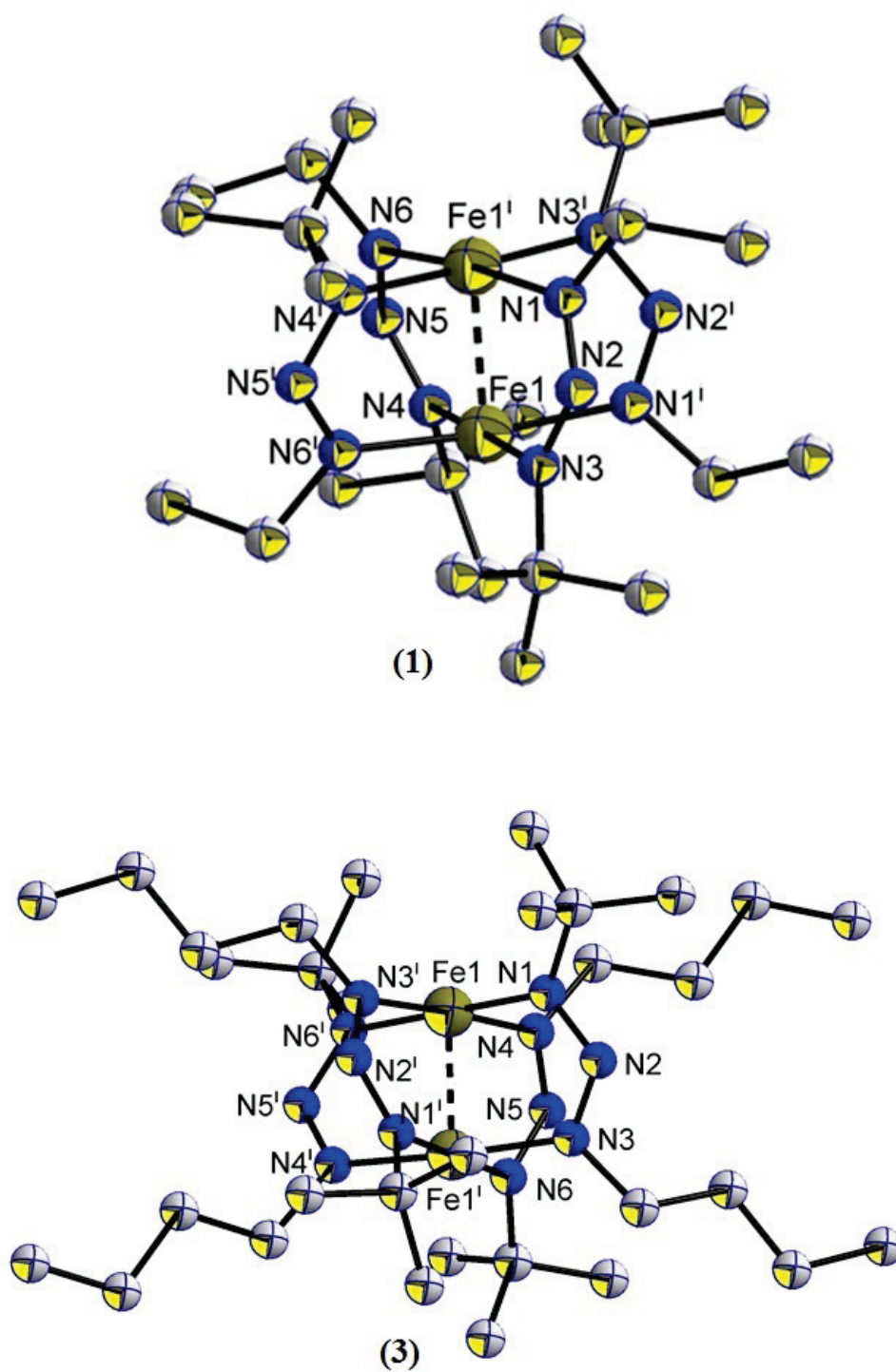


Figure 2.8 – Perspective view of 1 and 3 with thermal ellipsoids at 50% level. H-atoms are omitted for clarity.

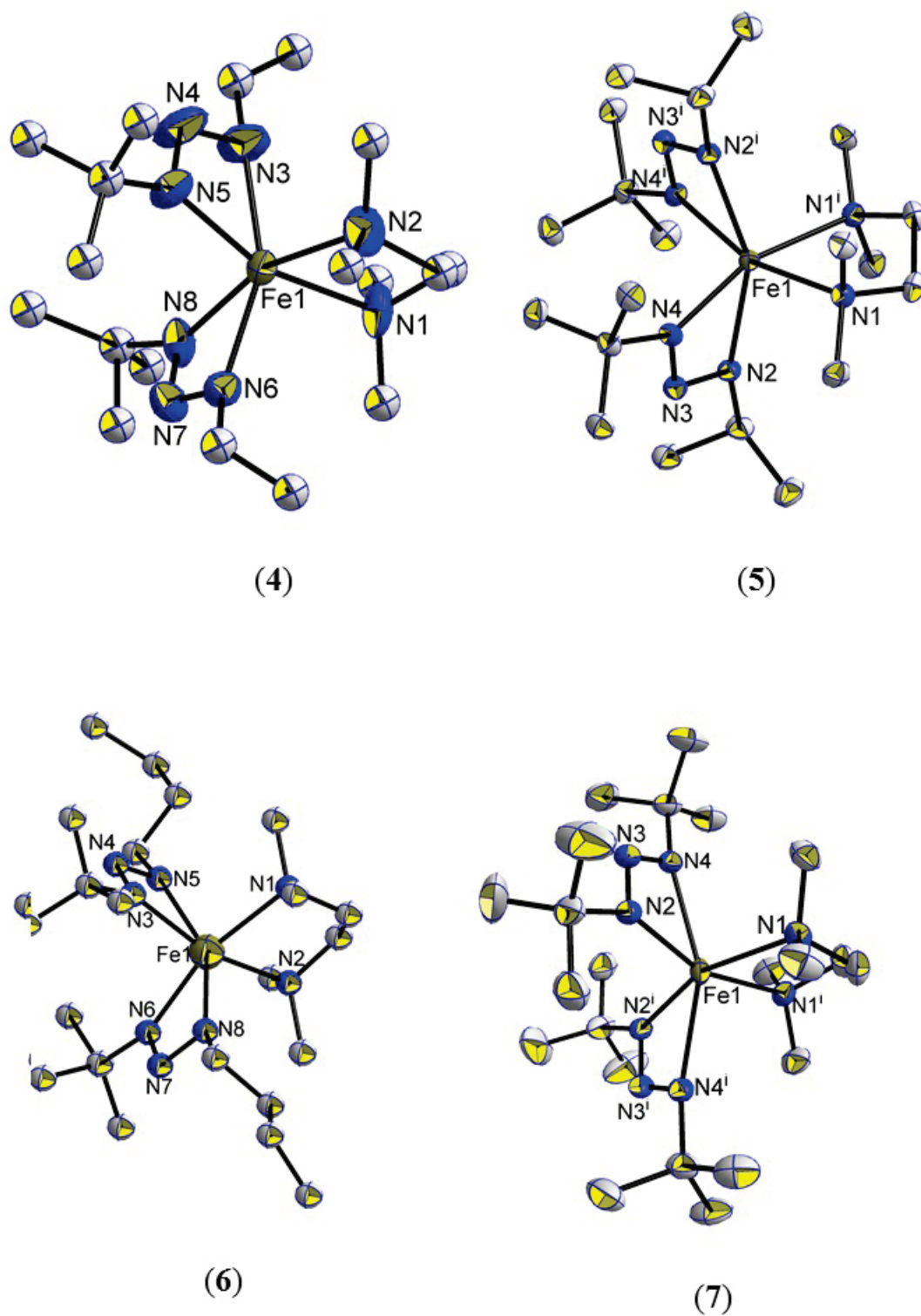


Figure 2.9 – Perspective view of 4-7 with thermal ellipsoids at 50% level. H-atoms are omitted for clarity.

Table 2.1 – Selected bond lengths of complexes **1** and **3**.

$[Fe_2(N_3^tBuEt)_4]$ ( <b>1</b> )		$[Fe_2(N_3^tBu^nBu)_4]$ ( <b>3</b> )	
Bond	Bond length (Å)	Bond	Bond length (Å)
Fe1-Fe1'	2.167(2)	Fe1-Fe1'	2.166 (7)
Fe1-N2	2.004 (7)	Fe1-N2	1.965(2)
Fe1-N4	1.929(7)	Fe1-N4	1.944(3)
Fe1-N11	1.973(6)	Fe1-N13	1.943(2)
Fe1-N13	1.938(6)	Fe1-N15	1.961(2)

Table 2.2 – Selected bond angles of complexes **1** and **3**.

$[Fe_2(N_3^tBuEt)_4]$ ( <b>1</b> )		$[Fe_2(N_3^tBu^nBu)_4]$ ( <b>3</b> )	
Bond	Angles (deg)	Bond	Angles (deg)
N11-Fe1-N2	89.67(3)	N2-Fe1-N4	90.49(1)
N2-Fe1-N4	90.15(3)	N2-Fe1-N13	89.59(1)
N4-Fe1-N13	92.21(3)	N13-Fe1-N15	90.83(1)
N13-Fe1-N11	88.12(3)	N2-Fe1-N4	89.06(1)
Fe1'-Fe1-N11	89.57(2)	N2-Fe1-N15	180.45(3)
N4-Fe1-N11	178.03(10)	N2-Fe1-N15	88.58(6)

Table 2.3 – Selected bond lengths of complexes **4** and **5**.

$[Fe(N_3^tBuEt)_2(TMEDA)]$ ( <b>4</b> )		$[Fe(N_3^tBu^iPr)_2(TMEDA)]$ ( <b>5</b> )	
Bond	Bond length (Å)	Bond	Bond length (Å)
Fe1-N1	2.270(2)	Fe-N2	2.306(2)
Fe1-N2	2.282 (7)	Fe-N6	2.144(2)
Fe1-N3	2.131(7)	Fe-N8	2.143(2)
Fe1-N5	2.125(6)	-	-
Fe1-N6	2.159(6)	-	-
Fe1-N8	2.144(3)	-	-

Table 2.4 – Selected bond angles of complexes **4** and **5**.

$[Fe(N_3^tBuEt)_2(TMEDA)]$ ( <b>4</b> )		$[Fe(N_3^tBu^iPr)_2(TMEDA)]$ ( <b>5</b> )	
Bond	Angles (deg)	Bond	Angles (deg)
N1-Fe1-N2	78.45(3)	N6-Fe-N8	59.83(6)
N3-Fe1-N5	60.06(3)	N2'-Fe-N6'	96.72(7)
N6-Fe1-N8	58.93(3)	N2-Fe-N21	162.44(4)
N2-Fe1-N6	103.64(3)	N2-Fe-N2'	79.52(2)

Table 2.5 – Selected bond lengths of complexes **6** and **7**.

$[Fe(N_3^tBu^nBu)_2(TMEDA)]$ ( <b>6</b> )		$[Fe(N_3^tBu)_2(TMEDA)]$ ( <b>7</b> )	
Bond	Bond length (Å)	Bond	Bond length (Å)
Fe-N2	2.315(8)	Fe1-N1	2.321 (7)
Fe-N6	2.302(9)	Fe1-N2	2.088(2)
Fe-N10	2.176(8)	Fe1-N4	2.380(3)
Fe-N12	2.154 (9)	N2-N3	1.314(2)
-	-	N3-N4	1.294(2)
-	-	C14-C14	1.496(4)

Table 2.6 – Selected bond angles of complexes **6** and **7**.

$[Fe(N_3^tBu^nBu)_2(TMEDA)]$ ( <b>6</b> )		$[Fe(N_3^tBu)_2(TMEDA)]$ ( <b>7</b> )	
Bond	Angles (deg)	Bond	Angles (deg)
N10-Fe-N12	59.88(3)	N1-Fe1-N1	78.15(1)
N21-Fe-N23	61.52(3)	N2-Fe1-N4	57.25(1)
N6-Fe-N23	100.11(3)	N1-Fe1-N2	91.54(1)
N2-Fe-N21	163.18(3)	N2-Fe1-N4	89.06(1)

### 2.3.2 Mössbauer spectroscopy

Mössbauer spectroscopic studies were carried out on the  $[Fe_2(N_3^tBuEt)_4]$  (**1**) and  $[Fe(N_3^tBu_2Et)_2(TMEDA)]$  (**4**) as representative complexes of the dimeric and monomeric species, respectively, to understand the oxidation and spin states of the iron centers in them. The samples were prepared in the glovebox and the sample holder was closed with grease to protect it from moisture and oxygen.

The Mössbauer spectrum of  $[Fe(N_3^tBu_2Et)_2(TMEDA)]$  (**4**) (Figure 2.10) at room temperature exhibits a doublet with an isomer shift  $\delta = 0.89$  mm/s and a quadrupolar shift  $\Delta = 2.58$  mm/s, which can be assigned without ambiguity to Fe(II) center.

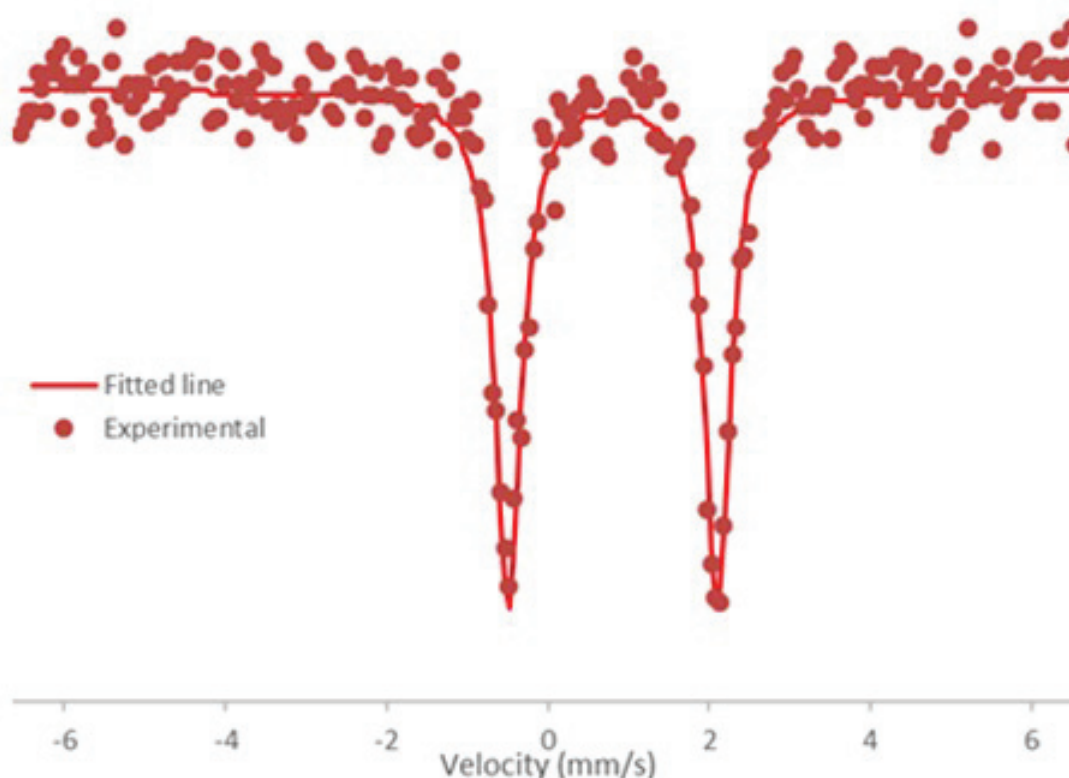


Figure 2.10 – Mössbauer spectra of  $[Fe(N_3^tBu_2Et)_2(TMEDA)]$  (**4**).

For (**1**), the Mössbauer spectrum was recorded at low temperature starting at 4 K, this dimer was then heated gradually up to room temperature with Mössbauer spectra being recorded at regular intervals (4, 77, 150 and 298 K) shown in Figure 2.11. Then it was cooled again and spectra were recorded at 250, 200 and 77 K (Figure 2.12).

All spectra were adjusted with three sub-spectra whose relative intensities varied as a

function of temperature.

The major species at 4K at  $\delta = 0.22$  mm/s with 70% relative intensity corresponds to the non-degraded low-spin iron (II) complex. The doublet with a high isomer shift (0.95 mm/s, 20% abundance) can be attributed to a complexed high spin Fe(II) or Fe(II)-Fe(III) species. The 3<sup>rd</sup> species is magnetic (50.7 T) with  $\delta = 0.95$  mm/s. It could correspond to an oxide or hydroxide  $Fe(O)_x(OH)_y$ . This species is characterized systematically at higher temperature by a superparamagnetic doublet and should, therefore, correspond to a species in the form of nanoscale particles.

Upon heating to 77, 150 and 298 K, the same three species are still present but with different intensity ratio and absence of magnetism for the  $Fe(O)_x(OH)_y$ , the latter could be due to a superparamagnetic behavior of very small particles. The spectrum obtained at room temperature showed an elevated intensity of the oxide or hydroxide component (49%) indicating that the oxidation process is amplified significantly at this temperature. The presence of these three species and their related ratios are little affected upon re-cooling this compound to 250, 200 and 77K.

In summary, the compound (**1**) in its non-oxidized state is characterized by a low spin Fe (II) irrespective of the temperature. Upon storage, it oxidizes slowly into  $Fe(O)_x(OH)_y$  species. This oxidation passes by a mono-oxidized dimeric intermediate Fe(II)-Fe(III) complex or a high spin Fe(II) complex.

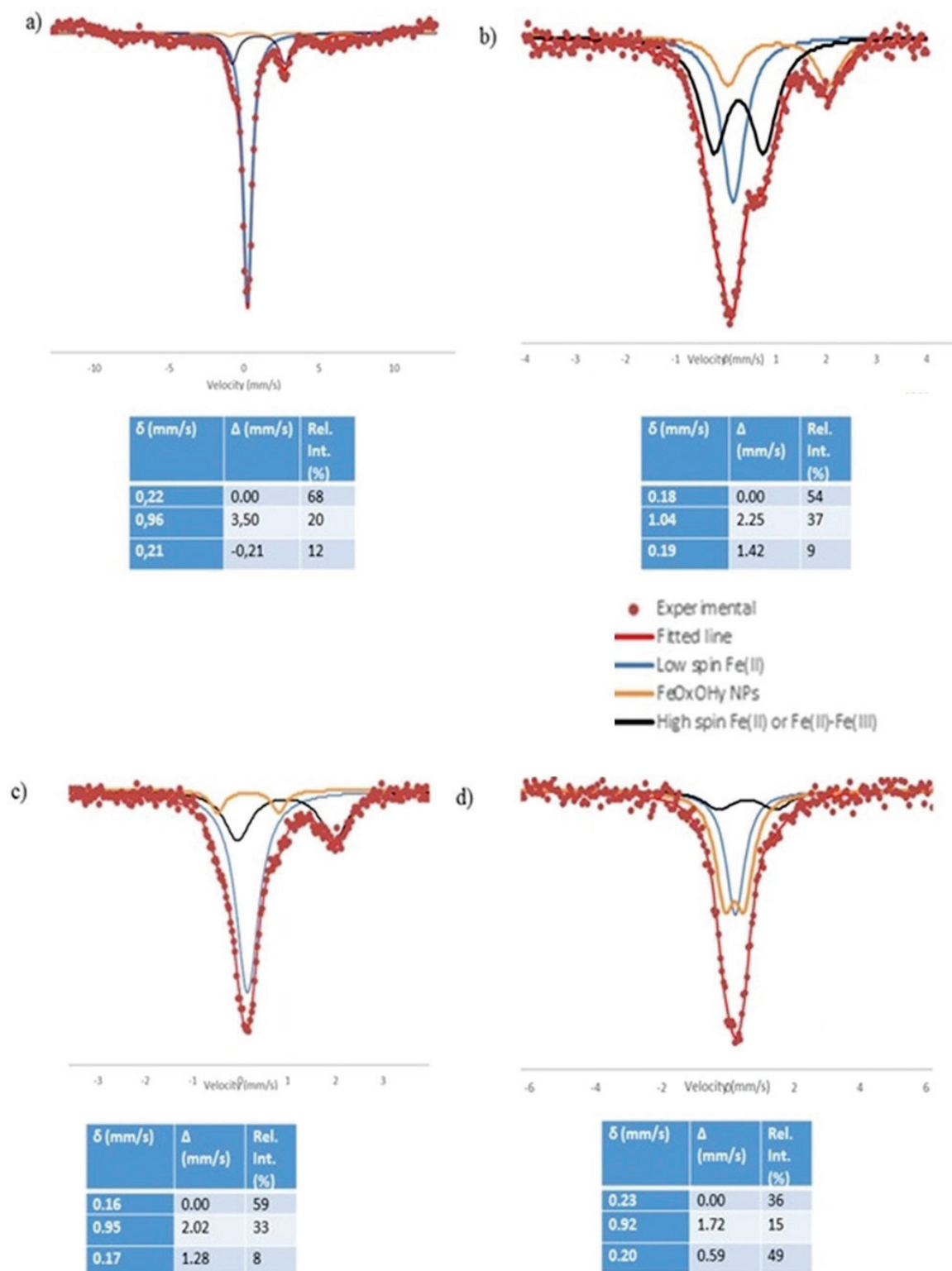


Figure 2.11 – Variable temperature Mössbauer spectra of  $[Fe_2(N_3^tBuEt)_4]$  (**1**) at 4.2K (a), 77K (b), 150K (c) and 298K (d) while being heated gradually.

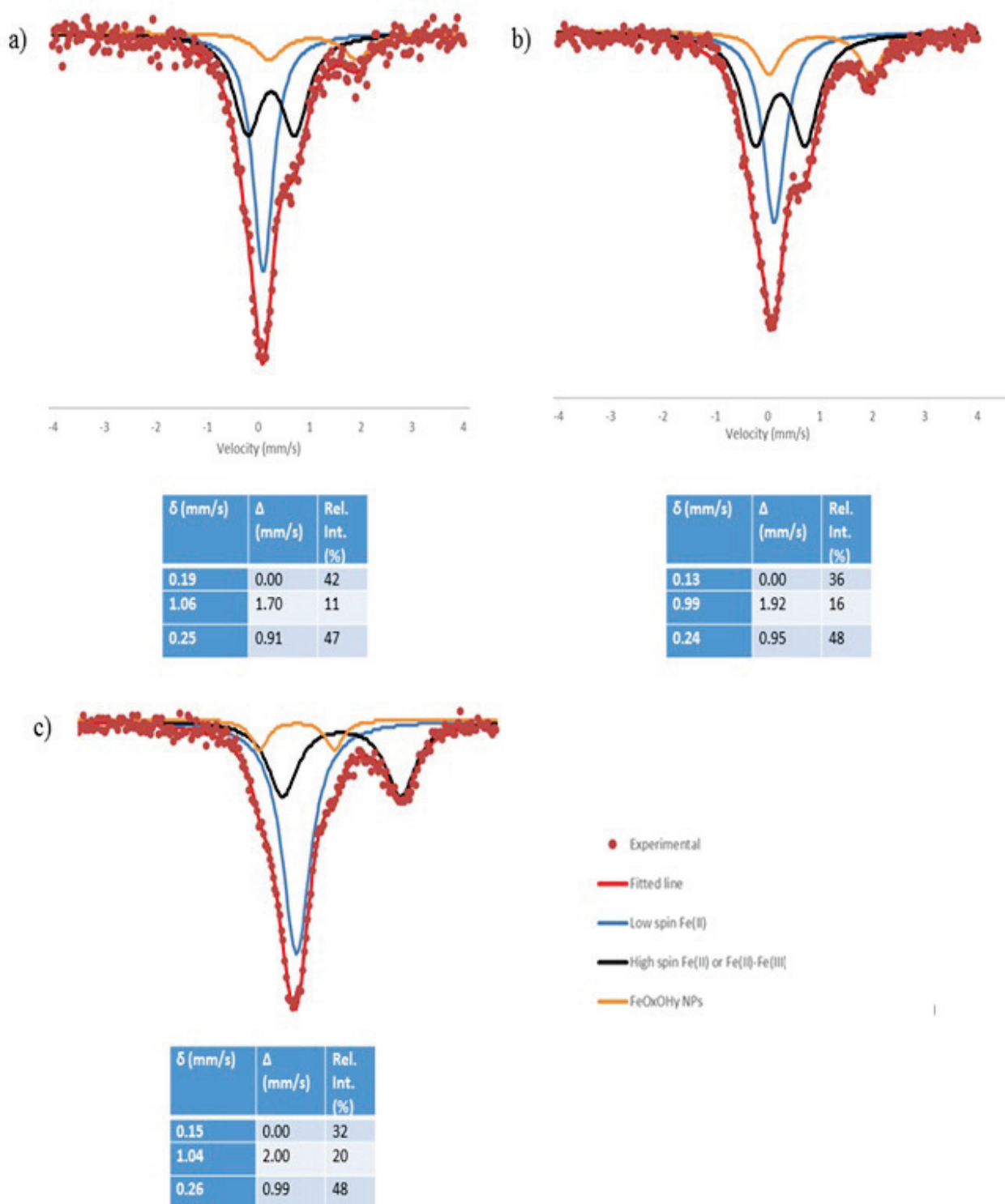


Figure 2.12 – Variable temperature Mössbauer spectra of  $[Fe_2(N_3^tBuEt)_4]$  (**1**) at 250K (a), 200K (b) and 77 K (c) while being cooled gradually.

### 2.3.3 Electron Paramagnetic Resonance EPR

EPR was done to understand the particular behavior of dimeric complexes in Mössbauer. Figure 2.13 a presents the EPR spectra of  $[Fe_2(N_3^tBuEt)_4]$  (**1**) in solid (blue curve) and solution (red and green curves for the *THF* and hexane, respectively), with standard cavity at 112 K. It shows the main peak at  $g=9.24$ , which corresponds to a high half integer spin state. Figure 2.13 b and c exhibit 3 axial species in low spin, respectively,  $g$  perpendicular = 2.24, 2.04 and 2.01. In the case of hexane, the high spin species is drastically diminished; however, the clusterization of iron(III) appears at  $g=2$  (large peak). Figure 2.14 shows the EPR spectra of  $[Fe_2(N_3^tBuEt)_4]$  (**1**) in solid phase in d (perpendicular mode): a) shows peaks corresponding to high spin at  $g=9.44$  and 4.26. The species at  $g=9.44$  exhibits Curie-Weiss behavior with changing temperature, b) shows the main peaks in low spin at respectively  $g_{\text{perpendicular}}=2.22$  and  $g_{\text{parallel}}=1.96$ . Figure 2.15 a) and b) show that the intensity of the imaginary magnetic susceptibility decreases with increasing temperature according to the Curie-Weiss law ( $1/\chi''$  is linear with increasing T).

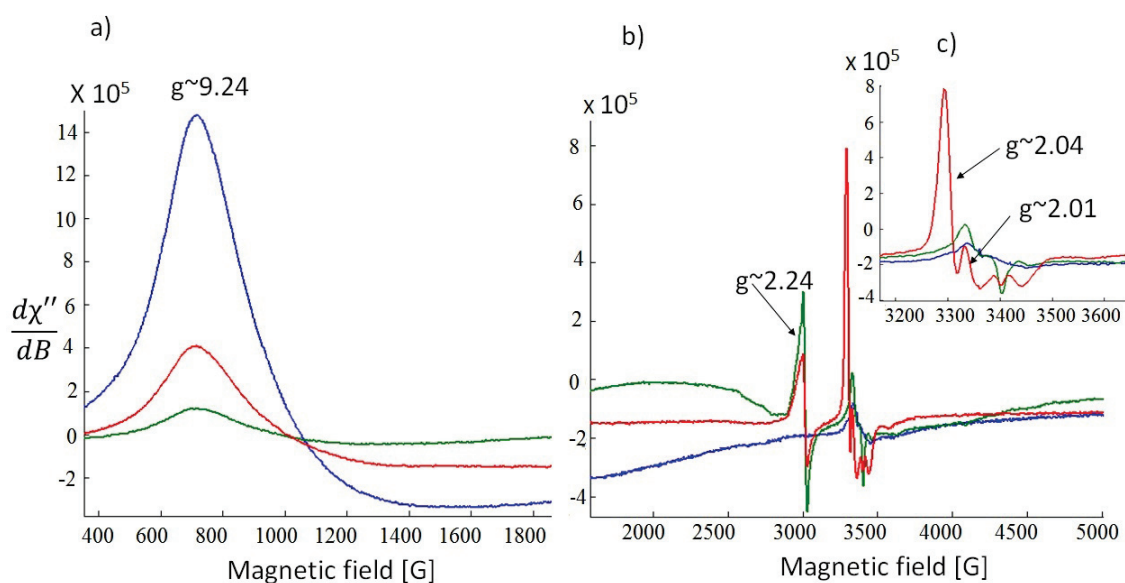


Figure 2.13 – EPR experimental spectrum of  $[Fe_2(N_3^tBuEt)_4]$  (**1**); blue: solid, red: in *THF* solution, green: in hexane solution, at 112K, standard cavity, a) low fields, and b) high fields.

Figure 2.16 shows the EPR spectra of  $[Fe_2(N_3^tBuEt)_4]$  (**1**) in solid phase in parallel mode: a) shows peaks corresponding to high spin at  $g=9.96$ , which does not exhibit Curie-Weiss behavior with changing temperature b) shows the low spin species at

g 2.22. The right peaks are resonance peaks coming from oxygen in the air in the epr tubes. Figure 2.17 a) and b) show the intensity of the imaginary magnetic susceptibility with increasing temperature. We can see antiferromagnetic interaction in this species.

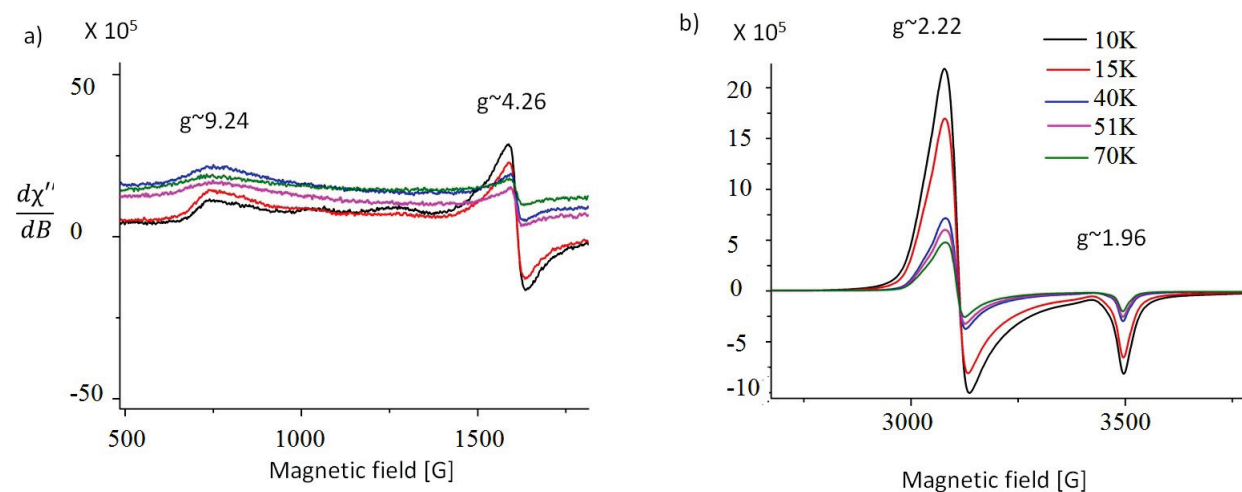


Figure 2.14 – EPR experimental spectrum of  $[Fe_2(N_3^tBuEt)_4]$  (**1**) solid, perpendicular mode: a) I<sub>ep</sub>r at low fields, and b) I<sub>ep</sub>r at high fields c)  $\chi''$  Vs T d)  $1/\chi''$  Vs T.

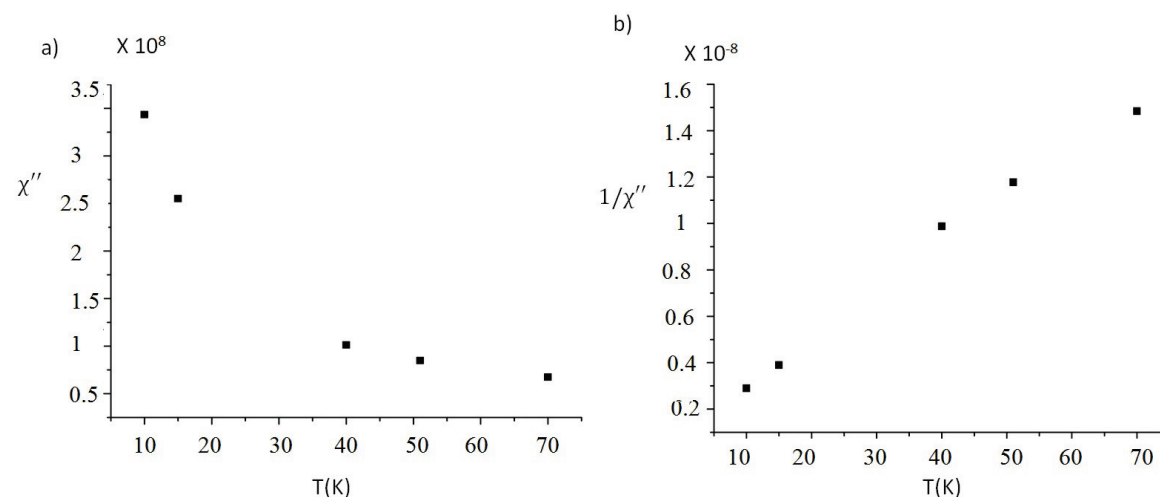


Figure 2.15 – EPR experimental spectrum of  $[Fe_2(N_3^tBuEt)_4]$  (**1**) solid, perpendicular mode: a)  $\chi''$  Vs T, and b)  $1/\chi''$  Vs T.

Figure 2.18 shows simulations spectrum of  $[Fe_2(N_3^tBuEt)_4]$  (**1**) solid: a) parallel mode at 20K,  $S = 2$   $g = [2.4, 2.4 \text{ and } 1.985]$   $D=2.098(4 \text{ cm}^{-1})$   $E=0.0478(4 \text{ cm}^{-1})$  b) standard cavity at 112K,  $S= 5/2$   $g= [2.45, 2.45 \text{ and } 1.9]$   $D=2.1(4 \text{ cm}^{-1})$   $E=0.1050(4 \text{ cm}^{-1})$  X-ray and Mössbauer analysis confirmed that the crystalline structure of  $[Fe_2(N_3^tBuEt)_4]$  (**1**) is in the Fe(II)-Fe(II) disposition. In EPR measurements, we can characterize the Fe(II) species as being oxidized. Even though the samples are

prepared in an inert atmosphere, they inevitably come in contact with traces of oxygen while being transferred to the EPR tubes, explaining the corresponding EPR signals. Beside Fe(II) dimers, Mössbauer results showed the presence of oxidized species that corresponded to dimeric complexes, with  $S=5/2$  and nanostructured Fe(III)-O (or Fe(III)-OH) species, which are superparamagnetic in nature. The EPR spectra presented in Figure 2.13 show a strong axial peak at  $g=9.24$  in the standard cavity, with no important low spin resolution. A simulation with  $S=5/2$ , as shown in Figure 2.18 b suggests that the dimer is in a Fe(III)-Fe(II) state in low symmetry. Note that most of peaks at  $g$  values superior than 9 in the literature, are attributed to  $S=5/2$  state which are not strongly resolved [57,58]. The EPR of this complex was also measured in solution phase using anhydrous *THF* and hexane as solvents. Their EPR signals, Figure 2.13 b and c show that solution in *THF* contains relatively more low spin axial species than hexane [59–61]. However, hexane allows the clustering of dimers (large peak in  $g=2$ ). The alteration of initial complex gives several monomeric axial and octahedral distorted species in low spin [60,62,63]. The solid sample used for EPR analysis in double cavity mode under He temperature seems to be more oxidized. Hence, in perpendicular mode, Figure 2.14 a and b show that the main species found is axial in low spin because of the triazenide equatorial ring ligation and Fe(III)-O (or OH) in  $z$  axis. We think that this species, with  $g_{\text{perpendicular}}=2.22$  and  $g_{\text{parallel}}=1.96$ , is a monomer. Note that this species is obtained in solution samples, Figure 2.13 b and c at higher temperature (112K, standard cavity), meaning that it is due to oxidation of Fe(II)-Fe(II) complex. Two minor species shown in a) with  $g=9.44$  and 4.26 could be attributed, respectively, to oxide nanoparticles and isolate Fe(III) in high spin which is tetragonally distorted. Figure 2.18 a and b confirm that the main axial species does not interact magnetically with other iron species. Their thermal behaviour follows Curie-Weiss law. The minor nanoparticle signal is more resolved in parallel mode (Figure 2.16), where  $g$  is 9.96. However, their magnetic susceptibility, Figure 2.17 a) and b), doesn't follow Curie-Weiss law, because of a weak antiferromagnetic interaction between neighbouring irons in the oxides [64], Neel temperature is about 20K. The simulation, shown in Figure 2.18 a confirmed that the spin state of the dipolar interaction takes an integer value, which must correspond to  $S=2$ . This spin state could be obtained from Fe(III) High spin and low spin in surface oxide structure. The minor species seen at  $g=2.22$ , corresponds to axial symmetry, shown in perpendicular mode. However, other peaks are those of oxygen which disappear when temperature is above 20K.

The low EPR signal of  $Fe(N_3^tBuEt)_2(TMEDA)$  (**4**) shown in Figure 2.19 means that the iron monomers are probably and mainly in Fe(II) state, in accordance with Mössbauer analysis. However, Fe (III) detected is in low spin, with large and isotropic

pic (cluster,  $g=2$ ) and in high spin ( $g=4.2$ ) transition. Note that in  $g=2$  region, there is some impurity peak due to cavity and Mn(II). The fine peak is due to a presence of radical in the powder of sample which is probably an impurity.

In conclusion, Mössbauer and EPR results are in agreement and show that dimers are unstable towards oxidation. They slowly oxidize into iron oxide/hydroxide NPs passing through a mono-oxidized Fe(II)-Fe(III) complex. Monomers are much more stable towards oxidation.

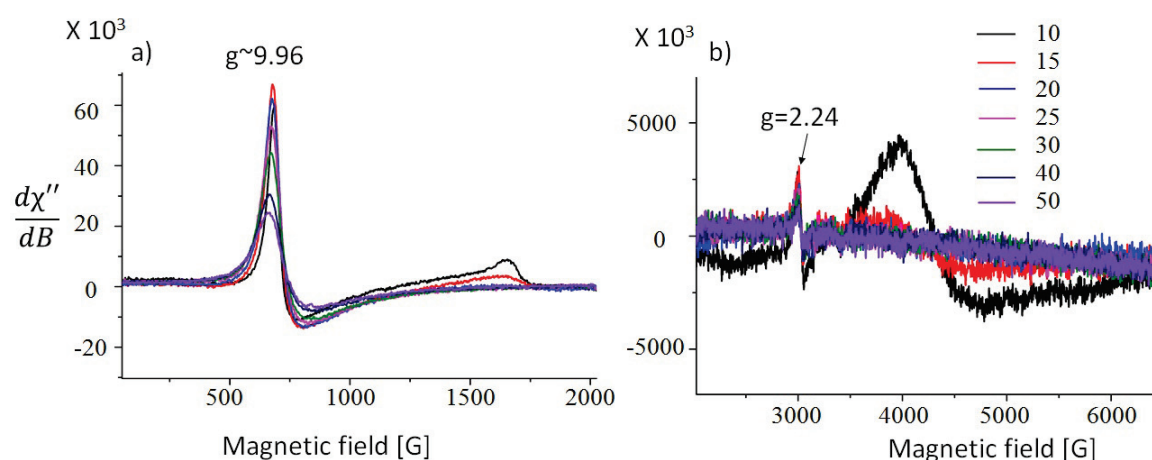


Figure 2.16 – EPR experimental spectrum of  $[Fe_2(N_3^tBuEt)_4]$  (**1**) solid in parallel mode: a) Epr at low fields, and b) Epr at high fields.

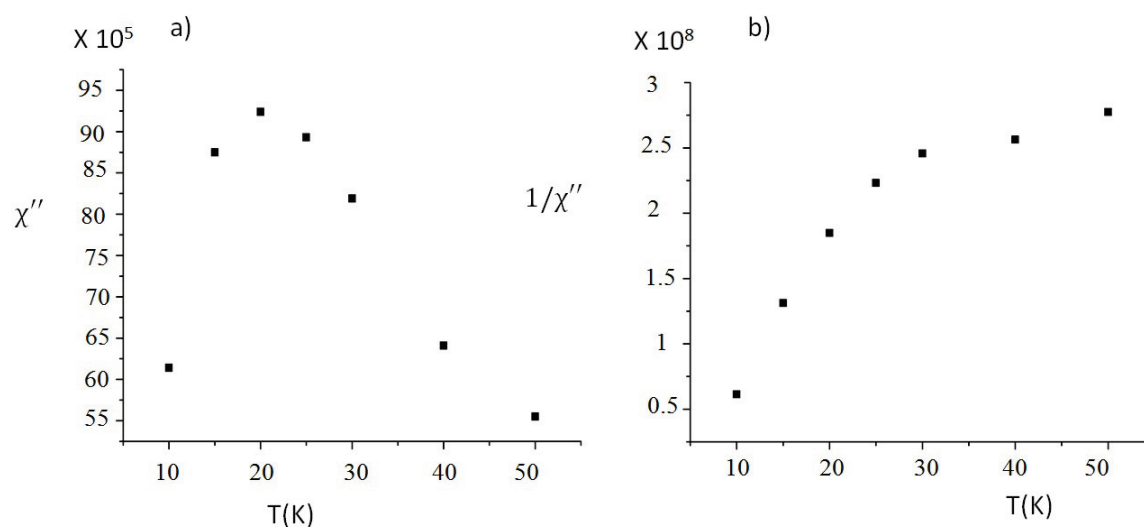


Figure 2.17 – EPR experimental spectrum of  $[Fe_2(N_3^tBuEt)_4]$  (**1**) solid in parallel mode: a)  $\chi''$  Vs T, and b)  $1/\chi''$  Vs T.

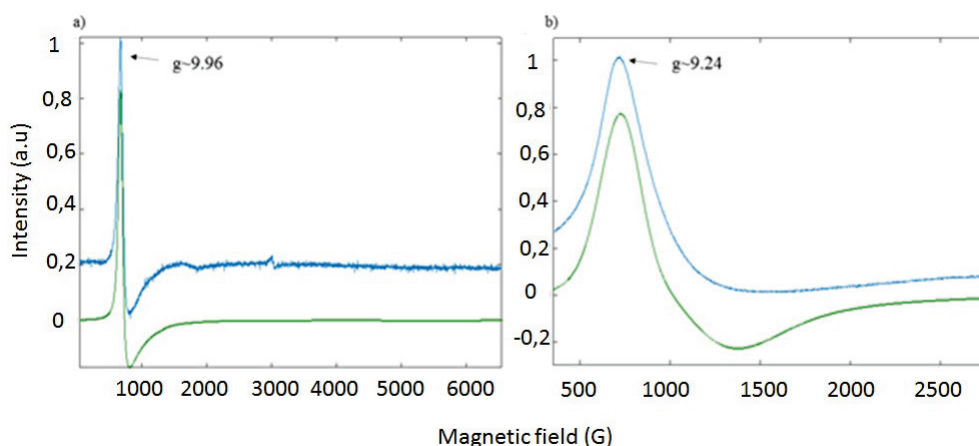


Figure 2.18 –  $[Fe_2(N_3^tBuEt)_4]$  (**1**) solid, a) blue: experimental @20K in parallel mode, green: simulated b) blue: experimental @112K with standard cavity, green: simulated.

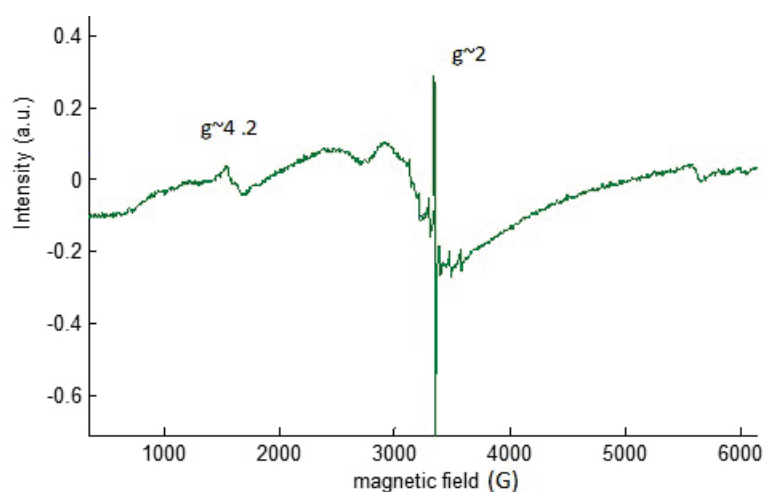


Figure 2.19 – EPR experimental spectrum of  $[Fe(N_3^tBuEt)_2(TMEDA)]$  (**4**) in solid state.

### 2.3.4 Electrochemistry

Cyclic voltammetry was performed on complexes **1-6** in order to understand the electrochemical properties of these complexes. Experiments were conducted under a constant flow of argon gas using a standard three-electrode setup with a glassy carbon working disc electrode and a platinum wire auxiliary electrode and calomel saturated electrode reference electrode. The complex solution in anhydrous THF was 1 or 2 mM in the supporting electrolyte of 0.1 M ( $nBu_4N$ )PF<sub>6</sub>. Under these experimental conditions, the ferrocene/ferricinium couple was used as an internal reference for potential measurements.  $[Fe_2(N_3^tBuEt)_4]$  (**1**),  $[Fe_2(N_3^tBu^iPr)_4]$  (**2**) and  $[Fe_2(N_3^tBu^nBu)_4]$  (**3**) showed an irreversible oxidation process at 1.78V and 1.73V

and 1,86V, respectively. It is clear from the voltammogram that  $[Fe_2(N_3^tBuEt)_4]$  (**1**) and  $[Fe_2(N_3^tBu^iPr)_4]$  (**2**) have a very close oxidation potential which is a bit lower than that of  $[Fe_2(N_3^tBu^nBu)_4]$  (**3**). In other words, the bulkiest ligand  $N_3^tBu^nBu$  leads to a complex with the highest oxidation potential.

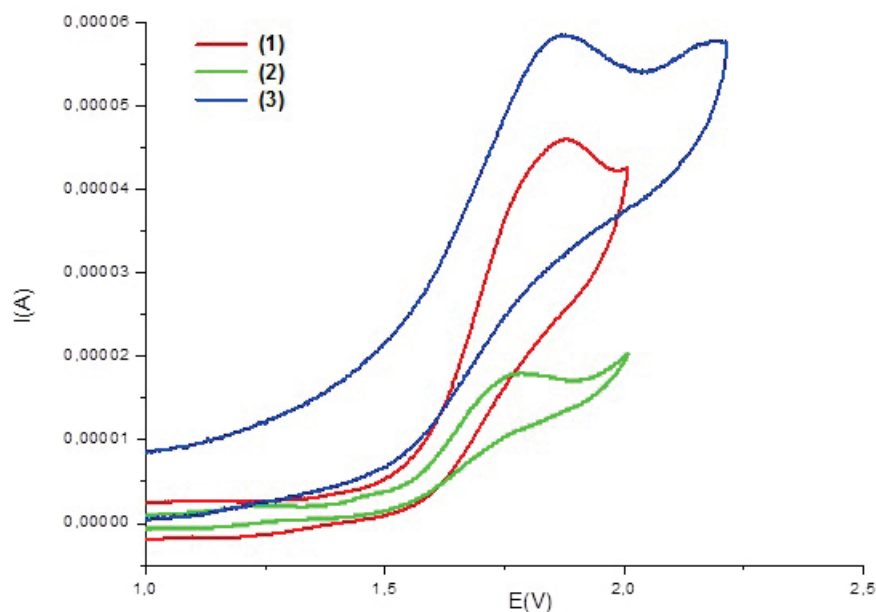


Figure 2.20 – Voltammogram of  $[Fe_2(N_3^tBuEt)_4]$  (**1**),  $[Fe_2(N_3^tBu^iPr)_4]$  (**2**) and  $[Fe_2(N_3^tBu^nBu)_4]$  (**3**).

To understand the electrochemical behavior of dimers, electrolysis has been performed on the representative example  $[Fe_2(N_3^tBuEt)_4]$  (**1**) in order to calculate the number of electrons involved in the oxidation process of these complexes.

Electrolysis is an electro-analytical process that determines the quantity of electricity (Q in coulomb) experimentally by completely oxidizing or reducing a known quantity of a chemical compound. The working electrode is kept at a constant potential and the current that flows through the circuit is measured. As the electroactive molecules are consumed, the current also decreases, approaching zero when the conversion is complete. Cyclic voltammetry of  $[Fe_2(N_3^tBuEt)_4]$  (**1**) was performed before electrolysis experiment in anhydrous dichloromethane in order to assess the potential needed to oxidize these complexes in an electrolysis experiment. Cyclic voltammetry was then done after electrolysis to verify if all the quantity has been consumed. The sample mass, molecular mass, number of electrons in the electrode reaction, and number of electrons passed during the experiment are all related by Faraday's laws. It follows that, if three of the values are known, then the fourth can be calculated. The formula is identified by:

$$Q = n \times F \times n_e$$

Where Q = electrical charge, measured experimentally by the software by calculating the area under the curve I (A) vs time (min), identified by:

n = number of moles of the compound

F = Faraday's constant = 96500

n<sub>e</sub> = number of electrons involved in the electrochemical process

The potential of the working electrode needed to completely oxidize the quantity of a chemical compound in an electrolysis experiment is determined by cyclic voltammetry and it corresponds to the oxidation peak of the compound. Number of electrons involved in the oxidation of  $[Fe_2(N_3^tBuEt)_4]$  (**1**):

Assuming that the electrochemical process is a one electron process:

$$Q_{\text{theoretical}} = m \times F \times 1 / M = 0.02 \times 96500 / 652.69 = 2.956 \text{ coulomb}$$

$$Q_{\text{experimental}} = 3.5 \text{ coulomb}$$

$$Q_{\text{exp}} / Q_{\text{theoretical}} = 3.5 / 2.956 = 1.18 \text{ electron}$$

Therefore, the oxidation of the dimers is a one electron process that corresponds to the oxidation from Fe(II) to Fe(III).

Similarly, all monomeric complexes show a one electron oxidation. However, their oxidation occurs at lower potential than those for dimeric complexes (Figure 2.21). The oxidation potential values were 1.17, 1.18 and 1.61V for  $[Fe(N_3^tBuEt)_2(TMEDA)]$  (**4**),  $[Fe(N_3^tBu^iPr)_2(TMEDA)]$  (**5**) and  $[Fe(N_3^tBu^nBu)_2(TMEDA)]$  (**6**), respectively. The lower oxidation potential for the monomers reflects an easier oxidation of these complexes as compared to dimers. This is contradictory to the results of obtained from Mössbauer and EPR experiments: Monomers are much more stable towards oxidation than dimers.

Number of electrons calculated in the oxidation of  $[Fe(N_3^tBuEt)_2(TMEDA)]$  (**4**) chosen as representative of the monomers is 1.07 electron, and as expected, the complex is consumed completely in the electrolysis experiment as attested by (Figure 2.22) by the absence of the oxidation peak after electrolysis. Therefore, the oxidation of the monomer is a one electron process that corresponds to the oxidation of the iron center from Fe(II) to Fe(III).

A comparison of the cyclic voltammogram of dimeric and monomeric iron complexes gives us the following conclusions:

1. All complexes show one electron, irreversible oxidation cycle.
2. Monomeric complexes have an oxidation potential that is inferior to those of dimeric complexes.

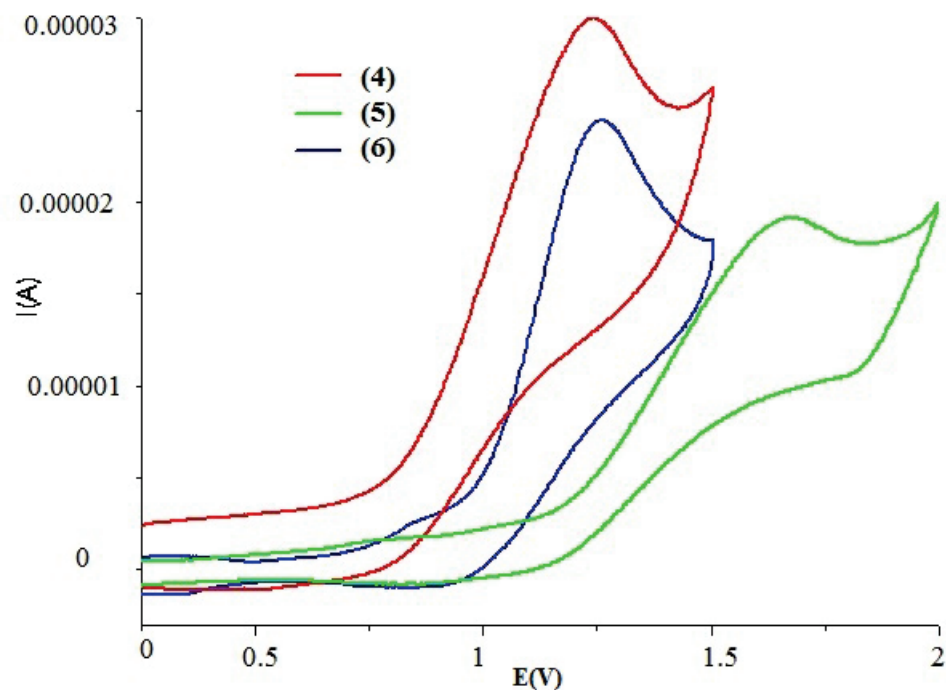


Figure 2.21 – Cyclic voltammogram of  $[Fe(N_3^tBuEt)_2(TMEDA)]$  (4),  $[Fe(N_3^tBu^iPr)_2(TMEDA)]$  (5) and  $[Fe(N_3^tBu^nBu)_2(TMEDA)]$  (6).

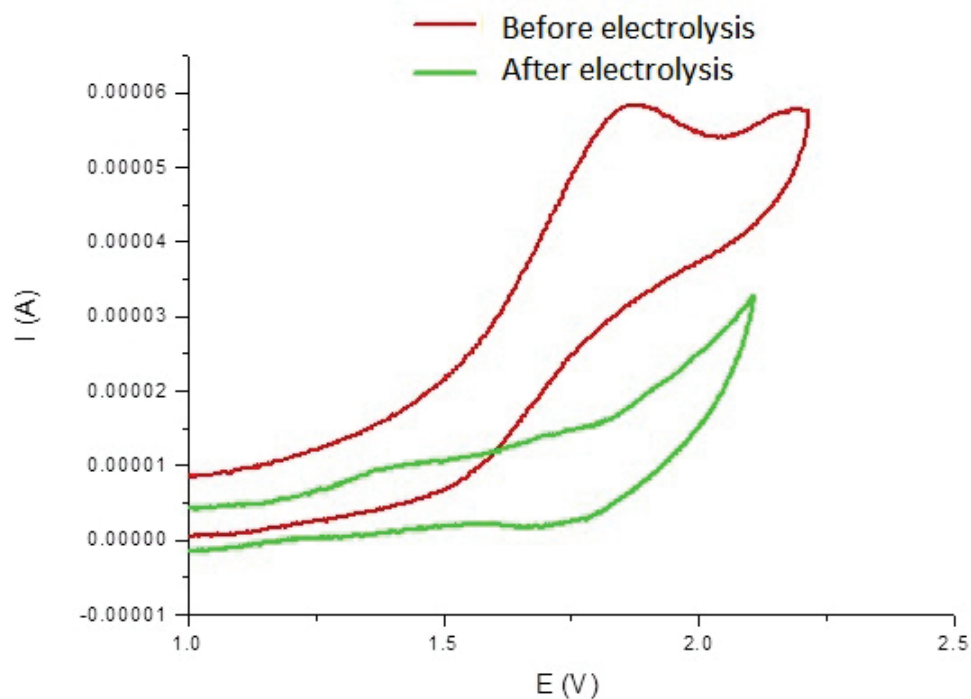


Figure 2.22 – Cyclic voltammogram of  $[Fe_2(N_3^tBuEt)_4]$  (1) in anhydrous  $CH_2Cl_2$ , 0.1 M  $(^nBu_4N)PF_6$ , 100 mV.

### 2.3.5 Thermal properties

TGA of  $[Fe_2(N_3^tBuEt)_4]$  (**1**) shows a three-step weight loss between 66 - 120°C, 120 - 150°C and 150 - 250°C. Each weight loss corresponds to the dissociation of one triazenide ligand. The residue left at 450°C is 24.18% which is much higher than the theoretical iron content (18%). Similarly,  $[Fe_2(N_3^tBu^iPr)_4]$  (**2**) shows a three-step weight loss between 50 - 130°C, 130 - 215°C and 215 - 420°C and each of these weight losses correspond to the loss of one triazenide ligand. This complex shows a low thermal stability and has a high percentage residue of 30% which is much higher than the theoretical iron content of 16.5%. As for  $Fe_2(N_3^tBu^nBu)_4$  (**3**), it shows a two-step weight loss between 65 - 155°C and 155- 370°C. The first weight loss corresponds to the dissociation of two ligands while the second weight loss corresponds to the loss of a third ligand. The third ligand dissociated needed a lot of energy as explained by the large temperature window of about 220°C. The residues upon reaching 450°C were 15.5 % matches the theoretical iron content of 15.4%.

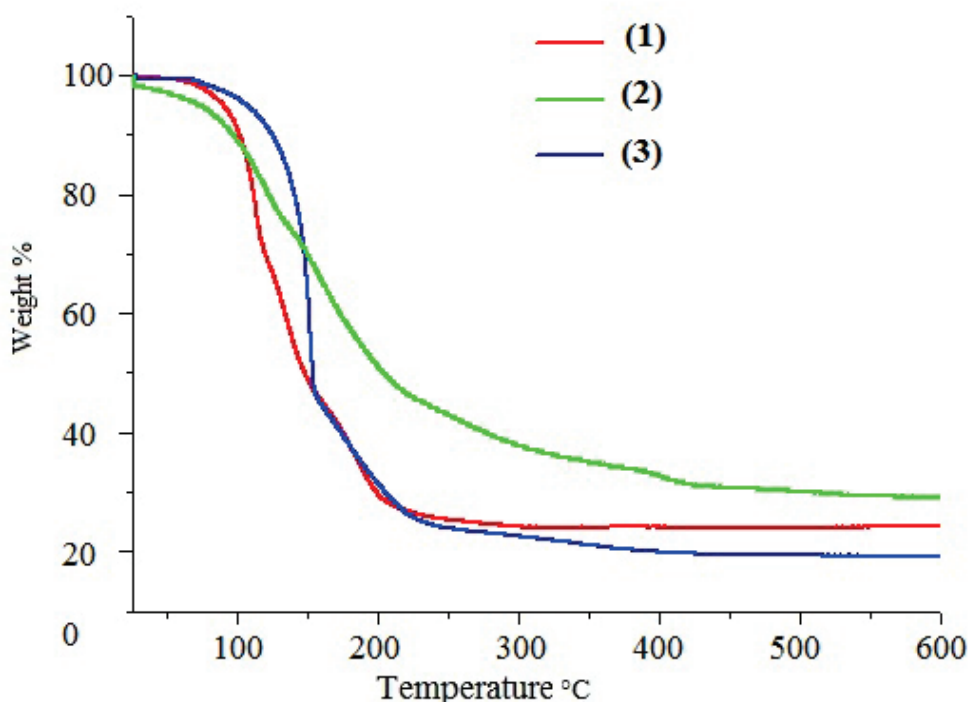


Figure 2.23 – TGA curves of  $[Fe_2(N_3^tBuEt)_4]$  (**1**),  $[Fe_2(N_3^tBu^iPr)_4]$  (**2**) and  $[Fe_2(N_3^tBu^nBu)_4]$  (**3**).

The incorporation of the TMEDA ligand and the eventual change in the structure to form monomeric complexes leads to different thermal behavior.  $[Fe(N_3^tBuEt)_2(TMEDA)]$  (**4**) shows a two-step weight loss at temperatures between

70 - 160°C, and 160 - 240°C with 21% residue upon reaching 450°C. The first step corresponded to the loss of the triazenide ligands. The second weight loss did not lead to the dissociation of the TMEDA ligand, but corresponds to the partial decomposition of this ligand to leave some organic residues.  $[Fe(N_3^tBu^iPr)_2(TMEDA)]$  (**5**) shows a three-step decomposition in the regions 50 - 130°C, 130 - 165°C and 165 - 250°C, respectively. The first weight loss corresponds to the dissociation of the TMEDA ligand whereas the second decomposition corresponds to the loss of one triazenide ligand. The third decomposition was not complete as the second triazenide ligand was not dissociated completely. This lead to an important residue left (28%), which is twice the theoretical iron content. It is worth noting that this is the least thermally stable complex among the monomers.  $[Fe(N_3^tBu^nBu)_2(TMEDA)]$  (**6**) shows a two-step weight loss in the regions between 70-150°C and 150- 220°C. Whereas two triazenide ligands were dissociated in the first decomposition step, the TMEDA was dissociated in the second step. The 14% residue left upon reaching 450°C is slightly higher than the theoretical iron content of 11%. It is the most thermally stable complex among all the iron(II) complexes reported here.  $[Fe(N_3^tBu_2)_2(TMEDA)]$  (**7**) shows a two-step weight loss at temperature between 70 - 150°C and 150 - 220°C with a slightly different behavior than the equivalent unsymmetrical ligand  $N_3^tBu^nBu$  in terms of ligands dissociated and thermal stability. TMEDA was lost in the first step, followed by one triazenide ligand and incomplete dissociation of the second triazenide ligand in the second step. This leads to a higher residue (21%) as compared to that obtained in the case of  $[Fe(N_3^tBu^nBu)_2(TMEDA)]$  (**6**). It is worth mentioning here that TGA residues of all monomers follow the order: theoretical content of Fe(0) < residue < calculated Fe oxides. This could be explained that monomeric iron triazenide complexes decompose at high temperatures and loose the ligands. This decomposition does not lead to the formation of Fe(0) nor of iron oxides (due to the absence of oxygen), but rather to iron complexes with unidentified organics.

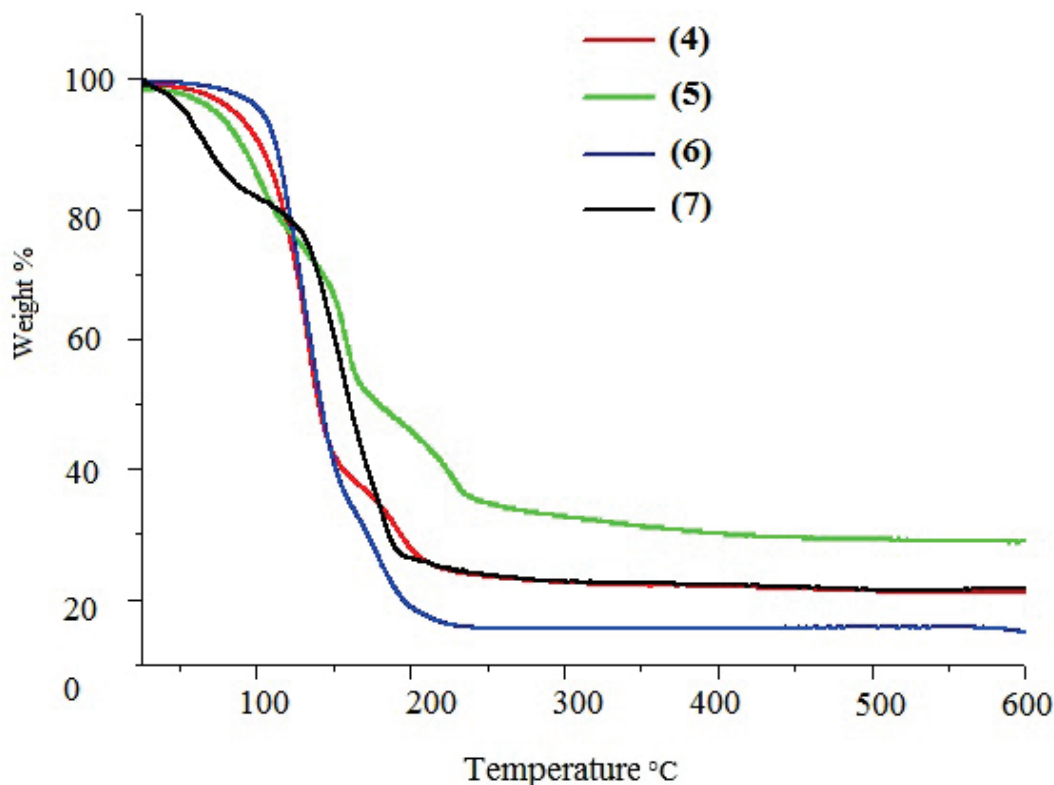


Figure 2.24 – TGA curves of  $[Fe(N_3^tBuEt)_2(TMEDA)]$  (4),  $[Fe(N_3^tBu^iPr)_2(TMEDA)]$  (5),  $[Fe(N_3^tBu^nBu)_2(TMEDA)]$  (6) and  $[Fe(N_3^tBu_2)_2(TMEDA)]$  (7).

Following conclusions can be drawn from the comparison of the thermogravimetric analysis of dimeric and monomeric iron complexes:

1. All complexes, regardless of whether monomeric or dimeric in nature, decompose partially while being transported into the vapour phase.
2. Thermal stability of the complexes depended on the ligands and the structure of the complexes (monomeric or dimeric). Generally speaking, i) the monomers were thermally more stable than dimers, and ii) complexes containing  $N_3^tBu^nBu$  ligand were more stable than those with the  $N_3^tBuEt$  and  $N_3^tBu^iPr$  ligands, the order of the stability being  $N_3^tBu^nBu > N_3^tBuEt > N_3^tBu^iPr$ . This trend is respected among the free ligands also.

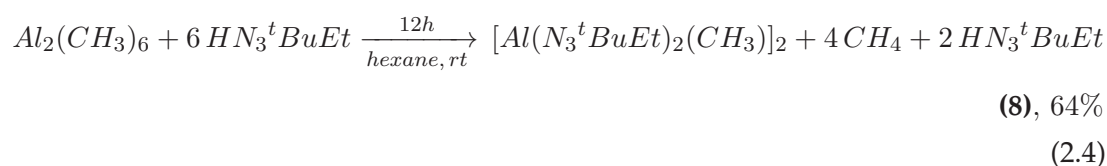
## 2.4 Aluminium triazenide complexes

Due to the oxophilicity and Lewis acidic nature of M(III) centers (M = Al, Ga, In), group 13 metal coordination compounds are typically best stabilized by hard Lewis

bases such as N- and/or O-based chelating ligands. So a motivation of the work reported in this chapter was to investigate novel aluminum precursors based on triazenide ligands. Another motivation was to modify DMEAA using triazene ligands in order to improve its properties. This modification can reduce the pyrophoric character of DMEAA that makes it delicate to handle and requires safety precautions. Also the addition of the triazene ligands can increase its stability and thus makes it more convenient to use for long term storage.

A series of aluminum triazenide complexes  $[Al(N_3^tBuEt)_2(CH_3)]_m$  (**8**),  $[Al(N_3^tBu^iPr)_3]_m$  (**9**),  $[Al(N_3^tBu^nBu)_3]_m$  (**10**),  $[Al(N_3^tBuEt)_3(py)_3]_m$  (**11**),  $[Al(N_3^tBuEt)_3]_m$  (**12**) and  $[Al(N_3^tBu_2)_3]_m$  (**13**) were synthesized and characterized by FT-IR, multinuclear NMR and TG-DTA. Six aluminum complexes have been prepared either by reacting a hexane solution of trimethyl aluminum  $Al_2(CH_3)_6$  with six equivalents of  $N_3^tBuR$  ( $R = Et, ^iPr, ^nBu$ ) in anhydrous hexane at room temperature or by reacting DMEAA with three equivalents of  $N_3^tBuR$  ( $R = Et, ^tBu$ ).

### 2.4.1 Starting from $Al_2(CH_3)_6$



Reactions of  $Al_2(CH_3)_6$  with six equivalents of the triazene ligands  $HN_3^tBuEt$  (**L1**) in hexane afforded yellow-orange liquids that crystallize at  $-20^\circ C$ . However, efforts for obtaining suitable x-ray single crystals were unsuccessful.  $^1H$  NMR spectra of complex with (**L1**) showed the presence of  $CH_3$  at  $-0.865$  ppm while  $^{27}Al$  NMR spectra showed multiple peaks that corresponded to tetra-, penta- and hexa-coordinated aluminum atoms indicating the presence of oligomers or of equilibrium in solution (or of impurities).  $^1H$  NMR and  $^{27}Al$  NMR spectra are shown in Figure 2.25 and Figure 2.26 respectively.

One would expect that the addition of six equivalents of triazenide ligands would lead to substitution of the six  $CH_3$  ligands *via* metathesis reaction. However, (**L1**) did not substitute all  $CH_3$  ligands.  $^1H$  NMR of  $[Al(N_3^tBuEt)_2(CH_3)]_m$  (**8**) showed the presence of one  $CH_3$  group coordinated to aluminium with a singlet at  $-0.85$  ppm. The high shielding effect is due to the electropositive character of the aluminium center and is slightly more deshielded in comparison to the  $Al_2(CH_3)_6$  peak which appears at  $-0.3$  ppm [65]. It seems that the weak inductive effect of (**L1**) which is due to the small substituent Et is a possible reason for the incomplete substitution of  $CH_3$  ligands.

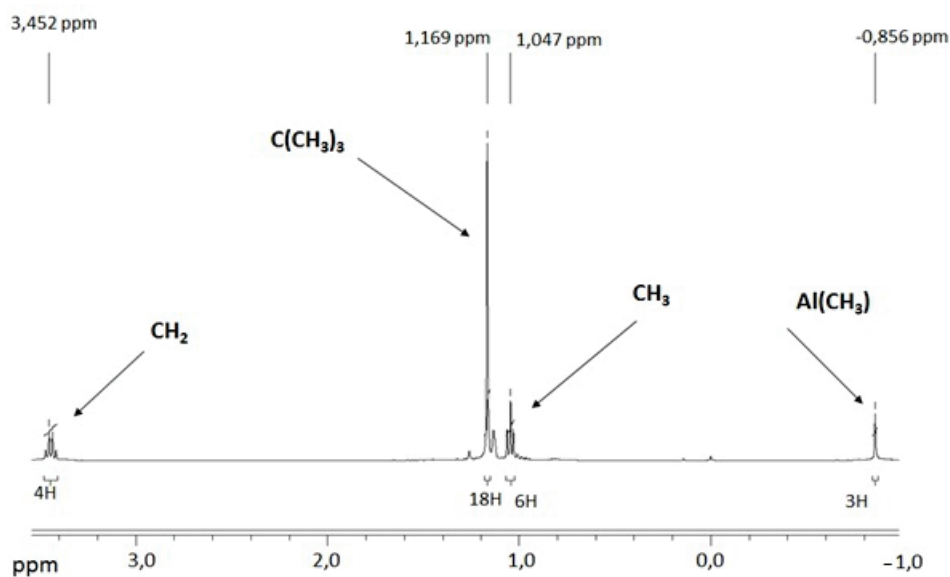


Figure 2.25 –  $^1\text{H}$  NMR spectrum of  $[\text{Al}(\text{N}_3^t\text{BuEt})_2(\text{CH}_3)]_m$  (**8**).

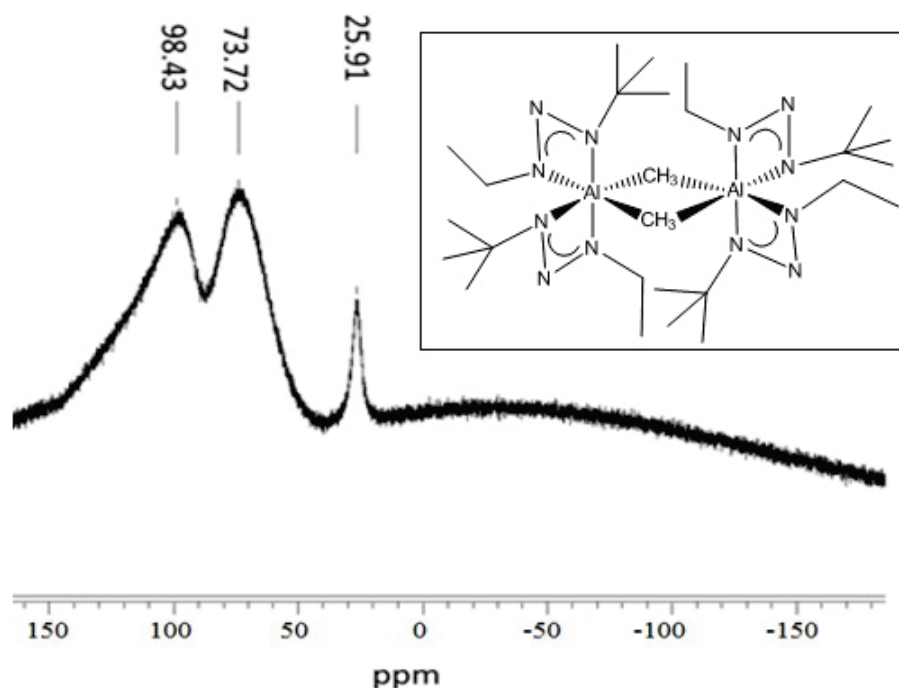
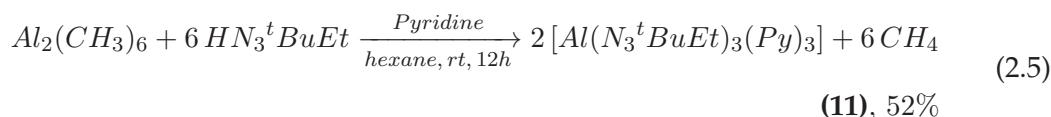


Figure 2.26 –  $^{27}\text{Al}$  spectrum of  $[\text{Al}(\text{N}_3^t\text{BuEt})_2(\text{CH}_3)]_m$  (**8**).

Under the same conditions, treatment of one equivalent of  $\text{Al}_2(\text{CH}_3)_6$  with four equivalents of (**L1**) and two equivalents of TMEDA did not yield the coordination of TMEDA as confirmed by NMR and instead the same complex  $[\text{Al}(\text{N}_3^t\text{BuEt})_2(\text{CH}_3)]_m$  (**8**) was obtained.

In contrast, the addition of few drops of anhydrous pyridine (Py) to  $\text{Al}_2(\text{CH}_3)_6$  and

six equivalents of **(L1)** leads to complete substitution of  $CH_3$  ligands. This complex crystallizes as light yellow crystals in a hexane/pyridine (10:1 ratio) mixture at  $-20^\circ\text{C}$ ; unfortunately X-ray data collected on a suitable crystal were not good enough to have a reasonable structure.



For complex **(11)**,  $^1H$  NMR spectrum (Figure 2.27) shows the presence of pyridine with a respective ratio **(L1)**:pyridine equals to one which demonstrates that pyridine is coordinated to the aluminium center while  $^{27}Al$  NMR studies (Figure 2.28) show only one broad peak at 74 ppm, indicating only one hexacordinated aluminium center. A proposed structure would be an octahedral monomeric complex coordinated with 3 monodentate triazenide ligands rather than bidentate ones, as presented in the inset of Figure 2.28.

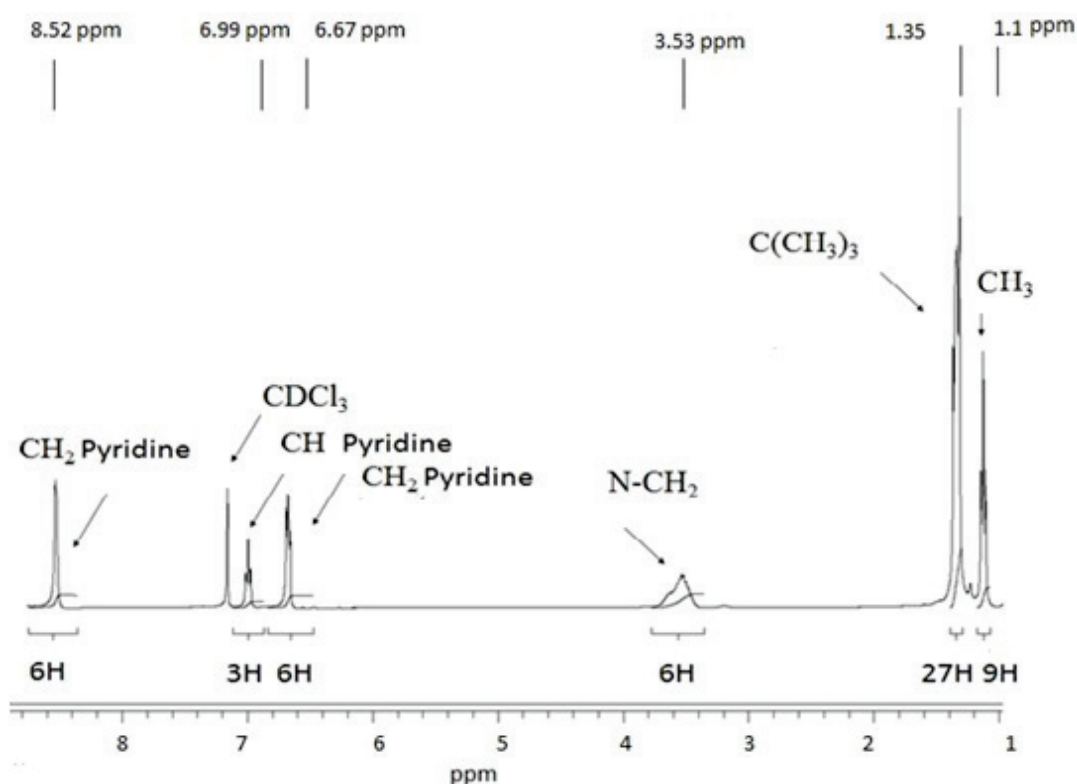


Figure 2.27 –  $^1H$  NMR spectrum of  $[Al(N_3^tBuEt)_3(py)_3]_m$  (**11**).

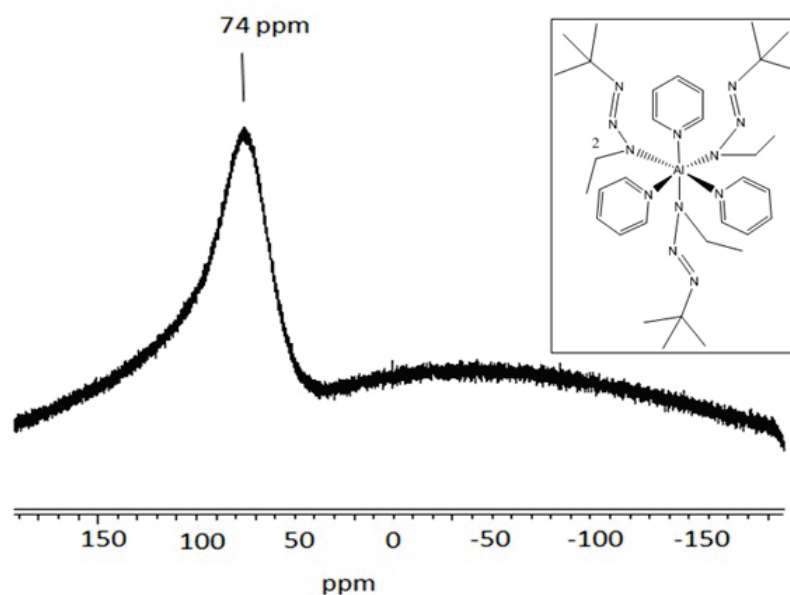
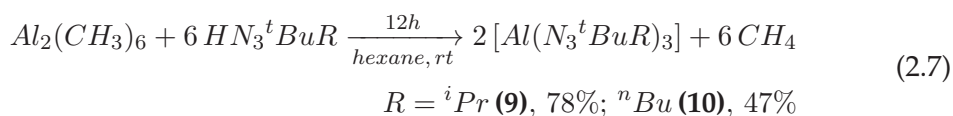


Figure 2.28 –  $^{27}\text{Al}$  NMR spectrum of  $[\text{Al}(\text{N}_3^t\text{BuEt})_3(\text{py})_3]_m$  (**11**).

In an attempt to prepare a hexacoordinated aluminium complex without the presence of a direct aluminium carbon bond, we investigated the use of aluminium *iso*-propoxide  $[\text{Al}(\text{O}^i\text{Pr})_3]_4$  as the aluminium source. Under the same conditions, treatment of freshly distilled  $[\text{Al}(\text{O}^i\text{Pr})_3]_4$  with excess of (**L1**) was carried out and the reaction mixture was refluxed in toluene for 24h. However, no reaction occurred as shown by NMR studies. This might be due to the higher stability of M-O bond of the alkoxide compound compare to the M-N one of the triazenide one and this, in spite of the favorable entropic effect of the chelating mode of the latter.



Contrary to (**L1**), reactions of  $\text{Al}_2(\text{CH}_3)_6$  with six equivalents of the more hindered *i*Pr and *n*Bu groups [(**L2**) and (**L3**)] resulted in the complete substitution of  $\text{CH}_3$  ligands and the isolation of  $[\text{Al}(\text{N}_3^t\text{Bu}^i\text{Pr})_3]_m$  (**9**) and  $[\text{Al}(\text{N}_3^t\text{Bu}^n\text{Bu})_3]_m$  (**10**) as orange crystals at  $-20^\circ\text{C}$  in 78% and 47% yield respectively that melt at around  $0^\circ\text{C}$ . Thus, increasing the size of the alkyl substituent on the ligand increases its inductive effect and its ability to fully substitute  $\text{CH}_3$  ligands.



$^1\text{H}$  NMR spectra of  $[\text{Al}(\text{N}_3^t\text{Bu}^i\text{Pr})_3]_m$  (**9**) and of  $[\text{Al}(\text{N}_3^t\text{Bu}^n\text{Bu})_3]_m$  (**10**) are shown in Figure 2.29 and Figure 2.31 respectively. The presence of a singlet at 1.14

ppm for **(9)** corresponds to hydrogens of *t*Bu group which are magnetically and chemically equivalent. In contrast, complex **(10)** shows three different singlets of hydrogens of *t*Bu at 1.11, 1.15 and 1.20 ppm. It also shows a broad multiplet at 3.39 ppm *N*–CH<sub>2</sub> (instead of a triplet). This indicates that **(10)** is present as stereoisomers in solution. Similar to **(8)**, <sup>27</sup>Al NMR spectra of complexes **(9)** and of **(10)** (Figure 2.30 and Figure 2.32 respectively) show the presence of multiple peaks (25.90 hexa coordinated, 73.26 tetra coordinated and at 97.60 ppm tetra coordinated) for **(9)**, and (27.56 hexa coordinated and at 74.89 ppm tetra coordinated) for **(10)**. Only the hexacoordinated complexes are shown in the inset figures of NMR spectra.

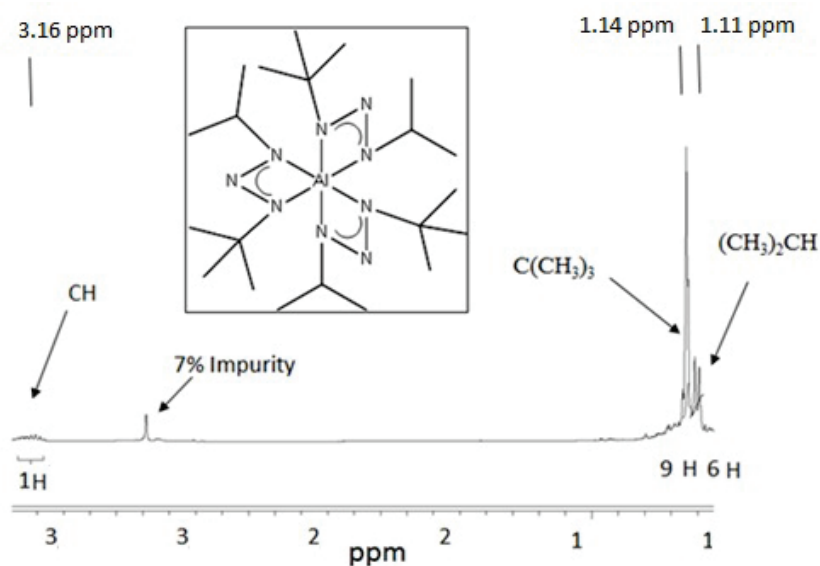


Figure 2.29 – <sup>1</sup>H NMR spectrum of [Al(N<sub>3</sub><sup>t</sup>Bu<sup>i</sup>Pr)<sub>3</sub>]<sub>m</sub> (**9**).

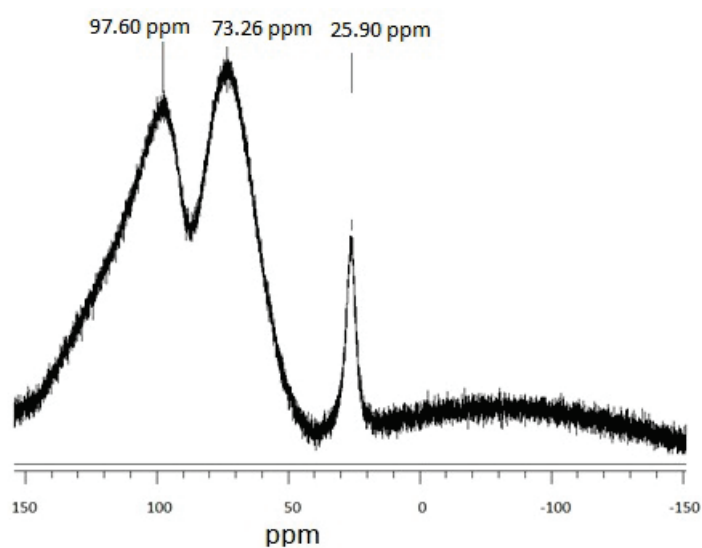


Figure 2.30 – <sup>27</sup>Al NMR spectrum of [Al(N<sub>3</sub><sup>t</sup>Bu<sup>i</sup>Pr)<sub>3</sub>]<sub>m</sub> (**9**).

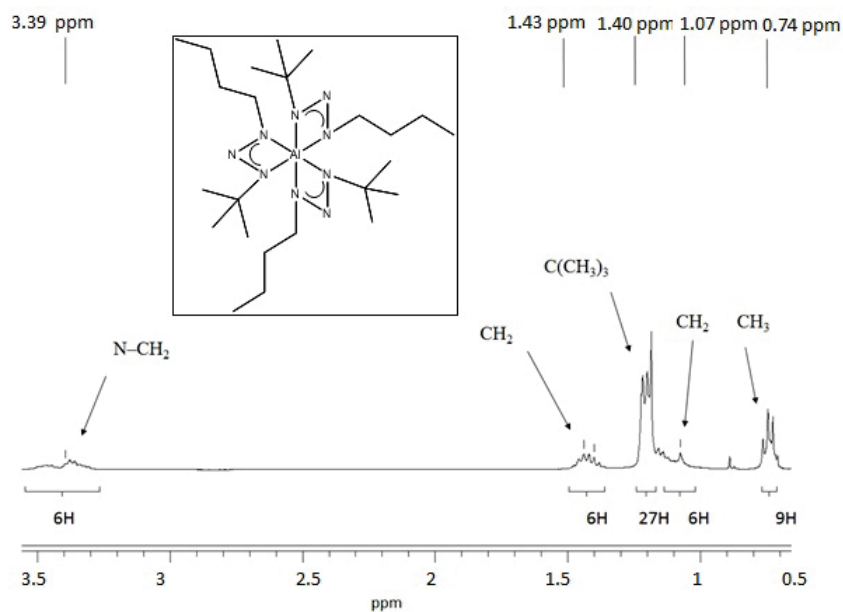


Figure 2.31 –  $^1\text{H}$  NMR spectrum of  $[\text{Al}(\text{N}_3^t\text{Bu}^n\text{Bu})_3]_m$  (10).

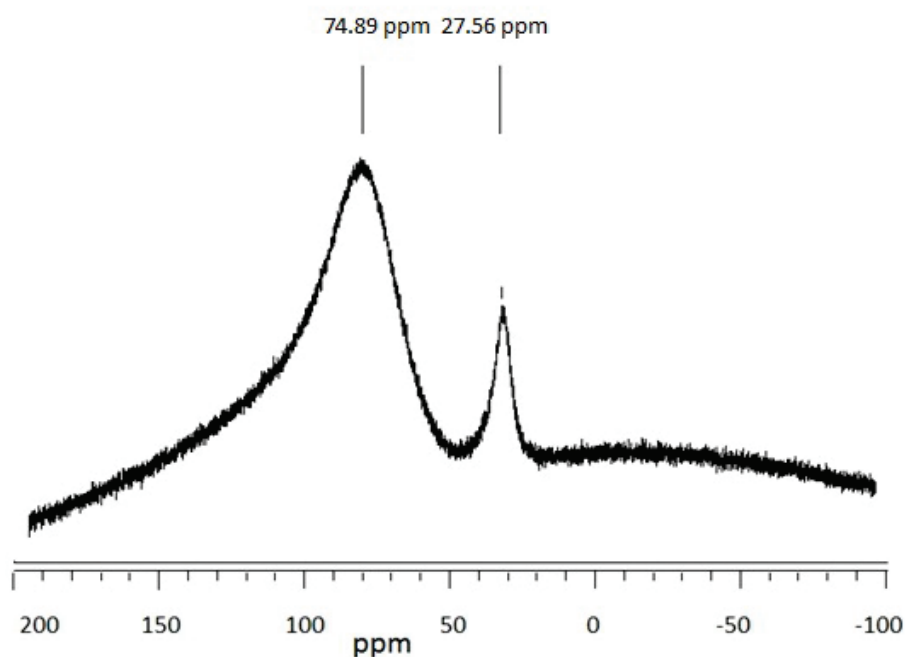


Figure 2.32 –  $^{27}\text{Al}$  NMR spectrum of  $[\text{Al}(\text{N}_3^t\text{Bu}^n\text{Bu})_3]_m$  (10).

#### 2.4.2 Starting from $\text{AlH}_3(\text{NMe}_2\text{Et})$

To a hexane solution of DMEAA was added dropwise at  $0^\circ\text{C}$ , three equivalents of  $\text{HN}_3^t\text{BuEt}$  (L1). The addition was accompanied with the evolution of gas ( $\text{H}_2$ , amine). Temperature was then increased slowly to room temperature and transparent

solution was stirred for further 12h. Solvents and volatile materials were removed under vacuum to give a white solid that was crystallized from toluene at  $-20^{\circ}\text{C}$ .  $^1\text{H}$  NMR spectrum of  $[\text{Al}(\text{N}_3^t\text{BuEt})_3]_m$  (**12**) is shown in Figure 2.33 which demonstrates the presence of one peak for  $^t\text{Bu}$  groups at  $\delta$  1.13 ppm. Broad multiplets are obtained for  $\text{NCH}_2$  and  $\text{CH}_3$ , instead of obtaining a quartet and a triplet, respectively suggesting hindered rotation of  $\text{CH}_2\text{CH}_3$  moiety and the presence of this complex as stereoisomers in solution. However,  $^{27}\text{Al}$  NMR spectrum (Figure 2.34) shows two peaks at 26.51 and at 75.51 ppm, suggesting a mixture of tetra and hexa coordinated species.

Using above approach, we also obtained aluminium complex with a symmetrically substituted triazene ligand  $[\text{Al}(\text{N}_3^t\text{Bu}_2)_3]_m$  (**13**) in order to check the impact of the asymmetry towards the volatilities of these derivatives. In solution, this complex exists as a mixture of tetra and hexa coordinated Al complexes (Figure 2.36).

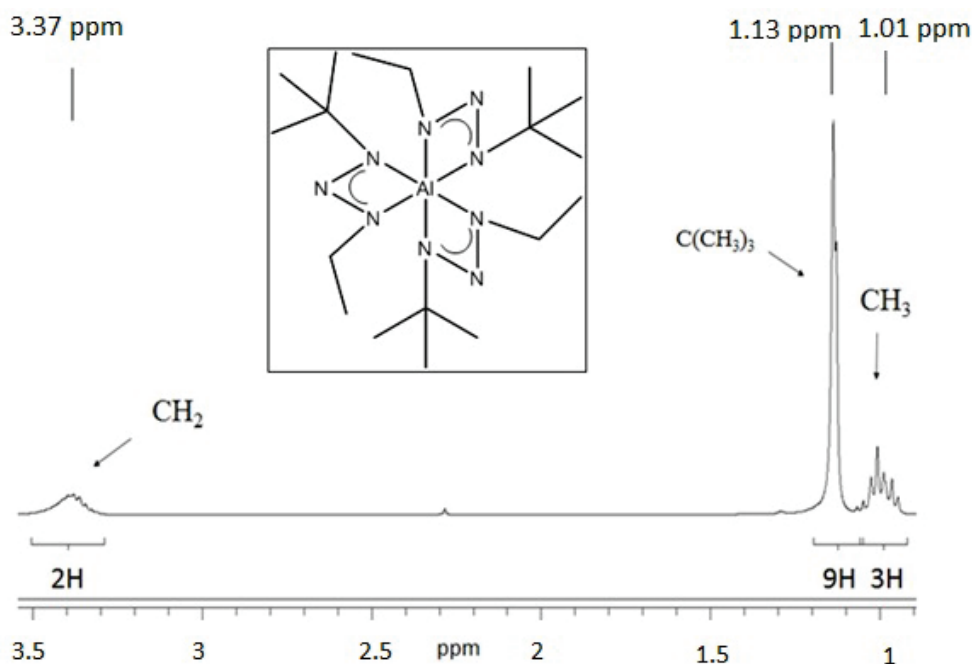
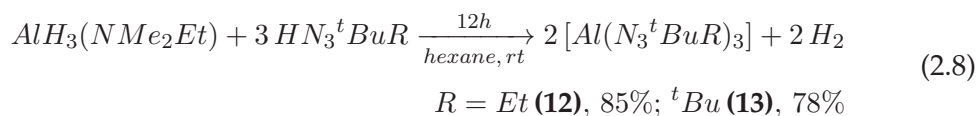


Figure 2.33 –  $^1\text{H}$  NMR spectrum of  $[\text{Al}(\text{N}_3^t\text{BuEt})_3]_m$  (**12**).

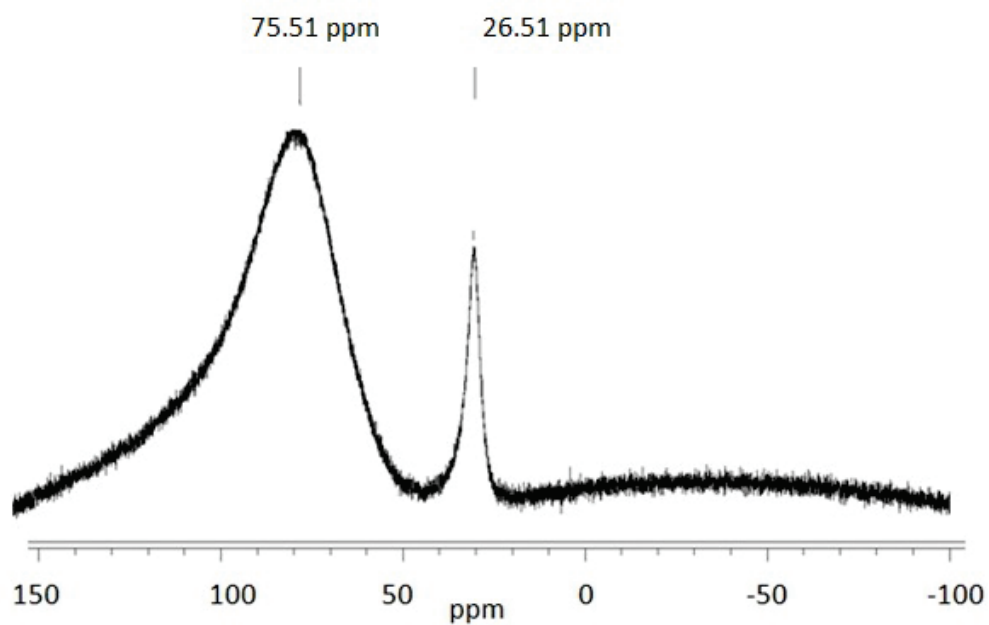


Figure 2.34 –  $^{27}\text{Al}$  NMR spectrum of  $[\text{Al}(\text{N}_3^t\text{BuEt})_3]_m$  (**12**).

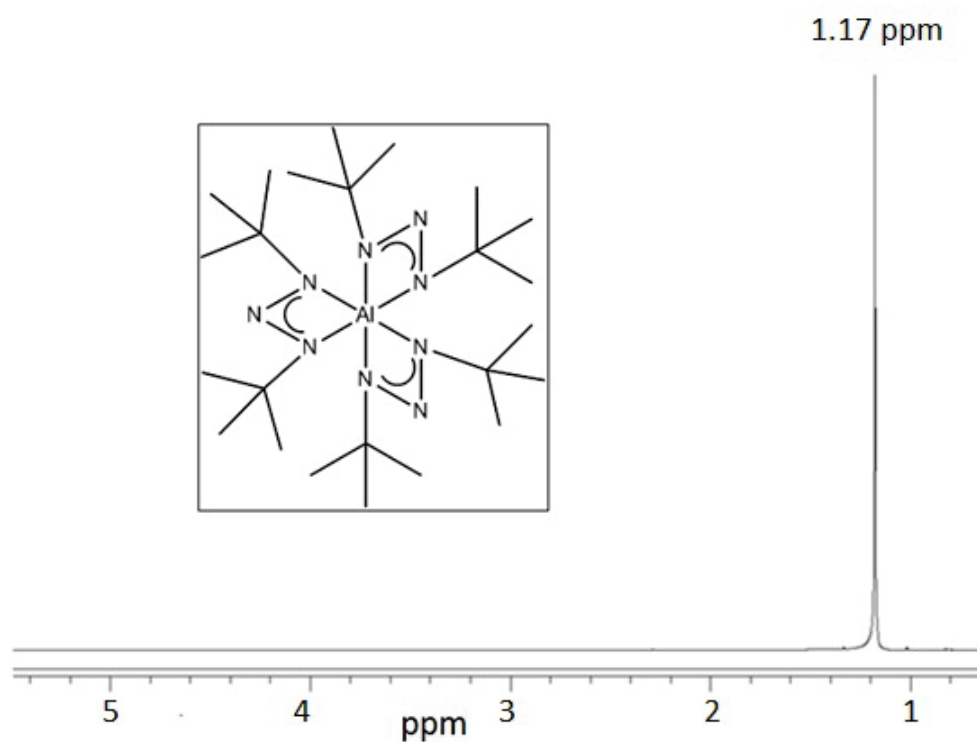


Figure 2.35 –  $^1\text{H}$  NMR spectrum of  $[\text{Al}(\text{N}_3^t\text{Bu}_2)_3]_m$  (**13**).

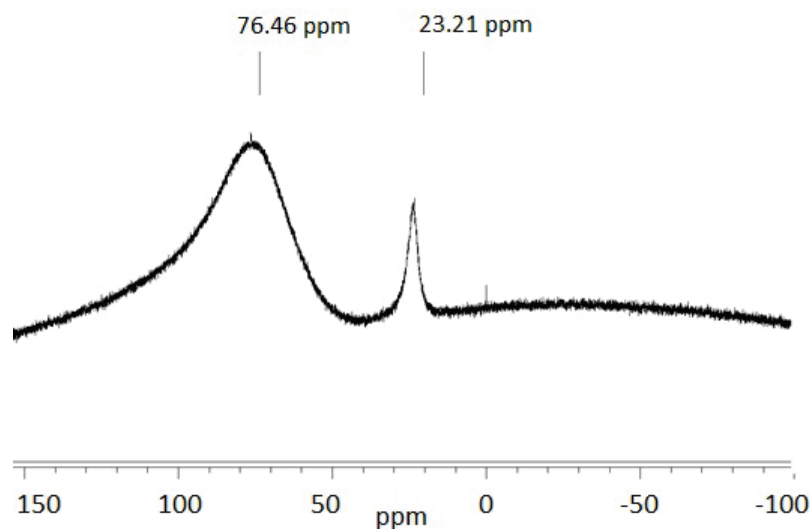


Figure 2.36 –  $^{27}\text{Al}$  NMR spectrum of  $[\text{Al}(\text{N}_3^t\text{Bu}_2)_3]_m$  (**13**).

In the view of all the above mentioned results, aluminium triazenides are not present in solution as a one complex, but rather as a mixture stereoisomers or in equilibrium in solution between different aluminium species. This could possibly be explained by the high lability of the triazenide ligands due to their weak chelating effect. The triazenide ligands act as bidentates. However, their high lability in solution leads to them acting as bidentates and monodentates and thus the presence of equilibrium in solution (Figure 2.37).

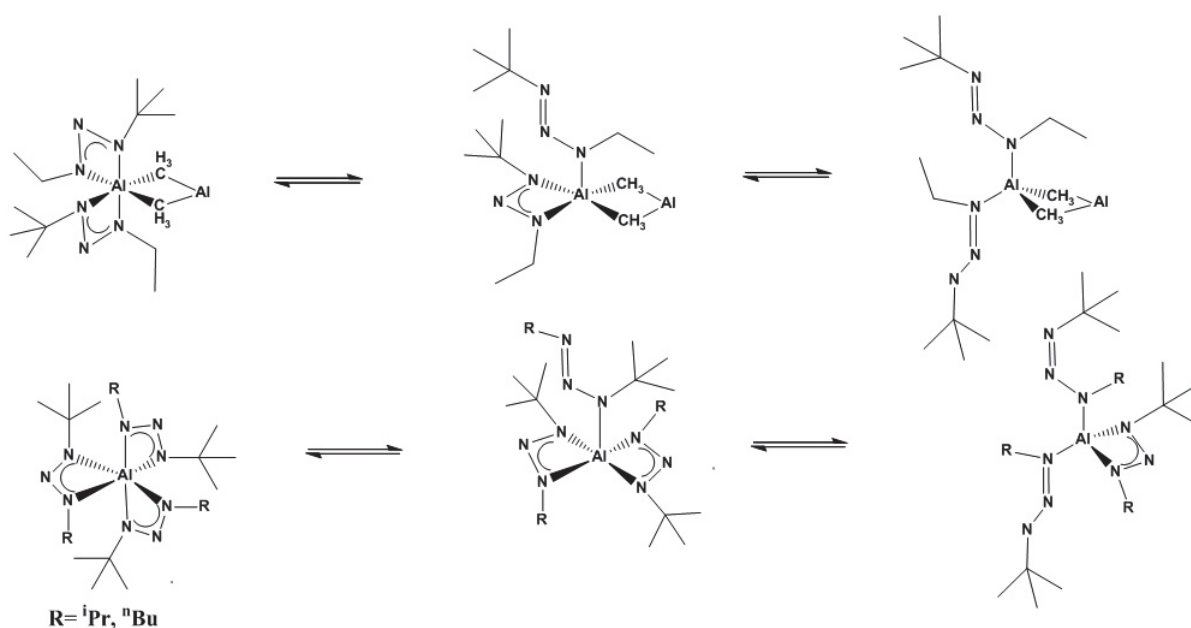


Figure 2.37 – Proposed equilibrium of aluminium triazenide complexes in solution.

### 2.4.3 Thermal behavior of aluminium triazenide compounds

Having synthesized a large range of aluminium triazenide compounds, we explored their thermal behaviors *via* TGA-TDA experiments under argon in order to determine the impact of the structure and the ligands on their volatility and their thermal stability. TGA curves of the three (L1)-based complexes  $[Al(N_3^tBuEt)_2(CH_3)]_m$  (**8**)  $[Al(N_3^tBuEt)_3(py)_3]_m$  (**11**) and  $[Al(N_3^tBuEt)_3]_m$  (**12**) showed a similar behavior with a one-step weight loss between 160 - 260°C and a residue content less than 14.5% upon reaching 450°C. This value is close to the theoretical weight for AlN (13.7%), closer than for  $Al_2O_3$  (17.1%). This means that either they have been transported in a gas phase accompanied by slight decomposition in spite of their significant structural difference or they have readily and quickly been decomposed to yield the same residue AlN. They all have similar volatility and thermal stability.

Changing to a heavier/bulkier ligand led to a different thermal behavior of  $[Al(N_3^tBu^iPr)_3]_m$  (**9**) and  $[Al(N_3^tBu^nBu)_3]_m$  (**10**). Indeed, these two complexes show a two-step weight loss, with the first weight loss corresponding to the dissociation of one triazenide ligand followed by the loss of the two remaining triazenide ligands in a second weight loss. They have a similar decomposition window between 125-180°C for the first weight loss and between 180-270°C for the second one. The residues left at 450°C are 13% for (**9**) and 16% for (**10**) with  $[Al(N_3^tBu^iPr)_3]_m$  slightly less thermally stable.

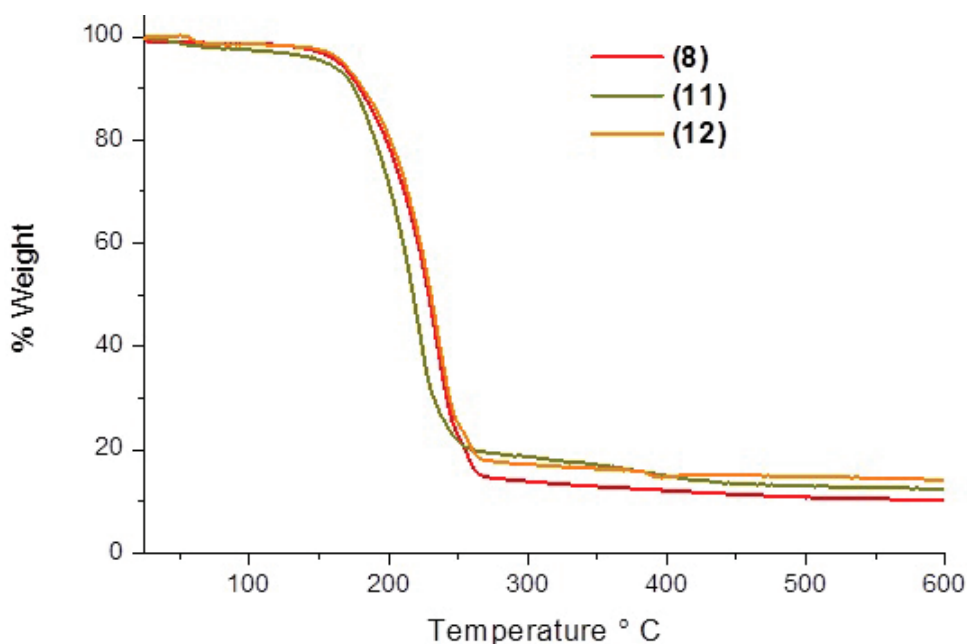


Figure 2.38 – TGA curves of  $[Al(N_3^tBuEt)_2(CH_3)]_m$  (**8**)  $[Al(N_3^tBuEt)_3(py)_3]_m$  (**11**) and  $[Al(N_3^tBuEt)_3]_m$  (**12**).

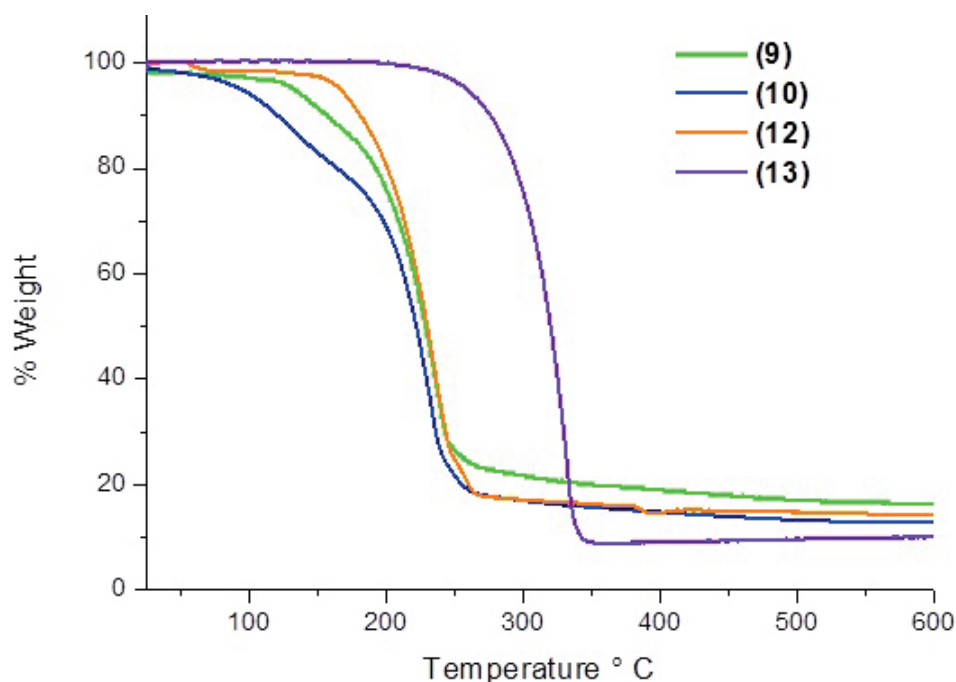


Figure 2.39 – TGA curves of  $[Al(N_3^tBu^iPr)_3]_m$  (**9**),  $[Al(N_3^tBu^nBu)_3]_m$  (**10**),  $[Al(N_3^tBuEt)_3]_m$  (**12**), and  $[Al(N_3^tBu_2)_3]_m$  (**13**).

The use of the triazene symmetrical ligand led to the compound  $[Al(N_3^tBu_2)_3]_m$  (**13**) with the highest thermal stability. TGA curve of this compound shows one weight loss between 290–350°C and the residues content upon reaching 450°C is 10% (close to the theoretical percent to get AlN of 8.27%). Nevertheless, sublimation experiments show that this complex can be sublimed at 270°C under  $10^{-4}$  mbar.

The comparison of the TGA curves of all aluminium complexes gives us the following conclusions:

1.  $[Al(N_3^tBuEt)_2(CH_3)_3]_m$  (**8**),  $[Al(N_3^tBuEt)_3(py)_3]_m$  (**11**),  $[Al(N_3^tBuEt)_3]_m$  (**12**), and  $[Al(N_3^tBu_2)_3]_m$  (**13**) can be successfully volatilized and are transported into the vapour phase *via* a single step weight loss TGA behaviour.
2. All complexes except  $[Al(N_3^tBu_2)_3]_m$  (**13**) have a similar weight loss temperature window.  $[Al(N_3^tBu_2)_3]_m$  (**13**) has the lowest volatility and is most stable thermally.
3. Thermal stability of the complexes depended on the nature of the ligands. Complexes with  $N_3^tBu^nBu$  are more stable than those with  $N_3^tBuEt$ . Complexes with  $N_3^tBu^iPr$  are the least stable. This trend is in agreement with those observed for the free ligands and the iron complexes.

## 2.5 Conclusion

Tetrakis(trimethylphosphino) dihydride Fe(II) complex has been synthesized and crystallized by sublimation as bright yellow crystals. However, the high kinetic instability of this complex as verified by the rapid color change into dark brown color when kept at  $-20^{\circ}\text{C}$  under argon atmosphere in a closed Schlenk had made all efforts of characterization unsuccessful. As a result, and under the same reaction conditions, replacing the trimethylphosphine ligand with *dmpe* seemed a better choice due to the incorporation of the bidentate ligand *dmpe* and consequently increasing the stability of the complex. The synthesis gave two different products depending on the hydride source with  $\text{LiAlH}_4$  giving the isostructural dihydride complex, however with a very low yield (8%). By using  $\text{NaBH}_4$  as the hydride source, a complex with one terminal hydride and bridging hydrogen to a  $\text{BH}_3$  moiety is obtained as characterized by single crystal XRD analysis. Thermogravimetric analysis shows that  $[\text{FeH}_2(\text{BH}_3)(\text{dmpe})_2]$  decomposes in a single step weight loss between  $175 - 295^{\circ}\text{C}$  which is compatible with the decomposition window of DMEAA. However, the organic residues upon reaching  $450^{\circ}\text{C}$  was 48 % which shows that this complex is not volatile enough for CVD applications.

Seven different novel triazinido complexes of Fe(II) have been synthesized, three of them without the incorporation of the Lewis base TMEDA. Single crystal XRD analysis shows that the complexes without TMEDA are binuclear with the triazine acting as a bridging ligand. TGA analysis show that all complexes, regardless if monomeric or dimeric are not volatilized while are transported into the vapour phase, but decompose by losing the ligands. Thermal stability of the complexes depended on the ligands and on the nature of the complexes (monomeric or dimeric). The thermal stability is in the order: monomers are more stable than dimers. Complexes with  $\text{N}_3^t\text{Bu}^n\text{Bu}$  more stable than those with  $\text{N}_3^t\text{BuEt}$ . Complexes with  $\text{N}_3^t\text{Bu}^i\text{Pr}$  are the least stable. This trend is respected to the free ligands,  $\text{HN}_3^t\text{Bu}^i\text{Pr}$  is the least stable among the ligands. Cyclic voltammetry shows that all complexes show an irreversible one electron oxidation process that corresponds to the oxidation of Fe(II) to Fe(III). The oxidation of monomers occurs at lower oxidation potential than that of dimers. Electrolysis results confirm the one electron oxidation process for the monomers. In the case of dimers, the one electron process corresponds to the oxidation of only one iron center. Mössbauer measurements show that the monomers are in +2 oxidation state and confirmed by EPR measurements. Low temperature Mössbauer experiments on  $[\text{Fe}_2(\text{N}_3^t\text{BuEt})_4]$  (**1**) show that the starting complex is in +2 oxidation state. This complex, upon storage, oxidizes into molecular iron species of oxide/hydroxide nanoparticles passing through a mono-oxidized intermediate

complex Fe(II)-Fe-(III) and confirmed by EPR measurements.

The reaction of trimethylaluminum with triazene ligands leads to full substitution of  $CH_3$  ligands  $N_3^tBu^iPr$  and  $N_3^tBu^nBu$ . However, the ligand  $N_3^tBuEt$  did not replace all the  $CH_3$  ligands. Under the same reaction conditions, the addition of few drops of anhydrous pyridine in reaction mixture was sufficient to remove all  $CH_3$  groups. DMEAA was successfully used as aluminium source to prepare triazenide complexes in mild reaction conditions. This changed its physical properties, namely pyrophoric character while maintaining volatility at moderate temperatures. All aluminium triazenides exist in solution as either stereoisomers or in equilibrium between different species with different coordination numbers. Substituents of the triazenide ligands impact strongly the electronic properties of the ligand, bigger substituents lead to complete  $CH_3$  ligand substitution.  $[Al(N_3^tBuEt)_3]$  (**12**),  $[Al(N_3^tBuEt)_2(CH_3)]$  (**8**),  $[Al(N_3^tBuEt)_3(py)_3]$  (**11**), and  $[Al(N_3^tBu)_3]$  (**13**) are volatile and are easily transported into the vapour phase. Furthermore,  $[Al(N_3^tBuEt)_2(CH_3)]$  (**8**),  $[Al(N_3^tBuEt)_3(py)_3]$  (**11**) are liquids at room temperature, which is a desired property for CVD precursor. This makes aluminium triazenide complexes promising CVD precursors for AlN films.

# 3

## Aluminium and Iron nanomaterials

### Contents

---

<b>3.1 Introduction</b> . . . . .	<b>61</b>
<b>3.2 Results and Discussion</b> . . . . .	<b>62</b>
3.2.1 Al CVD from DMEAA . . . . .	63
3.2.2 Iron CVD from iron triazenide complexes . . . . .	69
3.2.3 Iron nanomaterials from iron triazenides: solid state MOD . . . . .	72
<b>3.3 Conclusion</b> . . . . .	<b>78</b>

---

### 3.1 Introduction

In this chapter we first report aluminium MOCVD using DMEAA as precursor. We also report the preparation of iron nanomaterials via MOD (metal organic deposition) starting from the previously described iron triazenide precursors.

## 3.2 Results and Discussion

Deposition experiments of Al films were performed in a vertical, cylindrical, stagnant flow, warm wall, and stainless steel MOCVD reactor shown in Figure 3.1. Silicon flat coupons of dimensions  $20 \times 10 \times 1 \text{ mm}^3$  were used as substrates. Before deposition, their surface was etched in an HF bath (1 ml HF:10 ml  $H_2O$ ) for 1 minute, sonicated in an acetone and ethanol bath for 5 minutes, dried in Ar flow and baked in a furnace at  $60^\circ\text{C}$  for 20 minutes. They were weighed before and after deposition experiments for the determination of the mass gain over the experiment duration which corresponds to the deposition rate. In each experiment, the substrates were placed horizontally, on a 58 mm diameter susceptor (substrate holder) heated by a resistance coil gyred just below the surface. Substrates were facing the shower plate, which ensures a homogeneous gas distribution.

DMEAA was purchased from the company NanoMePS (Toulouse) and was supplied in a stainless steel bubbler equipped with a 3-valve bypass system. It was maintained at  $3^\circ\text{C}$  permanently; i.e. below the freezing point of the compound, thus strongly limiting its degradation. It was thermally regulated to  $7^\circ\text{C}$  during the experiments. At this temperature, the partial pressure of DMEAA is 0.7 Torr. Pure nitrogen (99,998%, Air Products) is fed through computer-driven mass flow controllers (MKS). Experiments were performed in fixed conditions, namely total pressure of the reactor  $P_{\text{tot}} = 10$  Torr, thermal regulation of the lines  $T_{\text{lines}} = 100^\circ\text{C}$  and of the walls of the reactor  $T_{\text{walls}} = 75^\circ\text{C}$ , while the  $N_2$  dilution gas flow ( $QN_2$ ,dilution) and the  $N_2$  carrier gas flow through the precursor ( $QN_2$ ,prec) equal 305 and 25 standard cubic centimeters per minute (sccm), respectively.

DMEAA in the input gas, equals to 2 sccm. Independent experiments were performed at eight different substrate temperatures,  $T_s$ , in the range  $140^\circ\text{C}$  -  $260^\circ\text{C}$ . The deposition time was 1 h in all experiments, including the time required for the nucleation to take place at each temperature. The nucleation delay, also known as incubation time, was assumed here as the time needed for the change of the surface color. It was evaluated by visual observation of the substrate surface through two windows mounted on the deposition chamber. In view of the observed time scale (min) such observation allows convenient and rather precise determination of the nucleation delay.

The deposition rate was evaluated directly by weight difference of the substrates before and after deposition, using a microbalance (Sartorius). Three independent weight measurements were carried out before and after each experiment and an average value was calculated. The maximum deviation from this average value was estimated by the difference between the minimum measured value before the experiment and the maximum measured value after the experiment, while the minimum deviation

was obtained by the difference between the minimum measured value after the deposition and the maximum measured weight before the deposition. In this way the average value of the weight was always within the limits of the maximum and minimum deviations. Samples morphology observations and estimation of the film thickness from cross section images of the film was performed using scanning electron microscopy (SEM) on a LEO 435 VP microscope running at 15 keV. This instrument also includes an energy dispersive spectrometer (EDS) and thus, it can be used for the determination of potential contamination contained in the film. For the quantification of the surface roughness, we used optical interferometry (Zygo NewView 100) capable of measuring surface roughness (Ra) down to 0.1 nm and peak-to-valley heights of up to several mm. Thus, the method was proper to quantify the average roughness of Al films which was limited to few  $\mu\text{m}$ .

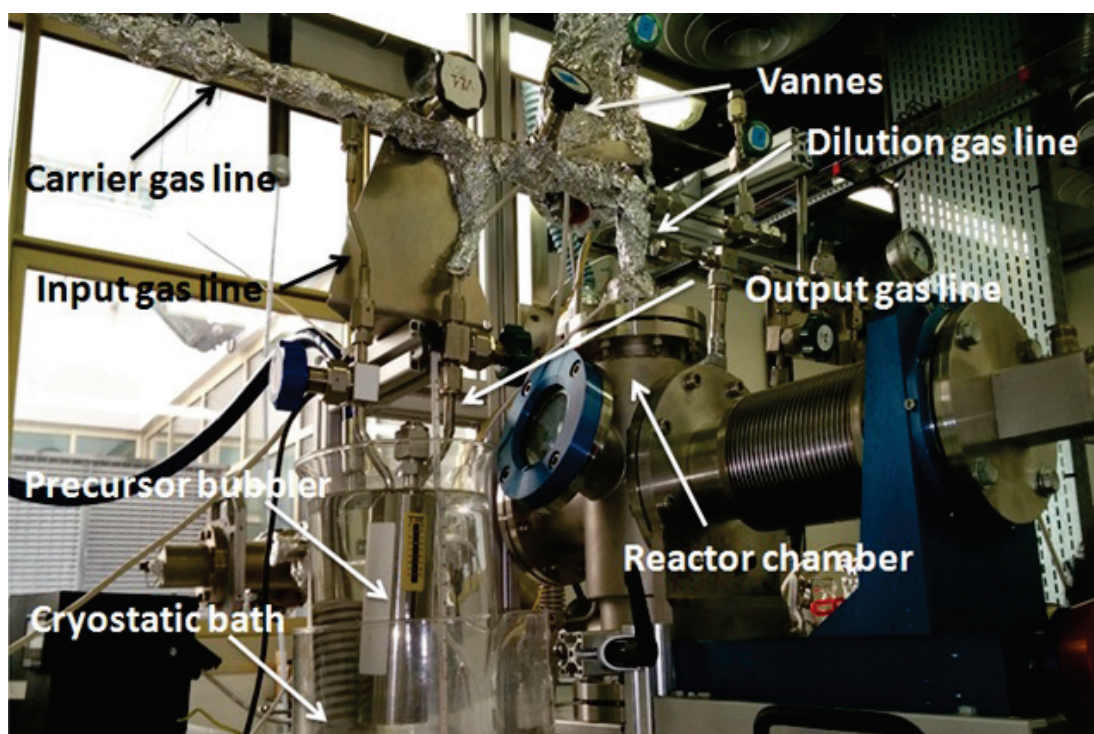


Figure 3.1 – MOCVD reactor setup.

### 3.2.1 Al CVD from DMEAA

All films obtained at temperature of the substrate ranging from 140°C to 260°C were characterized by scanning electron microscopy (SEM) and Energy-dispersive X-ray spectroscopy (EDS) was done on films obtained at 140°C and 200°C.

Figure 3.2 shows surface and cross section SEM images of Al films deposited at the low temperature of 140°C. Although there is measurable deposition rate by weight

difference, there were only scattered grains on the surface forming a rough and poorly developed film with poor uniformity. The grains were strongly faceted, which is characteristic of Al films.

As the temperature of the substrate increased to 215°C, the film growth rate increased and led to a more developed film that presents coalescence and uniformity (Figure 3.3). As the temperature increased to 260°C, the film and its grains were small but it is quite uniform (Figure 3.4). The cross section of the film at the center of the substrate shows that there is a very thin film, with tiny grains and the thickness is about 200 nm. On the right edge of the substrate, the grains of the film look like sticks, a trend which is also the same for the film at the left edge of the substrate. This clearly shows the effect of the higher temperature in the reactor: the precursor is highly consumed in the gas phase.

Table 3.1 – Experimental conditions of the deposition experiments of 1hr till 8<sup>th</sup> run and 2 hrs for the 9<sup>th</sup> run.

Deposition run	Surface Temperature (°C)	Pressure (Torr)	Dilution gas ( $N_2$ /sccm)	Carrier gas ( $N_2$ /sccm)	T gas lines (°C)
1st	180	10	305	25	100
2nd	260	10	305	25	100
3rd	160	10	305	25	100
4th	215	10	305	25	100
5th	140	10	305	25	100
6th	230	10	305	25	100
7th	200	10	305	25	100
8th	240	10	305	25	100
9th	120	10	305	25	100

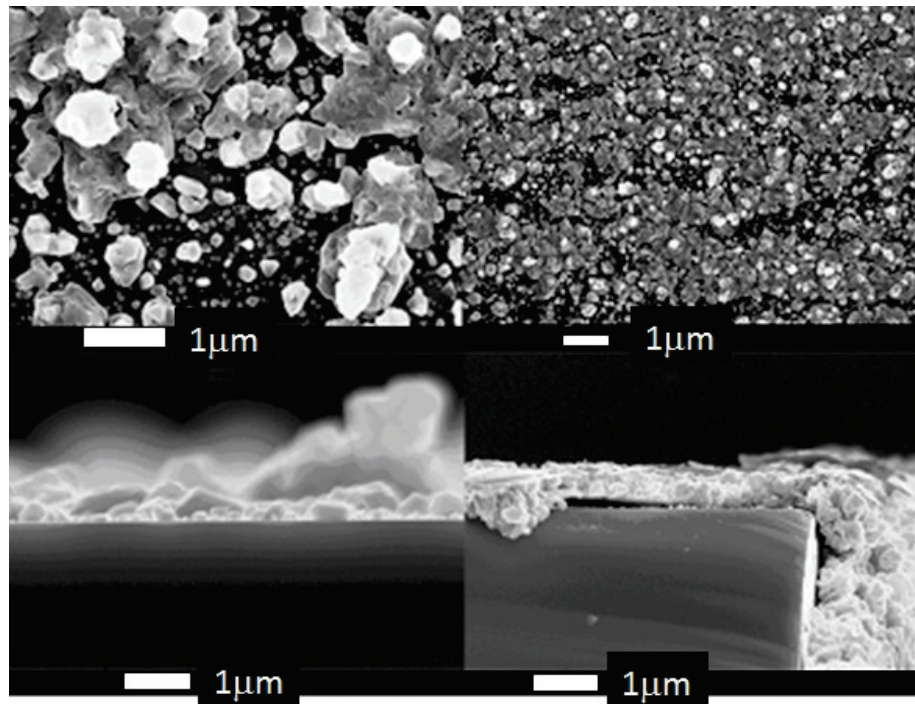


Figure 3.2 – SEM images of the films deposited at 140°C: a) and b) surface of the film at the center, c) cross section of the film in the center, d) cross section of the film on the right edge.

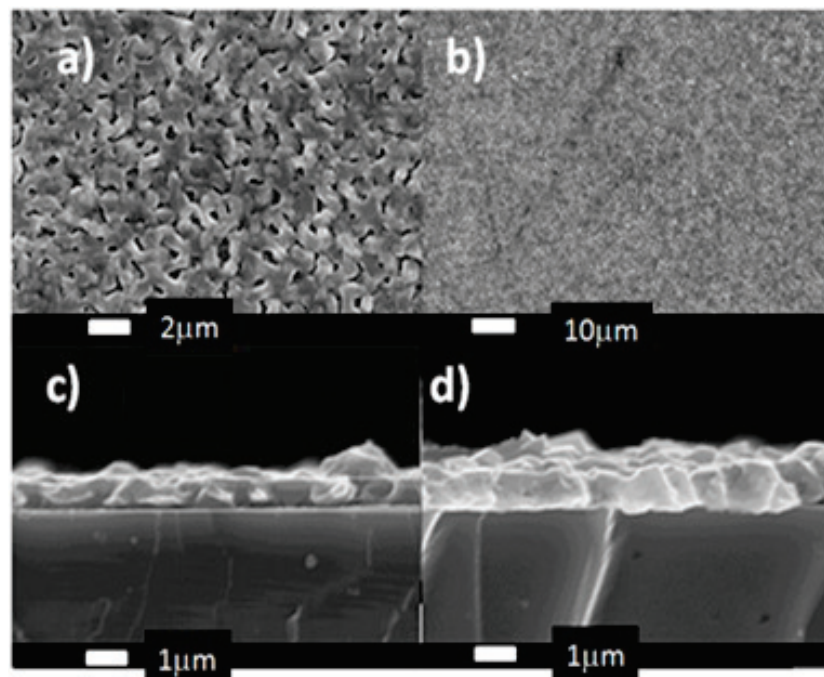


Figure 3.3 – SEM images of the films deposited at 215°C: a) and b) surface of the film at the center, c) cross section of the film in the center, d) cross section of the film on the right edge.

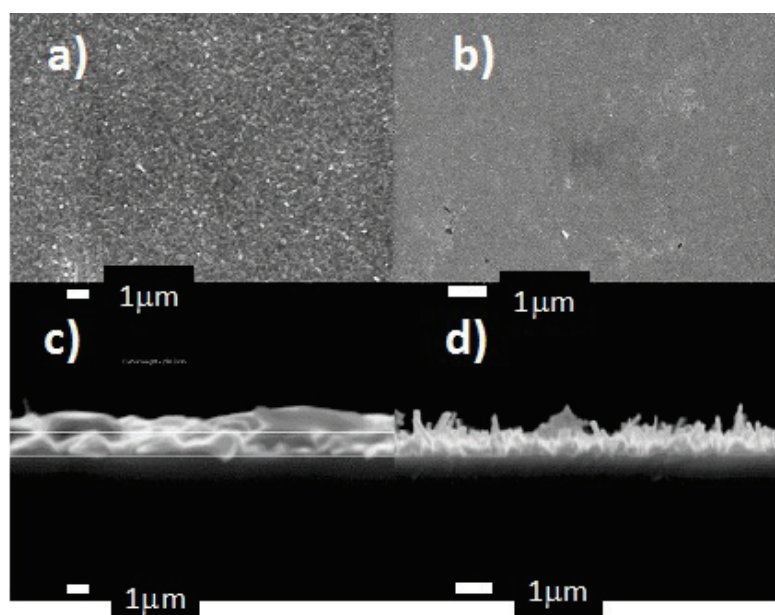


Figure 3.4 – SEM images of the films deposited at 260°C: a) and b) surface of the film at the center, c) cross section of the film in the center, d) cross section of the film on the right edge.

### Purity of the films

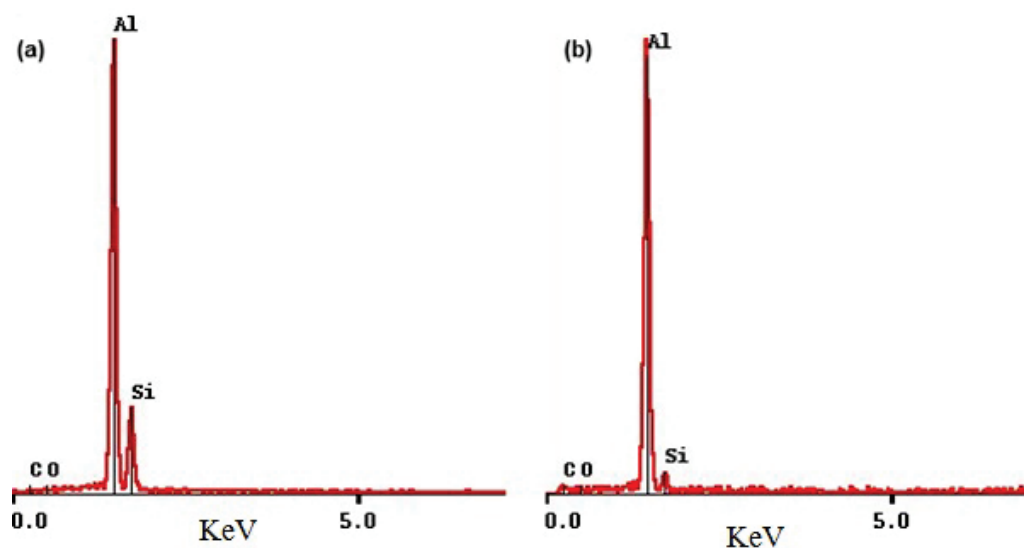


Figure 3.5 – EDS analysis of films deposited: a) 140°C; b) at 200°C.

Contamination of films (mainly O contamination due to the oxophilic nature of Al) was studied by qualitative EDS analysis at 140°C and at 200°C (Figure 3.5). The film

deposited at 140°C shows a pure aluminium film with no oxygen nor nitrogen contamination and the low deposition rate is confirmed by the detection of silicon from the uncovered Si surface. The films deposited at 200°C show also pure film without contamination. Si detection is lower compared to that at 140°C and is in agreement with the uniform and thicker film obtained at this temperature.

### Surface roughness

The films obtained at all temperatures were rough in terms of surface morphology. As opposed to the case of low temperatures in which the films obtained are in the form of only scattered grains, by increasing temperature the density of the film increases because grains coalesced. The RMS roughness of Al films deposited at the lowest temperature of 140°C is high (0.6  $\mu\text{m}$ ). RMS decreases with increasing temperature and shows a minimum value of 0.15  $\mu\text{m}$  at 200°C. Above this temperature RMS seems stable. At a surface temperature below 150°C, the Al films are not uniform and are composed of grains with a broad size distribution, resulting in high roughness. On the other hand, increasing temperatures up to 220°C results in smoother surface morphology with coalesced grains and decreasing open porosity with increasing deposition temperature. By comparing the thickness measured by mass difference and the corresponding determined from SEM cross sections, we can deduce that we have similar results. In particular, mass difference, assuming Al bulk density, gives an estimation of thickness of 907 nm and 833 nm for the films obtained at 200°C and 230°C, respectively, to be compared with 873 nm and 804 nm, respectively, determined from SEM cross sections. Finally, it can be deduced that by increasing surface temperature roughness decreases.

### Incubation time

A sharp color transition from reflecting grey to white allows the visual estimation of the incubation time (time necessary in order for the deposition to start after the DMEAA has been introduced into the reactor). A significant incubation time, 310 s, is observed at low Temperatures (140°C). It decreases almost linearly to 48 s at 240°C where it is stabilized. All the data of the characterizations are given in the Table 3.2 below.

Table 3.2 – Characterization data of aluminium films deposited.

Deposition run	Surface Temperature (°C)	Incubation time (s)	Roughness (nm)	Thickness (nm)	Growth rate (Å/min)
1st	180	120	375	-	156.0
2nd	260	-	-	-	44.7
3rd	160	130	630	-	146.9
4th	215	55	198	-	156
5th	140	310	600	-	121.5
6th	230	60	200	833	156.0
7th	200	100	180	907	164.0
8th	240	48	180	-	141.1
9th	120	-	-	-	-

According to these experiments, growth rate increased to a maximum at 200°C as shown in the Arrhenius plot (Figure 3.6) in what is believed to be the reaction limited regime.

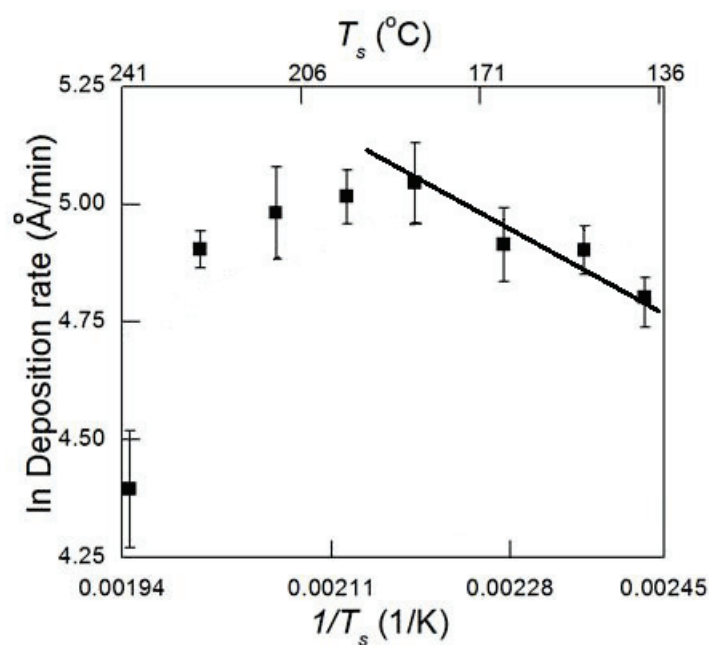


Figure 3.6 – Arrhenius plot of Al MOCVD from DMEAA.

The Arrhenius plot shows that as temperature reaches 200°C, the growth rate increases with the increase of the temperature reaching 200°C. After 200°C, the growth

rate decreases due to the higher decomposition rate of DMEAA in the gas phase leading to less precursor reaching the substrate surface. We used the growth rate to determine the activation energy ( $E_a$ ) of the surface decomposition of DMEAA in our condition of reactions. The activation energy  $E_{a,sur}$  is calculated from the slope of the deposition curve in the reaction-limited regime of the Arrhenius plot; its value comes out equal to 19.68 kJ/mol, in agreement with the value of 22.192 kJ/mol reported in the literature [66].

In conclusion, pure aluminum films have been successfully obtained using DMEAA as a precursor source in temperatures between 160 - 260°C. The films' morphology was characterized by SEM analysis and surface contamination was analyzed by EDS analysis. The deposition rate was evaluated directly by weight difference ( $\pm 10\mu\text{g}$ ) of the substrates before and after deposition, it increased to a maximum at 200°C after which it decreased significantly due to the increased decomposition of the precursor in the gas phase and not on the surface of the substrates. The films obtained were rough in terms of thickness and surface morphology. Increase of deposition temperature provided films with increased density and decreased surface roughness. The activation energy is estimated to be equal to 19.682 kJ/mol, in agreement with the value of 22.192 kJ/mol reported in the literature. The depositions featured high incubation time of 310 seconds at the lowest temperature. The incubation time decreased linearly with temperature and was lowest (48 seconds) at the highest temperature.

### 3.2.2 Iron CVD from iron triazenide complexes

$[Fe(N_3^tBuEt)_2(TMEDA)]$  (**4**) has been used as an MOCVD precursor for iron films in CIRIMAT Toulouse. However, it does not sublime up to temperature reaching 160°C, forming a brown paste that is poorly soluble in alkanes possibly indicating the loss of TMEDA ligand and the eventual polymerization.

To overcome the limitation of delivering this precursor into the CVD reactor, direct liquid injection (DLI) vaporizer technology was used. Deposition of iron films is performed in the previously described reactor. The only difference is that the reactor was equipped with DLI vaporizer. Glass and silicon dioxide are used as substrates. Their surface is sonicated in an acetone and ethanol bath for 5 minutes, dried in argon flow and baked in a furnace at 60°C for 30 minutes.  $[Fe(N_3^tBuEt)_2(TMEDA)]$  (**4**) is kept as a solution in dry heptane or octane in a concentration range of 0.07M-1.43M in a glass schlenck equipped with a 7-valve bypass system. It is maintained permanently at room temperature and covered with aluminium foil to avoid exposure to light. Experiments are performed in variable conditions, namely total pressure of the reactor, thermal regulation of the lines, of the walls of the reactor and of the vapbox,  $N_2$  and

$H_2$  gas flow rates, frequency and opening times of the injectors. The experimental conditions are summarized in table 3.3. A series of seven experiments were performed in the vapbox temperature range from 25°C to 130°C which corresponds to a temperature window before the first exothermal peak in the TGA curve of the precursor. Only experiments 1 and 4 (i.e. when the vapbox was heated to 100°C and 110°C respectively) showed film growth of a thickness of 50nm and 20nm respectively as shown by XRF analysis.

In all experiments, the injector system was blocked by a brown paste preventing the transport of the precursor into the reactor. Only experiment 4 leads to a black powder on the injector indicating the decomposition of the precursor into metallic iron inside the injector. A possible explanation for the formation of the brown paste was attributed to the loss of TMEDA during the transport of the precursor leading to the polymerization of iron.

In order to verify if polymerization of  $[Fe(N_3^tBuEt)_2(TMEDA)]$  (**4**) is responsible for blocking the injector, we tried the iron amide precursor  $[Fe\{N(SiMe_3)_2\}_2]$  with the same conditions as those used in experiment 7. Again no film growth was shown and the injector was blocked indicating no transport into the reactor. As a result, the injector was dismantled and cleaned and we started injecting heptane through the liquid injector in air in order to verify if it is still blocked. No problem was detected in the injection as solvent passed through the injector. Similarly, we injected  $[Fe\{N(SiMe_3)_2\}_2]$  solution through the injector for 5 min, where after that only the solvent passed leaving a solid residue stuck in the interior of the injector. Which shows that polymerization is not responsible for blocking the injectors.

This clearly evidences the transport problems of iron triazenide precursors and leaves the question of the deposition of iron films of both precursors unanswered. These experiments show that iron triazenide complexes are not compatible with CVD processes.

Table 3.3 – Experimental conditions for the CVD experiments of (4).

Experiment number	1	2	3	4	5	6	7
Surface temperature (°C)	200-300	200	200	200-240	270	270	200-420
Vapbox temperature (°C)	100	50	50	90	110	25	80
Walls temperature (°C)	25	25	25	75	25	25	75
Lines temperature (°C)	25	55	55	100	130	25	85
Pressure (Torr)	10	10	10-20	10	10	10-40	10
H <sub>2</sub> flow rate (sccm)	0	0	15-50	25	35	50	50
N <sub>2</sub> flow rate (sccm)	305	305	305	305	305	605	1000
F mixing injector (Hz)	3	3	3	4	5	4	4
F liquid injector (Hz)	1	1.5	1.5	2	2.5	2	2
liquid injector opening time (ms)	8	10	10	10	10	10	10
Solution conc. (M)	0.143	0.07	0.07	0.07	0.093	0.075	0.075
Precursor consumption (mmol)	1.43	0.84	0.77	2.11	0.93	0.9	0.75
Precursor consumption (ml)	10	12	11	30	10	12	10
Precursor consumption (g)	0.612	0.36	0.33	0.899	0.398	0.385	0.321

### 3.2.3 Iron nanomaterials from iron triazenides: solid state MOD

As iron triazenides were not suitable as MOCVD precursors, we carried out solid state decomposition experiments to prepare Fe(0) nanomaterials. Representative complexes  $[Fe_2(N_3^tBuEt)_4]$  (**1**) and  $[Fe(N_3^tBuEt)_2(TMEDA)]$  (**4**) are chosen for these experiments. These complexes are deposited on silica grains and were decomposed by heating them at 200°C for 1h under hydrogen atmosphere at a heating rate of 3°C/min, then letting to cool down at room temperature.

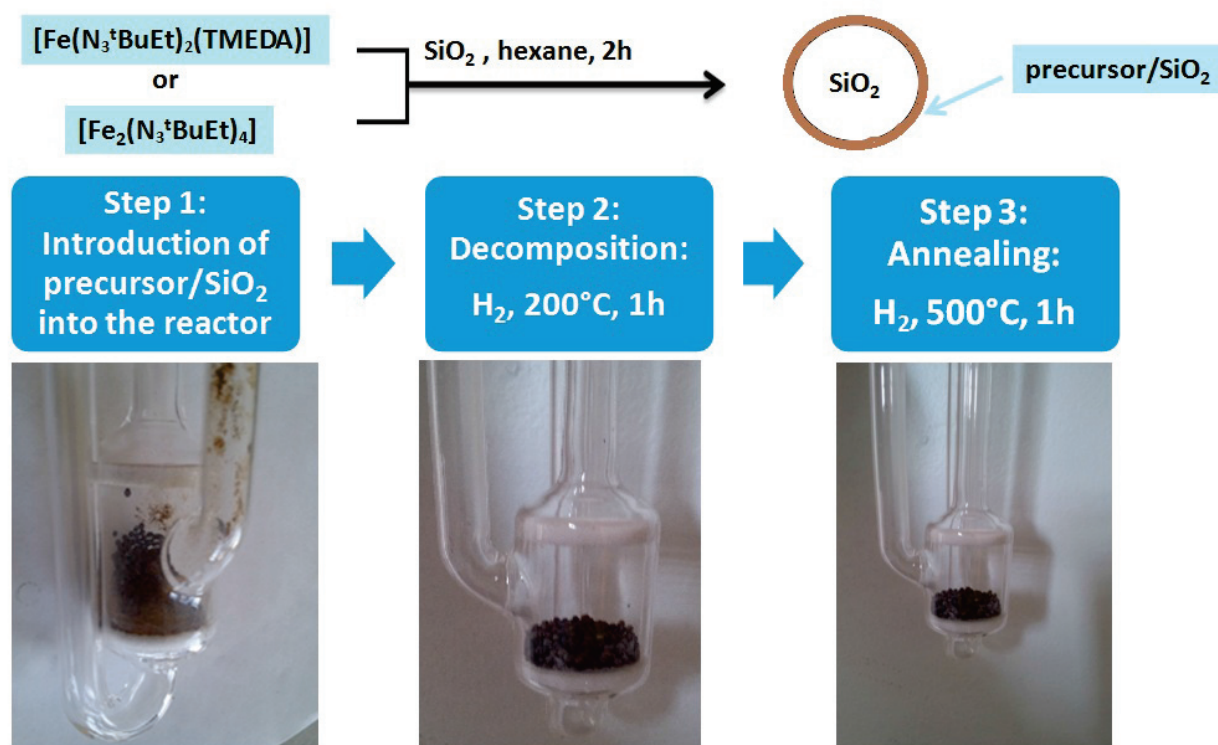


Figure 3.7 – Setup of thermolysis of  $[Fe_2(N_3^tBuEt)_4]$  (**1**) and  $[Fe(N_3^tBuEt)_2(TMEDA)]$  (**4**).

The obtained solid was then analysed by powder x-ray diffraction which showed it to be amorphous (Figure 3.8). The as-prepared solids were then treated thermally by increasing the temperature to 500°C at a heating rate of 3°C/min for 1 hour under hydrogen atmosphere to crystallize the solid. However, these calcined samples were still amorphous.

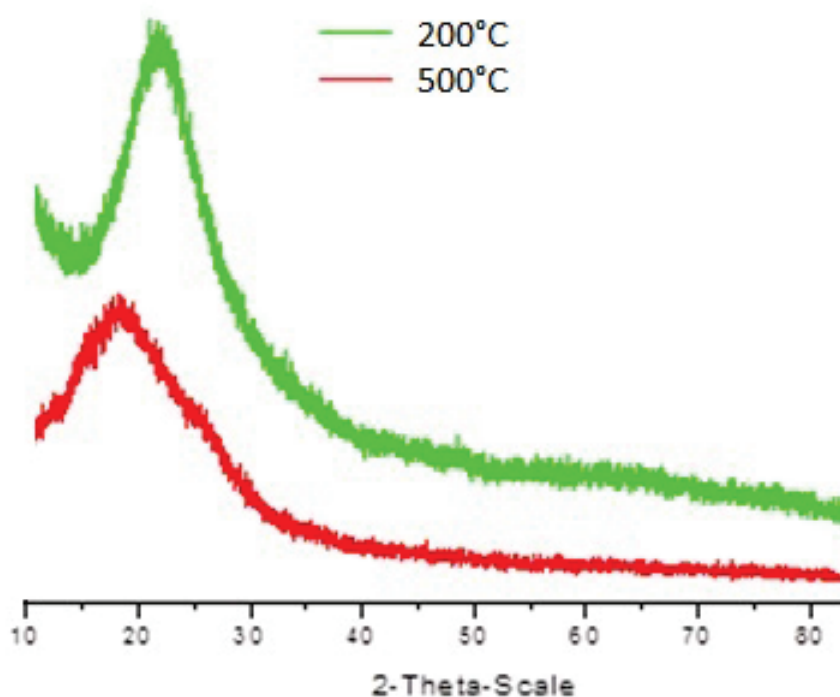


Figure 3.8 – Powder x-ray diffraction pattern for  $[Fe_2(N_3^tBuEt)_4]$  (**1**) under hydrogen treatment at 200°C and 500°C.

### X-ray photoelectron spectroscopy (XPS)

The surface characteristics of the decomposed complexes  $[Fe_2(N_3^tBuEt)_4]$  (**1**) and  $[Fe(N_3^tBuEt)_2(TMEDA)]$  (**4**) on silica were studied by XPS. Samples for XPS analysis were transported to the sample holder inside the glovebox to minimize exposure to humidity and oxygen. The Fe 2p core-level spectra of the solid obtained from the decomposition of  $[Fe_2(N_3^tBuEt)_4]$  (**1**) reveal only one weak Fe 2p<sup>3/2</sup> peak with 3% abundance which is attributed to Fe(0) at of 706.5 eV with fine differences to elemental iron (small shift, decreased half-width, reduced asymmetry) (Figure 3.9). These spectra reveal the presence of additional  $Fe_2O_3$  nanoparticles (Fe 2p<sup>3/2</sup> peak at 710.8 eV) indicating the oxidation of the iron nanoparticles on the surface. The fitting of the xps spectra of the decomposed complex (**1**) are shown in Figure 3.10. The composition of the sample obtained from the decomposition of (**1**) are summarized in Table 3.4.

XPS spectra of the solid obtained from the decomposition  $[Fe(N_3^tBuEt)_2(TMEDA)]$  (**4**) show only presence of FeO nanoparticles.

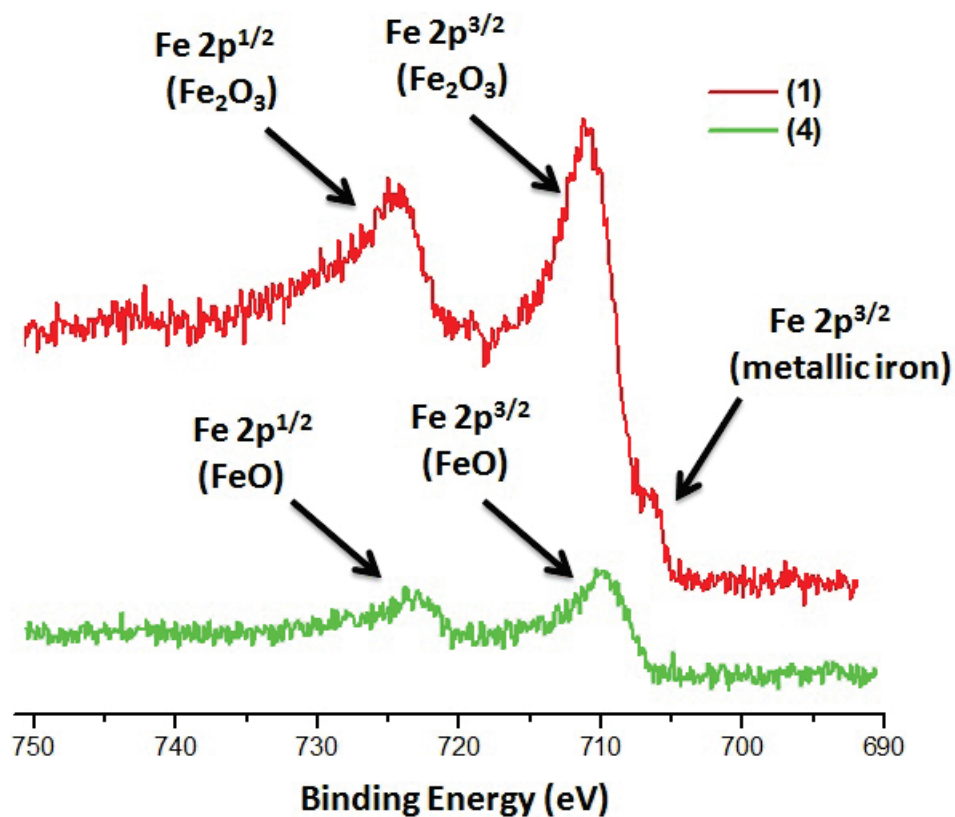


Figure 3.9 – Fe 2p XPS spectra of the decomposed complexes  $[Fe_2(N_3^tBuEt)_4]$  (1) and  $[Fe(N_3^tBuEt)_2(TMEDA)]$  (4) on silica.

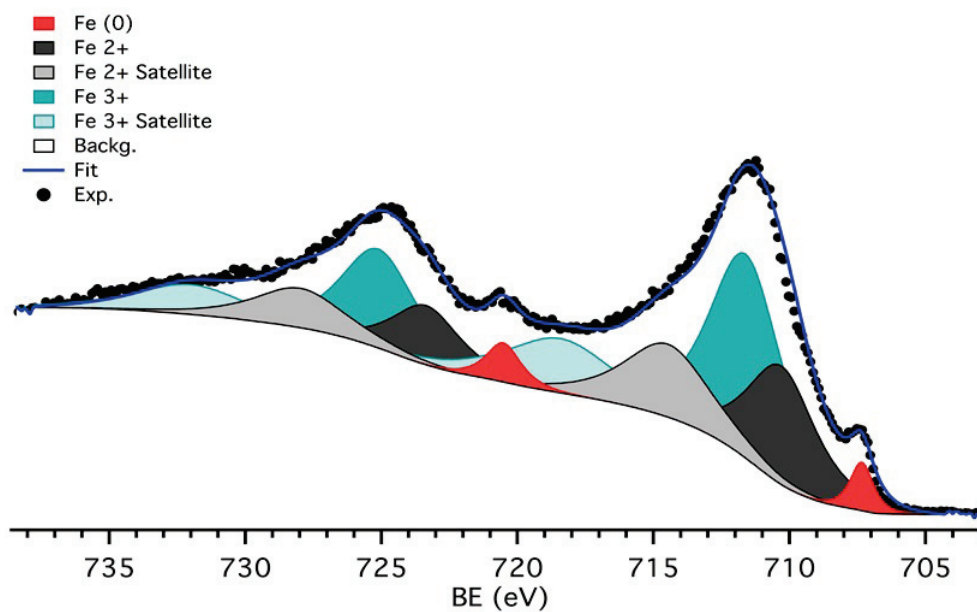


Figure 3.10 – Fitting of Fe 2p XPS spectra of the decomposed complex  $[Fe_2(N_3^tBuEt)_4]$  (1) on silica.

Table 3.4 – % atomic concentration and position in eV of species present after the decomposition of (1) on silica.

Species	Position (eV)	% atomic concentration
Fe(0)	707.3	3
Fe(II)	710.3	40
Fe(III)	711.6	57

To overcome the oxidation of the iron deposited on silica during the XPS sample preparation,  $[Fe_2(N_3^tBuEt)_4]$  (1) was decomposed *in situ* under  $H_2$  atmosphere by heating at 200°C for 1h with a heating rate of 2°C/min then the temperature was let to increase until 500°C and kept at this temperature for an additional hours. XPS data was recorded at 200°C and 500°C respectively. Fe 2p core-level spectra of (1) in Figure 3.11 reveal only presence of  $Fe_2O_3$  nanoparticles that indicates the oxidation of the iron nanoparticles on the surface. However, the spectra obtained at 500°C reveal one large signal corresponding to Fe(0) and a small peak that corresponds to FeO. In summary, the compound (1) decomposes into Fe (0) nanoparticles only when treated under  $H_2$  atmosphere at 500°C while treating it under  $H_2$  at 200°C resulted in  $Fe_2O_3$ .

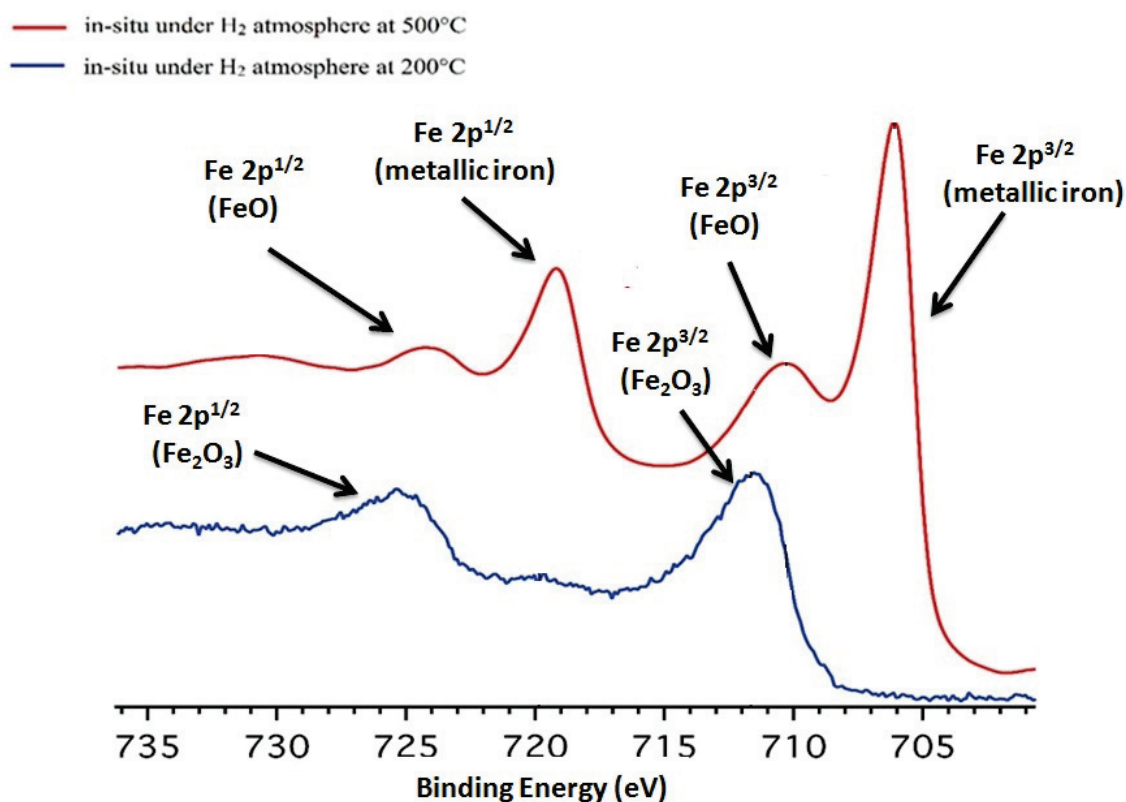


Figure 3.11 – *In situ* Fe 2p XPS spectra of the decomposed complex  $[Fe_2(N_3^tBuEt)_4]$  (1) at 200°C and 500°C.

### Iron nanomaterials from iron triazenides: MOD in Solution

It has been shown that the use of the cheap and mild reducing agent *diiso*-propylamine-borane reduces iron(II) complex  $[Fe\{N(SiMe_3)_2\}_2]$  to produce Fe(0) nanoparticles [67]. Guided by this study, we investigated the use of the iron triazenides as possible precursors for the preparation of Fe(0) nanoparticles *via* the use of the amine borane derivative. For comparison,  $[Fe\{N(SiMe_3)_2\}_2]$  (1.04 mg, 2.76 mmol) was dissolved in 45 ml of toluene. The homogeneous green solution was frozen under liquid nitrogen and 0.7 g (6.01mmol) of  $^iPr_2NH.BH_3$  in 5 ml toluene was added. The mixture was allowed to warm to room temperature to afford a dark solution. The mixture was further stirred overnight, and then toluene was evaporated to afford a black sticky solid. Further drying of the solid leads to dry black powder. Using similar method,  $[Fe(N_3^tBuEt)_2(TMEDA)]$  (**4**) (1.47g, 3.4mmol) was reacted with  $^iPr_2NH.BH_3$  (0.87 g, 7.57 mmol) to afford a sticky black solid. The Mössbauer study indicated complex nature of this material showing several iron species i.e., Fe(0) nanosized core containing Fe(0)/Fe<sup>2+</sup>/Fe<sup>3+</sup> or large Fe(0) particles on the surface. The different species, their isomer shifts and quadrupole splitting values as well as relative intensities are summarized in the Table 3.5. The overall percentage of iron in zero oxidation state is 71% which is an encouraging result.

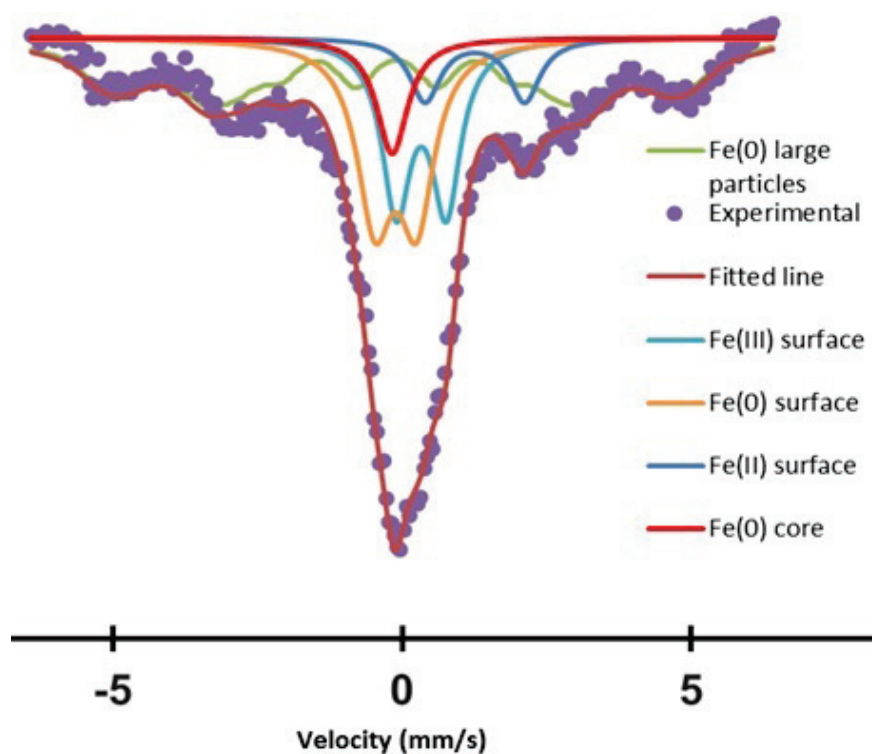


Figure 3.12 – Mössbauer spectrum of iron (0) nanoparticles prepared in solution decomposition of  $[Fe(N_3^tBuEt)_2(TMEDA)]$  (**4**).

Table 3.5 – Species present, isomer shifts, quadrupole splitting and relative intensities of iron (0) nanoparticles prepared in solution decomposition of  $[Fe(N_3^tBuEt)_2(TMEDA)]$  (**4**).

$\delta(mm/s)$	$\Delta(mm/s)$	Rel. Int. (%)	Species
-0.08	0.00	8	Fe(0)core
-0.02	0.72	26	Fe(0) surface
0.00	0.00	37	Fe(0) large particles
0.42	0.86	21	$Fe^{3+}$ surface
1.25	1.71	8	$Fe^{3+}$ surface

## TEM

Sample for TEM experiments have been prepared in C-4 ionic liquid in order to disperse and to protect the iron nanoparticles. A 2 mg sample was dissolved in 1ml of ionic liquid and was deposited on an ultrathin copper grid. Excess of ionic liquid was wiped with a filter paper. The grid was placed in a shutter to protect the iron nanoparticles from air. As shown in Figure 3.13, the nanoparticles present in the sample are well dispersed and show a coherent average size of 7 nm.

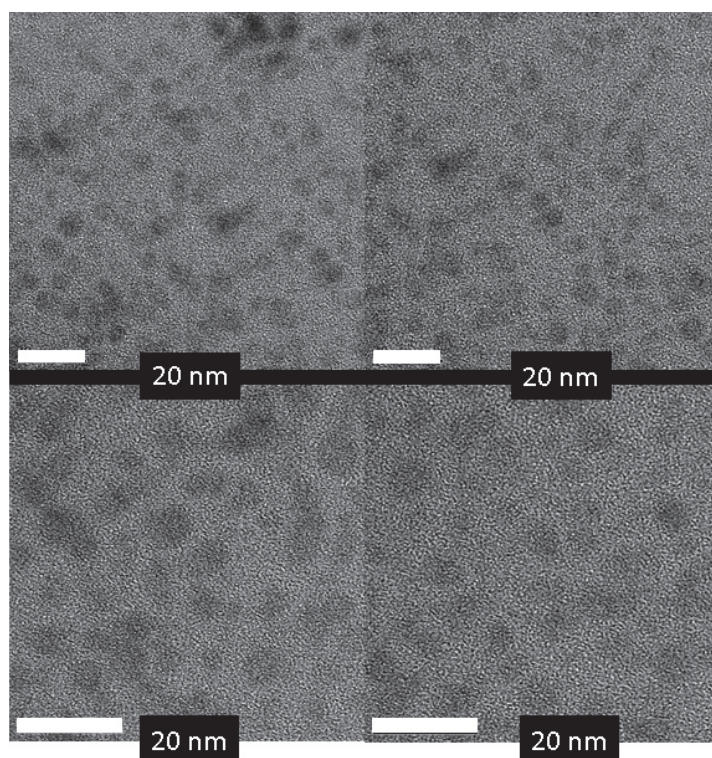


Figure 3.13 – TEM images of iron (0) nanoparticles prepared in solution decomposition of  $[Fe(N_3^tBuEt)_2(TMEDA)]$  (**4**).

## EDX

EDX analysis was done on samples of nanoparticles in a suspension of ionic liquid. The analysis shows the presence of oxygen (probably due to the fact that the sample transfer was in ambient air), Cu and C impurities come from the grid, N and S are due to the presence of the ionic liquid as it is not evaporated inside the TEM equipment. The sample shows a large amount of boron which comes from the use of  $iPr_2NH.BH_3$ .

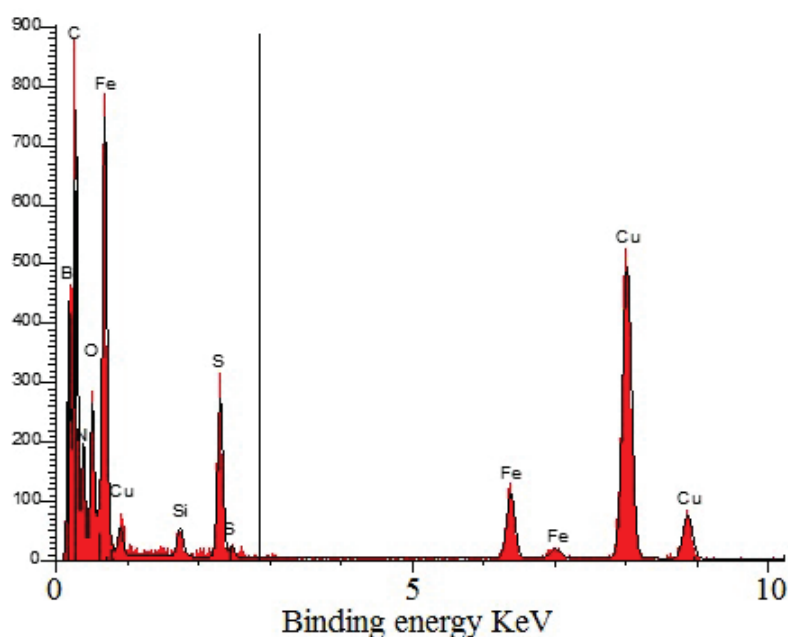


Figure 3.14 – EDX analysis on iron nanoparticles prepared from solution reduction in toluene.

## 3.3 Conclusion

DMEAA was successfully used for low temperature MOCVD of pure Aluminium films. Growth rate increased with temperature and decreased sharply after 240°C. All films had rough morphology that decreased with increasing the temperature. Iron triazenides are not suitable for DLI-MOCVD as they were unsuccessfully introduced into the reactor chamber.

*In situ* MOD in solid state of complexes  $[Fe_2(N_3^tBuEt)_4]$  (**1**) and  $[Fe(N_3^tBuEt)_2(TMEDA)]$  (**4**) under hydrogen atmosphere at 200°C leads mainly to iron oxide nanoparticles while that at and 500°C leads mainly to iron(0) nanoparticles with traces of iron oxides. However, the use of the cheap and mild reducing agent *diiso*-propylamine-borane in toluene at room temperature for 12h followed by reflux

for additional 8 hours leads to Fe(0) nanoparticles that are oxidized at the surface with the presence of some large Fe(0) particles in addition to Fe(II) and Fe(III) species on the surface.



# 4

## *Preparation and catalytic tests of $Al_{13}Fe_4$*

### Contents

---

4.1	Introduction . . . . .	81
4.2	Results and Discussion . . . . .	82
4.2.1	$Al_{13}Fe_4$ films <i>via</i> MOCVD . . . . .	82
4.2.2	$Al_{13}Fe_4$ nanoparticles <i>via</i> MOD . . . . .	85
4.3	Catalytic activity of $Al_{13}Fe_4$ nanoparticles and thin films for the semi hydrogenation of acetylene . . . . .	88
4.4	Conclusion . . . . .	90

---

### 4.1 Introduction

The intermetallic  $Al_{13}Fe_4$ , which represents the “site-isolation” concept of catalyst, is an active and selective catalyst for the hydrogenation of acetylene and butadiene.

However, it has been produced in the form of unsupported powder by the Czochralski method which limits its use in catalytic engineering. In this chapter we report the synthesis of  $Al_{13}Fe_4$  supported thin films on Si substrates and nanoparticles *via* sequential MOCVD and MOD in solution, respectively. These  $Al_{13}Fe_4$  nanoparticles and films were tested for the semi hydrogenation of acetylene.

## 4.2 Results and Discussion

### 4.2.1 $Al_{13}Fe_4$ films *via* MOCVD

In view of limited volatility and not so encouraging MOCVD results of the new iron(II) triazenides derivatives 1-7 (*vide supra* chapter 2), we used commercially available precursors DMEAA and  $Fe(CO)_5$  as the source of aluminium and iron, respectively, for the sequential MOCVD of the  $Al_{13}Fe_4$  films. This involved deposition of aluminium thin films followed by the iron films. The *in situ* annealing at 575°C of the formed films resulted in the formation of the desired  $Al_{13}Fe_4$  phase. No evidence of carbon contamination was found and only surface oxidation was observed. All deposition experiments have been conducted at Centre inter-universitaire de Recherche et d'Ingénierie des Matériaux (CIRIMAT), Toulouse. Deposition of Al films was performed in the reactor described earlier. Silica flat coupons were used as substrates and their surface was cleaned as mentioned earlier. They were weighed before and after deposition experiments for the determination of the mass gain over the experiment duration which corresponds to the deposition rate. DMEAA was supplied in a glass bubbler equipped with a stainless steel 3-valve bypass system.  $Fe(CO)_5$  was purchased from Acros chemicals and was stored at 4°C. A glass bubbler equipped with a stainless steel 3-valve bypass system was filled with 4 ml of  $Fe(CO)_5$  before each experiment and kept at -18°C during deposition. Pure nitrogen (99,998%, Air Products) was fed through computer-driven mass flow controllers (MKS). The deposition time was 1 h40 min for aluminium and 5 min for iron. Then the intermetallic compound was formed by the *in situ* thermal treatment at 575°C.

#### Film characterization

The phase composition of the samples was determined by X-ray powder diffraction in the  $2\theta$  range from  $10^\circ$  to  $90^\circ$ , which showed well-crystallized thin films with all the peaks indexing well with the calculated pattern  $Al_{13}Fe_4$  phase found in [9] and [68]. This confirms a large diffusion of Fe and Al to form the right phase. However, other minor peaks at  $2\theta$   $40^\circ$ ,  $50^\circ$  correspond to the  $Al_5Fe_2$  phase and the peak at  $39^\circ$

corresponds to pure aluminium. The  $Al_{13}Fe_4$  films prepared are not pure and the films are composed also of secondary phases.

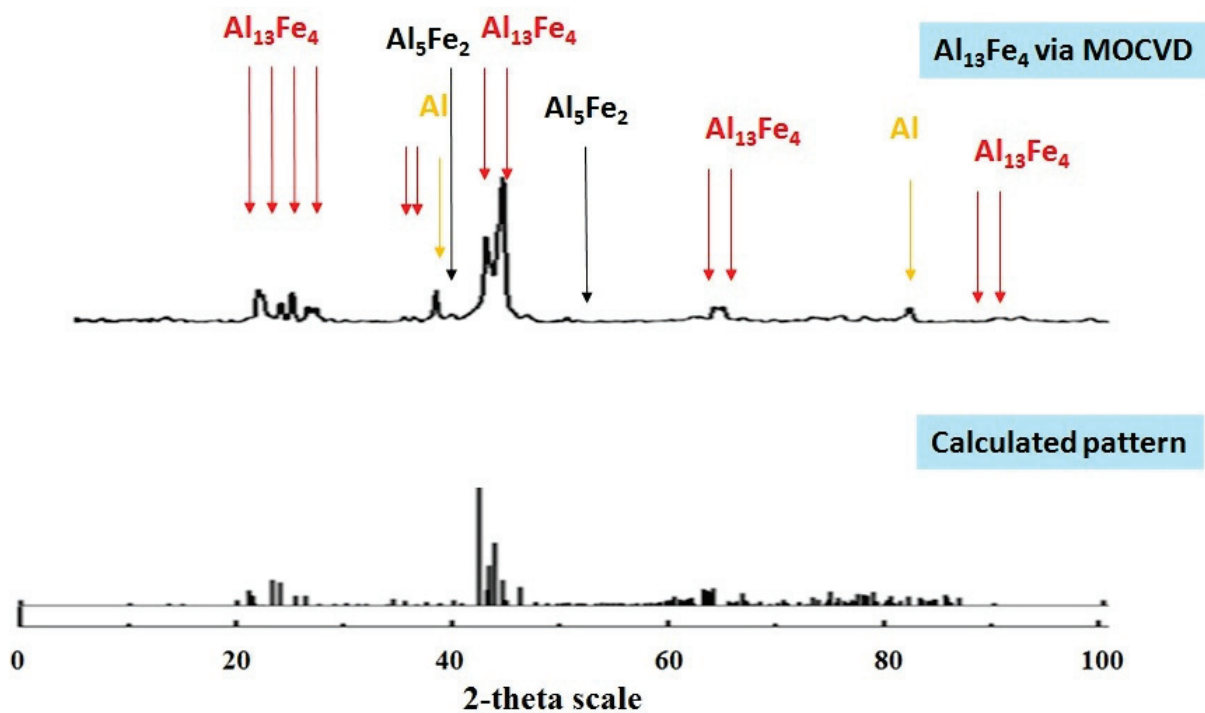


Figure 4.1 – XRD pattern of  $Al_{13}Fe_4$  film (top) with the calculated pattern (bottom).

The surface of the films was also characterized by XPS studies. Fe 2p core-level spectra of the films shown in Figure 4.2 revealed only one signal attributed to Fe(0) at 707 eV which showed a small shift and decreased half-width as compared to elemental iron which is characteristic of intermetallic compounds and can be thus attributed to  $Al_{13}Fe_4$ . The Al 2p peaks in XPS spectrum was split in a doublet at 72 eV and 75 eV and were attributed to Al and  $Al_2O_3$ , respectively. Thin alumina layer was present mostly on the surface of films and pores due to the exposure of films to ambient atmosphere.

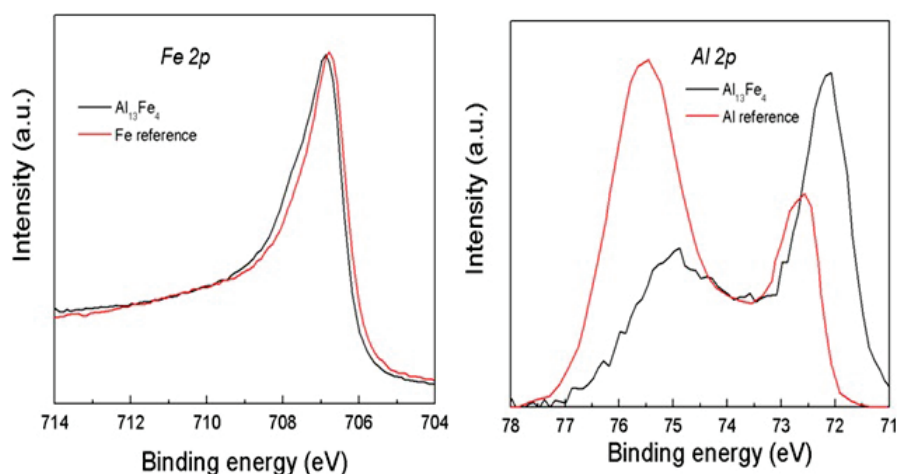


Figure 4.2 – XPS spectra of films prepared from sequential deposition.

The FIB-SEM images showed a fully developed film with very high roughness and high porosity as confirmed by cross-section images of the film. The films deposited had high thickness of  $27\ \mu\text{m}$ . An *in situ* quantitative EDX analysis on the cross section of the films showed mainly the presence of Al and Fe as represented by the intensity of the colors. It also showed the presence of oxygen and carbon impurities. Oxygen impurities was mainly in the form of alumina  $\text{Al}_2\text{O}_3$ . The atomic percentage of each element varied slightly depending on the position on the cross section. Aluminium was the most abundant element with abundance between 70.62%-75.49%. Iron was the second most abundant element which was present between 19.95% -23.12%. Oxygen was present between 4.44%-5.7%. Other elements are present in trace amounts.

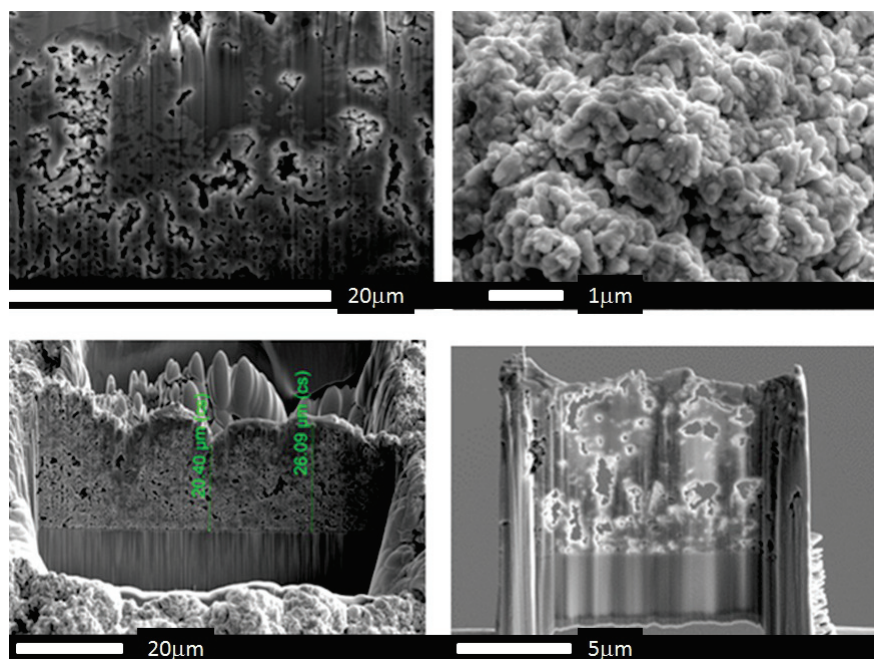


Figure 4.3 – FIB-SEM images of  $\text{Al}_{13}\text{Fe}_4$  films. Top: surface and bottom: cross section.

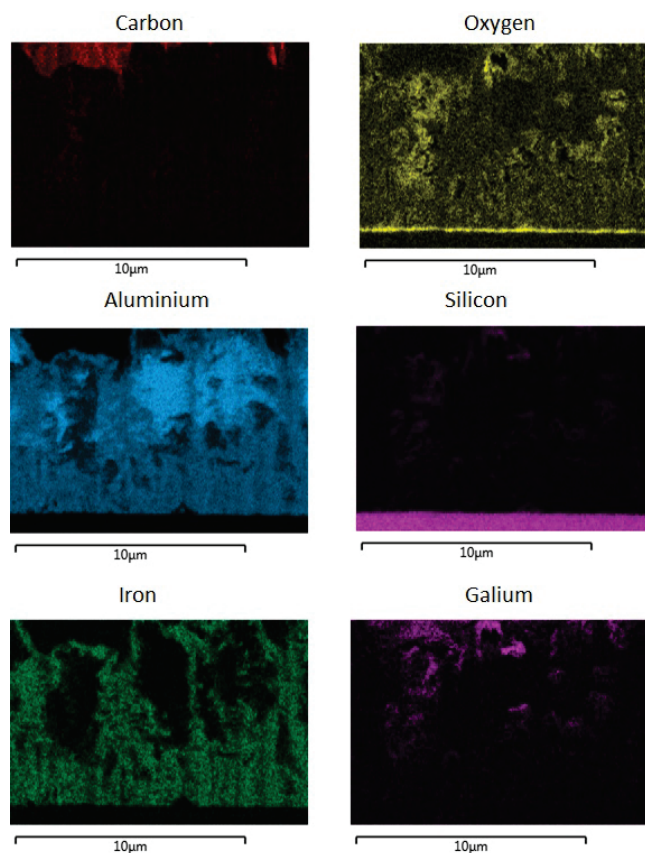


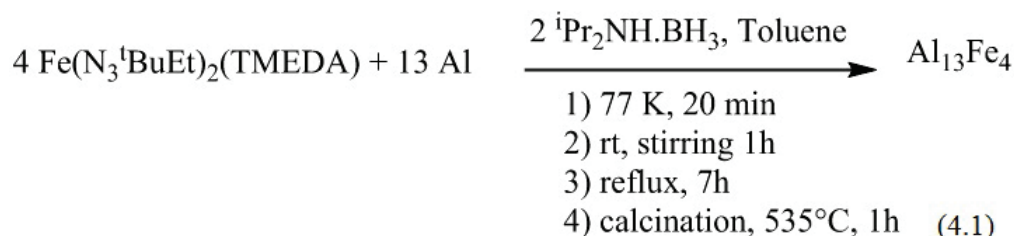
Figure 4.4 – Quantitative EDX spectra of  $Al_{13}Fe_4$  films.

#### 4.2.2 $Al_{13}Fe_4$ nanoparticles via MOD

Supported and unsupported metallic/intermetallic nanoparticles find an important application in heterogeneous catalysis. We evaluated the newly synthesized Fe(II) triazenides complexes, which have i) triazine ligand with poor electron donor properties, ii) a complete oxygen-free environment, and iii) high solubility in the organic solvents (*vide supra* chapter 2), as solution-phase precursors for the intermetallic  $Al_{13}Fe_4$  nanoparticles.

Extending the method used to prepare Fe(0) nanoparticles,  $Al_{13}Fe_4$  intermetallic nanoparticles were successfully prepared in toluene solution by using metallic aluminium and the iron triazenide precursors and *iso*-propylamine borane as a reducing agent. To a toluene solution containing unreduced Al powder and  $Fe(N_3^tBuEt)_2(TMEDA)$  (**4**) in appropriate molar ratio was added two equivalents of  $iPr_2NH.BH_3$  at 77K. The temperature was increased slowly to room temperature and was stirred for 1h. It was then refluxed for 7h. The reaction was accompanied by bubbling which is due to  $H_2$  and  $iPr_2NH$  gas evolution. Solvent was then evaporated to leave a sticky brown solid that was washed two times with hexane to give a brown

pasty powder. Thermal treatment at 535°C for 1h under vacuum resulted in the diffusion of Al and Fe and the formation of the intermetallic complex  $Al_{13}Fe_4$  as a black shiny powder as shown in the equation below:



The phase composition of the samples was determined by X-ray powder diffraction (Figure 4.5). The XRD pattern of the black powder obtained after calcination (which is similar to the pattern of the films obtained by MOCVD) could be indexed with JSPDS file no. 002-1213 of  $Al_{13}Fe_4$ . One difference is the intensity of the peak at 38.5° which is much more intense than that of the calculated spectrum. This peak corresponds to unreacted metallic aluminium. An average nanocrystallite size of ~50 nm was calculated from the Scherrer formula.

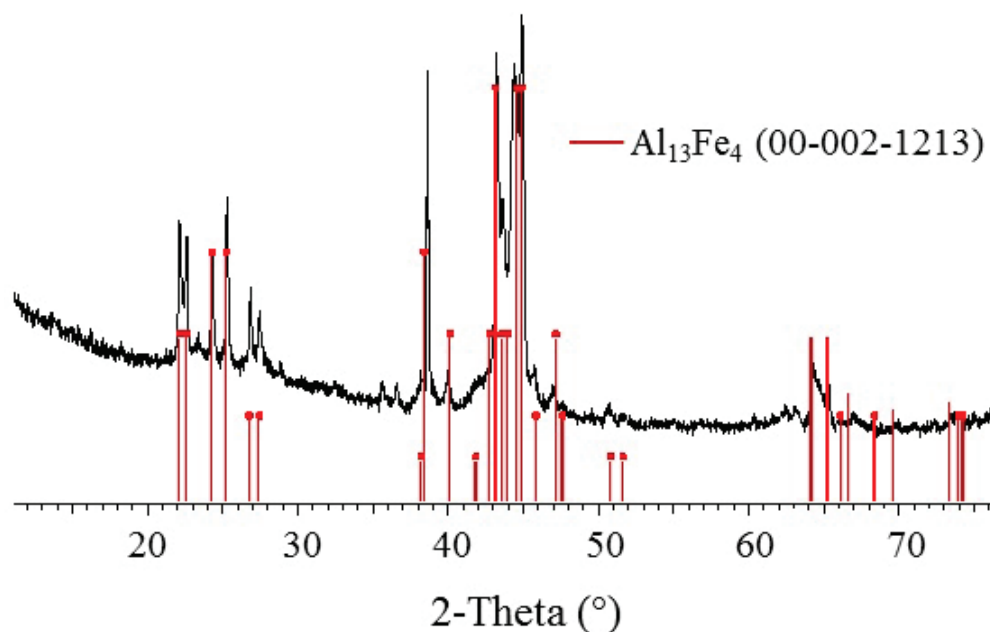


Figure 4.5 – XRD pattern of  $Al_{13}Fe_4$  powder.

TEM images show a well dispersed nanoparticles with large and uniform average size of about 50 nm, which is in accordance with the powder XRD results (Figure 4.6). An *in situ* quantitative EDX analysis of the nanoparticles confirmed the presence of

Al and Fe. It also showed the presence of oxygen and carbon impurities, the former one mainly in the form of alumina  $Al_2O_3$ . Contrary to the Fe(0) nanoparticles prepared by the same method in which a large amount of boron was detected (*vide supra* chapter 2), no such impurities were found here. In the least oxidized part, aluminium was present in 52% by atom, iron 10% and oxygen 30%.

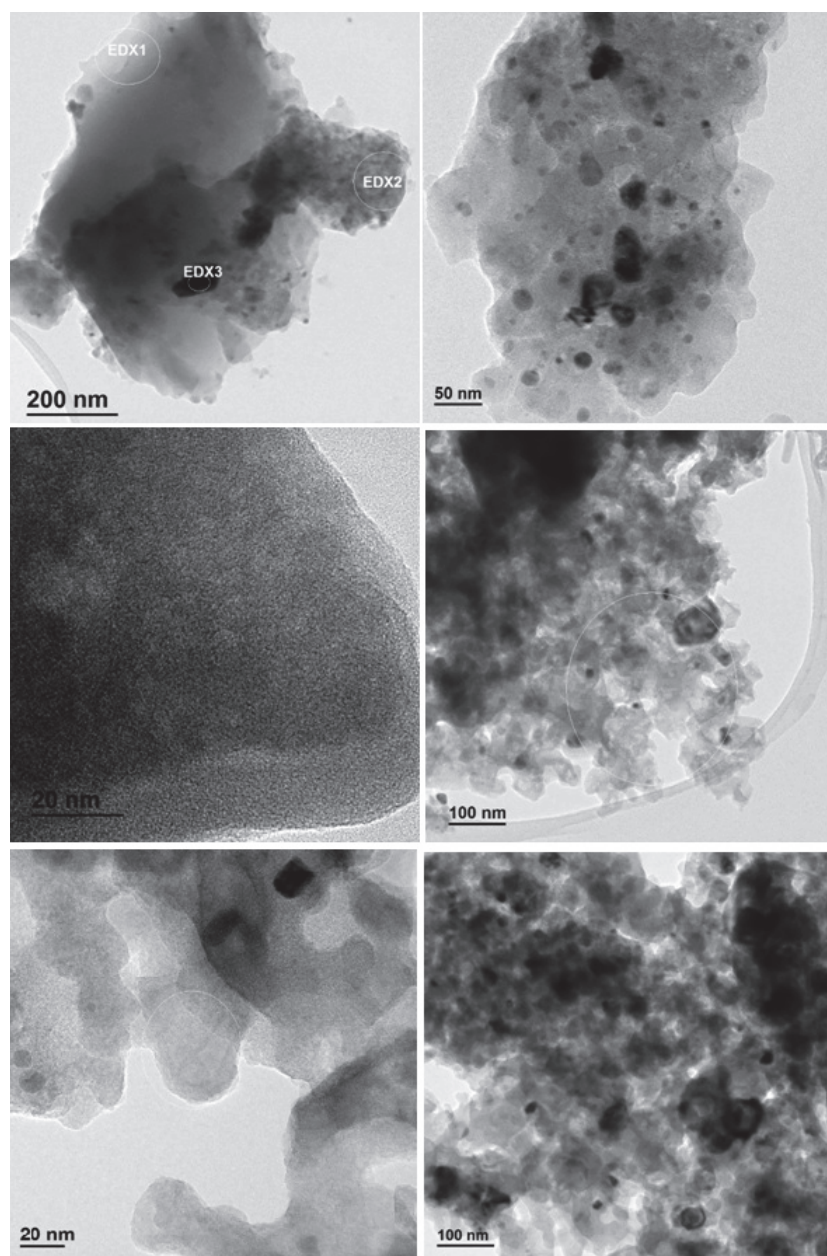


Figure 4.6 – HR-TEM images of  $Al_{13}Fe_4$  nanoparticles.

Table 4.1 summarizes the atomic composition in the least and most oxidized parts of the nanoparticles. The high amount of oxygen contamination is possibly due to the fact that the samples were prepared in air.

Table 4.1 – % atomic concentration of species present on the least oxidized part A and in the most oxidized one B in the sample of  $Al_{13}Fe_4$  nanoparticles.

% atomic concentration	Fe	Al	O	Si	Cl
A	11.3	54.16	32.06	1.4	1.08
B	8.16	3.25	80.25	-	-

### 4.3 Catalytic activity of $Al_{13}Fe_4$ nanoparticles and thin films for the semi hydrogenation of acetylene

Catalytic tests for the semi hydrogenation of acetylene were conducted on both  $Al_{13}Fe_4$  films on Si substrates as well as on  $Al_{13}Fe_4$  nanoparticles. Tests were carried out at atmospheric pressure in a continuous flow fixed-bed reactor which consisted of a cylindrical glass tube of 16 mm of diameter and it is equipped with a sintered glass filter in order to support the catalyst. The reactor was located in a ceramic furnace whose temperature was controlled *via* a thermocouple. The reactant gases ( $C_2H_2:H_2:He$ ) were mixed using mass-flow controllers (Brooks and Vögtlin Instruments) and flowed through the reactor at a total rate of  $50 \text{ ml}\cdot\text{min}^{-1}$ . The effluent gases were analyzed online using a Shimadzu GC-2014 gas chromatograph equipped with a Supelco alumina sulfate plot fused silica capillary column and a FID detector. Acetylene semi hydrogenation reactions have been conducted in different conditions:

1.  $C_2H_2:H_2:He = 2:10:88$  at  $50 \text{ ml}/\text{min}$  at  $200^\circ\text{C}$
2.  $C_2H_2:H_2:He = 0.5:5:94.5$  at  $50 \text{ ml}/\text{min}$  at  $200^\circ\text{C}$

The first catalytic experiment was conducted on  $Al_{13}Fe_4$  films without pretreatment of the catalyst surface, thereafter the other catalytic tests were preceded by a treatment at  $200^\circ\text{C}$  or more under  $H_2$  ( $40 \text{ ml}/\text{min}$ ) or air ( $50 \text{ ml}/\text{min}$ ) to try to regenerate the catalyst. After the reductive treatments of  $Al_{13}Fe_4$  films, the reactive mixture is immediately introduced in the reactor. On the contrary, after the oxidative treatment under air, the reactor was flushed with He before switching to the reactive mixture.

The first catalytic test was conducted on 25mg film without pretreatment. The catalytic sample was introduced in the reactor in a glove box and the whole is placed on the test bench under inert atmosphere ( $N_2$  without oxygen and moisture in contact with the catalyst).

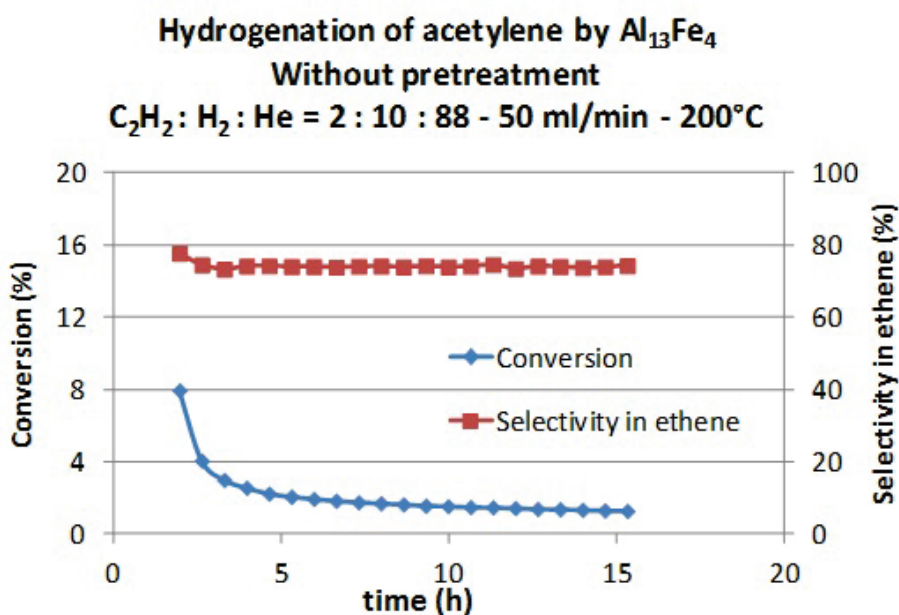


Figure 4.7 – Selectivity and conversion of acetylene semi-hydrogenation with 25 mg film sample without pretreatment.

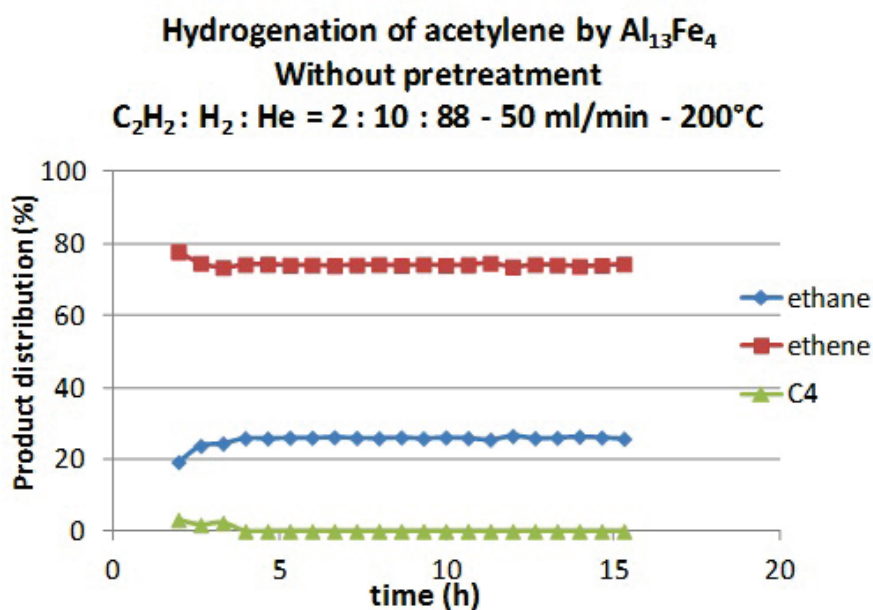


Figure 4.8 – Ethane, ethene and c4 product distribution after hydrogenation of acetylene by  $Al_{13}Fe_4$  film without pretreatment.

As shown in Figure 4.7, the catalyst showed at the beginning a weak activity of 8% and a high selectivity in ethylene of 80%. The products distribution is shown in Figure 4.8. Thus, ethane from total hydrogenation of acetylene and some C4 hydrocarbons produced by acetylene polymerization were also detected. However, the catalytic activity decreased with time to less than 2% after 15 hours on stream but the selectivity remained unchanged. In order to restore the catalytic activity of the catalyst, a reductive treatment has been conducted under hydrogen for four hours at 200°C or for 30 min at 350°C. However, only 1% of the activity has been restored and the selectivity was about 75%. Similarly, oxidative treatment under oxygen gas has been conducted at 200°C for 30 min. Again, only 1% activity has been observed and selectivity has suffered significantly and was only 60%. Unfortunately, the initial activity was never observed again whether after a reducing or oxidizing treatment on the first catalyst sample or on a new catalyst sample stored under inert atmosphere in a glove box ( $N_2$  without oxygen and moisture). Note that the activity of a reactor without sample was measured and was found less than 1%. The catalyst deactivation is possibly due to the formation of an alumina layer on the catalyst surface by residual oxygen and/or moisture. In conclusion this result requires confirmation on a fresh sample that will not be stored in the glove box.

Similarly, the catalytic activity of  $Al_{13}Fe_4$  nanoparticles was evaluated and showed a weak activity of only 1%. Again, higher activity was not observed whether after a reducing or oxidizing treatment of the catalyst sample. As the low catalytic activity is possibly due to the formation of alumina layer on the catalyst surface, the catalyst was treated with HCl in THF to eliminate alumina. Unfortunately, no catalytic activity was observed.

The catalytic evaluation of  $Al_{13}Fe_4$  has been extended to other hydrogenation reactions, more precisely 1,3-butadiene selective hydrogenation to 1-butene. The catalyst showed a weak catalytic activity of 2.5% but decreased just after one hour on stream to 1% conversion. Selectivity was 70%.

The weak catalytic activity could be due to many factors: the films and nanoparticles prepared are not pure  $Al_{13}Fe_4$ . The other phases present as impurities (metallic Al,  $Al_5Fe_2$ ) interfere during hydrogenation conditions and lower the catalyst activity.

## 4.4 Conclusion

The intermetallic  $Al_{13}Fe_4$  both as unsupported nanoparticles and supported thin films have been prepared by Metal Organic Deposition (MOD) and Chemical Vapor Deposition (CVD) methods, respectively, employing either indigenously synthesized new

metal triazenides or commercially available precursors. Both forms obtained had impurities of aluminium metal, aluminium oxides and  $Al_5Fe_2$  phase. Unsupported  $Al_{13}Fe_4$  nanoparticles with an average size of 50 nm have been prepared in toluene solution using Fe(II) triazenide and metallic Al powder as metal source and  $iPrNH.BH_3$  as a reducing agent. The oxygen impurity ranged from 34 to 80% due to the oxidation of the sample by moisture and humidity. The commercial precursors iron pentacarbonyl and dimethylethyamine alane, on the other hand, were successfully used in sequential MOCVD for the deposition of porous  $Al_{13}Fe_4$  films. Compared to  $Al_{13}Fe_4$  nanoparticles, the films contained much less amount of oxygen impurity ( $\sim 5\%$  mostly in the form of alumina). Acetylene semi-hydrogenation experiments of the prepared films and nanoparticles showed a very weak catalytic activity regardless of the treatment of the catalyst. Untreated catalysts as well as catalysts pretreated under  $O_2$  or  $H_2$  gas at  $200^\circ C$  were catalytically inactive in the hydrogenation of acetylene.



# 5

## Titanium, niobium and tantalum triazenide complexes

### Contents

---

<b>5.1</b>	<b>Introduction</b> . . . . .	<b>94</b>
<b>5.2</b>	<b>Results and Discussion</b> . . . . .	<b>97</b>
5.2.1	Synthesis and characterization of titanium, niobium and tantalum triazenide compounds . . . . .	97
5.2.2	Thermal behaviours of of titanium, niobium and tantalum triazenides . . . . .	101
5.2.3	X-ray crystal structure . . . . .	103
5.2.4	Titanium nanomaterials: MOD in solution . . . . .	104
5.2.5	Deposition of of NbN films using Niobium triazenide complex . . . . .	105
<b>5.3</b>	<b>Conclusion</b> . . . . .	<b>108</b>

---

## 5.1 Introduction

Transition metal nitrides exhibit a number of useful properties, including metallic behavior, extreme hardness, very high melting points, and higher chemical resistance. Among them, the TiN thin films are the most studied metal nitride films which are known to possess a number of properties and applications including its use as a diffusion barrier layer for metallization in integrated circuits because of its excellent electrical and mechanical properties [69] and for medical industry for bio-medical applications [70]. Metal nitride films containing niobium and tantalum, on the other hand, find applications in electronics [71], and as protective and hard coatings in sensors [72]. Chemical vapor deposition is a technique of choice for the preparation of such films since it offers the potential of conformal coverage and high deposition rates at moderate temperatures. However, it requires a suitable precursor. A survey of the literature reveals that there is scarcity of the suitable molecular precursors for the metal nitride films involving titanium, niobium and tantalum.  $TiCl_4$  was one of the initial reagents used as a source of titanium for the deposition of TiN films under high partial pressure of  $N_2$  and  $H_2$  and at temperature 850-1000°C. Subsequently, this precursor was used with  $NH(SiMe_3)_2$  at much lower temperature of 300-350°C to obtain TiN films with almost equal ratio of Ti and N [73]. The use of molecular titanium precursors for depositing TiN films was first reported by Sugiyama *et al.* [74] who used  $Ti(NMe_2)_4$  and  $Ti(NEt_2)_4$  (Figure 5.1, a and b) as single source precursors for the depositions over a range of temperatures (250–800°C) and substrates (quartz, graphite, stainless steel or copper plate). Advantages of the dialkylamide precursors, which are often liquids, include good volatility, generally low deposition temperatures, and their ability to deposit films at atmospheric pressure with concomitant high deposition rates. In the same study, they also used various amido- and imido titanium (IV) complexes as single source precursors such as  $[Ti(NMe_2)_3(^tBu)]$  and  $[Ti(R)_4]$  (R =  $NC_4H_8$ ,  $NC_5H_{10}$ ) (Figure 5.1, c-e). Films were grown between 300-450°C. Oxygen and carbon contamination was very high especially for the cyclic compounds  $[Ti(NC_4H_8)_4]$  and  $[Ti(NC_5H_{10})_4]$ . Winter *et al.* [75] reported  $[TiCl_4(NH_3)_2]$ ,  $[[Ti_2Cl_4(NNMe_2)_2(NHNMe_2)_2]$ ,  $[TiCl_2(Me_2NNMe)_2]$  and  $[TiCl_2(NR)(NH_2R)_2]_3$  (R =  $^iPr$ ,  $^tBu$ ) (Figure 5.1, f-j) as volatile single source precursors (transport temperatures 100-120°C) to titanium nitride films at substrate temperatures of > 600°C. While the carbon-free  $[TiCl_4(NH_3)_2]$  could be sublimed at about 100°C (0.1 torr), others such as  $[TiCl_2(N^iPr)(NH_2^iPr)_2]_3$  (MP = 76°C) were liquid under CVD conditions which provided gold-coloured TiN films with either undetectable or low chlorine contamination (2-4%). Carmalt *et al.* [76] reported two titanium guanidinate complexes  $[TiCl(NMe_2)_2^iPrNC - [N(SiMe_3)_2N^iPr]$  and  $[TiCl_2^iPrNC(NMe_2)N^iPr]$

(Figure 5.1, k and l) for the CVD of TiN films. The films obtained at 600°C showed almost undetectable chlorine contamination (less than 0.1%) and an oxygen impurity that was confined to the surface of the films only. However, these films contained a large amount of carbide contamination.

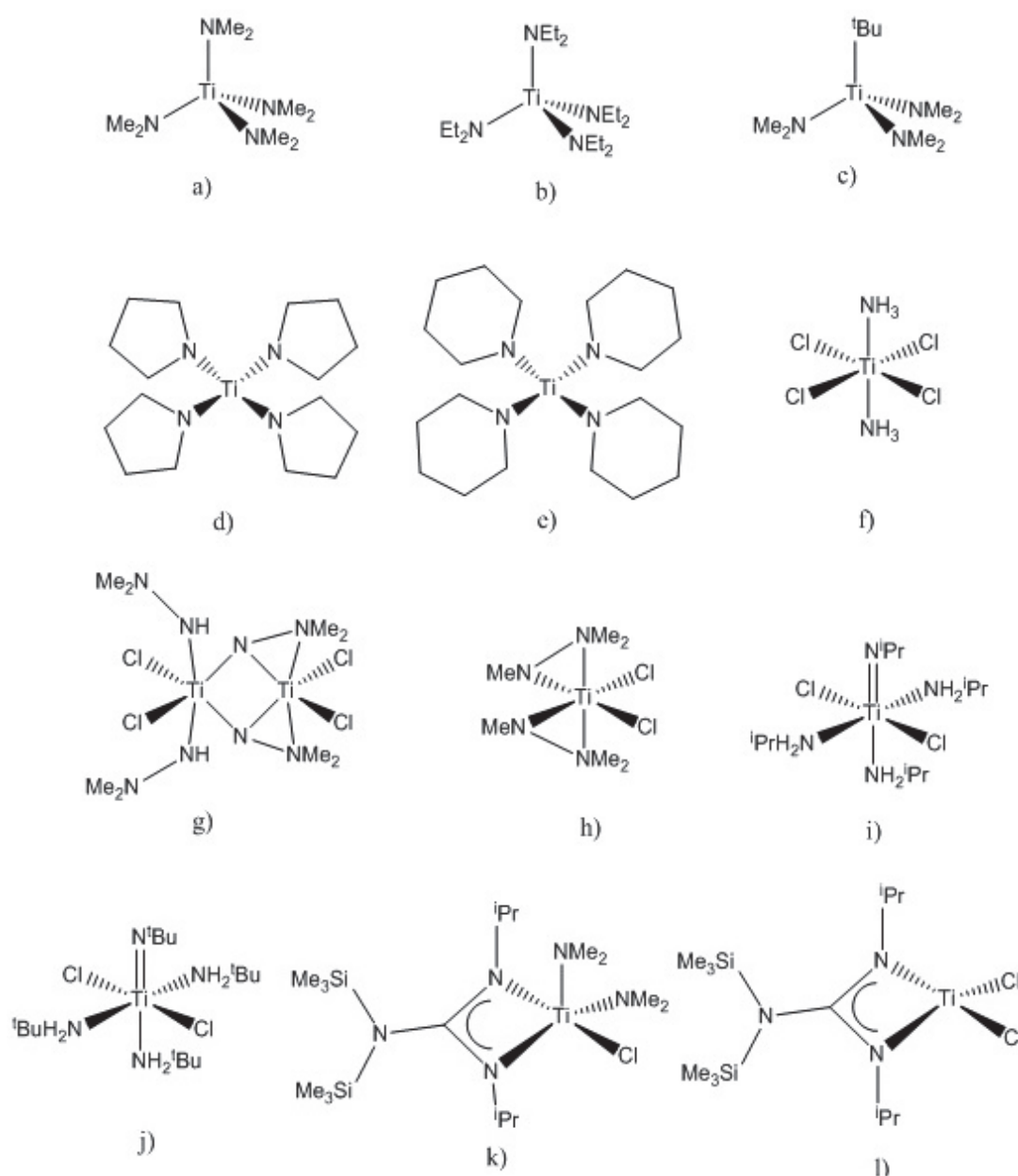


Figure 5.1 – Titanium CVD precursors reported in the literature for the deposition of TiN films.

Contrary to titanium, which shows predominantly tetravalency, niobium and tantalum have rich coordination chemistry with a range of formal oxidation states (from

-III to +V) [77]. Understanding their coordination chemistry with N-donor ligands is, therefore, the key for the development of new metal nitride functional materials containing these elements. Fischer *et al.* [78] have described the CVD of NbN films using three different niobium complexes:  $[Nb(NR_2)_3(N^tBu)]$  (R = Me and Et) and  $[Nb(N^tBu)(NMe_2)C(N^iPr)_2(NMe_2)_2]$  (Figure 5.2, a-c). For  $[Nb(NR_2)_3(N^tBu)]$ , CVD experiments were conducted at 100 Pa and at temperatures 500-700°C, which resulted NbN films contaminated with niobium carbide (NbC). Carbon impurities decreased by increasing the temperature but could not be eliminated completely. Oxygen impurities were significant as well.

For  $[(N^tBu) = Nb(NEt_2)_3]$ , CVD experiments at 100 Pa and temperatures 400-800°C using  $NH_3$  as the reactive gas led to a mixture of NbN and  $Nb_3N_4$  phases. Carbon and oxygen contamination were high but could be decreased by increasing the temperature. The mixed amido-imido-guanidinato complex  $[Nb(N^tBu)(NMe_2)C(N^iPr)_2(NMe_2)_2]$ , on the other hand, led to pure NbN films with no traces of carbon impurity at temperature 400-600°C, although the oxygen contamination was still high. Liu *et al.* [79] have reported NbN films employing two precursors  $[Nb(NEt_2)_4]$  and  $[(^tBuN) = NbN(C_2H_4)NEt_3]$  (Figure 5.2 d) in plasma enhanced CVD conducted at 1 Pa using  $N_2H_4$  plasma at temperatures 350-800°C. The obtained films were partially contaminated with oxygen and carbon.

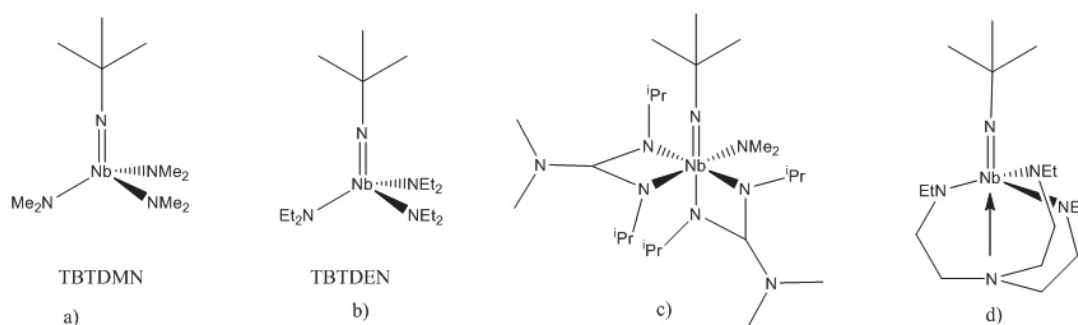


Figure 5.2 – Niobium CVD precursors reported in the literature for the deposition of NbN films.

Films of TaN [80] were grown by atmospheric pressure CVD at temperature range 350-580°C using  $TaCl_5$  and  $NH(SiMe_3)_2$ . In another work by Chen *et al.* [81],  $TaBr_5$  precursor was used as Ta source along with  $NH_3$  and  $H_2$  in a low pressure CVD (128 Pa) for tantalum nitride. The  $[(NEt_2)_3Ta = NEt]$  (Figure 5.3, a) was the first single source precursor to be used for the CVD of TaN films at 500 °C by Sugiyama *et al.* [74], although this precursor was mistakenly identified as  $Ta(NMe_2)_5$  initially. Oxygen and carbon contaminations were high. TaN films were

successfully prepared from  $[(NEt_2)_3Ta = N^tBu]$  (Figure 5.3, b) by Chiu *et al.* at temperature 450–650°C with low oxygen and carbon contamination [82]. Pure TaN films without carbon, oxygen, chloride or silicon impurities were deposited by Carmalt *et al.* [83] using  $[TaCl_3(NSiMe_3)(NC_5H_3Me_2\{3,5\})_2]$  (Figure 5.3, c) at 600°C.  $[(\mu_2 - MeN(CH_2)_2NMe)Ta(NMe_2)_3]$  (Figure 5.3, d) was used by Chen *et al.* [83] for the LPCVD growth of TaN using  $NH_3$  as the reactive gas. Cubic TaN films were deposited at temperatures 160–500°C. Carbon and oxygen contaminations were found to be low.

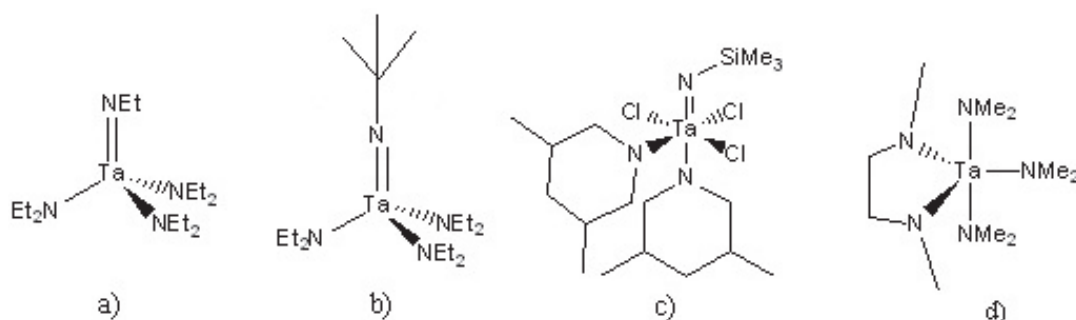


Figure 5.3 – Tantalum CVD precursors described in the literature for the deposition of TaN films.

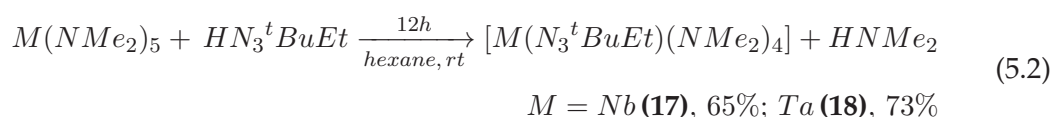
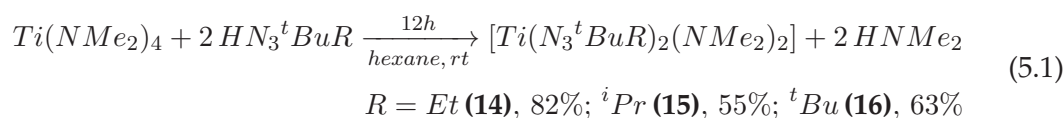
We extended triazenide chemistry to titanium, niobium and tantalum transition metals to obtain metal nitride or nitrogen doped metal oxide nanomaterials starting from these nitrogen rich precursors. We report in this chapter the synthesis and properties of a series of titanium, niobium and tantalum complexes containing the previously described triazene ligands using  $Ti(NMe_2)_4$ ,  $Nb(NMe_2)_5$  and  $Ta(NMe_2)_5$  as metal sources. All complexes obtained were solids at room temperature. Ti triazenide complexes were less volatile compared to the starting material  $Ti(NMe_2)_4$  while Niobium triazenides were more volatile than  $Nb(NMe_2)_5$ .

## 5.2 Results and Discussion

### 5.2.1 Synthesis and characterization of titanium, niobium and tantalum triazenide compounds

The treatment of  $Ti(NMe_2)_4$  with two equivalents of **(L1)**, **(L2)** and **(L4)** afforded the compounds  $[Ti(N_3^tBuR)_2(NMe_2)_2]$  [**(R = Et (14), *i*Pr (15), *t*Bu (16))**] which were crystallized from hexane at -20°C to give orange-colored crystals. In a similar procedure, equivalent reactions of the triazene ligands with  $M(NMe_2)_5$  (M= Ta, Nb) gave

$[Nb(N_3^tBuEt)(NMe_2)_4]$  (**17**) and  $[Ta(N_3^tBuEt)(NMe_2)_4]$  (**18**) in good yield. Yellow-orange crystals were obtained after crystallization from hexane at  $-20^\circ\text{C}$ .



$^1H$  NMR spectra of titanium triazenides (**14**)-(**16**) are shown in Figures 5.4, 5.5 and 5.6, respectively. These spectra exhibit one singlets each for Me and  $tBu$  group at  $\delta$  1.10-1.14-1.27 ppm and at 1.12-1.24-1.21 ppm, respectively, and a singlet at  $\delta$  3.25-3.19-3.27 ppm for  $N(CH_3)_2$  groups. While the methylene protons of the ethyl group on triazene ligand in (**14**) are not well-resolved, probably due to high fluxionality of the molecule at room temperature, the *iso*-propyl group in (**15**) appears expectedly as a doublet ( $CHMe_2$ ) and a septet ( $CHMe_2$ ).

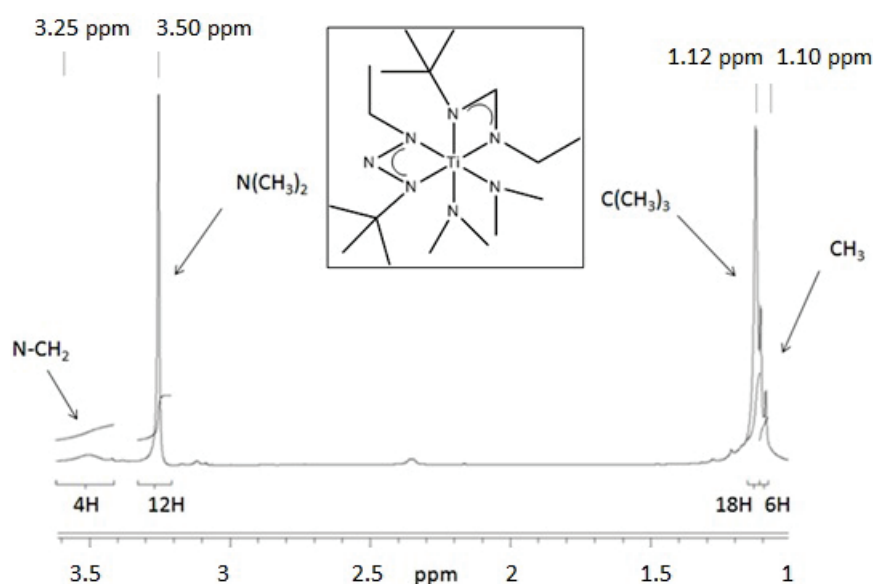


Figure 5.4 –  $^1H$  NMR spectrum of  $[Ti(N_3^tBuEt)_2(NMe_2)_2]$  (**14**).

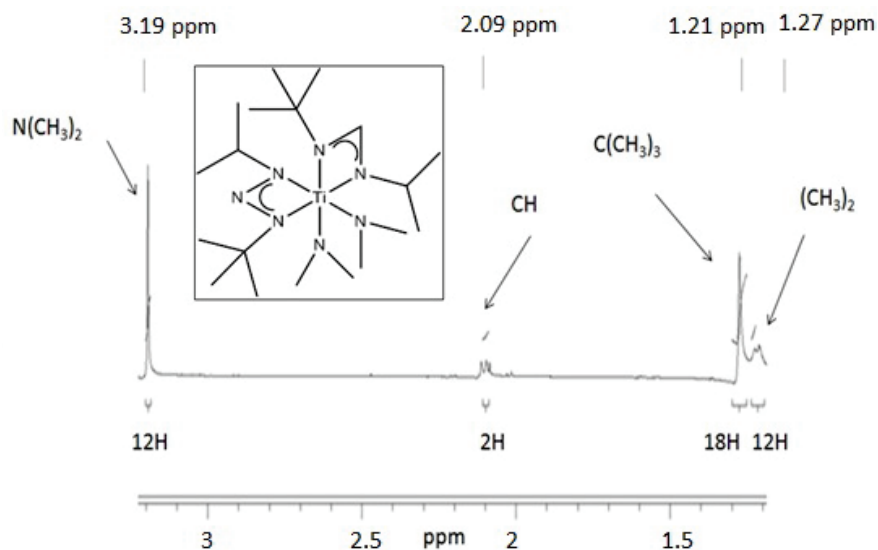


Figure 5.5 –  $^1\text{H}$  NMR spectrum of  $[\text{Ti}(\text{N}_3^t\text{Bu}^i\text{Pr})_2(\text{NMe}_2)_2]$  (15).

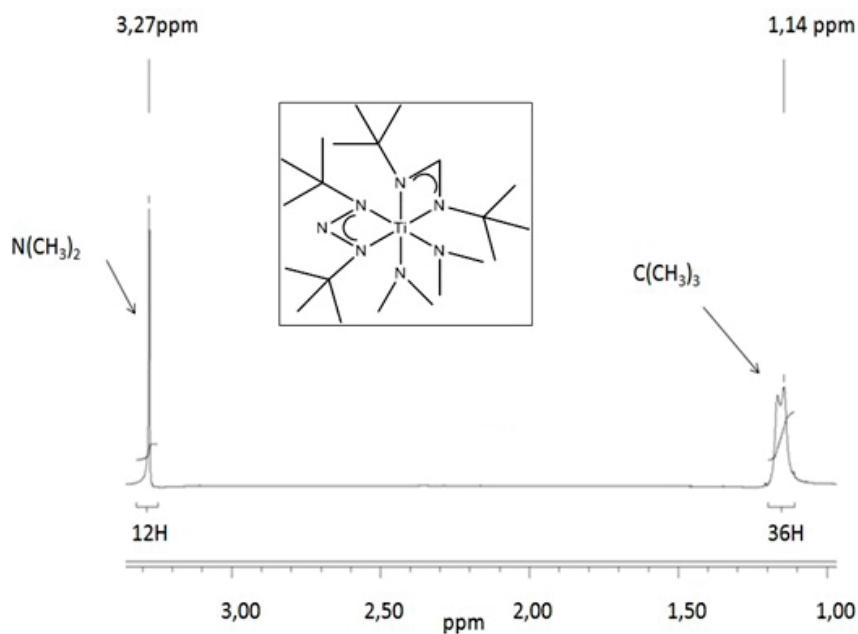


Figure 5.6 –  $^1\text{H}$  NMR spectrum of  $[\text{Ti}(\text{N}_3^t\text{Bu}_2)_2(\text{NMe}_2)_2]$  (16).

$^1\text{H}$  NMR of  $[\text{Nb}(\text{N}_3^t\text{BuEt})(\text{NMe}_2)_4]$  (17) and  $[\text{Ta}(\text{N}_3^t\text{BuEt})(\text{NMe}_2)_4]$  (18), shown in Figure 5.7 and Figure 5.8 respectively, are identical which demonstrate the presence of one singlet each for Me and  $^t\text{Bu}$  groups at  $\delta$  1.13–1.07 and 1.16–1.18 ppm, respectively, and a broad peak at  $\delta$  3.14–3.85 ppm corresponding to the four  $\text{N}(\text{CH}_3)_2$  groups.

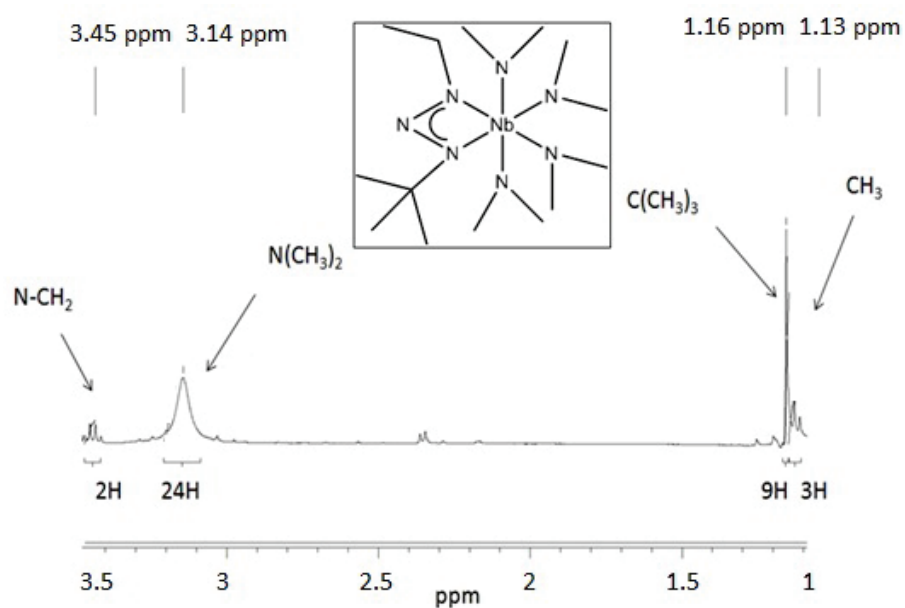


Figure 5.7 –  $^1\text{H}$  NMR spectrum of  $[\text{Nb}(\text{N}_3^t\text{BuEt})(\text{NMe}_2)_4]$  (17).

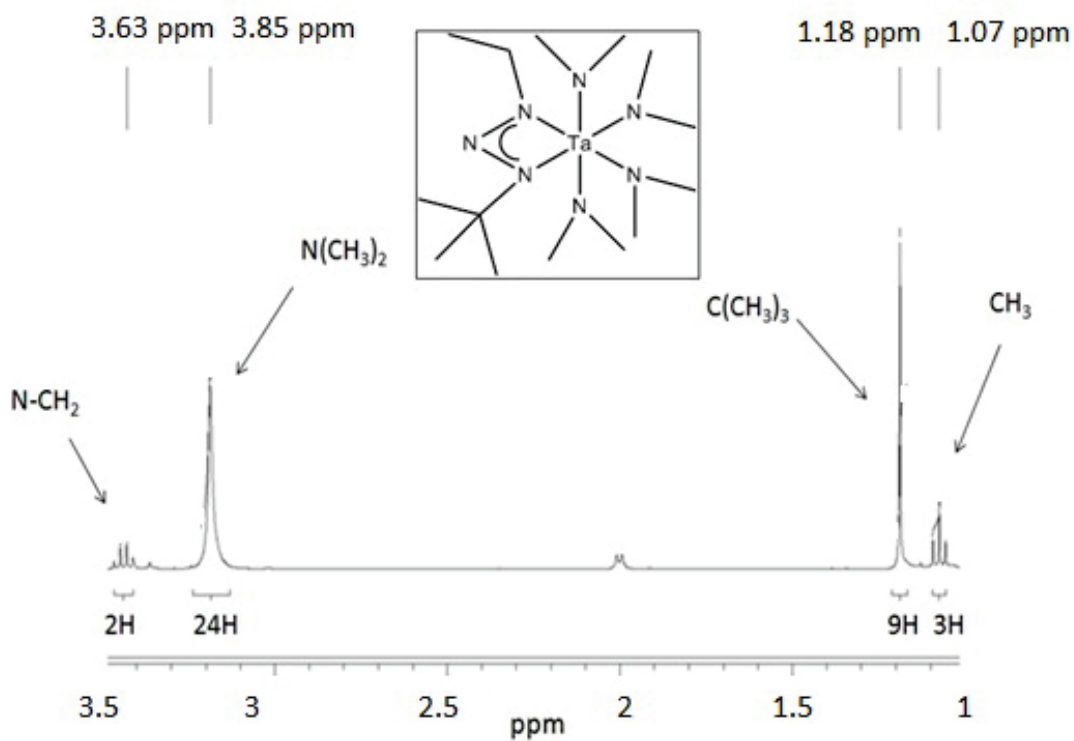


Figure 5.8 –  $^1\text{H}$  NMR spectrum of  $[\text{Ta}(\text{N}_3^t\text{BuEt})(\text{NMe}_2)_4]$  (18).

### 5.2.2 Thermal behaviours of of titanium, niobium and tantalum triazenides

The thermal behavior of new Ti(VI), Nb(V) and Ta(V) triazenides (**14-18**) was investigated under argon atmosphere in the 20-600°C temperature range by thermogravimetric analysis (TGA) (Figure 5.9 and Figure 5.10). For comparison, similar studies were also carried out for the starting homoleptic dimethylamide precursors  $Ti(NMe_2)_4$  and  $Nb(NMe_2)_5$ . It was hoped that these heteroleptic complexes bearing asymmetrically substituted triazenide and dimethylamide ligands would be more volatile than the homoleptic dimethylamide precursors. The 2- or 3-steps TG curves for the derivatives (**14-18**) show a distinct two-phase decomposition pattern i.e., partial removal of the dimethylamide ligands, followed by the loss of triazenide ligand(s). For these complexes, the decomposition is over before 450°C, the total percentage weight loss varying in the range 55-69%. The remaining weight of the residues (41, 31, 34, 42 and 46% for **14-18**, respectively) account much more than the theoretical value of MN (16, 15, 14, 27, and 39% for (**14-18**), respectively) or  $TiO_2/Nb_2O_5$  (20, 19, 17, and 33% for (**14-17**), respectively), which indicates incomplete decomposition due to the presence of argon atmosphere. However, the theoretical value of  $Ta_2O_5$  (45%) for (**18**) matches the remaining weigh of the residues which indicated that  $[Ta(N_3^tBuEt)(NMe_2)_4]$  (**18**) decomposes into  $Ta_2O_5$ .

A comparison of the TGA spectra of (**14-18**) gives us the following conclusions:

1. The heteroleptic triazenide derivatives are not volatile enough to be transported into the vapour phase in intact manner. For instance, Ti homoleptic dimethylamide precursor is much more volatile than the heteroleptic triazenide ones.
2. Among titanium derivatives (**14-16**), the thermal stability depended on the nature of the ligands. It is in the order:  $[Ti(N_3^tBu^iPr)_2(NMe_2)_2]$  (**15**)  $\approx [Ti(N_3^tBu)_2(NMe_2)_2]$  (**16**)  $> [Ti(N_3^tBuEt)(NMe_2)_4]$  (**14**).
3. The incorporation of triazenide ligand enhances the thermal stability of the heteroleptic complexes of niobium and tantalum  $M(N_3^tBuEt)(NMe_2)_4$  (M = Nb, Ta). For example, the remaining residue left for  $[Nb(N_3^tBuEt)(NMe_2)_4]$  (**17**) upon reaching 450°C was 41% which is much less than 58% residue observed for  $Nb(NMe_2)_5$ .

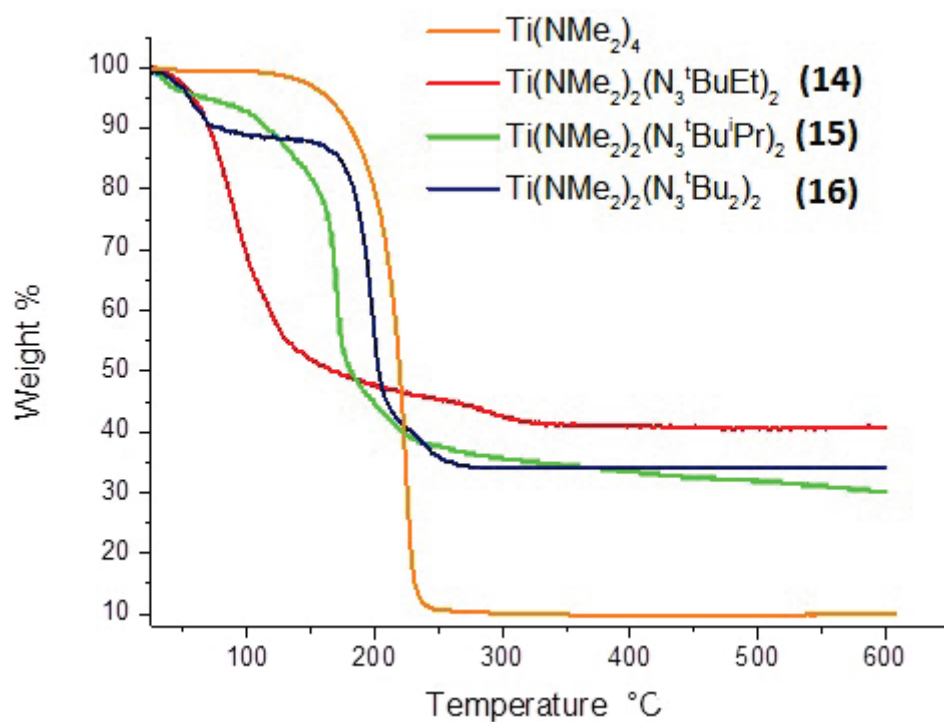


Figure 5.9 – TGA curves of titanium complexes.

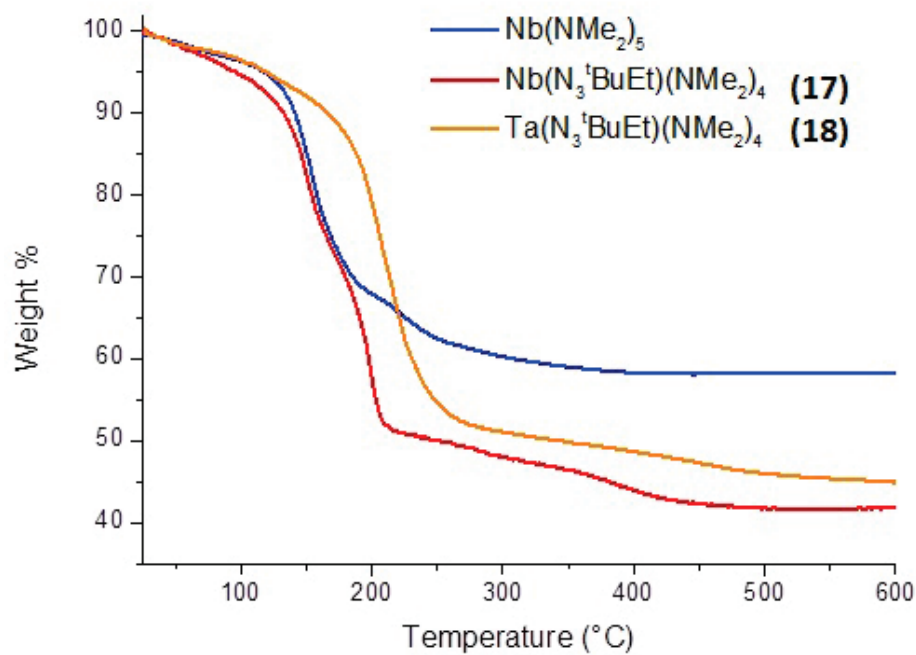


Figure 5.10 – TGA analysis of heteroleptic Nb and Ta triazenides.

Table 5.1 – TGA data of the the compounds 14-18.

Compound	% residues	Theoretical MN %	Theoretical $TiO_2/M_2O_5$ %
<b>14</b>	41	16	20
<b>15</b>	31	15 1	9
<b>16</b>	34	14	17
<b>17</b>	42	27	33
<b>18</b>	46	40	45

### 5.2.3 X-ray crystal structure

The titanium derivative  $[Ti(N_3^tBu_2)_2(NMe_2)_2]$  (**16**) crystallizes in monoclinic space group  $C2/c$  and adopts monomeric structure with distorted octahedral geometry around the metal center. The triazenide ligand shows  $\kappa 2$ , N-N coordination through the terminal nitrogen atom (Figure 5.11). The two dimethylamide groups are arranged in *cis*-position ( $\angle N1-Ti1-N1i = 98.9^\circ$ ). Selected bond lengths and angles are reported in Table 5.2. The titanium-nitrogen distances belonging to the triazenide ligand 2.11(2)-2.22(2) Å are significantly longer than those involving  $NMe_2$  (1.90(5) Å). These bond lengths and angles are consistent with the literature values on related complexes [84].

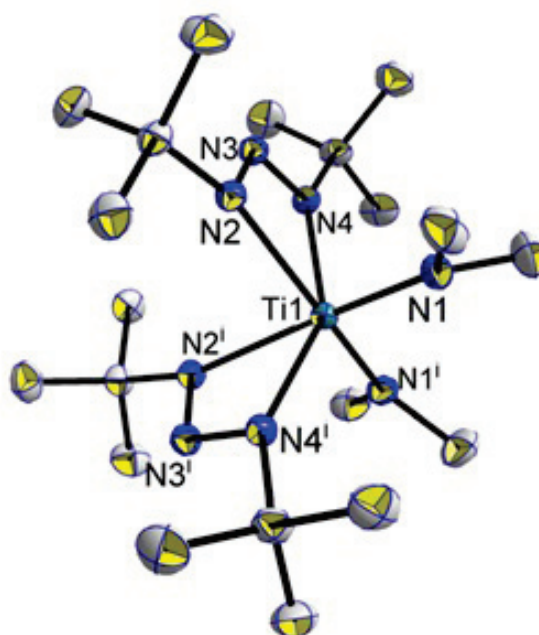


Figure 5.11 – Single crystal XRD structure of  $[Ti(N_3^tBu_2)_2(NMe_2)_2]$  (**16**). Ellipsoids are drawn at 50% probability and hydrogen atoms are omitted for clarity.

Table 5.2 – Selected bond lengths and angles of  $[Ti(N_3^tBu_2)(NMe_2)_2]$  (**16**).

Bond	Bond length (Å)	Bond	Bond angle (deg)
Ti-N1	1.909(4)	N2-Ti-N4	58.94
Ti-N2	2.223(2)	N1-Ti-N1i	98.94
Ti-N4	2.116(2)	-	-

### 5.2.4 Titanium nanomaterials: MOD in solution

As Ti triazenides were not volatile, we wanted to check its solution phase behavior and whether they can be easily reduced to Ti(III) (either as TiN or N-doped  $TiO_2$  which is desirable for photocatalysis). So  $[Ti(N_3^tBuEt)_2(NMe_2)_2]$  (**14**) was treated with two equivalents of  $iPr_2NH.BH_3$  and the resulting solution was stirred at room temperature for 24h. The orange solution was dried under vacuum and was dissolved in anhydrous hexane and left aging for 24h. The powder was filtered to give rise to a bright yellow powder that was amorphous as shown by powder XDR diffraction. This powder was crystalline at temperatures higher than 600°C.

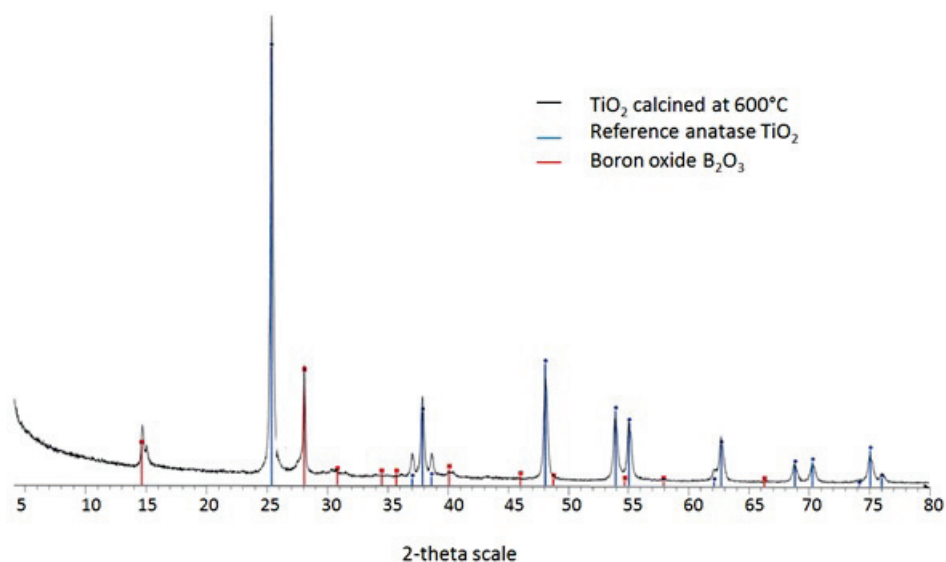


Figure 5.12 – Powder XRD pattern for the nanoparticles obtained from solution reduction of  $[Ti(N_3^tBuEt)_2(NMe_2)_2]$  (**14**) and calcined at 600°C under air.

The phase composition of the calcined sample at 600°C was determined by X-ray powder diffraction and could be indexed with JSPDS file no. 00-006-02972 of anatase alumina and 01-086-1157 of  $B_2O_3$ . This corresponds to boron-doped titania and previously reported by Parkin *et al.* [85]. However, they have prepared it *via* MOCVD.

This material is in itself interesting because boron doping of  $TiO_2$  leads to an inductive creation of electron acceptor levels [86] and improves its photocatalytic activity [87]. Although the titanium triazenide precursors were not volatile enough for CVD applications, however; they easily decomposed into functional nanomaterials. Future work will be dedicated to study the photocatalytic properties of this material.

### 5.2.5 Deposition of of NbN films using Niobium triazenide complex

Transport properties of  $[Nb(N_3^tBuEt)(NMe_2)_4]$  (17)

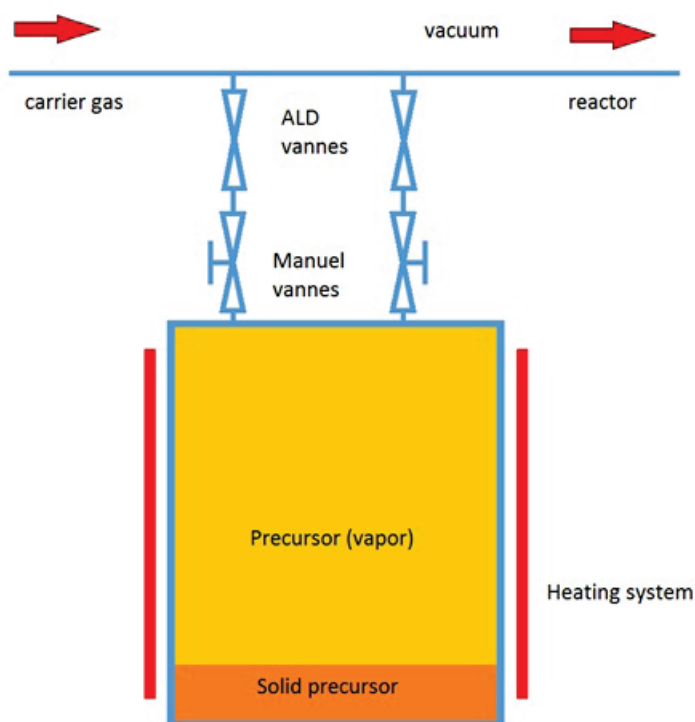


Figure 5.13 – Schematic representation of the reactor used for the deposition experiments.

Deposition experiments were done in SIMaP laboratory in Grenoble under the supervision of Dr. Arnaud Mantoux. This complex has been used because it fulfills our requirements for the design of CVD suitable precursors:

1. The lack of oxygen in the molecule: in fact, the element still more readily reacts with the metal than nitrogen; its presence would therefore lead to the formation of undesirable oxides.

2. The absence of chlorine in the molecule: the chlorinated compounds are extremely corrosive and lead to premature wear of the equipment.

The commercially available pentakisdimethylamidoniobium  $Nb(NMe_2)_5$  was tested for its transport properties as existing data on the use of this precursor are almost nonexistent.

### Mass transport properties of $Nb(NMe_2)_5$

The mass transport properties of  $Nb(NMe_2)_5$  were performed in the temperature range from 150 - 200°C. In all cases, the vapor pressure was found to be very low. This could be attributed to the solid state of the precursor because of which the stable feeding rate of the vaporized precursor cannot be maintained for a long period. On the other hand, the dimensions of the bubbler available are very large with respect to the amount of material to sublimate. It may also pose a problem of efficient heating.

### Precursor transportation of $Nb(N_3^tBuEt)(NMe_2)_4$ (17)

Given the unsatisfactory vapor pressure properties of  $Nb(NMe_2)_5$ , the heteroleptic triazenide derivative  $[Nb(N_3^tBuEt)(NMe_2)_4]$  (17) was tested for its mass transport properties. As shown by TGA, this precursor has a better thermal stability and volatility than the commercial  $Nb(NMe_2)_5$ . In all, two series of depositions were performed by heating the precursor at 150°C. In the first series, a thermal ALD was performed between 350 - 450°C with ammonia as nitrogen source. The second series employed plasma ALD, between 205 - 450°C, by adding a step with hydrogen plasma in the procedure. More specifically, thermal depositions were conducted according to these steps:

1. Precursor pulse for 5 seconds, nitrogen carrier gas (80 sccm)
2. Purge the reactor for 4 seconds with nitrogen gas
3. Ammonia: pulse 5 seconds, nitrogen carrier gas (200 sccm)
4. Purge the reactor for 4 seconds with nitrogen

The plasma-assisted deposition was performed according to this cycle:

1. Precursor pulse for 5 seconds, nitrogen carrier gas (80 sccm)
2. Purge the reactor for 4 seconds with nitrogen gas
3. Plasma  $H_2$ : 12 seconds with argon as carrier gas (80 sccm)

4. Purge the reactor for 2 seconds with nitrogen
5. Ammonia: pulse 5 seconds, nitrogen carrier gas (200 sccm)
6. Purge the reactor for 4 seconds with nitrogen depositions were carried out on crystalline silicon (100 samples) and analyzed by EDX, to get a glimpse of their chemical composition. These results were not quantitative, but comparable with each other as obtained under the same conditions

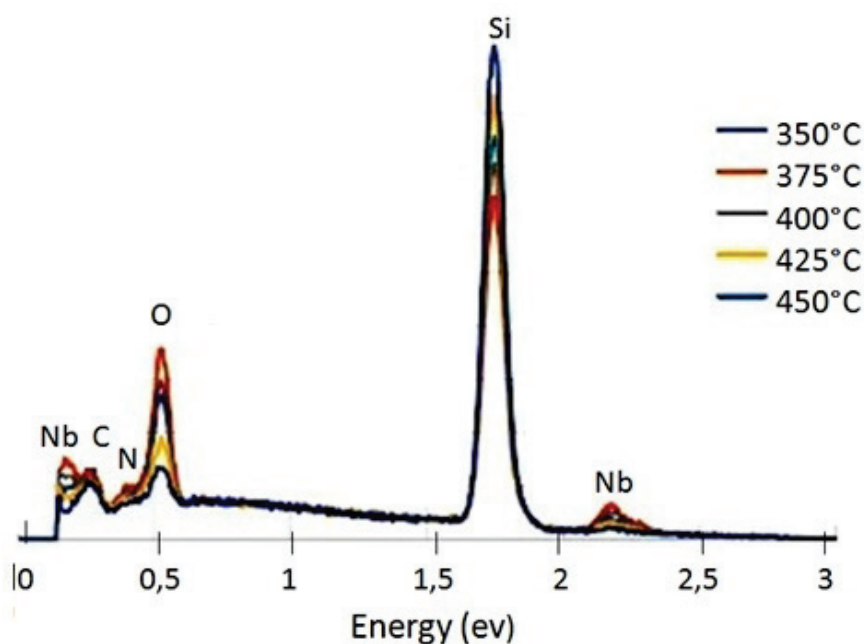


Figure 5.14 – EDX spectra of NbN films obtained by thermal ALD.

Whatever the experimental conditions used, the observations were identical. Comparing the intensity of the silicon peak with other elements, it was noted initially that the thickness of the layers is extremely low with the presence of nitrogen, oxygen and niobium. This proved the successful transportation of the precursor. Niobium peaks being very low in intensity, the amount of transported precursor was very low. This was further confirmed by the presence of weak nitrogen peaks (due to the small amount of precursor present, ammonia reacted little to the surface). However, significant presence of oxygen indicates that there is formation of a thin layer, the formation of oxynitride is more favored than the formation of a nitride film we wish to obtain.

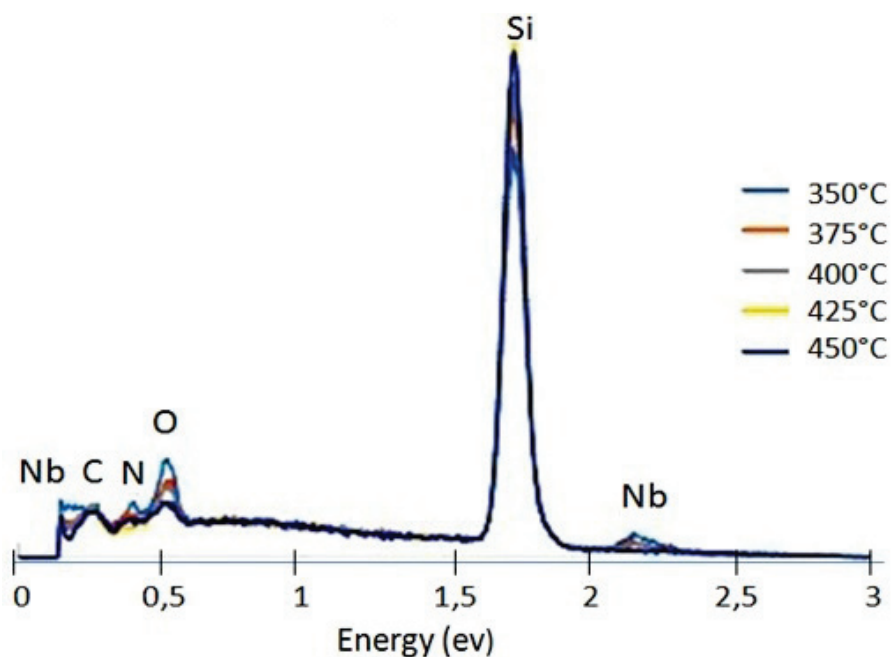


Figure 5.15 – EDX spectra of NbN films obtained by plasma assisted ALD.

### 5.3 Conclusion

Novel Ti, Nb and Ta triazenide complexes have been synthesized. Film deposition studies on  $[Nb(N_3^tBuEt)(NMe_2)_4]$  (**17**) show that the incorporation of the triazene ligand increased the volatility of the complex since it was successfully introduced into the ALD chamber at moderately low temperatures in contrary to the starting material  $Nb(NMe_2)_5$ . Comparing these results to those obtained in the same conditions with a commercial precursor  $Nb[(NC(CH_3)_3)_3(=NC(CH_3)_3)]$ , niobium triazenides are much less satisfactory in terms of amount of precursor introduced into the reactor and consequently the amount of film deposited. Also there is again the problem of oxygen contamination. Although these results are not very satisfactory regarding deposition of NbN films, transporting properties of niobium triazenides have nevertheless been observed, with improved mass transport compared to the commercial pentakisdimethylaminoniobium. ALD/CVD experiments could possibly be performed in a well-adapted reactor. Titanium triazenides were not volatile enough to be used as CVD precursors, but they decomposed into boron-doped titania which itself is a nanomaterial with enhanced photocatalytic activity.

# 6

## General Conclusions and Perspectives

The main objectives of this doctoral work were to develop novel oxygen-free molecular compounds and investigate their utility as precursors for metallic or nitrogen-doped metal oxides nanoparticles/ thin films via Metal Organic Deposition (MOD) or Metal Organic Chemical Vapor Deposition (MOCVD) methods. In particular, we intended to develop large-scale synthesis of the intermetallic  $Al_{13}Fe_4$  as supported films and/or nanoparticles by soft chemical methods and test its catalytic activity and selectivity for the semi-hydrogenation of acetylene. For this, we designed and synthesized new triazene ligands,  $HN_3^tBuR$  ( $R = Et, ^iPr, ^nBu, ^tBu$ ), featuring different alkyl substituents at 1,3-N centers. These nitrogen-rich and weakly electron donor ligands designed to facilitate the reduction of the metal center, were subsequently introduced in the precursor chemistry.

Starting from these ligands, we synthesized novel homo- and heteroleptic Al(III) and Fe(II) triazenides with the goal of using them as precursors for the large-scale production of metallic and intermetallic  $Al_{13}Fe_4$  nanoparticles and/or films by soft chemical methods. The homoleptic dimeric complexes of iron of the general formula  $[Fe_2(N_3^tBuR)_4]$  ( $R=Et, ^iPr, ^nBu$ ) showed multistep decomposition in

TGA experiments and high susceptibility towards oxidation by atmospheric oxygen. The addition of the ancillary ligand tetramethylethylenediamine (TMEDA), however, resulted in the formation of monomeric complexes of the general formula  $[Fe(N_3^tBuR)_2(TMEDA)]$  ( $R=Et, ^iPr, ^nBu, ^tBu$ ) which are more stable toward oxidation. Even though these monomeric complexes showed improved thermal characteristics as compared to the dimeric complexes, their volatility was still not up to the mark as CVD precursors. These, however, could be used in solution phase in the presence of a mild and cheap reducing agent  $^iPr_2NH.BH_3$  to obtain mainly Fe(0) particles (70%) along with some  $Fe^{2+}$  (8%) and  $Fe^{3+}$  species (21%), as indicated by the Mössbauer and TEM studies. The nanoparticles, however, had a high percentage of boron impurities. These could also be used to prepare  $Al_{13}Fe_4$  nanoparticles with average size of 50 nm in the presence of Al metal and  $^iPr_2NH.BH_3$ . Neither carbon nor nitrogen impurities were detected. Contrary to Fe(0) NPs,  $Al_{13}Fe_4$  NPs did not have boron contamination either. Although these novel Fe(II) triazenides could be used as precursors to metallic/intermetallic nanomaterials in solution phase, it would be necessary to enhance further the volatility of these precursors to be used as CVD precursors. In this regard, a mixed-ligand strategy employing two different ligands (i.e., heteroleptic triazenide complexes) might be useful in improving further the volatility. Alternatively, one could also assess the suitability of these Fe(II) triazenide derivatives either as Liquid Injection or Aerosol-Assisted MOCVD precursors. As the above reported metal triazenides were not sufficiently volatile, we used commercially available, simple but volatile metal precursors for the gas phase synthesis of metallic and intermetallic thin films.

Using DMEAA as aluminium precursor, we demonstrated the preparation of pure aluminium films *via* MOCVD at temperatures between 160 - 260°C. The films were rough in terms of surface morphology and thickness. Combining this aluminium precursor with iron precursor  $Fe(CO)_5$ , we also deposited successfully the intermetallic  $Al_{13}Fe_4$  films. The films obtained did not have any carbon or nitrogen impurities and showed only 5% surface oxygen impurity in the form of alumina. However, the material was not pure and secondary phases were obtained as well as metallic aluminium and alumina.

The precursor chemistry of triazene ligands was also extended to group 4 and 5 metals to obtain novel heteroleptic Ti(IV), Nb(V) and Ta(V) triazenide complexes  $[Ti(N_3^tBuEt)_2(NMe_2)_2]$  ( $R = Et, ^iPr$  and  $^tBu$ ),  $[Nb(N_3^tBuEt)(NMe_2)_4]$  and  $[Nb(N_3^tBuEt)(NMe_2)_4]$  as potential precursors for N-doped metal oxides or metal nitride nanomaterials. The preliminary MOCVD results on the niobium precursor  $[Nb(N_3^tBuEt)(NMe_2)_4]$  showed an improved transporting properties for this precursor as compared to the commercial  $Nb(NMe_2)_5$ .

The catalytic activity of the unsupported/supported  $Al_{13}Fe_4$  nanoparticles and films prepared was studied for the semi hydrogenation of acetylene. Catalytic tests were done either without pre-treatment of the catalyst or with treatment under  $O_2$  or  $H_2$  at  $200^\circ\text{C}$ . Under our conditions, no catalytic activity was observed. Reasoning that the weak catalytic activity was probably due to the formation of alumina, acid treatment was done in HCl in anhydrous ether. However, the catalyst was found inactive again. Complete characterisation of  $Al_{13}Fe_4$  nanoparticles as well as enhancing the catalytic activity of  $Al_{13}Fe_4$  nanoparticles and films by changing the hydrogenation conditions as well as the catalyst pre-treatment methods will be pursued in the future.

Future work will also involve enhancing the volatility of iron triazenide complexes by employing a mixed ligand strategy and to prepare aluminium nanomaterials starting from aluminium triazenides *via* MOCVD and/or MOD.



# 7

## General Experimental Part

### Contents

---

<b>7.1</b>	<b>Characterization methods</b> . . . . .	<b>114</b>
<b>7.2</b>	<b>Synthesis of the compounds</b> . . . . .	<b>118</b>

---

Manipulations of air sensitive compounds have been conducted using a vacuum-argon schlenk system using schlenks glassware as for synthesis and storage of compound. Cannulas equipped with filter papers are used for filtration. All glassware were dried in an oven at 120 °C for at least 1h before using and are degassed using three argon-vacuum cycles to remove humidity adsorbed on the glass. Argon used is deoxygenated and dehydrated using the system VARIAN. All solvents have been distilled using the system MBRAUN MB SPS-800 and were used without further purification. Sublimation experiments have been conducted in a water cooled sublimator at  $10^{-4}$  mbar using a turbo pump connected to a primary pump.



Figure 7.1 – Vacuum-Schlenk system with Schlenk glassware to work under inert atmosphere.

## 7.1 Characterization methods

### Infrared spectroscopy (FT-IR)

The infrared spectra were obtained on a Bruker Vector 22 FT-IR spectrometer at room temperature and registered from 4000 to 400  $cm^{-1}$ . FT-IR measurements for all air sensitive compounds have been prepared under argon flux between two KBr pallets and using the mineral oil Nujol (dried over 3Å molecular sieve) to form a suspension with the compounds. Organic ligands have been measured without Nujol as neat liquid films.

### Nuclear magnetic resonance (NMR)

$^1H$ ,  $^{13}C$  and  $^{27}Al$  spectra were obtained at 250 MHz on a BRUKER AVANCE HD 250 in  $C_6D_6$  and  $CDCl_3$  at 20 °C or at 400MHz on a BRUKER AVANCE HD 400 in  $C_6D_6$  and  $CDCl_3$  at 20 °C. NMR tubes have been kept in the oven at 120 °C prior to use. Samples have been prepared under a flux of argon. Deuterated solvents have been dried under 3Å molecular sieves and are stored at room temperature in a tightly closed ampule and are opened under argon.

### Thermogravimetric analysis (TGA)

TGA experiments were performed with a TGA/DSC 1 STARe System from Mettler Toledo. Around 2-15mg samples were heated under argon atmosphere at atmospheric pressure at a heating rate of 5 °C/min. The mass loss of the samples has been measured *via* a highly sensitive microbalance. Air sensitive samples for TGA were sealed in a 100ml aluminium crucibles in the glovebox. Fitting of the curves was done using

origin software in order to determine the volatility and thermal stability of the studied compounds.

### Electrochemical measurements

Electrochemical measurements were performed using an AMEL 7050 all-in-one potentiostat, using a standard three-electrode setup with a glassy carbon working disc electrode (diameter 3 mm), a platinum wire auxiliary electrode and a colomel standard electrode. The solutions were degassed with Argon gas and kept under this atmosphere during the electrochemical measurements. The complex solution in THF was 1 or 2 mM in the supporting electrolyte of 0.1 M (*n*-Bu<sub>4</sub>N)PF<sub>6</sub>. Under these experimental conditions, the ferrocene/ferricinium couple was used as an internal reference for potential measurements.

### Transmission electron microscopy (TEM)

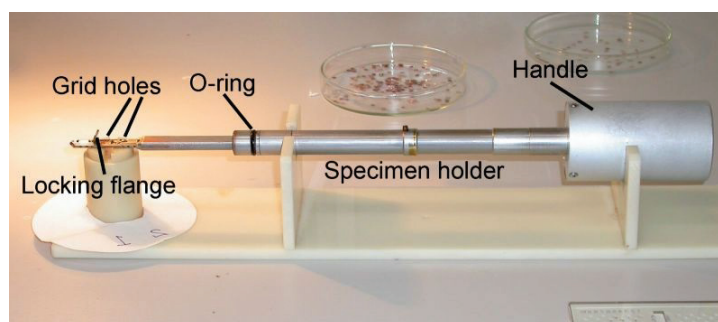


Figure 7.2 – TEM shuttle sample holder.

TEM experiments have been performed using a JEM-2100F with 200kV field emission (FE) and JEOL 2010 LaB6 with 200kV FE. Samples of iron nanoparticles have been prepared in the glovebox by dispersing them in C-4 ionic liquid. A 2 mg sample was dissolved in 1ml of ionic liquid and were deposited on an ultrathin copper grid. Excess of ionic liquid was wiped with a filter paper. The grid was then placed in a tightly closed shutter to protect the iron nanoparticles from air. Samples of Al<sub>13</sub>Fe<sub>4</sub> nanoparticles have been dispersed in ethanol in ambient air before being introduced into the machine.

### Electron paramagnetic resonance (EPR)

EPR experiments were done using X-band spectrometer (Elexys E500 with standard cavity and Bruker EMX plus with double mode cavity) for experiments done at 110K and using EMX double cavity mode, for the low temperature measurements (4.2K).

Microwave power 0.6- 6mW, modulation amplitude 5 G and field modulation 100 kHz were used. Solid state EPR spectra were recorded at -150K. Samples for solid EPR measurements have been prepared in the glovebox. Tubes for EPR in solution were prepared under a flux of argon.

### Mössbauer spectroscopy

The apparatus used for spectra collection was a home-made apparatus described elsewhere [88]. It includes a 100mCi  $^{57}\text{Co}/\text{Rh}$ -ray source and a conventional constant acceleration spectrometer. Samples for Mössbauer measurements were prepared in the glovebox and the sample holder was tightly closed using H60 APIEZON grease to protect from ambient atmosphere. Isomer shifts were given with respect to  $\alpha\text{-Fe}$ . All spectra were taken at room temperature under controlled atmosphere. Integrated areas under individual de-convoluted peaks were used to obtain the relative populations of different iron species, assuming an equal recoil-free fraction for all iron species. The parameters characterizing a Mössbauer spectrum were determined by least-squares fitting and minimizing the  $\chi^2$  quadratic function:

$$\chi^2 = \sum_i \frac{(y_i^{\text{th}} - y_i^{\text{exp}})^2}{y_i^{\text{exp}}} \times \frac{1}{N - K}$$

where N is the number of measured points, K the number of the parameters to be determined,  $y_i^{\text{exp}}$  and  $y_i^{\text{th}}$ , respectively, measured and calculated spectral values in velocity for each point i. The calculations were made using pure Lorentzian functions.

### X-ray photoelectron spectroscopy (XPS)

XPS is a quantitative surface analysis technique that measures the elemental composition of a surface with a depth of few tens of Å. XPS spectra were obtained by exposing a sample under vacuum ( $10^{-8}$  mbar) to X-ray beam which results in the emission of electrons from the surface of the sample. The kinetic energy of the emitted electrons is measured according to the formula:  $KE = h\nu - BE$ . The position of the peak in the spectra allows the determination of the elements present. The intensity of the peak is related to its concentration. Air sensitive samples were prepared in the glovebox and were placed inside the air tight shutter sample holder shown in Figure 7.3 which is in turn attached to the XPS machine. A simple rotation of the tap at the top right of the sample holder allows the introduction of samples into the XPS chamber without contact to ambient atmosphere.



Figure 7.3 – XPS shuttle sample holder.

### Powder X-Ray diffraction

Powder XRD patterns have been measured on a Bruker diffractometer D8A25. Air sensitive powder has been crushed slowly inside a glovebox to avoid heating the sample due to friction and consequently oxidizing it. The powder was then placed in a sample holder equipped with a kapton films to avoid exposure to ambient atmosphere as shown in Figure 7.4.



Figure 7.4 – X-ray sample holder equipped with a kapton film.

### Single crystal X-ray diffraction

A Suitable crystal was mounted on a Gemini kappa-geometry diffractometer (Agilent Technologies UK Ltd) equipped with an Atlas CCD detector and using Mo radiation ( $\lambda = 0.71073 \text{ \AA}$ ). Intensities were collected at 150 K by means of the CrysAlisPro software. Reflection indexing, unit-cell parameters refinement, Lorentz-polarization correction, peak integration and background determination were carried out with the CrysAlisPro software [84]. An analytical absorption correction was applied using the modeled faces of the crystal [89]. The resulting set of hkl was used for structure solution and refinement. The structures were solved by direct methods with SIR97 [90] and the least-square refinement on F2 was achieved with the CRYSTALS software [91].

All non-hydrogen atoms were refined anisotropically. The hydrogen atoms were all located in a difference map, but those attached to carbon atoms were repositioned geometrically. The H atoms were initially refined with soft restraints on the bond lengths and angles to regularize their geometry (C-H in the range 0.93-0.98, N-H in the range 0.86-0.89 and O-H = 0.82 (Å) and Uiso(H) (in the range 1.2-1.5 times Ueq of the parent atom), after which the positions were refined with riding constraints. The crystallographic and refinement data of the compounds **1**, **3-7** and **16** are given in table 7.1.

Table 7.1 – Crystallographic and refinement data for complexes **1**, **3**, **4**, **5**, **6**, **7** and **16**.

Compound	<b>1</b>	<b>3</b>	<b>4</b>	<b>5</b>	<b>6</b>	<b>7</b>	<b>16</b>
Empirical formula	$C_{24}H_{56}Fe_2N_{12}$	$C_{32}H_{72}Fe_2N_{12}$	$C_{18}H_{44}FeN_8$	$C_{22}H_{52}FeN_8$	$C_{20}H_{48}FeN_8$	$C_{22}H_{52}FeN_8$	$C_{20}H_{48}N_8Ti$
Formula weight	624.5	736.7	428.4	484.6	456.5	484.6	448.55
Crystal system	Orthorhombic	Monoclinic	Orthorhombic	Orthorhombic	Monoclinic	Monoclinic	Monoclinic
Space group	<i>Pccn</i>	<i>C2/c</i>	<i>Pna21</i>	<i>P21212</i>	<i>C2/c</i>	<i>C2/c</i>	<i>C2/c</i>
a (Å)	12.142(2)	19.116(2)	17.6602(3)	19.647(1)	9.865(1)	9.6188(2)	11.8280 (5)
b (Å)	12.407(3)	11.7866(8)	8.9362(2)	16.484(2)	16.262(2)	16.6011(2)	14.8086 (6)
c (Å)	21.375(3)	21.137(2)	15.8756(3)	8.9926(9)	16.402(2)	18.2778(3)	15.4402 (6)
$\alpha$ (°)	90	90	90	90	90	90	90
$\beta$ (°)	90	120.91(2)	90	90	92.28(1)	98.136(2)	96.261 (4)
$\gamma$ (°)	90	90	90	90	90	90	90
V (Å <sup>3</sup> )	3220(10)	4086(11)	2505.4(8)	2912.4(5)	2629.2(5)	2889.3(9)	2688.32 (19)
Z	4	4	4	4	4	4	4
$\mu$ (mm <sup>-1</sup> )	0.94	0.75	0.62	4.31	0.59	0.54	0.34
Temperature (K)	150	100	150	250	100	150	150
Measured reflections	4016	43003	33283	34851	18348	19548	12408
Independent reflections ( $R_{int}$ )	4015(0.065)	5396 (0.065)	6225	5157 (0.095)	3370 (0.056)	3556 (0.027)	3252 (0.031)
Data/restraints/parameters	3962/0/173	5387/0/208	6216/521/381	5125/334/281	3366/0/133	3552/0/141	3247/0/132
Goodness of fit	1.02	1.02	0.96	1.03	0.96	0.98	0.96
$R[F^2 > 2\sigma(F^2)]$	0.205	0.052	0.059	0.115	0.049	0.039	0.037
$wR(F^2)$	0.171	0.159	0.127	0.253	0.101	0.065	0.060
Residual electron density (e.Å <sup>-3</sup> )	-1.27 to 1.04	-1.15 to 0.80	-0.59 to 0.65	-0.70 to 0.92	-0.74 to 0.59	-0.45 to 0.66	-0.34 to 0.36

## 7.2 Synthesis of the compounds

All experiments have been performed under argon using Schlenk techniques. Anhydrous  $FeCl_2$ , bis(dimethylphosphosphino ethane) (*dmpe*), 1M Trimethylphosphine in anhydrous *THF* ( $PMe_3$ ), *sodiumborohydride* ( $NaBH_4$ ) and lithium aluminium hydride ( $LiAlH_4$ ), are purchased from Sigma-Aldrich and used without further purification. 2M solution of  $Al_2(CH_3)_6$  in anhydrous hexane was purchased from Sigma-Aldrich and used without further purification. Pyridine was purchased from sigma Aldrich and dried on 4Å molecular sieves.  $AlH_3(NMe_2Et)$  was freshly synthesized according to a previously reported method [92].  $Ta(NMe_2)_5$ ,  $Ti(NMe_2)_4$  and

$Nb(NMe_2)_5$  were purchased from Sigma Aldrich and were used without further purification.

### $[H_2Fe(PMe_3)_4]$

To 0.833g (6.57 mmol) of anhydrous  $FeCl_2$  in 40ml anhydrous ethanol was added 40ml (40 mol) of  $PMe_3$  in anhydrous  $THF$  and the green solution turned violet instantly and left stirring at room temperature for 1h. 0.748 g (19.77 mmol) of  $NaBH_4$  in 15 ml of anhydrous ethanol was added to the solution and stirred for 2.5h. Solvents and volatile materials were removed under vacuum to give a brown solid that was extracted with dry hexane and the orange filtrate was dried under vacuum to give an orange solid. Clear yellow crystals were obtained [m= 1.07g, yield = 45% /  $FeCl_2$ ].

Soluble in pentane, hexane, toluene.

Anal.: calcd for  $C_{12}H_{38}P_4Fe$  (M= 362.17  $g.mol^{-1}$ ): C 39.76, H 10.49, P 34,20; found C 39.16, H 10.01, P 34.76%.

FT-IR (Nujol,  $cm^{-1}$ ) 2377 m, 1440 s, 1376 s, 1294 m, 1194 m, 966 s, 719m.

### $[FeH_2(BH_3)(dmpe)_2]$

1 g (7.88 mmol) of  $FeCl_2$  dissolved in 7ml of anhydrous  $THF$  and stirred for 1h. Solvent was then removed under vacuum and the resulting solid was suspended in 30ml of Toluene and to it was added 1ml (6 mmol) of  $dmpe$  and the resulting purple green suspension was stirred for 2h. The resulting mixture was filtered and washed with toluene. The solvent was removed to give a green solid which was dissolved in 30 ml of  $THF$  and added to a stirred suspension of 0.462 g (12.2 mmol) of  $NaBH_4$  in 50 ml of  $THF$  via cannula and the yellowish mixture was stirred for 2 h. Solvent and volatile materials were removed under vacuum and the residue was extracted with pentane and the yellow filtrate was concentrated and kept at 3°C to form orange crystals.[m= 1.43g, yield = 49% /  $FeCl_2$ ].

Soluble in pentane, hexane, toluene.

Anal.: calcd for  $C_{12}H_{37}BP_4Fe$  (M= 371.96  $g.mol^{-1}$ ): C 38.71, H 9.95, B 2.91, P 33,30; found C 38.55, H 9.84, B 2.83, P 33.02%.

FT-IR (Nujol,  $cm^{-1}$ ) 2344 w (terminal B-H stretch), 2047 w (bridging Fe-H stretch), 1804 w (terminal Fe-H, 1460 m, 1365 m, 1270 w, 1052 w, 932 m, 724 w.

### $[H_2Fe(dmpe)_2]$

Similarly, 1 g (7.88 mmol) of  $FeCl_2$  was dissolved in 7ml of anhydrous  $THF$  and stirred for 1h. Solvent was then removed under vacuum and the resulting solid was suspended in 30ml of Toluene and to it was added 1ml (6 mmol) of  $dmpe$  and the resulting purple green suspension was stirred for 2h. The resulting mixture was filtered and washed with toluene. The solvent was removed to give a green solid which was dissolved in 30 ml of  $THF$  and added to a stirred suspension of 0.462 g (12.2 mmol) of  $LiAlH_4$  in 50 ml of  $THF$  via cannula and the grey mixture stirred for 2 h. Solvent and volatile materials removed under vacuum and the residue was extracted with pentane. Solvents from the light yellow filtrate were removed under vacuum to yield a white solid that was crystallized from pentane. [m= 0.25g, yield = 9% /  $FeCl_2$ ].

Soluble in pentane, hexane, toluene.

Anal.: calcd for  $C_{12}H_{34}P_4Fe$  (M= 358.13  $g.mol^{-1}$ ): C 40.20, H 9.49, P 34.59; found C 39.97, H 9.42, P 34.09%.

FT-IR (Nujol,  $cm^{-1}$ ) 1780 m (terminal Fe-H stretch), 1466 s, 1370 s, 1275 w, 1050 w, 916 s, 875 w, 815 w.

### *Tert*-butyl azide ( $tBuN_3$ )

*Tert*-butyl azide was synthesized according to the published procedure [93]. In brief, a solution of 220 g of  $H_2SO_4$  in 220 g of  $H_2O$  was prepared by the slow addition of the acid to the water at 0°C with strong agitation. While maintaining the temperature < 5°C, 14.4 g of  $NaN_3$  was added slowly. Once the sodium azide dissolved, 14.8 g of *tert*-butanol was added and the resulting solution was stirred for 5min. The solution was let to stand for 24h at room temperature, stirred for 5 min and let to stand for further 6h. The organic layer which floats above the aqueous layer was separated and extracted with 2M NaOH to remove all traces of  $HN_3$ , dried over  $Na_2SO_4$  and decanted in a bottle for long term storage. [m= 28g, yield = 70% / *tert*-butanol].

Soluble in pentane, hexane, toluene.

Anal.: calcd for  $C_4H_9N_3$  (M= 99.14  $g.mol^{-1}$ ): C 48.42, H 9.07, N 42.36; found C 48.59, H 9.17, N 42.21%.

FT-IR (neat liquid film,  $cm^{-1}$ ) 2961 s, 2870 s, 2860 w, 1678 s, 1617 s, 1568 m, 1515 s, 1391 m, 1280 s, 1144 s, 1078 s, 1013 m, 805 m, 670 m, 560 m.

$^1HNMR$  ( $CDCl_3$ , 23°C, ppm) 1.12 (s, 9H,  $C(CH_3)_3$ ).

$^{13}C$  ( $CDCl_3$ , 23°C, ppm) 29.92 ( $C(CH_3)_3$ ), 55.87 (N- $C(CH_3)_3$ ).

**(1,tert-butyl-3-ethyltriazeno)  $HN_3^tBuEt$  (L1)**

31 ml (62mmol) of EtMgCl in  $Et_2O$  was added dropwise *via* cannula to a stirred solution of 6.934 g (48.75 mmol) of the precursor  $^tBuN_3$  in 40  $Et_2O$  at 0°C and the solution was left stirring at room temperature for 3h. The yellow solution was then hydrolyzed at 0°C with a solution of 10%  $NH_4OH$ -10%  $NH_4Cl$  to give a white precipitate and a yellow solution. The organic phase was then separated and dried with  $Na_2SO_4$ . Ether was then removed under vacuum to give a yellowish solution which was fractionally distilled under vacuum to give a colourless liquid. [m= 4.88g, yield = 78% /  $^tBuN_3$ ]. Soluble in pentane, hexane, toluene.

Anal.: calcd for  $C_6H_{15}N_3$  (M= 129.13  $g.mol^{-1}$ ): C 55.75, H 11.61, N 32.52; found C 55.62, H 11.73, N 32.43%.

FT-IR (neat liquid film,  $cm^{-1}$ ) 3283 broad (N-H stretching), 2970 s, 2930 m, 2870 w, 1512 m, 1463 m, 1360 m, 1214 m, 1170 m, 1022 w, 690 w, 560 w.

$^1HNMR$ ( $CDCl_3$ , 23°C, ppm) 1.18 (t, 3H,  $CH_3$ ,  $J=7.31$  Hz), 1.22 (s, 9H,  $C(CH_3)_3$ ), 3.48 (q, 2H, N- $CH_2$ ,  $J=7.30$  Hz), 6.89 (broad s, NH).

$^{13}CNMR$  ( $CDCl_3$ , 23°C, ppm) 13.79 ( $CH_3$ ), 28.65 ( $C(CH_3)_3$ ), 31.15 (N- $CH_2$ ), 55.83 ( $C(CH_3)_3$ ).

E.S.I.M.S m/z= 130.13 (M+H), 102.12, 74.09.

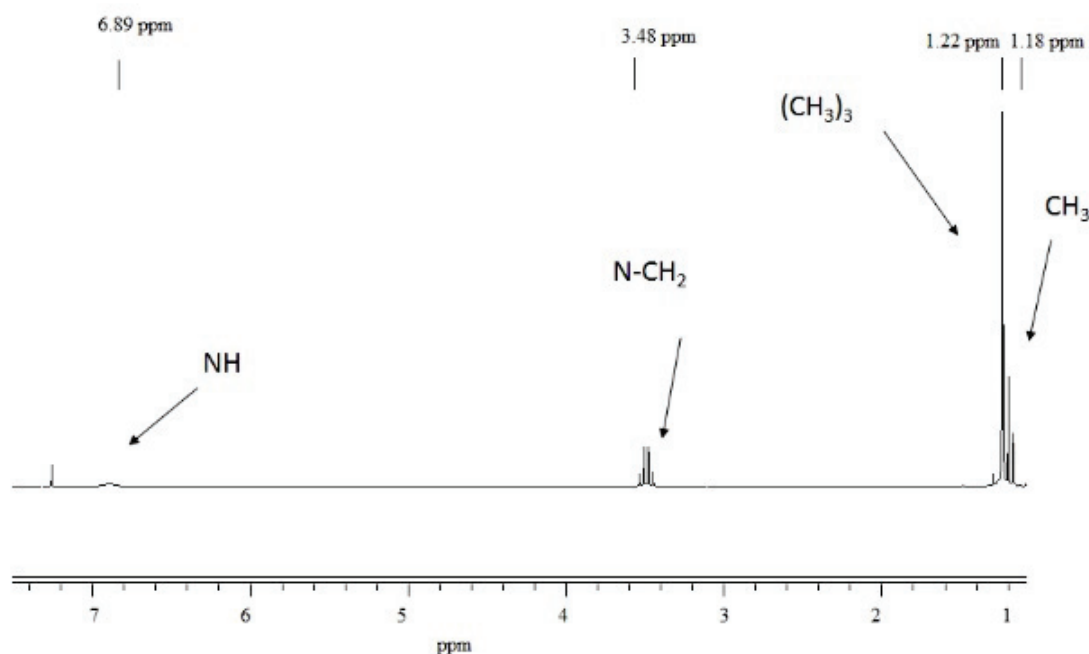


Figure 7.5 –  $^1H$  NMR spectrum of (L1).

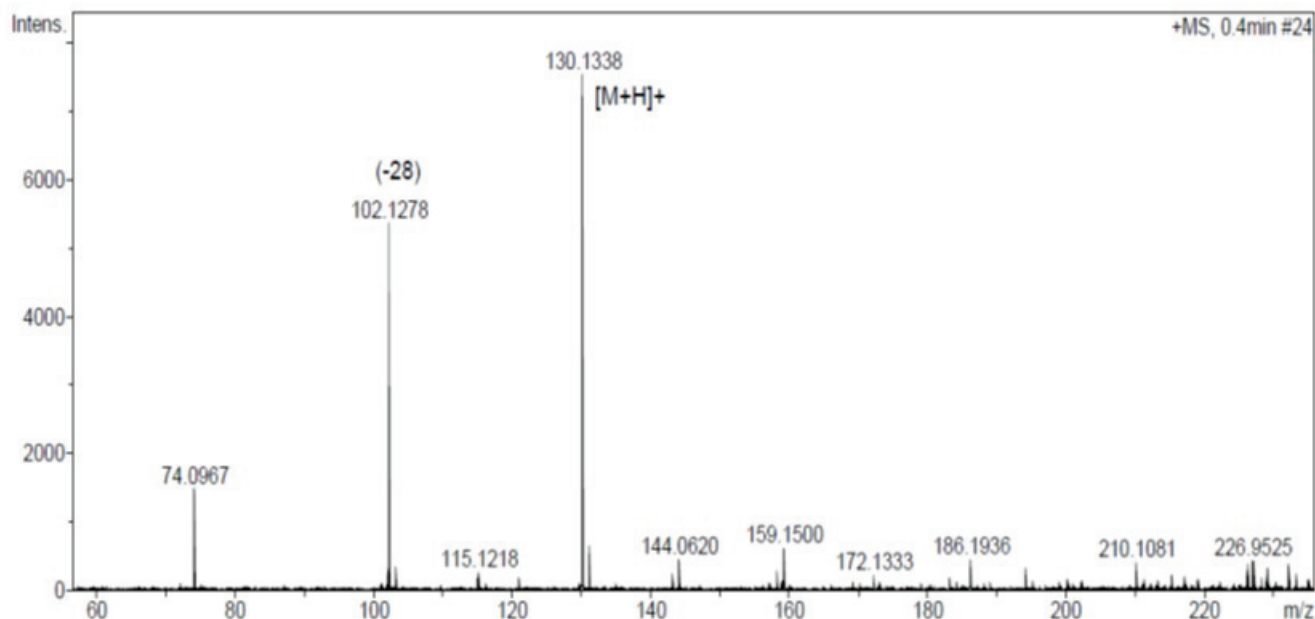


Figure 7.6 – Mass spectrum of (L1).

**(1,tert-butyl-3-iso-propyltriazeno)  $HN_3^tBu^iPr$  (L2)**

In a fashion similar to the preparation of (L1), 55ml (110mmol) of  $^iPrMgCl$  and 8.68g (87.5mmol) of  $^tBuN_3$  were reacted in  $Et_2O$  to afford a colourless liquid. [m= 2.56 g, yield = 20% /  $^tBuN_3$ ].

Soluble in pentane, hexane, toluene.

Anal.: calcd for  $C_7H_{17}N_3$  (M= 143.15  $g.mol^{-1}$ ): C 58.60, H 11.87, N 29.33; found C 58.78, H 11.94, N 29.14%.

FT-IR (neat liquid film,  $cm^{-1}$ ) 3248 broad (N-H stretching), 2976 s, 2930 m, 2860 m, 1506 s, 1450 m, 1360 s, 1220 s, 1173 m, 1036 w, 700 w, 593 w.

$^1HNMR$  ( $CDCl_3$ , 23°C, ppm) 1.05 (d, 6H,  $(CH_3)_2$   $J=6.41$  Hz), 1.19 (s, 9H,  $C(CH_3)_3$ ), 3.79 (septet, 1H, N-CH,  $J=6.49$  Hz), 6.66 (broad s, NH).

$^{13}CNMR$  ( $CDCl_3$ , 23°C, ppm) 22.08  $(CH_3)_2$ , 28.96  $(C(CH_3)_3)$ , 32.53 (N-CH), 57.73  $(C(CH_3)_3)$ .

E.S.I.M.S m/z= 144.14 (M+H), 116.14, 102.12.

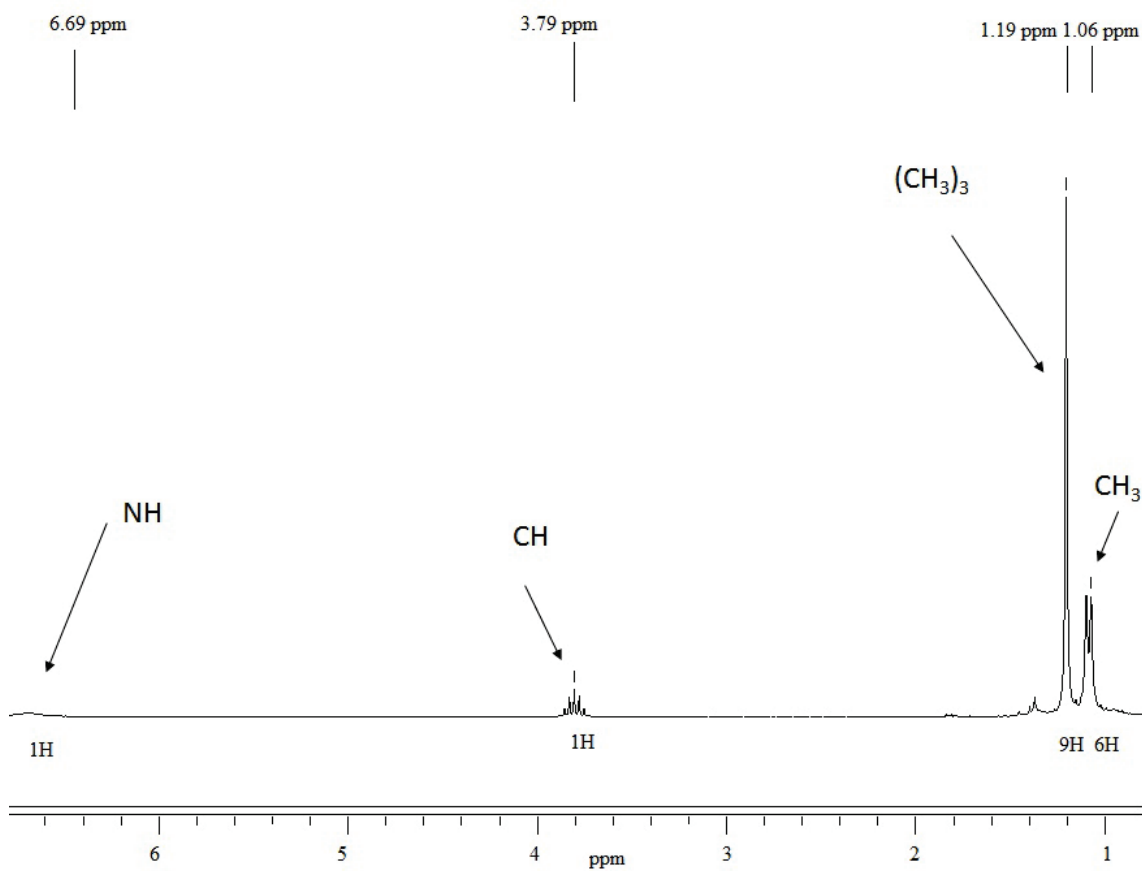
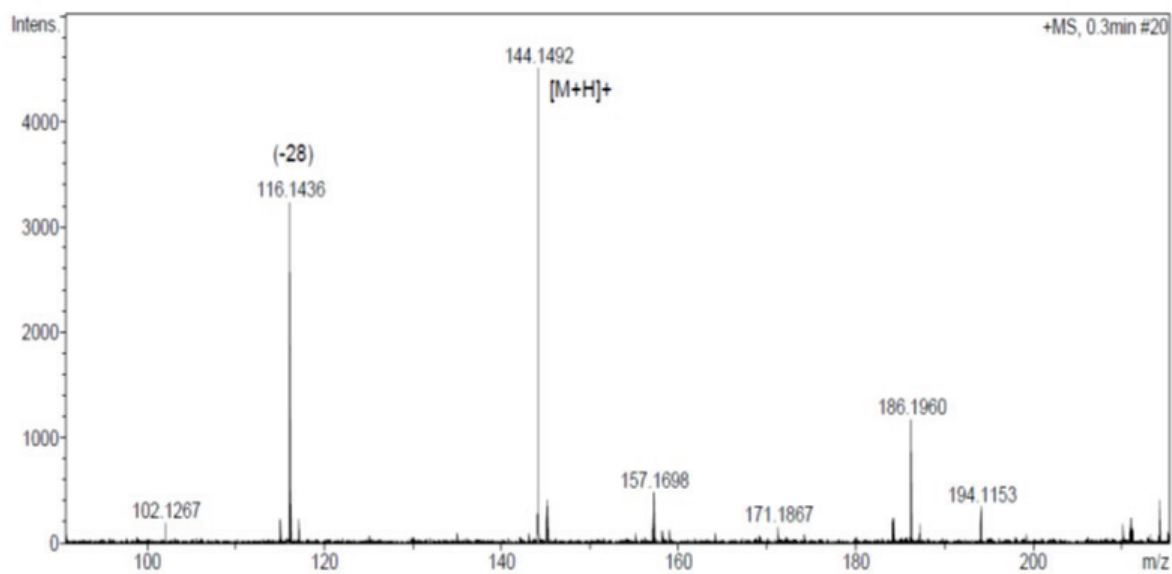
Figure 7.7 –  $^1\text{H}$  NMR spectrum of (L2).

Figure 7.8 – Mass spectrum of (L2).

**(1, butyl-3-*tert*-butyltriazeno)  $HN_3^tBu^nBu$  (L3)**

Similarly,  $HN_3^tBu^nBu$  was prepared by reacting 48 ml (48 mmol) of BuLi with 4.76 g (48 mmol)  $^tBuN_3$  in hexane. The crude yellow solution was fractionally distilled under vacuum at 50°C to give a colourless liquid. [m= 4.23 g, yield = 56% /  $^tBuN_3$ ].

Soluble in pentane, hexane, toluene.

Anal.: calcd for  $C_8H_{19}N_3$  (M= 157.17  $g.mol^{-1}$ ): C 61.08, H 12.08, N 26.72; found C 61.21, H 12.11, N 26.62%.

FT-IR (neat liquid film,  $cm^{-1}$ ) 3278 broad (N-H stretching), 2970 s, 2924 s, 2870 m, 1704 w, 1512 s, 1450 s, 1365 m, 1224 s, 1164 s, 1017 w, 740 w, 563 w.

$^1HNMR$  ( $CDCl_3$ , 23°C, ppm) 0.66 (t, 3H,  $CH_3$ ,  $J= 7.01$  Hz), 1.05 (broad, 2H,  $CH_2$ ), 1.11 (s, 9H,  $C(CH_3)_3$ ), 1.18 (broad, 2H,  $CH_2$ ), 3.3 (broad, 2H,  $N-CH_2$ ), 6.74 (broad s, 1H, NH).

$^{13}CNMR$  ( $CDCl_3$ , 23°C, ppm) 13.37 ( $CH_3$ ), 13.52 ( $CH_2$ ), 20.15 ( $CH_2$ ), 28.33 ( $N-CH_2$ ), 28.15 ( $C(CH_3)_3$ ), 56.32 ( $C(CH_3)_3$ ).

E.S.I.M.S  $m/z= 186.22$  (+28), 144.14 (M+H), 116.14, 130.15, 115.03, 74.09.

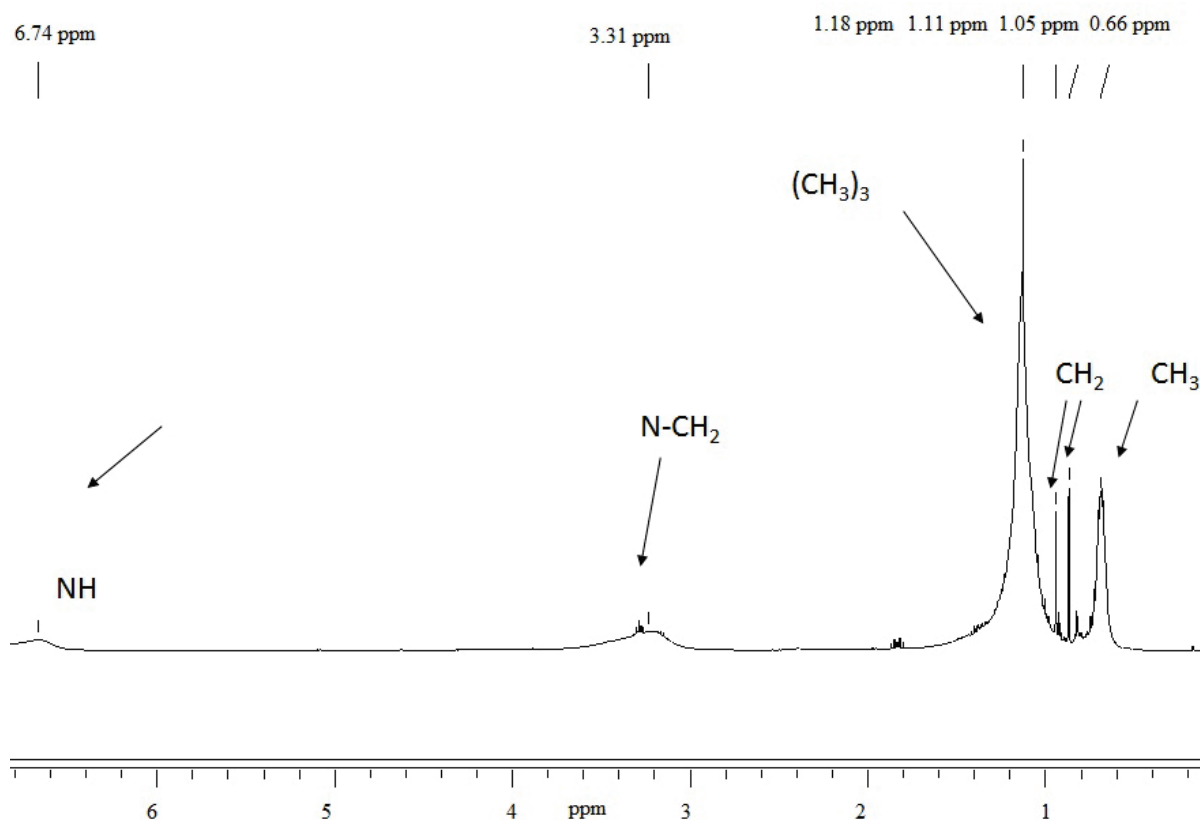


Figure 7.9 –  $^1H$  NMR spectrum of (L3).

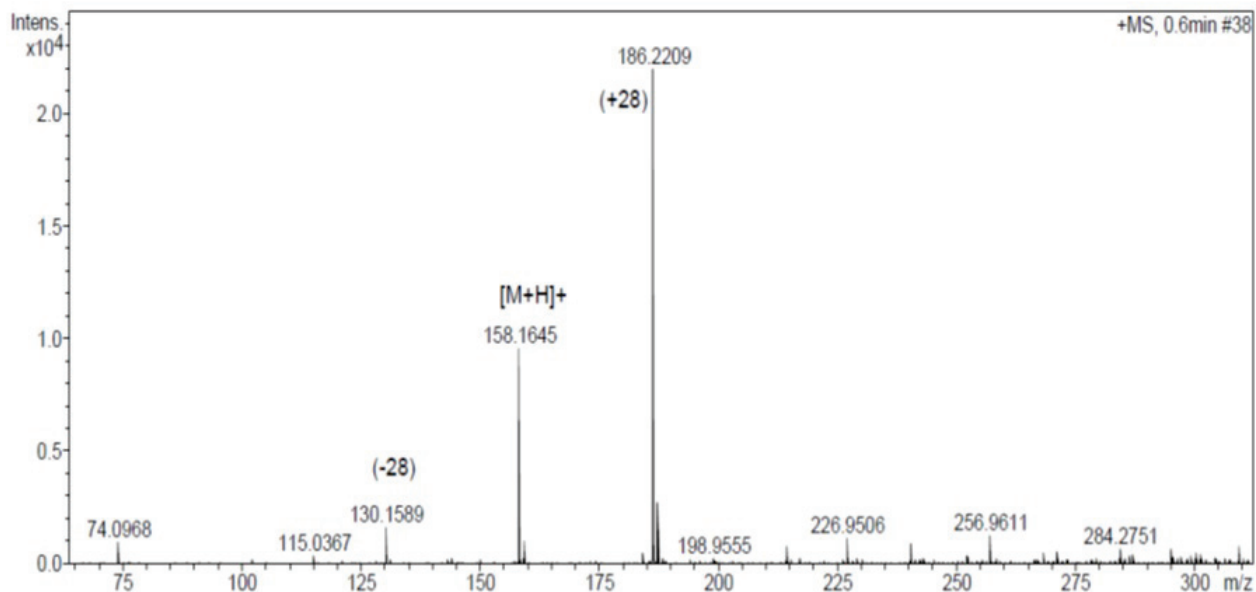


Figure 7.10 – Mass spectrum of (L3).

**(1,3-ditert-butyltriazene)  $HN_3^tBu_2$  (L4)**

Similarly, (L4) was prepared by reacting 52 ml (52 mmol) of  $tBuLi$  with 5.15 g (52 mmol)  $tBuN_3$  in hexane. The crude yellow solution was fractionally distilled under vacuum at 50°C to give a colourless liquid. [m= 6.12 g, yield = 75% /  $tBuN_3$ ].

Soluble in pentane, hexane, toluene.

Anal.: calcd for  $C_8H_{19}N_3$  (M= 157.17  $g.mol^{-1}$ ): C 61.08, H 12.08, N 26.72; found C 61.17, H 12.14, N 26.87%.

FT-IR (neat liquid film,  $cm^{-1}$ ) 3233 broad (N-H stretching), 2970 s, 2920 s, 2869 m, 2284 w, 2117 w, 2087 w, 1724 w, 1512 s, 1471 s, 1385 m, 1370 s, 1209 s, 1133 s, 1027 m, 932 w, 694 w, 599 m.

$^1HNMR$  ( $CDCl_3$ , 23°C, ppm) 1.15 ((s, 18H,  $C(CH_3)_3$ ), 6.72 (broad s, 1H, NH).

$^{13}CNMR$  ( $CDCl_3$ , 23°C, ppm) 14.026 ( $C(CH_3)$ ), 28.72 ( $C(CH_3)$ ).

E.S.I.M.S m/z= 157.17 (M+), 114.12, 86.07, 74.09, 57.07, 41.09.

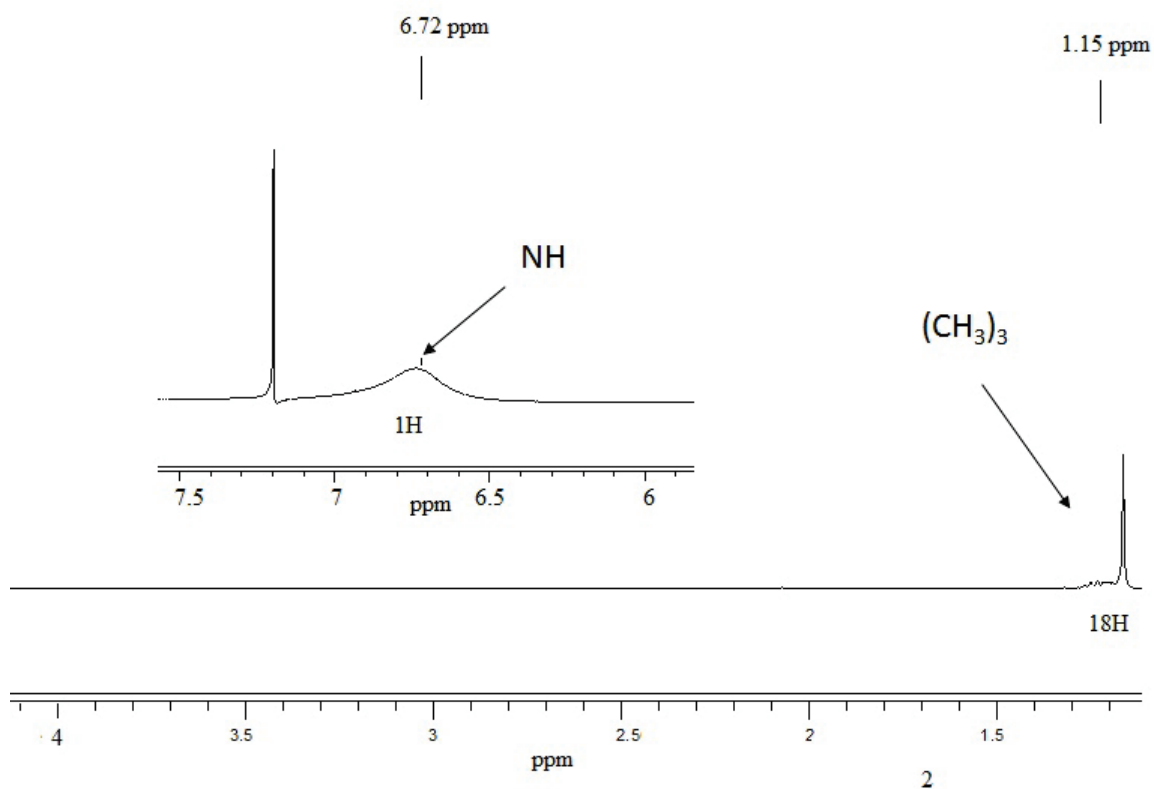
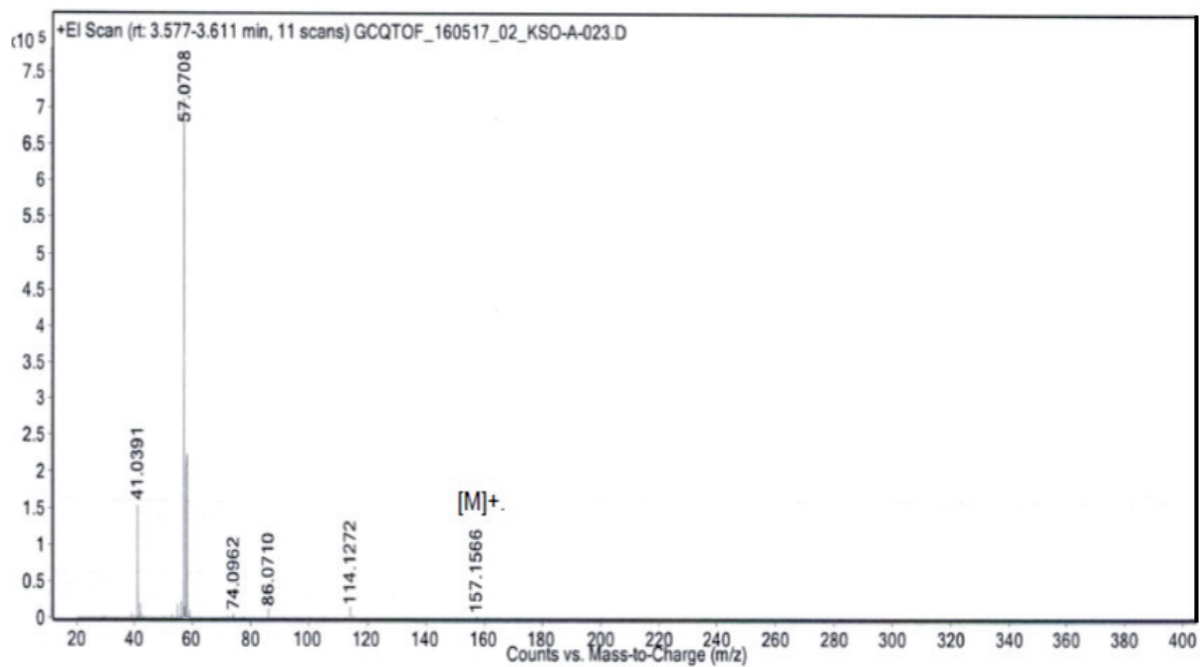
Figure 7.11 – <sup>1</sup>H NMR spectrum of (L4).

Figure 7.12 – Mass spectrum of (L4).

### Synthesis of $[Fe_2\{N_3^tBuR'\}_4]$ complexes

In a typical complexation reaction, two equivalents of the triazenide ligand was added at 0°C to a pre-stirred solution of the Fe(II) amide precursor and the temperature was let to increase gradually to room temperature and the dark brown solution was stirred overnight. Solvents and volatile materials were removed under vacuum to give a dark brown residue. Brown crystals of the complex were obtained by crystallization in dry hexane at -20°C.

Iron bis(trimethylsilyl)amide  $[Fe\{N(SiMe_3)_2\}_2]$  which is more reactive than the corresponding metal halide was used as the iron source in the iron coordination complexes to triazenide ligands. These amides react cleanly with protonated ligands to give the corresponding metal complexes.  $[Fe\{N(SiMe_3)_2\}_2]$  was prepared according to the published procedure [94].

#### $[Fe\{N(SiMe_3)_2\}_2]$

10.13g (62.8mmol) of  $HN[(SiMe_3)_2]_2$  dissolved in 80ml  $Et_2O$  was stirred and kept 0°C. 19.2ml (48mmol) of BuLi was added to give a turbid white solution which was stirred at room temperature for 2h. This suspension was warmed to 40°C and added *via* cannula to a suspension of  $FeCl_2$  in  $Et_2O$  and stirred at 0°C for 12h. The green solution was then filtered and the green filtrate was dried under vacuum to give a green oil to which was added dry hexane and stirred at room temperature for 3h. The solution was then filtered to leave a white solid (LiCl) and the filtrate dried under vacuum to give green oil which was distilled under vacuum (dieckmann distillation) at 125°C-135°C oil bath temperature to give a green oil. [m= 4.33 g, yield = 48 % /  $FeCl_2$ ].

Soluble in pentane, hexane, toluene.

Anal.: calcd for  $C_{12}H_{36}N_2Si_4Fe$  (M= 376.61  $g.mol^{-1}$ ): C 38.23, H 9.55, N 7.43, Si 29.73; found C 38.34, H 9.68, N 7.38, Si 29.84%.

FT-IR (Nujol,  $cm^{-1}$ ) 1250 s, 1240 s, 1175 w, 1020 m, 990 s, 970 s, 845 s, 825 s, 783 m, 745 m, 700 w, 657 m, 628 w, 605 m, 355 s.

#### Bis(1-*tert*-butyl, 3-ethyl triazenido) iron(II) $[Fe_2(N_3^tBuEt)_4]$ (1)

To a pre-stirred solution of 0.891g (2.36mmol) of  $[Fe\{N(SiMe_3)_2\}_2]$  in dry hexane was added at 0°C 0.673g (4.72mmol) of  $HN_3^tBuEt$  in anhydrous hexane *via* cannula. The temperature was allowed to increase gradually to room temperature and the dark brown residue was stirred for 18h. Volatile materials were removed under vacuum. Brown crystals of the complex were obtained by crystallization in anhydrous hexane

at  $-20^{\circ}\text{C}$ . [ $m = 0.792\text{g}$ , yield = 54% /  $[\text{Fe}\{\text{N}(\text{SiMe}_3)_2\}_2]$ ].

Soluble in pentane, hexane, toluene.

Anal.: calcd for  $\text{C}_{24}\text{H}_{56}\text{N}_{12}\text{Fe}_2$  ( $M = 624.47\text{ g.mol}^{-1}$ ): C 46.12, H 8.96, N 26.90; found C 46.21, H 9.06, N 26.82%.

FT-IR (Nujol,  $\text{cm}^{-1}$ ) 1678 w, 1516 m, 1461 m, 1375 m, 1305 m, 1203 w, 1078 w, 1017 w, 972 w.

### Bis(1- *tert*-butyl, 3- *iso*-propyl triazenido) iron(II) $[\text{Fe}_2(\text{N}_3^t\text{Bu}^i\text{Pr})_4]$ (2)

In a fashion similar to the preparation of (1), 0.859g (2.47 mmol) of  $[\text{Fe}\{\text{N}(\text{SiMe}_3)_2\}_2]$  was reacted with 0.78g (4.95 mmol) of  $\text{HN}_3^t\text{Bu}^i\text{Pr}$  in anhydrous hexane. Brown crystals of the complex were obtained by crystallization in anhydrous hexane at  $-20^{\circ}\text{C}$ . [ $m = 1.12\text{ g}$ , yield = 67% /  $[\text{Fe}\{\text{N}(\text{SiMe}_3)_2\}_2]$ ].

Soluble in pentane, hexane, toluene.

Anal.: calcd for  $\text{C}_{28}\text{H}_{58}\text{N}_{12}\text{Fe}_2$  ( $M = 674.53\text{ g.mol}^{-1}$ ): C 49.81, H 8.59, N 24.90; found C 49.93, H 8.68, N 24.82%.

FT-IR (Nujol,  $\text{cm}^{-1}$ ) 1451 m, 1355 m, 1241 s, 1200 m, 1108 m, 1032 m, 992 s, 840 s, 674 m, 613 w, 553 w.

### Bis(1-butyl, 3-*tert*-butyl triazenido) iron(II) $[\text{Fe}_2(\text{N}_3^t\text{Bu}^n\text{Bu})_4]$ (3)

Similarly, (3) was prepared by reacting 0.832g (2.21mmol) of  $[\text{Fe}\{\text{N}(\text{SiMe}_3)_2\}_2]$  with 0.570g (5.17mmol) of  $\text{HN}_3^t\text{Bu}^n\text{Bu}$  in anhydrous hexane. Brown crystals of the complex were obtained by crystallization in anhydrous hexane at  $-20^{\circ}\text{C}$ . [ $m = 1.60\text{ g}$ , yield = 61% /  $[\text{Fe}\{\text{N}(\text{SiMe}_3)_2\}_2]$ ].

Soluble in pentane, hexane, toluene.

Anal.: calcd for  $\text{C}_{32}\text{H}_{60}\text{N}_{12}\text{Fe}_2$  ( $M = 724.58\text{ g.mol}^{-1}$ ): C 52.99, H 8.28, N 28.13; found C 43.09, H 8.19, N 28.03%.

FT-IR (Nujol,  $\text{cm}^{-1}$ ) 1673 w, 1512 m, 1456 s, 1388 s, 1300 m, 1265 m, 1209 m, 1027 w, 734 w, 660 w, 580 w.

### Synthesis of the $[\text{Fe}(\text{N}_3^t\text{BuR}')_2(\text{TMEDA})]$

#### Bis(1-*tert*-butyl, 3- ethyl triazenido) (tetramethylethyline diamino) iron(II) $[\text{Fe}(\text{N}_3^t\text{BuEt})_2(\text{TMEDA})]$ (4)

To a stirred solution of 0.974g (2.58mmol) of  $[\text{Fe}\{\text{N}(\text{SiMe}_3)_2\}_2]$  in dry hexane was added at  $0^{\circ}\text{C}$  0.814g (5.17mmol) of  $\text{HN}_3^t\text{BuEt}$  in anhydrous hexane *via* cannula. Then 0.4ml (2.6 mmol) of N, N, N', N'-Tetramethylethylenediamine (TMEDA) was added.

The temperature was allowed to increase gradually to room temperature and the dark brown residue was stirred for 6h. Volatile materials were removed under vacuum to give a dark brown residue. Brown crystals of the complex were obtained by crystallization in dry hexane at  $-20^{\circ}\text{C}$ . [m= 0.53 g, yield = 48% /  $[\text{Fe}\{\text{N}(\text{SiMe}_3)_2\}_2]$ ].

Soluble in pentane, hexane, toluene.

Anal.: calcd for  $\text{C}_{18}\text{H}_{44}\text{N}_8\text{Fe}$  (M=428.44  $\text{g}\cdot\text{mol}^{-1}$ ): C 50.41, H 10.26, N 26.14; found C 50.53, H 10.35, N 26.22%.

The complex was paramagnetic and showed broad signals in the  $^1\text{HNMR}$  spectrum in  $\text{CDCl}_3$ .

FT-IR (Nujol,  $\text{cm}^{-1}$ ) 1673 w, 1461 s, 1381 m, 1345 s, 1280 s, 1203 s, 1170 m, 1068 w, 1032 m, 952 m, 800m, 725 w, 610 m, 563 w.

### **Bis(1- *tert*-butyl, 3- *iso*-propyl triazenido) (tetramethylethyline diamino) iron(II) [ $\text{Fe}(\text{N}_3^t\text{Bu}^i\text{Pr})_2(\text{TMEDA})$ ] (5)**

In a similar fashion to the preparation of (4), complex 5 was prepared by reacting 0.938 g (2.48mmol) of  $[\text{Fe}\{\text{N}(\text{SiMe}_3)_2\}_2]$  with 0.705 g (4.96 mmol) of  $\text{HN}_3^t\text{Bu}^i\text{Pr}$  and 0.38 ml (2.48 mmol) of TMEDA in dry hexane (yield= 63%). [m= 0.72 g, yield = 63% /  $[\text{Fe}\{\text{N}(\text{SiMe}_3)_2\}_2]$ ].

Soluble in pentane, hexane, toluene.

Anal.: calcd for  $\text{C}_{20}\text{H}_{48}\text{N}_8\text{Fe}$  (M=456.49  $\text{g}\cdot\text{mol}^{-1}$ ): C 52.57, H 10.51, N 24.53; found C 52.46, H 10.61, N 24.60%.

FT-IR (Nujol,  $\text{cm}^{-1}$ ) 1684 w, 1512 m, 1466 m, 1360 m, 1265 m, 1220 m, 1150 m, 1103 m, 1027 m, 815 m, 583 w.

### **Bis(1- *tert*-butyl, 3- butyl triazenido) (tetramethylethyline diamino) iron(II) [ $\text{Fe}(\text{N}_3^t\text{Bu}^n\text{Bu})_2(\text{TMEDA})$ ] (6)**

Similarly, (6) was prepared by reacting 0.832g (2.21mmol) of  $[\text{Fe}\{\text{N}(\text{SiMe}_3)_2\}_2]$  in dry hexane at  $0^{\circ}\text{C}$  0.69g (4.42mmol) of  $\text{HN}_3^t\text{Bu}^n\text{Bu}$  and 0.34ml (2.21 mmol) of TMEDA. [m= 0.49g, yield = 46% /  $[\text{Fe}\{\text{N}(\text{SiMe}_3)_2\}_2]$ ].

Soluble in pentane, hexane, toluene.

Anal.: calcd for  $\text{C}_{22}\text{H}_{52}\text{N}_8\text{Fe}$  (M=484.54  $\text{g}\cdot\text{mol}^{-1}$ ): C 54.48, H 10.73, N 23.11; found C 54.57, H 10.78, N 23.02%.

FT-IR (Nujol,  $\text{cm}^{-1}$ ) 1506 w, 1470 s, 1355 s, 1289 s, 1224 s, 1200 s, 1068 m, 1027 m, 946 m, 795 m, 633 w, 578 w, 467 w.

**Bis(1-3 di*tert*-butyl triazenido) (tetramethylethyline diamino) iron(II)**  
 $[Fe(N_3^tBu_2)_2(TMEDA)]$  (7)

Similarly, (7) was prepared by reacting 0.962g (2.55mmol) of  $[Fe\{N(SiMe_3)_2\}_2]$  in dry hexane at 0°C 0.81g (5.17mmol) of  $HN_3^tBu_2$  and 0.40ml (2.55 mmol) of TMEDA. [m= 1.01 g, yield = 82% /  $[Fe\{N(SiMe_3)_2\}_2]$ ].

Soluble in pentane, hexane, toluene.

Anal.: calcd for  $C_{22}H_{52}N_8Fe$  (M=484.54  $g.mol^{-1}$ ): C 54.48, H 10.73, N 23.11; found C 54.41, H 10.67, N 23.18%.

FT-IR (Nujol,  $cm^{-1}$ ) 1459 s, 1375 s, 1257 m, 1180 w, 1089 w, 1005 w, 920 m, 842 m, 718 m.

**Dimethyl ethyl amine alane (DMEAA)  $AlH_3[N(CH_3)_2(CH_2CH_3)]$**

3.77g of  $AlCl_3$  (28.3 mmol) was added to 3.6 g of  $LiAlH_4$  (94.8 mmol) and pentane (100 ml) at 0°C. 12.2 ml of dimethylethylamine  $[(CH_3)_2(CH_2CH_3)]NH$  (112 mmol) was syringed slowly onto the slurry, which was then allowed to warm to room temperature and stirred overnight. The resulting solution was filtered from the light grey precipitate into another vessel and was stored at -40°C for 24 h, affording a white crystalline solid. The Schlenk tube was then placed in a cold ethanol bath at -30°C and the pentane was removed by filtration. The residue was allowed to warm to room temperature, at which point the solid melted to afford a clear colourless liquid. Pentane was added to remove any unreacted dimethylethylamine. The reaction mixture was then cooled to -30 °C and the pentane was removed by filtration once again. Any remaining liquid was removed under vacuum [m= 1.02g, yield = 35% /  $Al_2(CH_3)_6$ ].

Soluble in pentane, hexane, toluene.

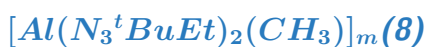
Anal.: calcd for  $C_4H_{14}NAl$  (103.14  $g.mol^{-1}$ ): C 46.54, H 13.57, N 13.57; Not done.

FT-IR (Nujol,  $cm^{-1}$ ) 2979s, 2942m and 2834w ( $\nu C-H$ ); 1771sbr ( $\nu Al-H$ ); 1464w, 1388s ( $C-H$ ); 1237w, 1189w ( $\nu C-H$ ); 1097w, 1028w, 930w, 878w ( $\nu C-N$ ); 751m ( $\nu H-Al-H$ ); 659w ( $\nu H-Al-H$ ).

$^1H$  NMR ( $C_6D_6$ , 23°C, ppm) 0.72 (t, 3H,  $CH_3$ ,  $J = 7.30$  Hz), 1.87 (s, 6H,  $N-CH_3$ ) 2.20 (q, 2H,  $N-CH_2$ ,  $J = 7.30$  Hz), 4.13 (br, 3H,  $AlH_3$ )

$^{13}C$  NMR ( $C_6D_6$ , 23°C, ppm) 9.86 ( $N-CH_3$ ), 44.93 ( $CH_3$ ), 54.65 ( $N-CH_2$ ).

$^{27}Al$  NMR ( $C_6D_6$ , 23°C, ppm) 136.00 (broad, tetra coordinated).

**Methyl-bis(1-tert-butyl-3-ethyltriazenido)****Aluminium(III)**

3.25 ml (6.5 mmol) of  $Al_2(CH_3)_6$  was reacted with 2.5g (19.35 mmol) of  $HN_3^tBuEt$  at 0°C in 50 ml dry hexane. Temperature was raised slowly to room temperature and the reaction mixture was stirred at room temperatures for 12h. Solvents were removed under vacuum. The isolated product was obtained *via* crystallization in hexane at -20°C. Crystals melt back to a yellow liquid at room temperature [m= 1.26g, yield = 64% /  $Al_2(CH_3)_6$ ].

Soluble in pentane, hexane, toluene.

Anal.: calcd for  $C_{13}H_{31}N_6Al$  (298.40  $g \cdot mol^{-1}$ ): C 52.28, H 10.39, N 28.15; found C 51.36, H 10.05, N 27.98%.

FT-IR (Nujol,  $cm^{-1}$ ) 1457 m, 1366 s, 1295 s, 1260 s, 1219 s, 1068 m, 1020 w, 896 w, 796 w, 614 m, 528 s.

$^1H$  NMR ( $C_6D_6$ , 23°C, ppm) -0.85 (s, 3H, Al -  $CH_3$ ), 1.04 (t, 6H,  $CH_3$ ,  $J = 7.22$  Hz), 1.16 (s, 18H, ( $C(CH_3)_3$ ), 3.42 (q, 4H, N- $CH_2$ ,  $J = 7.20$  Hz).

$^{13}C$  NMR ( $C_6D_6$ , 23°C, ppm) 16.80 (Al -  $CH_3$ ), 28.20 ( $CH_3$ ), 28.90 ( $CH_3$ )<sub>3</sub>, 29.51 ( $C(CH_3)_3$ ), 44.32 (N -  $CH_2$ ).

$^{27}Al$  NMR ( $C_6D_6$ , 23°C, ppm) 25.90 (tetra coordinated), 73.71 (penta coordinated), 98.42 (penta coordinated).

**Tris(1-tert-butyl-3-iso-propyltriazenido)****Aluminium(III)**

1.15 ml (2.3 mmol) of  $Al_2(CH_3)_6$  was reacted with 1g (6.93 mmol) of  $HN_3^tBu^iPr$  in 50ml anhydrous hexane and stirred at room temperature for 12h. Solvent and volatile materials have been evaporated under vacuum. The isolated compound is in the form of light yellow liquid, [m= 0.81g, yield = 78% /  $Al_2(CH_3)_6$ .]

Soluble in pentane, hexane, toluene.

Anal.: calcd for  $C_{21}H_{48}N_9Al$  (452.98  $g \cdot mol^{-1}$ ): C 55.63, H 10.60, N 27.82; found C 54.46, H 10.35, N 27.69%.

FT-IR (Nujol,  $cm^{-1}$ ) 2617 w, 1457 s, 1361 s, 1295 s, 1260 s, 1225 s, 1190 s, 1124 m, 1099 m, 1028 m, 932 w, 801 w, 664 s, 614 m, 558 s.

$^1H$  NMR ( $C_6D_6$ , 23°C, ppm) 1.11 (d, 18H,  $CH(CH_3)_2$ ,  $J = 6.55$  Hz), 1.14 (s, 27 H,  $C(CH_3)_3$ ), 3.61 (m, 3H, N-CH,  $J = 6.62$  Hz).

$^{13}C$  NMR ( $C_6D_6$ , 23°C, ppm) 22.47 ( $CH_3$ )<sub>2</sub>, 29.28 ( $CH_3$ ), 28.90 ( $C(CH_3)_3$ ), 49.94 ( $C(CH_3)_3$ ), 55.59 (N-CH).

$^{27}Al$  NMR ( $C_6D_6$ , 23°C, ppm) 25.13 (hexa coordinated), 78.81 (penta coordinated).

**Tris(1-butyl-3-*tert*-butyltriazenido) Aluminium(III)  $[Al(N_3^tBu^nBu)_3]_m$  (10)**

This complex was prepared by reacting 1.3 ml (2.6 mmol) of  $Al_2(CH_3)_6$  in dry hexane at 0°C with 1.22 g (7.8 mmol) of  $HN_3^tBu^nBu$  in dry hexane. Solvent and volatile materials have been removed under vacuum to obtain a yellow liquid, [m= 0.61g, yield = 47% /  $Al_2(CH_3)_6$ .]

Soluble in pentane, hexane, toluene.

Anal.: calcd for  $C_{24}H_{54}N_9Al$  (495.73 g.mol<sup>-1</sup>): C 58.10, H 10.89, N 25.42; found C 57.66, H 10.55, N 25.09%.

FT-IR (Nujol, cm<sup>-1</sup>) 1462 m, 1352 m, 1311 s, 1265 s, 1205 m, 1109 w, 1033 w, 528 w.

<sup>1</sup>H NMR ( $C_6D_6$ , 23°C, ppm) 0.74 (t, 9H,  $CH_3$ ,  $J = 7.54$  Hz), 1.07 (m, 6H,  $CH_2$ ), 1.18, 1.20, 1.21 (three singlets 27H, ( $C(CH_3)_3$ ), 1.43 (sextet, 6H,  $CH_2$ ,  $J = 7.54$  Hz) 3.39 (m, 6H, N- $CH_2$ ).

<sup>13</sup>C NMR ( $C_6D_6$ , 23°C, ppm) 13.62 ( $CH_3$ ), 20.34 (- $CH_2$ -), 27.96 ( $C(CH_3)_3$ ), 30.30 ( $C(CH_3)_3$ ), 51.12 ( $CH_2$ ), 55.58 (N -  $CH_2$ )

<sup>27</sup>Al NMR ( $C_6D_6$ , 23°C, ppm) 27.56 (hexa coordinated), 74.89 (tetra coordinated).

**Tris(1-*tert*-butyl-3-ethyltriazenido)-tris(pyridine) Aluminium(III)  $[Al(N_3^tBuEt)_3(py)_3]_m$  (11)**

To a stirred solution of 1.5 ml (3 mmol) of  $Al_2(CH_3)_6$  in 5 ml of dry pyridine was added at 0°C 0.8g (6.1 mmol) of  $HN_3^tBuEt$ . The temperature was allowed to increase gradually to room temperature and the light yellow solution was stirred for 12h. Volatile materials are removed under vacuum to give a light yellow powder. Light yellow crystals of the complex were obtained by crystallization in a mixture of pyridine/dry hexane at -20°C, [m= 2.01g, yield = 52% /  $Al_2(CH_3)_6$ .] Crystals melt back to liquids at room temperature.

Soluble in pentane, hexane, toluene.

Anal.: calcd for  $C_{33}H_{57}N_{12}Al$  (648 g.mol<sup>-1</sup>): C 61.11, H 8.80, N 25.93; found C 60.99, H 8.69, N 25.11%.

FT-IR (Nujol, cm<sup>-1</sup>) 2718 w, 2481 w, 2364 w, 2284 w, 2274 w, 2178 w, 1461 s, 1360 s, 1300 s, 1108 m, 1068 m, 1032 m, 891 m, 795 m, 714 m, 605 m, 527 m.

<sup>1</sup>H NMR ( $C_6D_6$ , 23°C, ppm) 1.13 (t, 9H,  $CH_3$ ,  $J = 7.22$  Hz), 1.31, 1.33, 1.36 (three singlets, 27H,  $C(CH_3)_3$ ,  $J = 11.31$  Hz), 3.53 (broad, 6H, N- $CH_2$ ), 6.67 (t, 6H,  $CH_2$ , pyridine,  $J = 11.31$  Hz), 6.99 (t, 6H,  $CH_2$ , pyridine,  $J = 7.56$  Hz), 8.52 (s, 3H, CH, pyridine).

<sup>13</sup>C NMR ( $C_6D_6$ , 23°C, ppm) 15.57 ( $CH_3$ ), 16.60 ( $C(CH_3)_3$ ), 29.36, 30.06 30.34 (three signals, ( $C(CH_3)_3$ ), 45.72 (N -  $CH_2$ ), 55.42 ( $CH_2$ , pyridine), 55.63 ( $CH_2$ , pyridine),

55.79 (CH, pyridine).

$^{27}\text{Al}$  NMR ( $C_6D_6$ , 23°C, ppm) 75.68 (hexa coordinated)

### Tris(1-*tert*-butyl-3-ethyltriazenido) Aluminium(III) [ $Al(N_3^tBuEt)_3$ ]<sub>m</sub> (12)

[ $Al(N_3^tBuEt)_3$ ]<sub>m</sub> (12) was prepared by reacting 0.678 g (6.7 mmol) of DMEAA in dry hexane at 0°C with 1.74 g (13.5 mmol) of  $HN_3^tBuEt$ . Temperature was let to increase to room temperature and the resulting colourless solution was stirred at room temperature for 12h. Solvent has been removed under vacuum to give a white solid that crystallizes in hexane at -20°C, [m= 2.37g, yield = 85% / DMEAA].

Soluble in pentane, hexane, toluene.

Anal.: calcd for  $C_{18}H_{42}N_9Al$  (411.56 g.mol<sup>-1</sup>): C 52.48, H 10.21, N 30.62; found C 51.66, H 10.05, N 30.09%.

FT-IR (Nujol, cm<sup>-1</sup>) 1456 s, 1375 m, 1305 s, 1269 m, 1214 m, 1073 w, 1032 w, 896 w, 800 w, 719 m, 689 w, 619 w, 537 m.

$^1H$  NMR ( $C_6D_6$ , 23°C, ppm) 1.01 (m, 9H,  $CH_3$ ,  $J=7.36$  Hz), 1.13 (s, 27H,  $C(CH_3)_3$ ), 3.37 (broad, 6H,  $N-CH_2$ ,  $J=6.67$  Hz).

$^{13}HNMR$  ( $C_6D_6$ , 23°C, ppm) 15.27 ( $CH_3$ ), 27.41( $C(CH_3)_3$ ), 29.32 ( $N-CH_2$ ), 44.69 ( $C(CH_3)_3$ ).

$^{27}Al$  NMR ( $C_6D_6$ , 23°C, ppm) 25.54 (hexa coordinated), 72.08 (tetra coordinated).

### Tris(1,3-di*tert*-butyltriazenido) Aluminium(III) [ $Al(N_3^tBu_2)_3$ ]<sub>m</sub> (13)

To 0.62 g (6.1 mmol) of DMEAA was added at 0°C 1.9 g (12.2 mmol) of  $HN_3^tBu_2$  and the resulting colourless solution was stirred at room temperature for 12h. Volatile materials were removed under vacuum. The isolated white powder was crystallized in anhydrous toluene [m= 2.35g, yield = 78% / DMEAA].

Soluble in pentane, hexane, toluene.

Anal.: calcd for  $C_{24}H_{54}N_9Al$  (495.73 g.mol<sup>-1</sup>): C 58.10, H 10.89, N 25.42; found C 57.64, H 10.44, N 24.89%.

FT-IR (Nujol, cm<sup>-1</sup>) 2637 m, 2521 w, 2375 w, 2279 w, 2158 w, 2122 w, 2014 w, 1880 w, 1578 w, 1456 s, 1365 s, 1305 s, 1259 s, 1199 s, 1027 m, 932 m, 770 m, 719 m, 629 s, 573 s, 553 s, 507 m, 437 m.

$^1HNMR$  ( $C_6D_6$ , 23°C, ppm) 1.17 (s, 54H,  $CH_3$ ).

$^{13}CNMR$  ( $C_6D_6$ , 23°C, ppm) 29.92 ( $CH_3$ ), 55.87 ( $C(CH_3)_3$ ).

$^{27}Al$  NMR ( $C_6D_6$ , 23°C, ppm) 23.75, (hexa coordinated), 76.09 (tetra coordinated).

**bis(1- *tert*-butyl, 3- ethyl triazenido)bis(dimethylamido)Titanium(IV)**  
**[ $Ti(N_3^tBuEt)_2(NMe_2)_2$ ] (14)**

Similarly, this complex was prepared by reacting 1.39g (6.2 mmol) of  $Ti(NMe_2)_4$  with 1.6 g (12.4 mmol) of  $HN_3^tBuEt$  in anhydrous hexane. Light orange-violet crystals of the complex were obtained by crystallization in anhydrous hexane at  $-20^\circ C$  that melt at room temperature. [m= 1.99g, yield = 82% /  $Ti(NMe_2)_4$ ].

Soluble in pentane, hexane, toluene.

Anal.: calcd for  $C_{16}H_{40}N_8Ti$  ( $392.40\text{ g.mol}^{-1}$ ): C 48.92, H 10.19, N 28.54; found C 48.84, H 10.09, N 28.61%.

FT-IR (Nujol,  $cm^{-1}$ ) 2751 m, 1457 s, 1371 s, 1350 s, 1280 m, 1209 w, 967 m, 737w.

$^1H$ NMR ( $CDCl_3$ ,  $23^\circ C$ , ppm) 1.10 (t, 6H,  $CH_3$ ,  $J=7.27$  Hz), 1.12 (s, 18H,  $C(CH_3)_3$ ), 3.25 (s, 12H,  $N(CH_3)_2$ ), 3.50 (broad s, 4H,  $N-CH_2$ ).

$^{13}C$ NMR ( $CDCl_3$ ,  $23^\circ C$ , ppm) 15.89 ( $CH_3$ ), 29.77 ( $C(\underline{CH_3})_3$ ), 33.41 ( $N-CH_2$ ), 49.96 ( $N(CH_3)_2$ ), 58.06 ( $\underline{C}(CH_3)_3$ ).

**bis(1- *tert*-butyl, 3- *iso*-propyl triazenido)bis(dimethylamido)Titanium(IV)**  
**[ $Ti(N_3^tBu^iPr)_2(NMe_2)_2$ ] (15)**

Similarly, this complex was prepared by reacting 1g (4.4 mmol) of  $Ti(NMe_2)_4$  with 1.15 g (8.8 mmol) of  $HN_3^tBu^iPr$  in anhydrous hexane. Light orange-violet crystals of the complex were obtained by crystallization in anhydrous hexane at  $-20^\circ C$ . [m= 1.01g, yield = 55% /  $Ti(NMe_2)_4$ ].

Soluble in pentane, hexane, toluene.

Anal.: calcd for  $C_{18}H_{44}N_8Ti$  ( $420.46\text{ g.mol}^{-1}$ ): C 39.95, H 10.46, N 26.63; found C 40.07, H 10.37, N 26.58%.

FT-IR (Nujol,  $cm^{-1}$ ) 2763 w, 1461 s, 1375 m, 1255 w, 1209 w, 956 w, 729w.

$^1H$ NMR ( $CDCl_3$ ,  $23^\circ C$ , ppm) 1.21 (d, 12H,  $(CH_3)_2$ ,  $J=5.47$  Hz), 1.27 (s, 18H,  $C(CH_3)_3$ ), 2.09 (m, 2H, CH,  $J=6.36$  Hz), 3.19 (s, 12H,  $N(CH_3)_2$ ).

$^{13}C$ NMR ( $CDCl_3$ ,  $23^\circ C$ , ppm) 24.32 ( $CH_3$ )<sub>2</sub>, 28.78 ( $C(\underline{CH_3})_3$ ), 32.17 (N-CH), 41.72 ( $N(CH_3)_2$ ), 58.26 ( $\underline{C}(CH_3)_3$ ).

**bis(1- *ditert*-butyl triazenidobis(dimethylamido)Titanium(IV)**  
**[ $Ti(N_3^tBu_2)_2(NMe_2)_2$ ] (16)**

Similarly, this complex was prepared by reacting 0.6g (2.64 mmol) of  $Ti(NMe_2)_4$  with 1.15 g (6.58 mmol) of  $HN_3^tBu_2$  in anhydrous hexane. Light orange-violet crystals of the complex were obtained by crystallization in anhydrous hexane at  $-20^\circ C$ . [m= 0.75 g, yield = 63% /  $Ti(NMe_2)_4$ ].

Soluble in pentane, hexane, toluene.

Anal.: calcd for  $C_{20}H_{48}N_8Ti$  ( $448.51 \text{ g.mol}^{-1}$ ): C 53.51, H 10.70, N 24.97; found C 53.59, H 10.60, N 24.89%.

FT-IR (Nujol,  $cm^{-1}$ ) 2814 s, 2768 s, 1450 s, 1411 s, 1396 s, 1360 s, 1280 s, 1245 s, 1200 s, 1088 s, 1038 m, 947 s, 760 w, 623 s, 563 s.

$^1H$ NMR( $CDCl_3$ ,  $23^\circ C$ , ppm) 1.14 (d, 36H,  $C(CH_3)_3$ ,  $J=8.75$  Hz), 3.27 (s, 12H,  $N(CH_3)_2$ ).

$^{13}C$ NMR( $CDCl_3$ ,  $23^\circ C$ , ppm) 29.88 ( $C(\underline{C}H_3)_3$ ), 30.58 ( $N(CH_3)_2$ ), 59.24 ( $\underline{C}(CH_3)_3$ ).

### **1,tert-butyl, 3-butyl triazenido tetrakis(dimethylamido) Niobium(V)** **$[Nb(N_3^tBuEt)(NMe_2)_4]$ (17)**

This complex was prepared by reacting 1g (3.2 mmol) of  $Nb(NMe_2)_5$  with 0.412 g (3.2 mmol) of  $HN_3^tBuEt$  in anhydrous hexane. Volatile materials have were under vacuum. Light yellow-orange crystals of the complex were obtained by crystallization in dry hexane at  $-20^\circ C$ . [m= 0.82g, yield = 65% /  $Nb(NMe_2)_5$ ].

Soluble in pentane, hexane, toluene.

Anal.: calcd for  $C_{14}H_{38}N_7Nb$  ( $397.40 \text{ g.mol}^{-1}$ ): C 42.74, H 9.56, N 4.66; found C 42.68, H 9.51, N 24.74%.

FT-IR (Nujol,  $cm^{-1}$ ) 2763 w, 1461 s, 1371 s, 1275 w, 1209 w, 963 m, 724w.

$^1H$ NMR( $CDCl_3$ ,  $23^\circ C$ , ppm) 1.13 (t, 3H,  $CH_3$ ,  $J=7.25$  Hz), 1.16 (s, 9H,  $C(CH_3)_3$ ), 3.14 (s, 24H,  $N(CH_3)_2$ ), 3.45 (q, 2H,  $N-CH_2$ ,  $J=7.25$  Hz).

$^{13}C$ NMR( $CDCl_3$ ,  $23^\circ C$ , ppm) 15.16, ( $CH_3$ ), 29.38 ( $C(\underline{C}H_3)_3$ ), 32.17( $N-CH_2$ ), 48.72 ( $N(CH_3)_2$ ), 59.43 ( $\underline{C}(CH_3)_3$ ).

### **1,tert-butyl, 3-ethyl triazenido tetrakis(dimethylamido) Tantalum(V)** **$[Ta(N_3^tBuEt)(NMe_2)_4]$ (18)**

To a stirred solution of 1 g (2.5 mmol) of pentakis(dimethylamino)tantalum(V)  $Ta(NMe_2)_5$  in dry hexane was added at  $0^\circ C$  0.32g (2.5 mmol) of  $HN_3^tBuEt$  in anhydrous hexane *via* cannula. The temperature was allowed to increase gradually to room temperature and stirred for 12h. Volatile materials were removed under vacuum to give an orange powder. Light yellow-orange crystals of the complex were obtained by crystallization in anhydrous hexane at  $-20^\circ C$ . [m= 0.88g, yield = 73% /  $Ta(NMe_2)_5$ ].

Soluble in pentane, hexane, toluene.

Anal.: calcd for  $C_{14}H_{38}N_7Ta$  ( $485.44 \text{ g.mol}^{-1}$ ): C 34.61, H 7.82, N 20.18; found C 34.69, H 7.94, N 20.11%.

FT-IR (Nujol,  $cm^{-1}$ ) 2771 m, 1455 s, 1366 s, 1275 w, 1209 m, 963 m, 730w.

$^1\text{H NMR}$  ( $\text{CDCl}_3$ ,  $23^\circ\text{C}$ ,  $\text{ppm}$ ) 1.074 (t, 3H,  $\text{CH}_3$ ,  $J=7.26$  Hz), 1.18 (s, 9H,  $\text{C}(\text{CH}_3)_3$ ), 3.85 (s, 24H,  $\text{N}(\text{CH}_3)_2$ ), 3.63 (q, 2H,  $\text{N}-\text{CH}_2$ ,  $J=7.25$  Hz).

$^{13}\text{C NMR}$  ( $\text{CDCl}_3$ ,  $23^\circ\text{C}$ ,  $\text{ppm}$ ) 15.26 ( $\text{CH}_3$ ), 29.38 ( $\text{C}(\text{CH}_3)_3$ ), 32.57 ( $\text{N}-\text{CH}_2$ ), 45.85 ( $\text{N}(\text{CH}_3)_2$ ), 57.01 ( $\text{C}(\text{CH}_3)_3$ ).

### Transport tests of Nb

From TGA data of  $\text{Nb}(\text{NMe}_2)_5$ , a heating temperature of  $150^\circ\text{C}$  seemed appropriate. This precursor which is in the form of black powder was placed in a bubbler type PicoHot300 which consists of a cylindrical receptacle whose upper face comprises an inlet tube and an outlet tube. They are themselves each equipped with a manual valve and an ALD automatic valve. The bubbler is surrounded by a device for heating the precursor up to  $300^\circ\text{C}$ . On heating at appropriate temperature, the precursor sublimates and can then be transported by a neutral carrier gas (hydrogen in this case). This carrier gas arrives in the course bubbler through the inlet valve and is fed back into the reaction chamber through the outlet valve. The flow rate of the carrier gas is set by the user. Finally, a sensor measures the pressure in the gas line and displays it versus time. To check if  $[\text{Nb}(\text{N}_3^t\text{BuEt})_2(\text{NMe}_2)_2]$  (**17**) can be transported, a simple test was performed. The 2 input valves are opened for a few seconds then closed. The same was done with exit valves. Then we can check on the display if there is a peak overpressure.

# Bibliography

- [1] M. Armbrüster, K. Kovnir, M. Friedrich, D. Teschner, G. Wowsnick, M. Hahne, P. Gille, L. Szentmiklósi, M. Feuerbacher, M. Heggen, F. Girgsdies, D. Rosenthal, R. Schlögl, and Y. Grin, *Nat. Mater.*, vol. 11, no. 8, p. 690, 2012.
- [2] P. Gille and B. Bauer, *Cryst. Res. Technol.*, vol. 43, no. 11, p. 1161, 2008.
- [3] A. Bos and K. Westerterp, *Chem. Eng. Process.*, vol. 32, no. 1, p. 1, 1993.
- [4] A. Molnar, A. Sarkany, and M. Varga, *J. Mol. Catal. A: Chem*, vol. 173, no. 1–2, p. 185, 2001.
- [5] H. Arnold, F. Dobert, J. Gaube, G. Ertl, H. Knoerzinger, and J. J. Weitkamp, *Handbook of Heterogeneous Catalysis*, VCH, Weinheim, p. 2156, 1997.
- [6] N. Stoloff, *Mater. Sci. Eng. A*, vol. 258, p. 1, 1998.
- [7] D. Morris and M. A. Morris-Munoz, *Adv. Eng. Mater.*, vol. 13, p. 43, 2011.
- [8] T. B. Massalski, H. Okamoto, P. R. Subramanian, and L. Kacprzak, *Binary Alloy Phase Diagrams, 2nd Edition*, 1990.
- [9] J. Grin, U. Burkhardt, and K. Ellner, M.; Peters, *Z. Kristall.*, vol. 209, no. 6, p. 479, 1994.
- [10] L. Piccolo, *Chem. Commun.*, vol. 49, p. 9149, 2013.
- [11] C. Vahlas, *Book Series on Complex Metallic Alloys*, vol. 49, p. 81, 2010.
- [12] A. C. Jones, *Chem. Vap. Deposition*, vol. 4, no. 5, 1998.
- [13] A. C. Jones, D. J. Houlton, S. A. Rushwarth, J. A. Flanagan, J. R. Brown, and G. W. Critchlow, *Chem. Vap. Deposition*, vol. 1, no. 1, p. 24, 1995.
- [14] R. A. Levy, M. L. Green, and P. K. Gallagher, *J. Electrochem. Soc.*, vol. 131, no. 9, p. 2175, 1984.

- [15] R. Bhat, M. Koza, C. Chang, S. Schwarz, and T. Harris, *J. Cryst. Growth*, vol. 77, no. 1, p. 7, 1986.
- [16] M. G. Simnionds, E. C. Phillips, J. W. Hwang, and W. L. Gladfelter, *Chemtronics*, vol. 3, p. 155, 1991.
- [17] M. G. Simnionds and W. L. Gladfelter, *The Chemistry of Metals CVD*, Weinheim, 1994.
- [18] K. Liu, D. Shen, J. Zhang, X. Wu, B. Li, Y. Lu, and X. Fan, *Solid State Commun.*, vol. 140, no. 1, p. 33, 2006.
- [19] R. Kaplan and N. Bottka, *Appl. Phys. Lett.*, vol. 41, no. 10, p. 972, 1982.
- [20] P. J. Walsh and N. Bottka, *J. Electrochem. Soc.*, vol. 131, no. 2, p. 444, 1984.
- [21] P. A. Lane, P. J. Wright, P. E. Oliver, C. L. Reeves, A. D. Pitt, J. M. Keen, M. C. L. Ward, M. E. G. Tilsley, and N. A. Smith, *Chem. Vap. Deposition*, vol. 3, no. 2, p. 97, 1997.
- [22] F. Senocq, F. Duminica, F. Maury, T. Delsol, and C. Vahlas, *Solid State Commun.*, vol. 153, no. 12, p. G1025, 2006.
- [23] G. J. M. Dormans, *J. Cryst. Growth*, vol. 108, no. 3-4, p. 806, 1991.
- [24] R. Feurer, M. Larhafi, R. Morancho, and R. Calsou, *Thin Solid Films*, vol. 167, no. 1, p. 195, 1988.
- [25] S. Park, S. Lim, and H. Choi, *Chem. Mater.*, vol. 18, no. 22, p. 5150, 2006.
- [26] L. C. Kalutarage, P. D. Martin, M. J. Heeg, and C. H. Winter, *J. Am. Chem. Soc.*, vol. 135, no. 34, p. 12588, 2013.
- [27] M. C. Karunaratne, T. J. Knisley, G. S. Tunstall, M. Heeg, and C. H. Winter, *Polyhedron*, vol. 52, p. 820, 2013.
- [28] L. C. Kalutarage, P. D. Martin, M. J. Heeg, and C. H. Winter, *Inorg. Chem.*, vol. 52, no. 9, p. 5385, 2013.
- [29] L. C. Kalutarage, M. J. Heeg, P. D. Martin, M. J. Saly, D. S. Kuiper, and C. H. Winter, *Inorg. Chem.*, vol. 52, no. 3, p. 1182, 2013.
- [30] T. J. Knisley, M. J. Saly, M. J. Heeg, J. L. Roberts, and C. H. Winter, *Organometallics*, vol. 30, no. 18, p. 5010, 2011.

- [31] A. N. Cloud, L. M. Davis, G. S. Girolami, and J. R. Abelson, *J. Vac. Sci. Technol., A*, vol. 32, no. 2, 2014.
- [32] G. Chandra, A. D. Jenkins, M. F. Lappert, and R. C. Srivastava, *J. Chem. Soc. A*, p. 2550, 1970.
- [33] F. T. Edelmann, *Chem. Soc. Rev.*, vol. 38, p. 2253, 2009.
- [34] Z. Li, A. Rahtu, and R. G. Gordon, *J. Electrochem. Soc.*, vol. 153, no. 11, p. C787, 2006.
- [35] H. Li, D. B. Farmer, R. G. Gordon, Y. Lin, and J. Vlassak, *J. Electrochem. Soc.*, vol. 154, no. 12, p. D642, 2007.
- [36] V. Krisyuk, A. N. Gleizes, L. Aloui, A. Turgambaeva, B. Sarapata, N. Prud'Homme, F. Senocq, D. Samélor, A. Zielinska-Lipiec, D. de Caro, and C. Vahlas, *J. Electrochem. Soc.*, vol. 157, no. 8, p. D454, 2010.
- [37] B. S. Lim, A. Rahtu, and R. G. Gordon, *Nat. Mater.*, vol. 2, no. 11, p. 749, 2003.
- [38] P. Griess, *Liebigs Ann.*, vol. 121, no. 3, p. 257, 1862.
- [39] O. Dimroth, *Chem. Ber.*, vol. 39, no. 4, p. 3905, 1906.
- [40] C. A. Rouzer, M. Sabourin, T. L. Skinner, E. J. Thompson, T. O. Wood, G. N. Chmurny, J. R. Klose, J. M. Roman, R. H. Smith, and C. J. Michejda, *Chem. Res. Toxicol.*, vol. 9, no. 1, p. 172, 1996.
- [41] T. A. Connors, P. M. Goddard, K. Merai, W. C. J. Ross, and D. E. V. Wilman, *Biochem. Pharmacol.*, vol. 25, no. 3, p. 241, 1976.
- [42] K. C. Nicolaou, C. N. C. Boddy, H. Li, A. E. Koumbis, R. Hughes, S. Natarajan, N. F. Jain, J. M. Ramanjulu, S. Brase, and M. E. Solomon, *Chem. Eur. J.*, vol. 5, no. 9, p. 2602, 1999.
- [43] L. Jones, J. S. Schumm, and J. M. Tour, *J. Org. Chem.*, vol. 62, no. 5, p. 1388, 1997.
- [44] W. Wirschun, M. Winkler, K. Lutz, and J. Jochims, *J. Chem. Soc. Perkin Trans.*, p. 1755, 1998.
- [45] M. Corbett and B. Hoskins, *Inorg. Nucl. Chem. Lett.*, vol. 6, no. 3, p. 261, 1970.
- [46] E. Pfeiffer, *Thesis, Triazenido and related ligands in metal-cyclopentadienyl complexes of Mo, W, Fe, Co, Ni and Pd, Amsterdam, 1979.*

- [47] D. H. Gerlach, W. G. Peet, and E. L. Muetterties, *J. Am. Chem. Soc.*, vol. 94, no. 13, p. 4545, 1972.
- [48] M. V. Baker and L. D. Field, *Appl. Organomet. Chem.*, vol. 4, no. 5, p. 551, 1990.
- [49] F. Dumestre, B. Chaudret, C. Amiens, P. Renaud, and P. Fejes, *Appl. Organomet. Chem.*, vol. 4, no. 5, p. 551, 1990.
- [50] S. T. Barry, *Coord. Chem. Rev.*, vol. 257, no. 23-24, p. 3192, 2013.
- [51] A. K. Maity, A. J. Metta-Magana, and S. Fortier, *Inorg. Chem.*, vol. 54, no. 20, p. 10030, 2015.
- [52] L. Fohlmeister, C. Liu, S. Schulten, B. Moubaraki, A. Stasch, J. D. Cashion, K. S. Murray, L. Gagliardi, and C. Jones, *Angew. Chem. Int. Ed.*, vol. 51, no. 33, p. 8294, 2012.
- [53] B. S. Lim, A. Rahtu, J. S. Park, and R. G. Gordon, *Inorg. Chem.*, vol. 42, no. 24, p. 7951, 2003.
- [54] S. R. Foley, G. P. A. Yap, and D. S. Richeson, *Inorg. Chem.*, vol. 41, no. 16, p. 4149, 2002.
- [55] T. J. J. Sciarone, C. Nijhuis, A. Meetsma, and B. Hessen, *Dalton Trans.*, vol. 41, p. 4896, 2006.
- [56] C. A. Nijkuis, E. Jellema, T. J. J. Sciarone, A. Meetsma, P. H. M. Budzelaar, and B. Hessen, *Eur. J. Inorg. Chem.*, vol. 11, p. 2089, 2005.
- [57] T. R. Holman, C. Juarez-Garcia, M. P. Hendrich, L. J. Que, and E. Munck, *J. Am. Chem. Soc.*, vol. 112, no. 21, p. 7611, 1990.
- [58] C. Krebs, R. Davydov, J. Baldwin, B. M. Hoffman, J. M. Bollinger, and B. H. Huynh, *J. Am. Chem. Soc.*, vol. 122, no. 22, p. 5327, 2000.
- [59] T. Ikeue, Y. Ohgo, T. Saitoh, M. Nakamura, H. Fujii, and M. Yokoyama, *J. Am. Chem. Soc.*, vol. 122, no. 17, p. 4068, 2000.
- [60] A. V. Astashkin, A. M. Raitsimring, A. R. Kennedy, T. K. Shokhireva, and F. A. Walker, *J. Phys. Chem. A*, vol. 106, no. 1, p. 74, 2002.
- [61] L. A. Yatsunyk and F. A. Walker, *Inorg. Chem.*, vol. 43, no. 14, p. 4341, 2004.
- [62] O. Y. Lyakin, R. V. Ottenbacher, K. P. Bryliakov, and E. P. Talsi, *ACS Catal.*, vol. 2, no. 6, p. 1196, 2012.

- [63] G. Simonneaux, V. Schuenemann, C. Morice, L. Carel, L. Toupet, H. Winkler, A. X. Trautwein, and F. A. Walker, *J. Am. Chem. Soc.*, vol. 122, no. 18, p. 4366, 2012.
- [64] Y. Z. Zheng, W. Xue, M. L. Tong, X. M. Chen, F. Grandjean, and G. J. Long, *Inorg. Chem.*, vol. 47, no. 10, p. 4077, 2008.
- [65] P. H. Yang, K. F. Liou, and Y. T. Lin, *J. Organomet. Chem.*, vol. 307, no. 3, p. 273, 1986.
- [66] T. W. Jang, W. Moon, J. T. Baek, and B. T. Ahn, *Thin Solid Films*, vol. 333, no. 1-2, p. 137, 1998.
- [67] F. Pelletier, D. Ciuculescu, J. G. Mattei, P. Lecante, M. J. Casanove, N. Yaacoub, J. M. Greneche, C. Schmitz-Antoniak, and C. Amiens, *Chem. Eur. J.*, vol. 19, no. 19, p. 6021, 2013.
- [68] P. Popčević, A. Smontara, J. Ivkov, M. Wencka, M. Komelj, and P. Jeglič, *Phys. Rev. B*, vol. 81, no. 18, p. 184203, 2010.
- [69] M. Wittmer, B. Studer, and H. Melchior, *J. Appl. Phys.*, vol. 52, p. 5722, 1981.
- [70] M. Islam, R. Whurer, and M. Berkahn, *Mater. Forum*, vol. 32, p. 129, 2008.
- [71] Y. Gotoh, M. Nagao, T. Ura, H. Tsuji, and J. Ishikawa, *Nucl. Instrum. Methods Phys. Res. Sect. B*, vol. 148, no. 1-4, p. 925, 1999.
- [72] I. Ayerdi, E. Castano, A. Garcia-Alonso, and J. Gracia, *Sens. Actuators A*, vol. 60, no. 1-3, p. 72, 1997.
- [73] A. Newport, C. J. Carmalt, I. P. Parkin, and S. A. O'Neill, *J. Mater. Chem.*, vol. 12, no. 6, p. 1906, 2002.
- [74] K. Sugiyama, S. Pac, Y. Takahashi, and S. Motojima, *J. Electrochem. Soc.*, vol. 122, no. 11, p. 1545, 1975.
- [75] C. H. Winter, J. W. Proscia, A. L. Rheingold, and T. S. Lewkebandara, *Inorg. Chem.*, vol. 33, no. 6, p. 1227, 1994.
- [76] C. Carmalt, A. C. Newport, S. A. O'Neill, I. P. Parkin, A. P. White, and D. J. Williams, *Inorg. Chem.*, vol. 44, no. 3, p. 615, 2005.
- [77] T. Waters, A. G. Wedd, M. Ziolek, and I. Nowak, *Comprehensive Coordination Chemistry II*, vol. 4, p. 241, 2004.

- [78] A. Baunemann, D. Bekermann, T. B. Thiede, H. Parala, M. Winter, C. Gemel, and R. A. Fischer, *Dalton Trans.*, vol. 28, p. 3715, 2008.
- [79] X. Liu, J. R. Babcock, M. A. Lane, J. A. Belot, A. W. Ott, M. V. Metz, C. R. Kannewurf, R. P. H. Chang, and T. J. Marks, *Chem. Vap. Deposition.*, vol. 7, no. 1, p. 25, 2001.
- [80] A. Newport, J. E. Bleau, C. J. Carmalt, I. P. Parkin, and S. A. O'Neill, *J. Mater. Chem.*, vol. 14, no. 22, p. 3333, 2004.
- [81] X. Chen, G. G. Peterson, C. Goldberg, G. Nuesca, H. Frisch, A. E. Kaloyeros, B. Arkles, and J. Sullivan, *J. Mater. Res.*, vol. 14, no. 5, p. 2043, 1999.
- [82] M. H. Tsai, S. C. Sun, H. T. Chiu, C. E. Tsai, and S. H. Chuang, *Appl. Phys. Lett.*, vol. 67, no. 8, p. 1128, 1995.
- [83] T. Chen, C. Xu, T. H. Baum, G. T. Stauf, J. F. Roeder, A. G. DiPasquale, and A. L. Rheingold, *Chem. Mater.*, vol. 22, no. 1, p. 27, 2010.
- [84] T. S. Lewkebandara, P. J. Mckarns, B. S. Haggerty, G. P. A. Yap, A. L. Rheingold, and C. H. Winter, *Polyhedron*, vol. 17, no. 1, p. 1, 1997.
- [85] M. Quesada-Gonzalez, N. D. Boscher, G. R. Han, and I. P. Parkin, *Appl. Mater. Interfaces*, vol. 8, p. 25024, 2016.
- [86] T. H. Xu, C. L. Song, Y. Liu, and I. P. Parkin, *J. Zhejiang Univ. Sci. B*, vol. 7, p. 299, 2006.
- [87] R. Quesada-Carera, C. Sotelo-Vazquez, J. A. Darr, and I. P. Parkin, *Appl. Cat. B*, vol. 160, p. 582, 2014.
- [88] J. M. Millet, C. Virely, M. Forissier, P. Bussiere, and J. C. Vedrine, *Hyperfine Interact.*, vol. 46, no. 1-4, p. 619, 1989.
- [89] R. C. Clark and J. S. Reid, *Acta Cryst.*, vol. A51, no. 6, p. 887, 1995.
- [90] A. Altomare, C. Giacovazzo, A. Guagliardi, A. Grazia, G. Moliterni, and R. Rizzi, *J. Appl. Cryst.*, vol. 32, no. 5, p. 963, 1999.
- [91] P. W. Betteridge, J. R. Carruthers, R. I. Cooper, K. Prout, and D. Watkin, *J. Appl. Cryst.*, vol. 36, no. 6, p. 1487, 2003.
- [92] T. D. Humphries, K. T. Munroe, A. Decken, and G. S. McGrady, *Dalton Trans.*, vol. 42, no. 19, p. 6965, 2013.

- [93] J. C. Bottaro, P. E. Penwell, and R. J. Schmitt, *Synth. Commun.*, vol. 27, no. 9, p. 1456, 1979.
- [94] R. A. Anderson, K. Faegri, J. C. Green, A. Haaland, M. F. Lappert, W. P. Leung, and K. Rypdal, *Inorg. Chem.*, vol. 27, no. 10, p. 1782, 1988.



# List of publications

## Articles

[1] I. G. Aviziotis, T. Duguet, **K. Soussi**, G. Kokkoris, N. Cheimarios, C. Vahlas and A. Boudouvis, "Investigation of the kinetics of the chemical vapor deposition of aluminum from dimethylethylamine alane: experiments and computations", *Phys. Status Solidi C*, vol. 12, no. 7, P. 923, 2015.

[2] **K. Soussi**, S. Mishra, E. Jeanneau, J. M. Millet, L. Khrouz, B. Le Guennic, J. B. Tommasino, and S. Daniele, " Asymmetrically substituted triazene as poor donor ligands in precursor chemistry of iron(II) for the synthesis of iron based metallic and intermetallic nonocrystals" , to be submitted soon.

[3] **K. Soussi**, S. Mishra, E. Jeanneau, and S. Daniele, " Synthesis and precursor chemistry of novel transition metal triazenides" , manuscript under preparation.

## Oral communications

[4] **K. Soussi**, S. Mishra, I. G. Aviziotis, T. Duguet, A. Boudouvis, C. Vahlas, and S. Daniele, "Revêtements Al et Fe par MOCVD dans des conditions compatibles : Vers de nouveaux catalyseurs intermétalliques," *Matériaux*, Montpellier, France, 24-28 Nov. 2014.

[5] **K. Soussi**, S. Mishra, E. Jeanneau and S. Daniele, "Asymmetric ligand approach to design volatile molecular precursors for the Al-Fe intermetallic catalyst," *EuCheMS*, Seville, Spain, 2016.

## Posters

[6] **K. Soussi**, S. Mishra, and S. Daniele , "MOCVD of Fe and Al thin films under compatible conditions for the preparation of intermetallic catalyst coatings," *Journée des doctorants, Université Lyon1*, Villeurbanne, France, may 2014.

- [7] K. Soussi, I. G. Aviziotis, T. Duguet, S. Mishra, A. Cabiac, C. Thomazeau, T. Cseri, A. G. Boudouvis, S. Daniele and C. Vahlas, "MOCVD of Fe and Al coatings under compatible conditions: towards intermetallic catalyst coatings," *C-Mac days*, Zagreb, Croatia, 8-11 Dec. 2014.